Resonant Aeroacoustic Source Localisation In Ducted Bluff Body Flows

---

Shane Leslie Finnegan

Department of Mechanical & Manufacturing Engineering

Parsons Building

Trinity College

Dublin 2

Ireland

March 2011

A thesis submitted to the University of Dublin in partial fulfilment of the requirements for the degree of Ph.D.

Declaration

I declare that I am the author of this report and that all work described herein is my own, unless otherwise referenced. Furthermore, this work has not been submitted in whole or part, to any other university or college for any degree or qualification.

I authorise the library of Trinity College, Dublin to lend this thesis.

Shane Finnegan, March 2011

Abstract

The energy transfer mechanism between the flow field and the sound field in a heat exchanger tube array is not well understood. To address this, an investigation of the flow-acoustic coupling in ducted bluff bodies is presented. The theory of vortex sound developed by Howe [1] is used to identify which regions of the flow field have positive contribution (sound generation) and negative contribution (sound absorption) to acoustic resonance. This study differs from previous ones as a conceptual approach using particle image velocimetry (PIV), finite element analysis (FEA) and a single microphone has been developed to experimentally resolve the components in Howe's integral. This approach has been successfully applied to two tandem cylinders, four cylinders in a group and inline tube bundles. For each configuration, first mode resonance was forced via loudspeakers. For two tandem cylinders, "lock-on" occurs before and after acoustic-Strouhal coincidence. It is found that vortex shedding in the gap region between the cylinders and vortex shedding in the wake forms the dominant sources before acoustic-Strouhal coincidence. These vortices are highly synchronised. After acoustic-Strouhal coincidence, vortex shedding in the downstream wake forms the dominant sources as the shear layers in the gap region act as strong sinks. For the inline array, vortex shedding between the first and second rows of cylinders is found to have the strongest influence on the generation of acoustic resonance. However, synchronised structures formed from deeper rows also have a significant contribution. The acoustic response of four cylinders is similar to that of two tandem cylinders as "lock-in" occurs before and after acoustic-Strouhal coincidence. However, the energy transfer mechanisms are quite different as the flow velocities at which resonance occur, are not the same. It is proposed that the vortex convection velocity in the wake of the cylinders is an important parameter and should be included when classifying bluff body resonance, particularly when comparing different geometric configurations.

Acknowledgements

So many people have contributed towards my work. Without your input, this thesis would be so much less.

I would like to thank my supervisor, Dr. Craig Meskell whose help and support has been invaluable. You always knew the right path out of the dark forest that is ducted bluff body resonance. I would also like to thank Prof. Samir Ziada of McMaster University and Prof. Peter Oshkai of the University of Victoria whose knowledge and experience in the field were great assets. I would also like to express my gratitude to the rest of the academic staff in Mechanical Engineering, particularly Prof. John Fitzpatrick and Dr. Gareth Bennett for their informative input.

Thanks must also be given to the administrative and technical staff. Particularly Joan Gillen who took care of all my clerical requests, John Gaynor who provided IT support and Mick Reilly and his team in the work shop who all helped construct my test section.

Thank you to everyone in the Fluids Lab. You have all made my time in the office very enjoyable. In particular, I would like to thank Dr. John Mahon for sharing his expertise in everything that is experimental fluid mechanics. What will the Fluids Lab do when you leave!

To all of my friends, thank you for taking a keen if not confused interest in my work. You distracted me when wind tunnels and lasers all became too much! To my Mum and Dad and my sister Andrea I sincerely thank you for the help and advice you have always given me. Your immense support in everything I do is the reason I am where I am.

I would lastly, like to thank Niamh. My loving girlfriend. Words cannot express how truly grateful I am that you are in my life. Your patience and understanding knows no bounds and without you by my side I would not have been able to complete this thesis. For this I am deeply indebted to you.

"It's All In A State Of Mind"

If you think you are beaten, you are,
If you think you dare not, you don't,
If you like to win, but you think you can't,
It's almost a "cinch" you won't.
If you think you'll lose, you've lost,
For out in the world you find
Success begins with a fellow's will;
It's all in the state of mind.

Walter D. Wintle (Adapted)

Contents

List of Figures

Nomenclature

Symbol	Description
A	Area
$\underline{A}, \underline{B}, \underline{C}$	Vector quantities
B	Total enthalpy
D	Cylinder diameter
D_c	Side-branch depth
E	Net acoustic energy transfer per streamwise location per cycle
E^*	Normalised net acoustic energy transfer per streamwise location per cycle
F_i	Dipole strength per unit area
$I1, I2$	Particle intensity of the first and second PIV image frames
I_D	Dipole intensity
I_Q	Quadrupole intensity
L	Transverse centre-to-centre pitch
L/D	Transverse pitch ratio
L_c	Side-branch diameter
Ma	Mach number
N	Number of PIV acquisitions
P	Streamwise centre-to-centre pitch
P/D	Streamwise pitch ratio
P^*	Normalised acoustic pressure
P_g^*	Normalised acoustic pressure based on gap velocity
P_a	Acoustic pressure amplitude
P_{FEA}	Spatial acoustic pressure solved by ANSYS
$\widehat{P}_{FEA}$	Temporal acoustic pressure distribution

Symbol	**Description**
P_{M1}	Temporal acoustic pressure measured by M1
Re, Re_{v_∞}	Reynolds number based on mainstream velocity
Re_{v_g}	Reynolds number based on gap velocity
S	A surface or contour
St, St_u	Strouhal number based on mainstream velocity
St_a	Strouhal number based on duct natural acoustic frequency
St_g	Strouhal number based on gap velocity
T	Staggered centre-to-centre pitch
T_{ij}	Lighthills stress tensor - Quadrupole strength per unit volume
T_u	Turbulence intensity
U_a	Acoustic particle velocity
$\widehat{U}_a$	Acoustic velocity amplitude
$\widehat{U}_a/V_\infty$	Dimensionless acoustic velocity ratio based on mainstream velocity
$\widehat{U}_a/V_g$	Dimensionless acoustic velocity ratio based on gap velocity
U_r	Reduced velocity based on mainstream velocity
U_{rg}	Reduced velocity based on gap velocity
V	Hydrodynamic velocity field
V_g	Gap velocity
V_∞	Mainstream flow velocity
c	Speed of sound in air (343 m/s)
dx, dy	Most probable PIV particle displacements
dt	Time between PIV laser pulses
f_a	Natural acoustic frequency of the duct
f_a/f_v	Frequency ratio
f_e	Excitation frequency other than f_a
f_{samp}	Data acquisition sampling frequency
f_v	Vortex shedding frequency
h	Height of the duct
i, j	[1, 1]

Symbol	Description
k	Wave number
$\underline{n}$	Unit vector normal to a surface
p	Hydrostatic pressure
p_{ij}	Stress between adjacent fluid elements in the i, j directions
r	Distance between the source and the observer
s	Correlation spatial coordinate
t	Time
u	Streamwise velocity field component
u'	Streamwise Fluctuating velocity
$\overline{u}$	Mean streamwise velocity
v	Transverse velocity field component
$\widehat{v}$	Incompressible velocity field $(V + U_a)$
v_i, v_j	Velocity in the i, j directions
x	Streamwise direction
x/D	Normalised streamwise direction
x_i, x_j	Spatial coordinates in the i, j directions
y	Transverse direction
y/D	Normalised transverse direction
$\mathbf{x}$	Acoustic receiver coordinate
$\mathbf{y}$	Acoustic source coordinate
α	Cylinder configuration orientation to the oncoming flow
δ_{ij}	Delta function in the i, j directions
ϕ	Phase of the acoustic pressure time signal
$\nabla\Phi$	Acoustic particle velocity
Γ	Circulation
λ	Wavelength
μ	Kinematic viscosity
ν	Dynamic viscosity
$\Pi, \Pi_{gen}, \Pi_{abs}$	Acoustic power, generation, absorption

Symbol	**Description**
ρ, ρ_0	Density, mean density
τ	Data acquisition period
θ	Angle between a source and observer
ω	Vorticity
$\overline{\omega}$	Mean vorticity enclosed within a contour
$\Re$	Volumetric flow field
Ψ	Non-dimensional Buckingham-Pi group
ζ	Peak-locking coefficient
DEHS	Diethylhexylsebacate
FFT	Fast Fourier Transfer
$HW1$	Hotwire 1
$HW2$	Hotwire 2
ITB	Inline tube bundle
$M1$	Microphone 1
PIV	Particle Image Velocimetry
RMS	Root Mean Square
SPL	Sound Pressure Level
2TC	Two tandem cylinders
4C	Four cylinders

Chapter 1

Introduction

1.1 Motivation

Standing near the pier of a marina on a windy day, one may notice a loud whistling noise radiating from the yachts. This piercing noise is a classic case of an aeolian tone. The mechanism generating this sound is the culmination of the interaction between the vortices being shed from the mast and the halyards of one yacht with another as the wind funnels through. Interactions of the vortices shed from these types of bluff bodies have been well established and finds particular relevance in the generation of noise in various engineering applications.

One such application is a shell and tube heat exchanger typically found in an industrial power plant. A heat exchanger consists of an array of cylinders encased in a duct exposed to cross flow. Vortex shedding from the cylinders generates a pressure disturbance which reflects off surrounding surfaces and creates a feedback loop. This feedback enhances the shedding process and a standing wave of the duct may become excited. This phenomenon is referred to as acoustic resonance and is a major design concern. When a system resonates it is accompanied by a significantly increased acoustic pressure compared to that at off-resonant conditions. Eisinger and Sullivan [3] have measured sound pressures of 3436 Pa (164.7 dB) in a full service heat exchanger. This pressure significantly exceeded the dynamic head of the mean flow through the bundle and the system entered into a vibratory state. Such operating conditions are indeed a major design concern as continued use may induce a violent vibration of the long slender pipes which in turn could lead to failure of the heat exchanger. Moreover, from a health and safety point of view, the

elevated sound pressures associated with acoustic resonance can be harmful to the plant workers.

Subsequently a significant body of knowledge has been developed over the years. Particular attention has been given to the flow structure/acoustic response of the system and the mechanisms generating the resonance are broadly understood. However, the locations at which these mechanisms have their greatest contribution remains uncertain. In other words, the precise regions where the heat exchanger is "noisy" and "quiet" is unknown. Therefore a study of the flow-acoustic coupling in an array of tubes, modelling a heat exchanger, seems warranted.

1.2 Objectives

Although well studied, the main objective of this work is to further improve our understanding of the resonant acoustic behaviour in an array typical of a heat exchanger. In particular, the energy transfer mechanism between the flow field and the sound field is of interest, as it will identify those regions of the system which generate acoustic resonance and those regions of the system which suppress acoustic resonance.

The theory of vortex sound developed by Howe [1], which relates the acoustic power generated in an isentropic mean flow to its characteristic quantities is used as the basis of this work. Previous studies utilising Howe's theory have mostly been numerical or analytic due to the difficulty in resolving the flow field characteristics around bluff body systems experimentally. This study endeavours to use mainly experimental means.

Studying the flow-acoustic interaction mechanisms in tube bundles is difficult because of their geometric complexity. Therefore, simplified geometric configurations are investigated initially. Two tandem cylinders and four cylinders orientated in a group are studied as they can be considered to be the constituent components of a full inline array. The motivation of these studies is to prepare for the challenges set by the inline array as each configuration adds a new level of complexity to the previous one. They are essentially stepping stones towards studying full inline arrays.

The two tandem cylinder study has a similar focus to that of Mohany [4] and Mohany and Ziada [5]. Its primary objective is to develop an initial understanding of the basic

mechanism generating acoustic resonance. A second, equally important objective is to test the suitability of the conceptual approach for studying flow-acoustic coupling of any ducted bluff body by using experimental means. This is achieved by comparison of the observed experimental results with previously completed numerical simulations of the process obtained from literature.

The acoustic response of four cylinders in a group has been largely neglected and this study sheds new light onto our understanding of ducted bluff body resonance. The objective of this part of the work is similar to the tandem cylinder configuration tests, in that it will investigate the suitability of using the conceptual approach for studying more complex geometries. Moreover, the effect of parameters such as the transverse spacing ratio, the streamwise spacing ratio and the oncoming flow velocity are evaluated. Studies by other authors have shown these parameters to be influential on the acoustic resonance mechanisms for other geometries.

1.3 Thesis outline

This thesis is separated into seven further chapters. Chapter two introduces the state of the art and details some areas of the literature that have not been addressed. An in depth explanation of the physical flow structure and acoustic response of the three tested configurations is given so as to properly introduce the subject. Chapter three describes the conceptual approach that was applied in this study. The basis of all the experiments hinges on the methods described herein. A derivation of Howe's integral is provided in this chapter. Chapter four details the experimental facilities used to study the energy transfer mechanisms between the flow field and the sound field. Chapter five describes the results from the two tandem cylinder configuration, Chapter six will highlight the results from the four cylinder configurations and Chapter seven illustrates the results from the full inline tube array. Often, reference to the other configurations is made in these chapters as the underlying physics appear to be the same. Each results chapter has a summary section where the main conclusions drawn from work are conveyed. The final chapter summarises the main observations and critically assesses what further research might be usefully pursued in the area.

Chapter 2

Literature Review

2.1 Introduction

This chapter details some of the work completed by other authors. It is divided in to three main sections. The first and second sections describe the fluid mechanics and acoustic behaviour of ducted bluff body flows, whilst the third section describes a brief introduction to aeroacoustic theory.

2.2 Fluid mechanics of bluff bodies

2.2.1 Flow over a single cylinder

2.2.1.1 Vortex shedding

The essential flow behaviour over a single cylinder in cross flow has been well established and described by various texts on fluid mechanics, see Massey [6] for example. When a cylinder interacts with a fluid in cross flow, retarded viscous flow forms a boundary layer along the surface of the cylinder at the front stagnation point. The velocity of the fluid relative to the cylinder is zero at the surface, but increases rapidly to that of the mainstream flow throughout the boundary layer thickness. As this boundary layer is very small in comparison to the characteristic diameter of the cylinder, high velocity gradients exist. As a result, the shear stress in the flow is high and a shear layer forms from the surface of the cylinder when the boundary layer separates. Separation occurs due to an adverse pressure gradient in the flow. Figure 2.1 shows the velocity and pressure distributions in the boundary layer along the top of a cylinder. The development of the

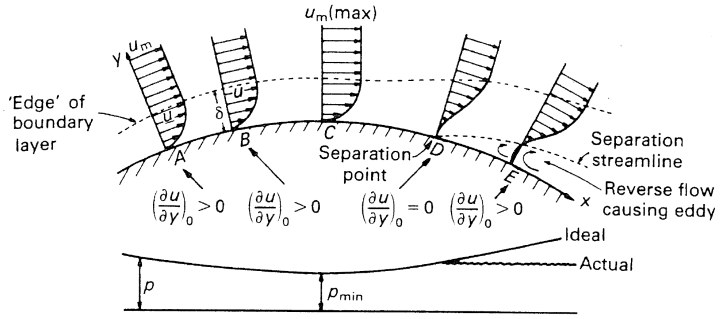

Figure 2.1: Boundary layer development of a circular cylinder, Massey [6].

boundary layer and the location of the separation points on the cylinder depends on the Reynolds number, Re, which is a non-dimensional ratio between the viscous and inertial forces in the flow. The Reynolds number for a cylinder is defined as

$$Re = \frac{\rho V_\infty D}{\mu} \tag{2.1}$$

where ρ is the density of the fluid, μ is the kinematic viscosity and D is the cylinder diameter.

Gerrard [7] classified the mechanisms of vortex shedding in the formation region. This is usually defined as the region between the cylinder and that point where fluid from outside the wake first crosses the axis of the cylinder [7]. Figure 2.2 shows the formation region by means of filament lines within the rolled-up shear layers. It is clear to see that the flow follows three paths. Path 'a' is the flow entrained by the strengthening vortex, path 'b' is the flow entrained by the shear layer whilst path 'c' is a reversed flow that makes its way into the interior formation region. The flow of path 'c' bears vorticity of the opposite sign to that of the entrained flow but is much weaker than that of the shear layer flow [7]. The circulation of these flows vary separately with increasing Reynolds number. The circulation of flow 'a' will not increase with Reynolds number but the circulation of flow 'b' (which is governed by the length of the turbulent shear layer) will. This results in the weakening of the circulation of flow 'c'. In fact, most of flow 'c' remains in the interior formation region and is cancelled by the flow shed from the other side of the cylinder in the next half period [7]. The vortex formed by these three flows will continue to grow in strength as it is fed circulation from the shear layer. At some instant when the vortex is strong enough, it will draw the other shear layer, which has oppositely

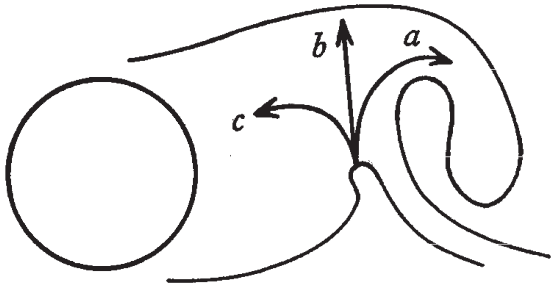

Figure 2.2: Vortex formation region showing entrained flows, Gerrard [7].

signed circulation, across the width of the cylinder [7]. Providing the drawn shear layer has sufficient vorticity it will effectively cut off the vortex from the shear layer. Following this, the vortex will no longer increase in strength [7]. This vortex is then considered to be shed from the cylinder [7] and will dissipate as it propagates downstream.

The separated vortex (along with the other vortices shed before it) forms a vortex street in the wake of the cylinder. The wake is a region downstream of the cylinder characterised by local velocity variations and is one of four sub-regions discussed by Zdravkovich [8] when he classified the disturbed flow surrounding a cylinder. Figure 2.3 shows these four regions which are defined as:

(i) Narrow retarded flow region

(ii) Cylinder boundary layer

(iii) Displaced and accelerated flow region

(iv) Separated flow wake region

Similarly to the formation of the boundary layer on the cylinder, the flow structure in the wake region depends on Reynolds number. Lienhard [9] classified the structure of the separated flow in the wake region into six different regimes. They are shown in Fig. 2.4 and classified as

- Stokes flow ($0 < Re < 5$): In this situation the inertial forces are negligible and the streamlines are symmetric around the cylinder. No separation occurs at these Reynolds numbers.

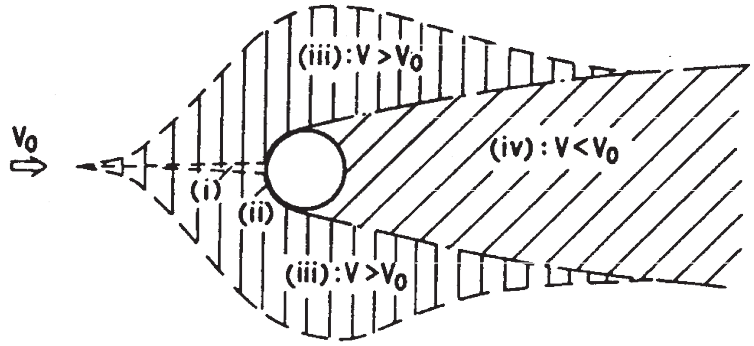

Figure 2.3: Regions of disturbed flow for a single cylinder, Zdravkovich [8].

- Steady Separation ($5 < Re < 40$): Increased Reynolds number causes symmetric separation of the boundary layer from both sides of the cylinder. At these Reynolds numbers, eddies remain steady and in location. The length of the wake is limited because the streamlines come together behind the vortices which are referred to as Föpple vortices.

- Periodic Laminar Shedding ($40 < Re < 150$): Föpple vortices become elongated and unstable. They begin to roll up in a periodic fashion. For $40 < Re < 150$ periodicity is governed by wake instability and remains stable up to a Reynolds number of 150.

- Transition and turbulent vortex shedding ($150 < Re < 3 \times 10^5$) : Fluctuations and vorticity in the shear layers are now turbulent leaving the cylinder. At Reynolds numbers above 300, vortex shedding is fully turbulent and any periodicity disappears around 48 diameters downstream of the cylinder.

- Turbulent boundary Layer ($3 \times 10^5 < Re < 3.5 \times 10^6$): The laminar boundary layer becomes fully turbulent after exceeding $Re_{crit} = 3 \times 10^5$. The exact value of Reynolds number at which this occurs depends on the free stream turbulence and surface roughness of the cylinder. Additionally, the wake is narrower, more disorganised and no vortex street is formed.

- Turbulent Periodic Vortex Shedding ($Re > 3.5 \times 10^6$): Vortices are shed from a turbulent boundary layer but turbulent vortex periodicity has been re-established.

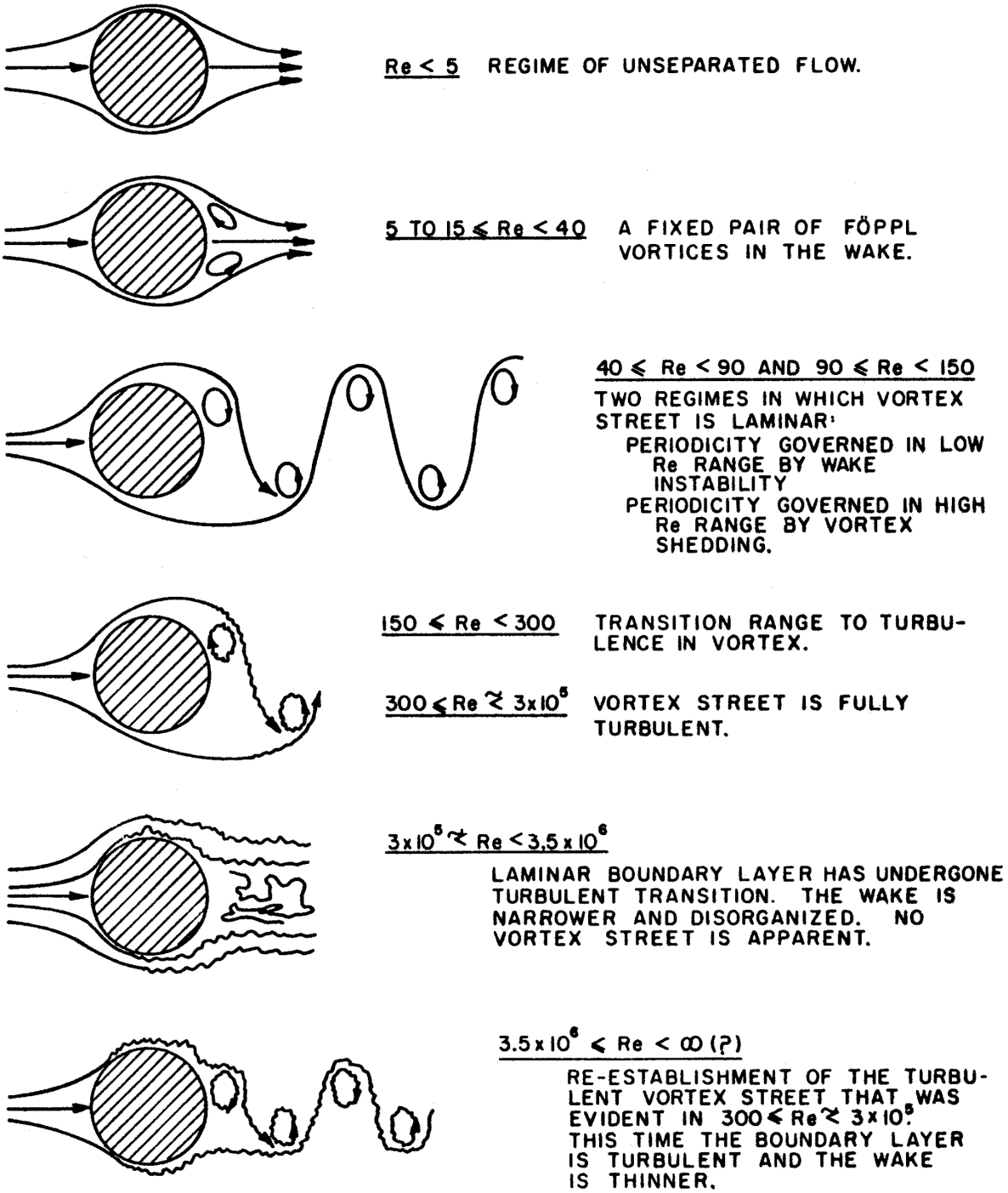

Figure 2.4: Separated flow wake structure at various Reynolds number, Lienhard [9].

2.2.1.2 Strouhal number

The vortex shedding mechanism for a single cylinder has been well examined. One useful way to describe vortex shedding is the Strouhal number, St which is defined by Eqn. 2.2. The Strouhal number is a dimensionless quantity that describes the frequency at which vortex shedding occurs.

$$St = \frac{f_v D}{V_\infty} \tag{2.2}$$

The Strouhal number for a single cylinder is dependent on the Reynolds number of the incoming flow. Figure 2.5 plots the variation of Strouhal number with Reynolds number found experimentally by Lienhard [9]. The cross-hatch represents the envelope in which his data and the data of many other authors fit and according to Lienhard [9] only shows a 10% spread in Strouhal number. As can be seen from Fig. 2.5, for $300 < Re < 10^5$, where the flow exhibits fully turbulent vortex shedding and a laminar cylinder boundary layer, the Strouhal number is fairly constant with a value of about 0.2. This is the accepted nominal value for a circular cylinder. The regions outside the turbulent vortex shedding regime show a rather different behaviour. Below $Re = 300$, the Strouhal number is not constant with respect to Reynolds number whilst above $Re = 10^5$, the Strouhal number shows large variability. The inverse of the Strouhal number is called the reduced velocity, U_r. Defined in Eqn. 2.3, this quantity is a usefull way of expressing the flow velocity in a duct when comparing different acoustic resonance regimes.

$$U_r = \frac{V_\infty}{f_v D} \tag{2.3}$$

2.2.2 Flow over two tandem cylinders

2.2.2.1 Geometric definitions

The flow around multiple cylinder configurations, which is more complicated than the single cylinder case has been well researched due to its importance in engineering applications, e.g. tube bundles, compressors, boilers etc. The arrangement of cylinders can be described by their relative angle of orientation α, their diameter D and their centre-to-centre pitch. The simplest application of these arrangements is either the two tandem

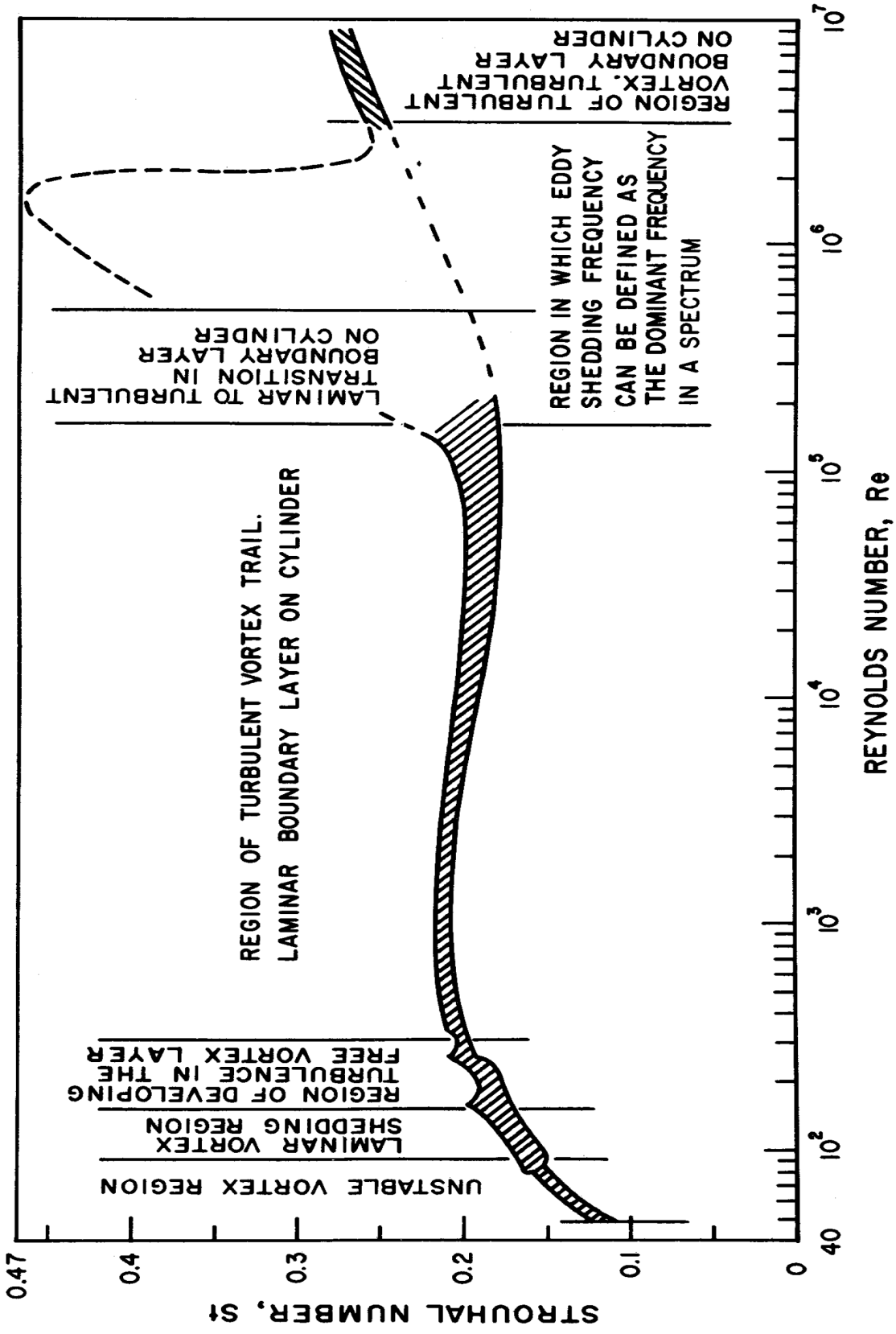

Figure 2.5: Strouhal number versus Reynolds number for a single cylinder, Lienhard [9].

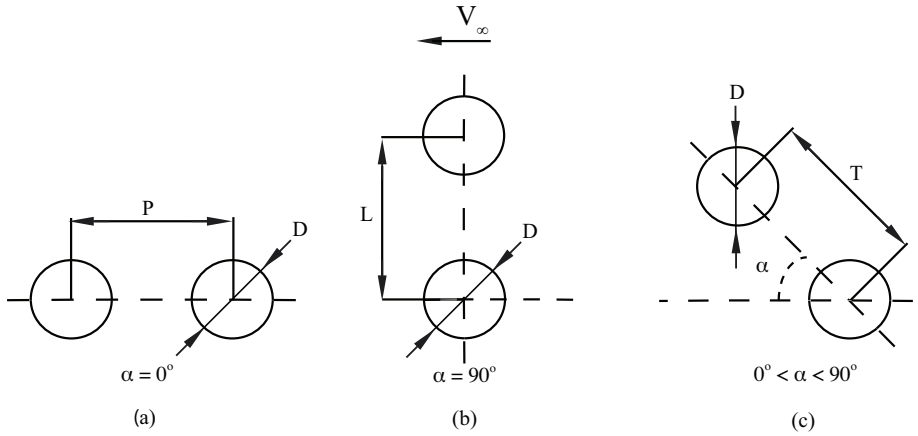

Figure 2.6: Schematics of various two cylinder configurations. (a) Tandem configuration (b) Side-by-side configuration (c) Staggered configuration.

cylinder case or the side-by-side arrangement. In a tandem arrangement ($\alpha = 0°$), one cylinder is placed directly downstream of the other. The centre-to-centre pitch is equal to P. In a side-by-side arrangement ($\alpha = 90°$), both cylinders sit together in the transverse direction. The centre-to-centre pitch is equal to L. The most complex configuration is the staggered arrangement where the downstream cylinder is at some angle between $0° < \alpha < 90°$. Its centre-to-centre pitch is equal to T. Figure 2.6 shows a schematic of the various arrangements.

2.2.2.2 Flow structure

When a tandem cylinder arrangement is subjected to cross flow, vortex shedding occurs from the upstream cylinder. The structure and interference pattern of the shed vortices depend on the particular arrangement and has been discussed by Zdravkovich [10]. He described three categories of interference depending on the location of the downstream cylinder with respect to the upstream cylinder. These various interference regions can be seen in Fig. 2.7 and are summarised as:

- Wake interference : The downstream cylinder is near to the upstream cylinder wake but is not in close proximity.
- Proximity interference : The cylinders are close to each other.
- No interference : The cylinders are staggered such that no wake interaction or interference occurs.

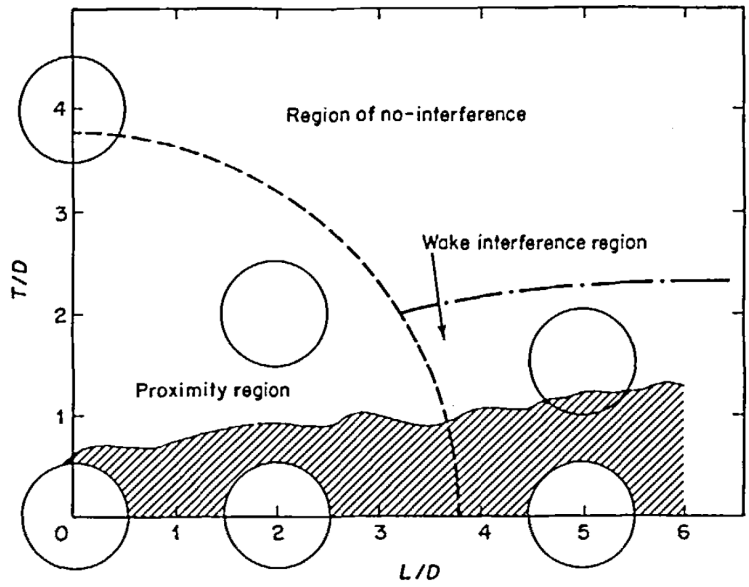

Figure 2.7: Classification of tandem cylinder interference regions, Zdravkovich [10].

Tandem cylinder arrangements fall into either the proximity interference regime, the wake interference regime or a combination of both and basically exhibit two forms of wake interference: with and without eddy shedding from the upstream cylinder [11]. For configurations with $1 < P/D < 1.1 - 1.3$, the shear layers separated from the upstream cylinder over-shoot the downstream cylinder, effectively buffeting it. The vortex street then forms in the wake of the two cylinders and is similar to that of a single cylinder. For configurations with $1.1 - 1.3 < P/D < 3.5 - 3.8$, the shear layers from the upstream cylinder reattach onto the upstream side of the downstream cylinder. This reattachment can either occur alternatively, permanently or intermittently. These geometries are in the proximity interference region. It should be noted that in general, only tandem cylinders with pitch ratios $P/D > 3.8$ can experience vortex shedding in the interstitial gap between the cylinders [11]. For tandem cylinders with $3 < P/D < 4$, a bistable[1] regime may exist. However, this is highly dependent on the Reynolds number [11]. This behaviour was also observed by Ljungkrona *et al.* [12] for configurations with $P/D = 4$. Using flow visualisation, they noticed that the shear layers would roll up to form distinct vortices in the gap between the cylinders at high Reynolds number. Yet, for low Reynolds number,

[1] An intermittent change-over between vortex shedding and no vortex shedding can occur, i.e., either two can occur.

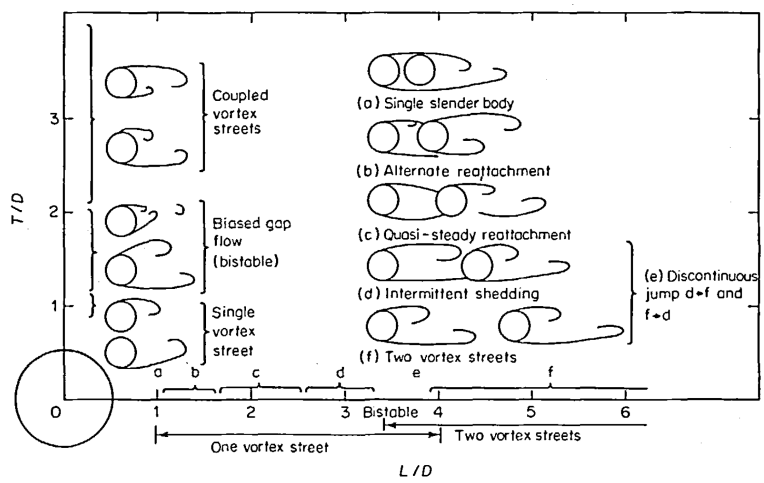

Figure 2.8: Classification of two cylinder wake interference regimes, Zdravkovich [10].

they found that the shear layers reattached. That is to say, they observed vortex shedding in the gap for high velocity flows but not for low velocity flows.

For configurations with $3.8 < P/D < 5-6$, coupled eddy shedding occurs between the upstream and downstream cylinders and a binary vortex street forms in the wake of the configuration. The key feature of a binary vortex street is that the vortices shed from the upstream cylinder and the downstream cylinder are synchronised with the same frequency and phase. For $P/D > 5-6$, uncoupled vortex shedding occurs from both cylinders and two different vortex shedding frequencies occur. The transition from coupled to uncoupled vortex shedding between orientations depends on the Reynolds number. Figure 2.8 is reproduced from Zdravkovich [10] and summarises the different wake interference regimes.

Sumner *et al.* [13] developed their own classification of the wake interference regime when they completed an in-depth investigation of the flow pattern for two staggered cylinders at various angles of incidence (α). They completed a combination of flow-visualisation and PIV experiments in a water towing tank. They sub-classified the wake interference regime into: single bluff body type 1 (SBB1), shear layer reattachment (SLR) and vortex impingement (VI). In SBB1, the shear layers from the upstream cylinder roll up behind the downstream cylinder and form a Von Karman vortex street in the wake. For SLR, the shear layer emanating from the upstream cylinder reattaches to the downstream cylinder and subsequently forms a vortex street in the downstream wake. For this regime, the authors noticed no discernible vortex formation occurring in the gap region between

the cylinders [11]. In VI, the gap region is sufficiently large that fully developed Von Karman vortices form and impinge on the downstream cylinder. As a result, further Karman vortices are shed from the downstream cylinder creating a very complicated wake structure. It is noteworthy that the pitch ratios of the cylinder configurations in the sub-classifications of Sumner *et al.* [13] nearly matched those of Zdravkovich [11] exactly.

2.2.2.3 Strouhal number

For a single cylinder, a linear increase in the mainstream flow velocity results in a linear increase in vortex shedding frequency. Thus, the Strouhal number remains constant for turbulent vortex shedding over a range of cylinder diameters. This is not the case for tandem cylinder configurations which are significantly more complex in nature. Interference between the two cylinders can have a strong influence on the eddy shedding frequency. Xu and Zhou [14] completed an in depth investigation of the Strouhal numbers in the wake of two tandem cylinders at numerous pitch ratios and Reynolds numbers. Their study spanned $Re = 800 - 4.2 \times 10^4$ and $P/D = 1 - 15$ and combined hotwire and flow visualisation. It was observed that the Strouhal number strongly depends on both the pitch ratio and the Reynolds number of the flow.

In terms of pitch ratio, the results of Xu and Zhou [14] are given in Fig. 2.9. As can be seen, the variation of the Strouhal number with pitch ratio is quite spread and hence depends on the flow regime. In the SSB1 regime where the shear layers emanating from the upstream cylinder roll up behind the downstream cylinder, the Strouhal number rapidly reduces with increasing pitch ratio. For SLR regimes, the Strouhal number decreases slightly in the range $2 < P/D < 3$ but exhibits a big jump from $St = 0.14 - 0.17$ for $3 < P/D < 5$. For $P/D = 2.5$, Xu and Zhou [14] measured a Strouhal number of 0.148 which is in good agreement with the current study and also with the work of Mohany [4]. In the vortex impingement regime, the Strouhal number increases slowly with pitch ratio and becomes nearly constant for $P/D > 10$. The solid black line in Fig. 2.9 corresponds to the results found by Igarashi [15].

Xu and Zhou [14] also commented on the variation of the Strouhal number with Reynolds number and deemed it to be very complicated. They split it into four categories based on the observed flow regimes. With regards to the SLR type flow ($1.1 - 1.3 <$

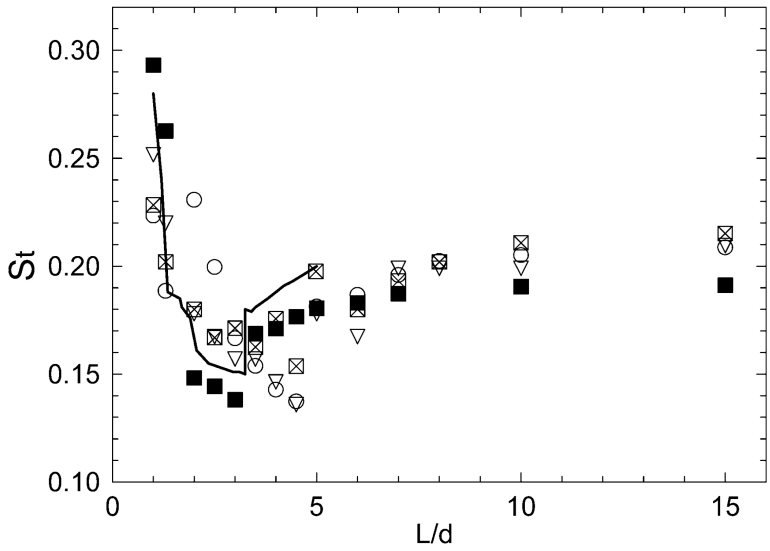

Figure 2.9: Variation of the Strouhal number with the streamwise pitch ratio for two tandem cylinders (L/d in the figure). ▽ $Re = 1.2\times10^3$; ⊠ $Re = 2.9\times10^3$; ◯ $Re = 7\times10^3$; ■ $Re = 4.2\times10^4$, Xu and Zhou [14].

$P/D < 3.5 - 3.8$) they noticed that the Strouhal number increases rapidly for $Re > 10^3$ and then decreases slowly for $Re > 10000$. It then becomes less dependent on Reynolds number as $Re \rightarrow 5\times10^4$. Figure 2.10 shows a plot of the Strouhal number versus Reynolds number for two tandem cylinders with $P/D = 2.5$. As can be seen, the slow decrease in Strouhal number with Reynolds number was also noticed by Hall *et al.* [2], Mohany [4] and Igarashi [15]. The general trend of the data agree well across a wide range of Reynolds numbers. However, there is some variability. This is most likely due to differences in the amount of three-dimensionality in the flow caused by different aspect ratios for each of the studies. Mohany[4] had a maximum aspect ratio of 6 compared to 17 by Hall *et al.* [2] and 40 by Xu and Zhou [14]. Although not shown on the graph, for $Re > 5\times10^4$, Mohany [4] found that Strouhal number becomes constant at a value of 0.15 ± 0.003 and is independent of both the Reynolds number and the pitch ratio for configurations in the range $1.2 < P/D < 3$.

2.2.3 Flow around four cylinders

Heat exchangers consist of a number of tubes orientated in a bundle and a group of four cylinders may be considered a constituent part of that bundle. The geometric parameters

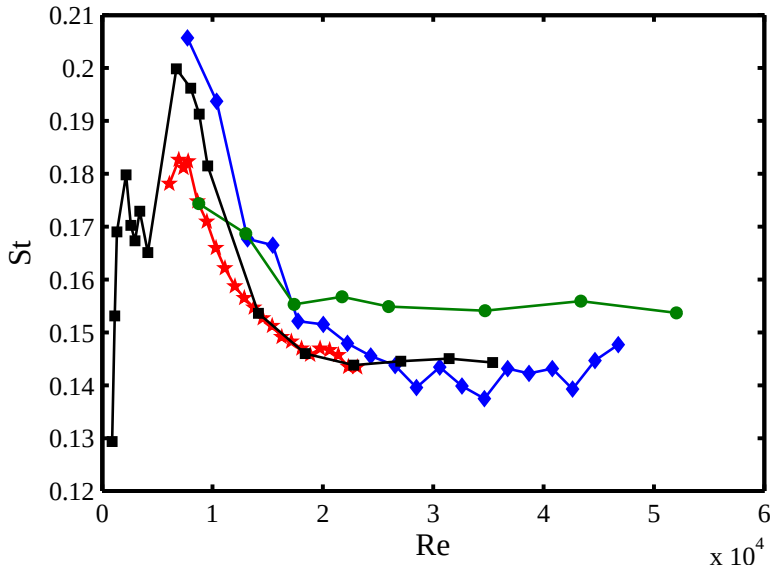

Figure 2.10: Variation of the Strouhal number with Reynolds number observed by various authors for two tandem cylinders with $P/D = 2.5$. ● Igarashi [15]; ★ Hall *et al.* [2]; ■ Xu and Zhou [14]; ♦ Mohany [4].

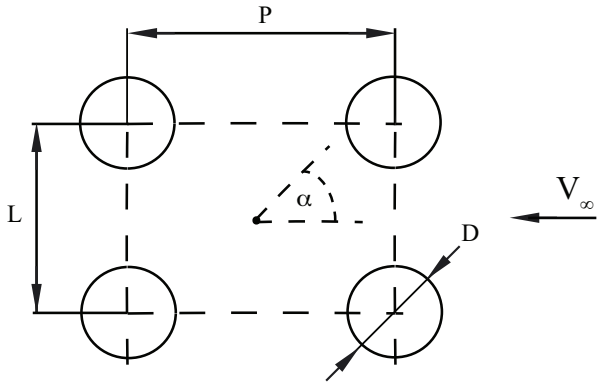

Figure 2.11: Geometric parameters for a group of four cylinders.

of four cylinders are defined in Fig. 2.11 as the streamwise centre-to-centre pitch, P, the transverse centre-to-centre pitch L, the cylinder diameter, D and the angle of orientation, α. In this study, the angle of interest is $\alpha = 0°$ and the cylinders are orientated in a way which is indicative of the geometry in an inline tube bundle. Four cylinders orientated in this way may also be considered to be two pairs of two tandem cylinders sitting side-by-side. Thus, the flow structure is a hybrid between that of two tandem cylinders and two side-by-side cylinders. If $P = L$, the orientation is a square and it is more convenient to use only P to describe the configuration. Otherwise, it is necessary to use P and L.

Numerical simulation of the flow field characteristics around four cylinders orien-

tated in a square have been completed by Lam *et al.* [16] and Farrant *et al.* [17] for $1.6 \leq P/D \leq 5.0$ and for Reynolds numbers, $Re \leq 200$. They both found that the flow regime can exhibit in-phase vortex shedding, anti-phase vortex shedding or synchronised vortex shedding between the cylinders. Flow visualisation by Lam *et al.* [16] agreed well with their own simulations and with those of Farrant *et al.* [17]. Lam and Lo [18] and Lam and Fang [19] have experimentally studied the flow field characteristics for similar configurations but at higher Reynolds numbers of $Re = 2100$ and $Re = 12800$ respectively. Their studies concentrated on the vortex shedding characteristics from the cylinders and the effect of their orientation with respect to the oncoming flow. The dependence of the Strouhal number on the spacing ratio between the cylinders measured by Lam and Lo [18] can be seen in Fig. 2.12. In this graph, the Strouhal number is measured behind each cylinder in the configuration. For large spacing ratios, $P/D > 3.94$ the Strouhal number behind each cylinder is close to that of a single cylinder. However, below $P/D = 3.94$, St_3 and St_4 decrease whilst St_1 and St_2 disappear completely. This occurs because regular vortex shedding behind the upstream cylinders is "suppressed" [18]. The shear layers either reattach to the downstream cylinder or buffet them completely. This is similar to that seen for two tandem cylinders. Below $P/D = 1.7$ there exists a high frequency shedding component and a low frequency shedding component. This is highlighted by the separation in the Strouhal data. Lam and Lo [18] attributed this to a bistable feature in the flow where the wake behind one cylinder is "narrow", whilst the wake behind the other is "wide". The "narrow" wake corresponds to the high frequency component and is due to biased flow. When the gap flow between the cylinders is biased, it favours the "narrow" wake. The "wide" wake corresponds to the low frequency component. According to Lam and Lo [18], initiation of this flow behaviour is due to the deflection of the outer shear layers from the upstream cylinders after they roll up beside one of the downstream cylinders.

These studies provided good insight into the flow structure around four cylinders orientated in a square. However, the Reynolds numbers of these tests were far removed from those of interest in this study. Also, these studies concentrated on configurations that were strictly orientated in a square. Effects on the flow field due to independent changes in the streamwise or transverse pitch ratio is of interest. Furthermore, the effect

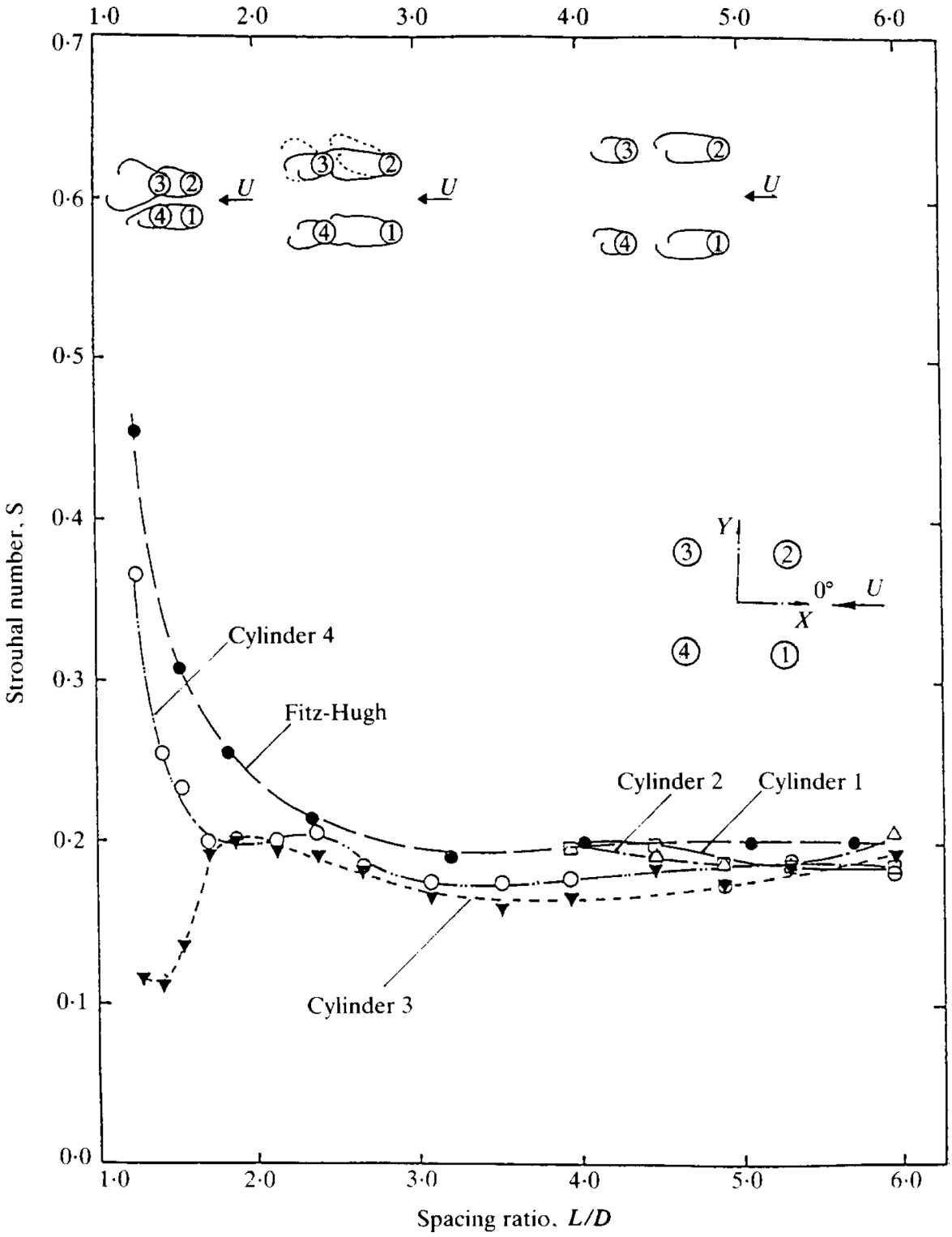

Figure 2.12: Variation of the Strouhal number with the pitch ratio for four cylinders orientated in a square, $Re = 2100$, Lam and Lo [18].

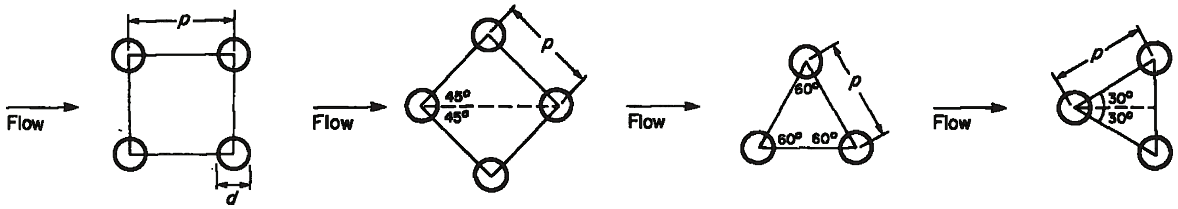

Figure 2.13: Schematics of common tube array patterns. (a) Normal square; (b) Rotated square; (c) Parallel triangular; (d) Normal triangular, adapted from Weaver and Fitzpatrick [20].

of acoustic resonance appears to have been neglected and there has been no investigation of flow-acoustic coupling around a group of four cylinders completed. As a group of four cylinders may be considered a constituent part of an inline tube bundle, investigation of their acoustic behaviour may be beneficial to understanding the flow-acoustic mechanisms in a heat exchanger better.

2.2.4 Flow through an inline tube bundle

Heat exchangers consist of a number of tubes closely packed together. A very important characteristic of a heat exchanger is the geometric pattern that the cylinders form. In their review of cross flow induced vibrations in tube arrays, Weaver and Fitzpatrick [20] defined four standard array patterns. They are normal square, parallel triangular, rotated square and normal triangular. A schematic of these array patterns is shown in Fig. 2.13. These closely packed tube bundles are prone to various excitation mechanisms and a significant bounty of work has been completed into understanding the instabilities that trigger these mechanisms. The patterns of interest in this study are normal square arrays as well as the rectangular square arrays where $P/D \neq L/D$.

The normal square pattern has the same streamwise and transverse centre-to-centre pitch, hence the name square. As with four cylinders, the effect of the streamwise and transverse spacing is of interest. Thus, from here on, a normal square array will be referred to as an inline tube array and the streamwise and transverse pitch ratios (P/D and L/D) will be given. These are the same as defined in Fig. 2.11.

Due to the geometry of an inline tube bundle, the flow field through the array forms jet-like lanes in the gaps between neighbouring columns of cylinders. Moreover, confined

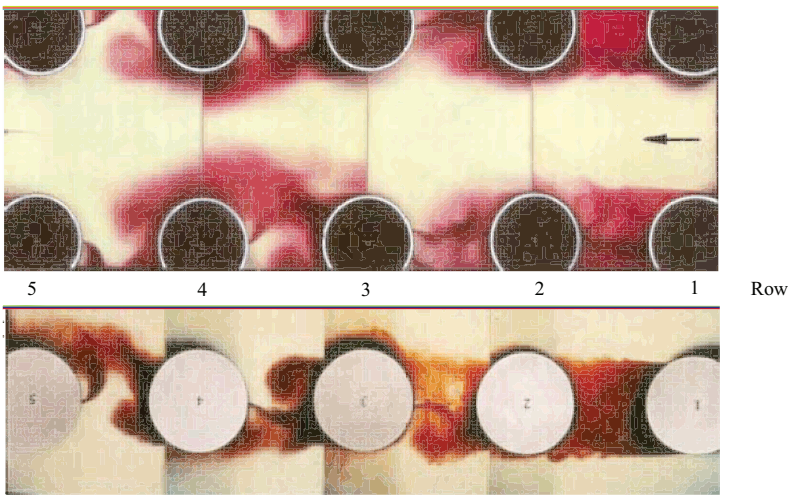

Figure 2.14: The jet instability mechanism that dominates vorticity shedding excitation for inline tube bundles at off resonant conditions. The top image shows the flow lanes whilst the bottom image shows the flow wakes, Ziada and Oengören [21].

wakes behind each cylinder in that column are formed [21]. Much work has been completed on the instabilities in these flow lanes and wakes by Ziada *et al.* [22] and Ziada and Oengören [21, 23]. It has been found that characteristics of the flow are dependent on the spacing between the cylinders, the Reynolds number and the location in the array. This highlights the complexity of the system. The overall flow structure through an array with intermediate spacing ($P/D = 1.75$, $L/D = 2.25$) observed by Ziada and Oengören [21] under non-resonant conditions can be seen in Fig. 2.14. The top image shows the instability structure in one of the flow lanes for the first five rows in the array whilst the bottom picture shows the confined wakes. After the third row large scale vortices form symmetrically with respect to the centreline of the flow lane. This structure is dictated by the symmetric jet instability caused by flow separation from the first row of tubes [21]. In the wake of the cylinders, vortices form anti-symmetrically due to their size and corresponding mass transfer [21]. Although not shown in Fig. 2.14, this anti-symmetric vortex pattern causes the jet instability between neighbouring flow lanes to be 180° out-of-phase.

Ziada *et al.* [22] investigated an array with small spacing ($P/D = 1.4$, $L/D = 1.5$). They found that the overall flow structure in the lanes was similar to that of an intermediately spaced array as jet-instability forms symmetrically on each side of a lane. However, in the wakes they observed a significantly different flow structure. The close streamwise

spacing of the tubes only allowed vortices to form in the thin shear layers, which meant they were very small and had negligible mass transfer [22]. As a result, they formed symmetrically which caused the jet instability between neighbouring lanes to be in-phase.

Ziada and Oengören [23] studied largely spaced arrays ($P/D = 3.25$, $L/D = 3.75$) and found that vortex shedding through the tubes can occur at two different modes. Exactly which type of vortex shedding occurs strongly depends on the turbulence levels in the duct [23]. For low turbulence levels ($T_u \approx 0.1\%$), the flow structure is identical to that observed for intermediate spacing ratios [24]. However, for high turbulence levels ($T_u \approx 1.0\%$), the flow structure is dominated by a local wake instability where alternating vortex shedding in the wake of each cylinder becomes independent of those in neighbouring wakes [23].

The Strouhal number of an inline array is dependent on the spacing between the tubes. Furthermore, according to Fitzpatrick *et al.* [25], the Strouhal number is also dependent on the measurement location and the Reynolds number. For inline arrays with small spacing ratios, Weaver *et al.* [26] and Ziada *et al.* [22] have both reported multiple Strouhal dependencies. For intermediate and largely spaced arrays, Ziada and Oengören [21, 23] only observed one Strouhal dependency. However, it should be noted that for large spacing ratios, the overall Strouhal number changes with turbulence intensity. Figure 2.15(a) shows the relationship between the Strouhal number and the pitch ratio for normal square arrays measured by Weaver *et al.* [26]. St_u is the Strouhal number based on the upstream velocity and the cylinder diameter. The solid black line in the figure represents the expression

$$St_u = \frac{1}{2\,(X_p - 1)} \tag{2.4}$$

which can be used to predict the Strouhal number based on the streamwise pitch ratio ($X_p \equiv P/D$). Care must be taken when using Eqn. 2.4 as it does not account for the multiple Strouhal numbers observed in closely spaced arrays [26].

In an inline tube bundle, the flow is squeezed into the flow lanes. This results in a gap velocity that is higher than that in the freestream. The gap velocity, V_g can be related to V_∞ by

$$V_g = \left[\frac{L}{(L-D)}\right] V_\infty. \tag{2.5}$$

The Strouhal number of vortex shedding in an inline array for various streamwise and transverse spacing ratios based on V_g can be seen in Fig. 2.15(b).

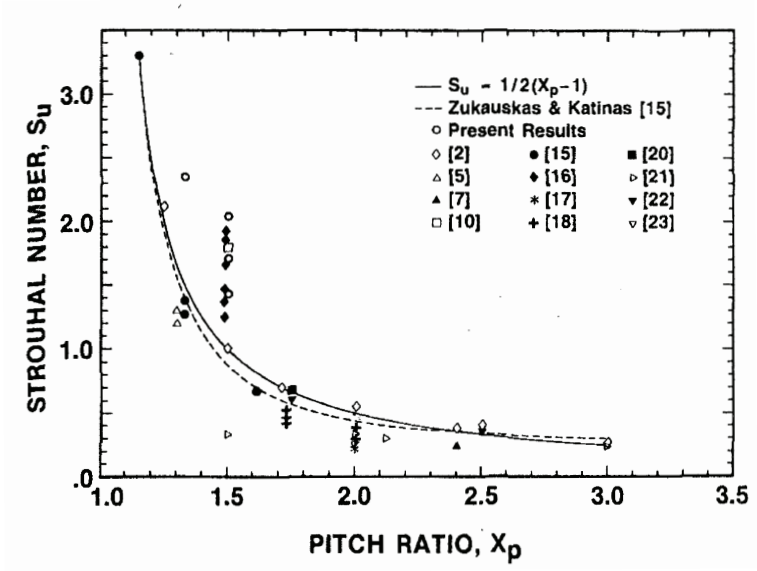

(a) St_u for normal square arrays ($x_p \equiv P/D$), Weaver *et al.* [26].

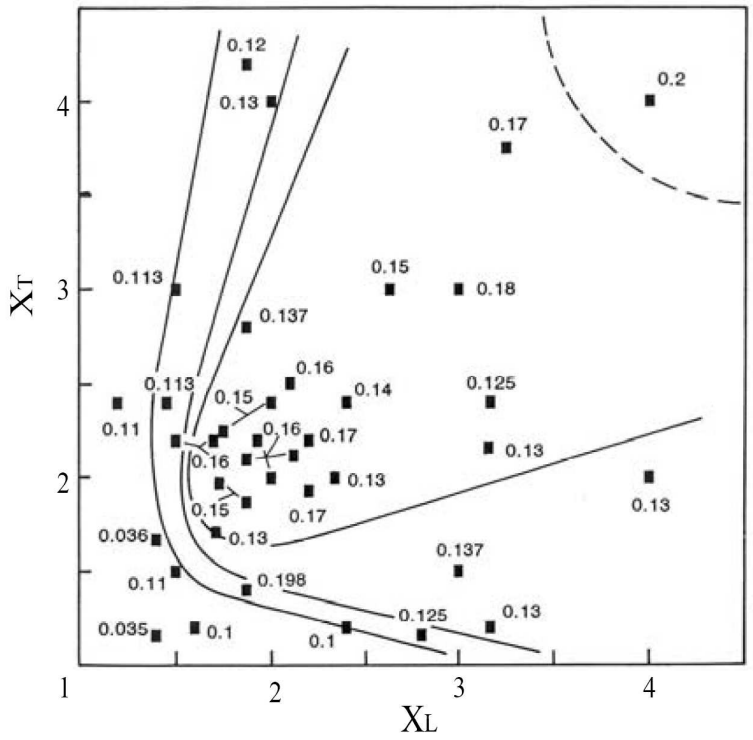

(b) St_g for inline arrays ($X_L \equiv P/D$ and $X_t \equiv L/D$), Ziada [24].

Figure 2.15: Strouhal numbers for an inline tube arrays.

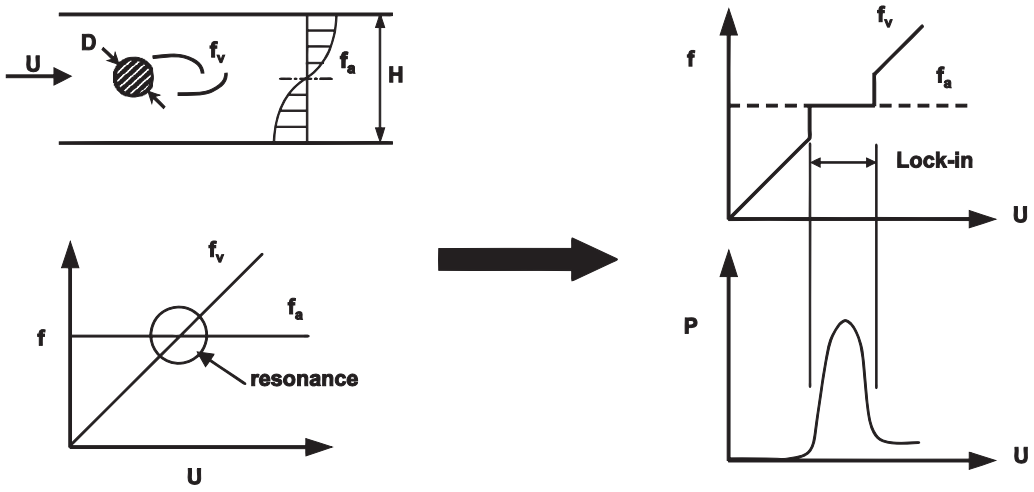

Figure 2.16: Schematic of the acoustic "lock-in" phenomenon, Mohany and Ziada [5].

2.3 Resonant acoustic behaviour of bluff bodies

Flow-excited acoustic resonance is a phenomenon that occurs when the vortex shedding frequency, f_v, from a bluff body (or a group of bluff bodies) housed in a duct approaches the natural frequency of that duct, f_a. When the two frequencies coincide, the acoustic mode of the duct becomes excited by the dipole-like mechanism of vortex shedding and a strong acoustic resonance can be induced [27]. A key mechanism of this excitation is "lock-in", where the acoustic field entrains the hydrodynamic flow field and can control the vortex shedding frequency. Figure 2.16 shows a schematic of the "lock-in" process. During "lock-in", the vortex shedding and acoustic mode enhance each other. This results in a sudden spike-like increase in the acoustic pressure. If this increased acoustic pressure exceeds the dynamic head of the flow, possible damage could be inflicted on the tubing and duct [20]. Also, acoustic resonance is not continuous, i.e. it only occurs over a finite range of velocities as it eventually subsides at higher flow velocities when the unsteady fluid forces overcome the acoustic forces. The width of this range is dependent on many factors, including the number of cylinders, their relative orientation and their diameter to name a few. Much work has been completed into understanding how acoustic resonance is affected by these factors.

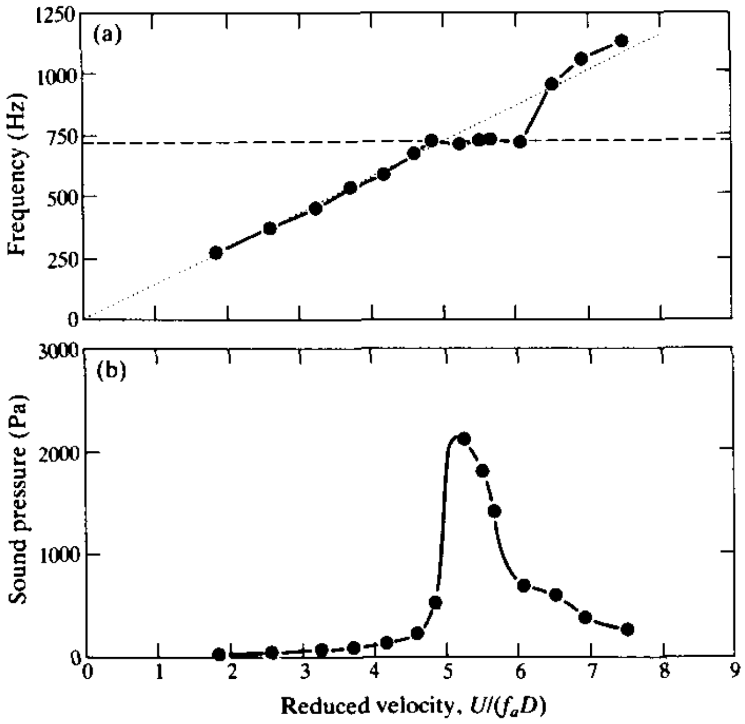

Figure 2.17: Typical aeroacoustic response of a single cylinder, Blevins and Bressler [28].

2.3.1 Acoustic resonance of a single cylinder

2.3.1.1 Natural acoustic resonance

For single cylinders in cross-flow, "lock-in" occurs when the vortex shedding frequency is close to that of the natural frequency of the duct, and only at sufficiently high sound pressure levels (SPL). That was the findings of Blevins and Bressler [28] and Mohany and Ziada [5]. Blevins and Bressler [28] completed experiments on the self-excited acoustic resonance of a single cylinder in a wind tunnel. They recorded the aeroacoustic responses of a range of different cylinder diameters at increasing flow velocities by using microphones. A typical result is shown in Fig. 2.17. As can be seen, the amplitude and frequency of vortex shedding increases with flow velocity until f_v approaches the first acoustic mode of the duct, f_a. At this point, "lock-in" occurs as f_v becomes entrained to f_a and the acoustic pressure experiences a strong increase. Mohany and Ziada [5] completed similar work and found similar results. They reported that acoustic resonance of single cylinders occur over a single range of flow velocities. Moreover, they agreed with Blevins and Bressler [28] that the mechanism of acoustic resonance is vortex shedding.

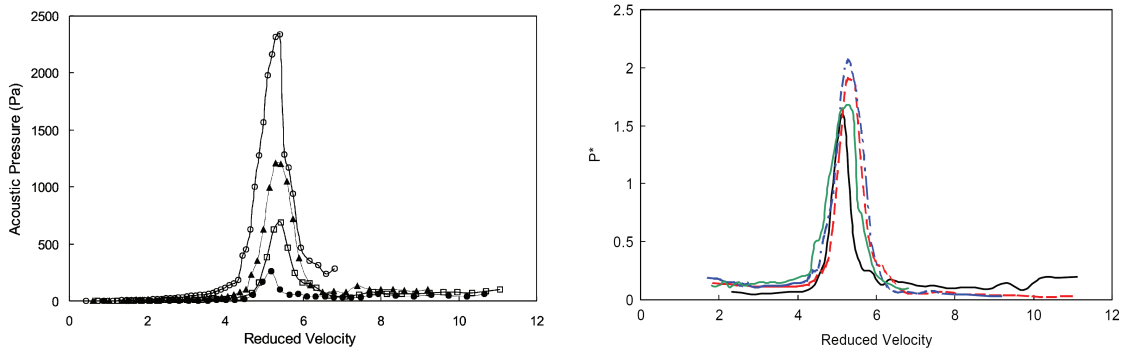

(a) • $D = 12.7$ mm; □ $D = 15.9$ mm; △ $D = 19$ mm; ○ $D = 25.4$ mm.

(b) — $D = 12.7$ mm; – – $D = 15.9$ mm; — $D = 19$ mm; – · – $D = 25.4$ mm.

Figure 2.18: The aeroacoustic response of a single cylinder with different diameters, Mohany and Ziada [5].

Both authors noticed that cylinders with larger diameters induced stronger acoustic resonances (higher maximum acoustic pressures) and wider ranges over which "lock-in" could be sustained. Figure 2.18(a) shows the acoustic pressures measured by Mohany and Ziada [5] over their range of reduced velocities and cylinder diameters. As can seen, larger cylinders induce larger acoustic pressures. Larger cylinders also require larger flow velocities to trigger resonance. Mohany and Ziada [5] related this observation directly to the Strouhal number. Remember, for $300 < Re < 10^5$, $St \approx 0.2$. Thus, it is sensible that a higher flow velocity is needed to obtain a vortex shedding frequency equal to the natural acoustic frequency (which is fixed) as the cylinder diameter increases.

Mohany and Ziada [5] also found that the strength of the acoustic resonance is proportional to the dynamic head in the duct and used this fact to explain the effect of the cylinder diameter. Figure 2.18(b) shows the normalised acoustic pressure (P^*) for the same reduced velocities and cylinder diameters in Fig. 2.18(a). The normalised acoustic pressure is defined as

$$P^* = \frac{P_a}{\frac{1}{2}\rho V_\infty^2 Ma}, \tag{2.6}$$

where Ma is the Mach number. Since the data in Fig. 2.18(b) nearly collapses, the strength of the acoustic resonance can be considered proportional to the dynamic head. As larger cylinder diameters induce higher dynamic heads, they also induce stronger acoustic resonances.

Blevins and Bressler [28] proposed their own empirical equation to predict the maximum acoustic pressure at resonance. They found that the strength of the acoustic pressure can be described by

$$P_{rms,max} = (12.5\rho\frac{V_\infty^2}{2})(\frac{V_\infty}{c})(\frac{D}{h}) \tag{2.7}$$

where c is the speed of sound in air and V_∞/c is the Mach number. The regression used to fit this equation to their data was based on Mach number as it was found to be superior to Reynolds number in correlating the resonant sound pressure [28]. The standard deviation of the fit was 26% and it is interesting to note that Eqn. 2.7 accounts for the dynamic head in the flow as well as the blockage ratio of the cylinders D/h.

2.3.1.2 Forced acoustic resonance

Forced acoustic resonance is different from natural acoustic resonance in that an externally imposed sound field is applied across the cylinder using loudspeakers. Blevins [29] completed work on the "lock-in" phenomenon for an isolated cylinder exposed to a forced acoustic field, as did Hall *et al.* [2] and Kacker and Hill [30]. These authors all reported that application of an external sound wave can shift the frequency of vortex shedding, f_v to that of the applied acoustic frequency, f_e. However, this can only occur when the two frequencies are close to each other. Furthermore, the degree to which the vortex shedding frequency can be shifted is dependent on the amplitude of the applied sound. Both Blevins [29] and Hall *et al.* [2] noticed that larger applied amplitudes could induce larger shifts. They also noticed that the sound field could shift the vortex shedding frequency either up or down, i.e. either to higher frequencies or lower frequencies. However, as Blevins [29] pointed out, greater shifts could be achieved when the f_v was greater than f_e. In other words, if f_e corresponded to the first natural acoustic frequency of the duct (f_a), a greater shift in the vortex shedding frequency can be achieved after acoustic-Strouhal coincidence, not before. In terms of acoustic resonance, this means the effect of an imposed acoustic wave is that it widens the "lock-in" range of the system. The degree of shift in f_v before acoustic-Strouhal coincidence reported by both Blevins [29] and Hall *et al.* [2] seems to be similar to that of natural acoustic resonance reported Blevins and Bressler [28] and Mohany and Ziada [5]. This indicates that when "locked-in", the mech-

anisms maintaining the resonance are the same and that a forced acoustic system is a good simulation of a naturally resonant one.

The effect of an externally applied acoustic wave on vortex shedding can be seen in Fig. 2.19(a). It shows the spectra measured from a pressure tap along the surface of the cylinder used by Hall *et al.* [2]. As can be seen, for natural vortex shedding, a broad peak exists in the spectrum. However, when a sound wave with an amplitude equal to 5% of the mean flow velocity is applied, the peak narrows and increases in magnitude.

This observation was shared by Blevins [29]. With no applied sound, he reported that vortex shedding consisted of "strings of coherent cyclical events which have frequencies that wander randomly about the nominal vortex shedding frequency." These "strings of coherent cyclical events" had poor correlation and a poor phase relationship along the length of the cylinder. That is to say, the flow was highly three dimensional. The opposite occurred in the presence of an applied sound wave as a strong regularisation between the anemometer time signals was measured. This included an increase in their amplitude and a significant reduction in their phase difference along the length of the cylinder. That is to say, the flow was highly two dimensional. Figure 2.20 shows the coherence measured by Blevins [29] between one flush-film anemometer and another probe near the cylinder for the cases of no applied sound and applied sound equal to 250Pa (142 dB). It is clear that the sound wave drastically increases the coherence between the probes and effectively forces the vortex shedding to be two dimensional, even at larger distances away from the cylinder.

The applied sound field can shift the vortex shedding process if the two frequencies are close and the amplitude of the excitation is sufficiently large. If the excitation frequency coincides with f_a and "lock-in" occurs, it is expected that the structure of the "locked-in" flow field will be similar to that found by Blevins [29] and Hall *et al.* [2]. That is to say the spectra will exhibit a dominant narrow band peak and the vortex shedding will be strongly two-dimensional. However if the two frequencies are sufficiently close, yet "lock-in" does not occur, the flow field is expected to be modulated. A modulated flow was observed by Hall *et al.* [2] and consists of frequency components at non-linear combinations of f_v and f_a. Figure 2.19(b) shows an example of a modulated flow measured by Hall *et al.* [2].

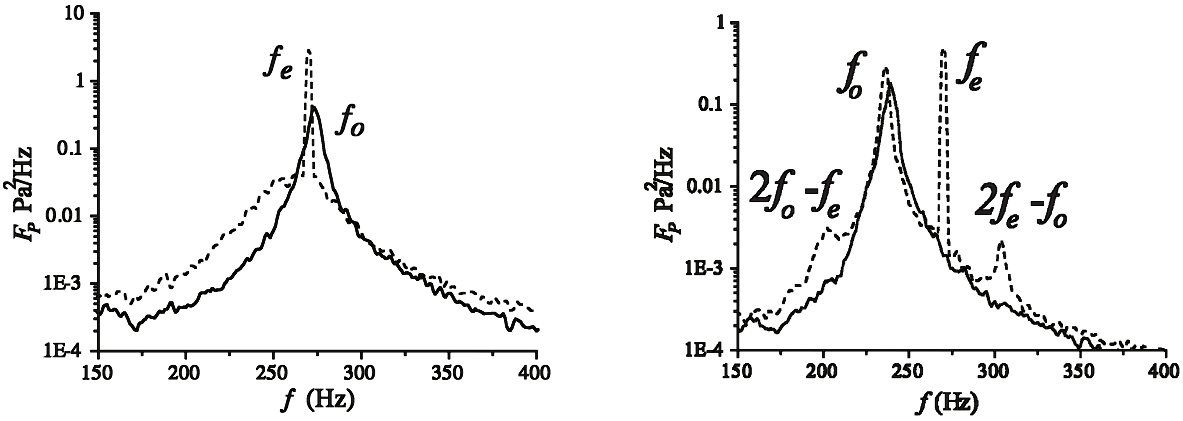

(a) $--$ $U_a/V_\infty = 5.15\%$; $-$ no applied sound, $Re = 14400$ and $f_a/f_v = 0.99$.

(b) $--$ $U_a/V_\infty = 1.29\%$; $-$ no applied sound, $Re = 12300$ and $f_a/f_v = 1.11$.

Figure 2.19: Typical pressure spectra of two tandem cylinders used by Hall *et al.* [2] for a single cylinder. (a) Response when the flow field is "locked-in" to the acoustic field. (b) Response when the flow field is not "locked-in" to the acoustic field showing modulation.

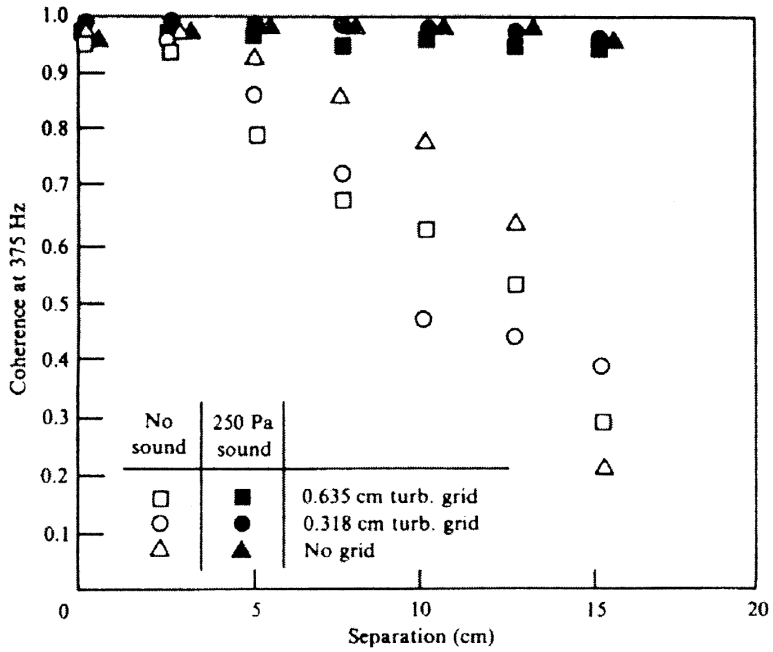

Figure 2.20: Effect of a sound wave on the spanwise coherence of vortex shedding, Blevins [29].

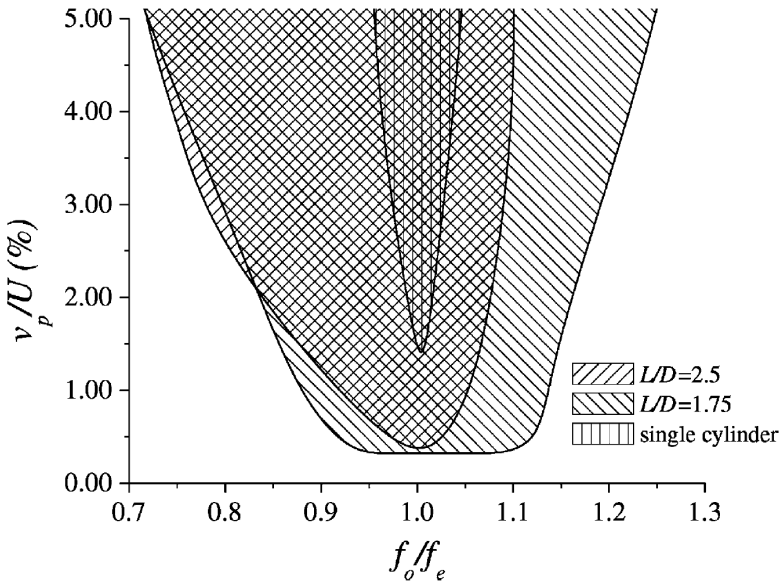

Figure 2.21: Comparison of the "lock-in" ranges between single and two tandem cylinders. V is the mainstream flow velocity, v_p is the acoustic particle velocity, f_0 is the natural vortex shedding frequency and f_e is the frequency of the externally applied sound, Hall *et al.* [2].

2.3.2 Acoustic resonance of two tandem cylinders

The Aeroacoustic response of a single cylinder is fairly well understood. However there are still many unresolved issues regarding more complex structures with multiple cylinders in close proximity. Hall *et al.* [2], Mohany and Ziada [5, 31], Mohany [4] and Fitzpatrick [32] have all contributed to resolving some of these issues for the case of two tandem cylinders. Hall *et al.* [2] investigated configurations in the proximity interference region while Mohany [4] and Mohany and Ziada [5, 31] have investigated configurations in the proximity interference and wake interference regions. It has been found that the aeroacoustic response of two tandem cylinders in the proximity interference region differs substantially from that of a single cylinder under similar flow conditions, particularly concerning the width of the acoustic "lock-in" range. Hall *et al.* [2] reported that tandem cylinders tend to have a wider "lock-in" range compared to isolated cylinders, which makes them more susceptible to acoustic resonance. Figure 2.21 compares the "lock-in" ranges of a single cylinder with the two tandem cylinder configurations tested by Hall *et al.* [2]. The single cylinder case only "locks-in" near acoustic-Strouhal coincidence whilst the tandem cylinder arrangements can "lock-in" well above acoustic-Strouhal coincidence *and* well below

acoustic-Strouhal coincidence.

Even though Hall *et al.* [2] used forced acoustic excitation, it is interesting to note that Mohany and Ziada [5] reported similar findings for naturally induced acoustic resonance. They observed that tandem cylinder configurations with certain centre-to-centre pitch ratios actually resonate over two flow velocity ranges and not just a single velocity range. One of the velocity ranges occurred at high flow velocities (above acoustic-Strouhal coincidence), and was referred to as coincidence resonance. The other resonance range, which occurred at low flow velocities (before acoustic-Strouhal coincidence), was classified as pre-coincidence resonance. Figure 2.22 shows the aeroacoustic characteristics measured by Mohany [4] for a tandem cylinder configuration with $P/D = 2.5$. The two velocity ranges are clearly defined and it is obvious that "lock-in" occurs well before acoustic-Strouhal coincidence and well beyond it. Since coincidence resonance is triggered at acoustic-Strouhal coincidence, Mohany [4] postulated that vortex shedding in the wake of the cylinders is the mechanism of excitation. However, for pre-coincidence resonance he attributed shear layer instability in the gap region as the source of excitation, not vortex shedding. The current delimiter between pre-coincidence and coincidence acoustic resonance is the point at which acoustic-Strouhal coincidence occurs. Interestingly, there is a clear drop in the SPL of Fig. 2.22 at acoustic-Strouhal coincidence ($U_r \approx 7.1$). This means the system is non-resonant during the transition between pre-coincidence and coincidence acoustic resonance.

The existence of pre-coincidence resonance is highly dependent on both the spacing between the cylinders and the diameter of the cylinders. Furthermore, there is a mutual relationship between the cylinders spacing and the cylinder diameter as well. For example, for $P/D = 1.5$, Mohany [4] found that a cylinder diameter of 18.4 mm was needed to excite pre-coincidence resonance whilst for $P/D = 2.5$, a much smaller diameter of 12.7 mm was needed. In general, for configurations within the proximity interference region, larger spacing ratios require smaller cylinder diameters to induce pre-coincidence. Mohany [4] found that larger cylinders are more susceptible to pre-coincidence resonance and induce a more intense and wider "lock-in" range. This is because changing the cylinder diameter changes the dynamic head at which resonance occurs as well as other important properties such as the shear layer reattachment length and the acoustic radiation from

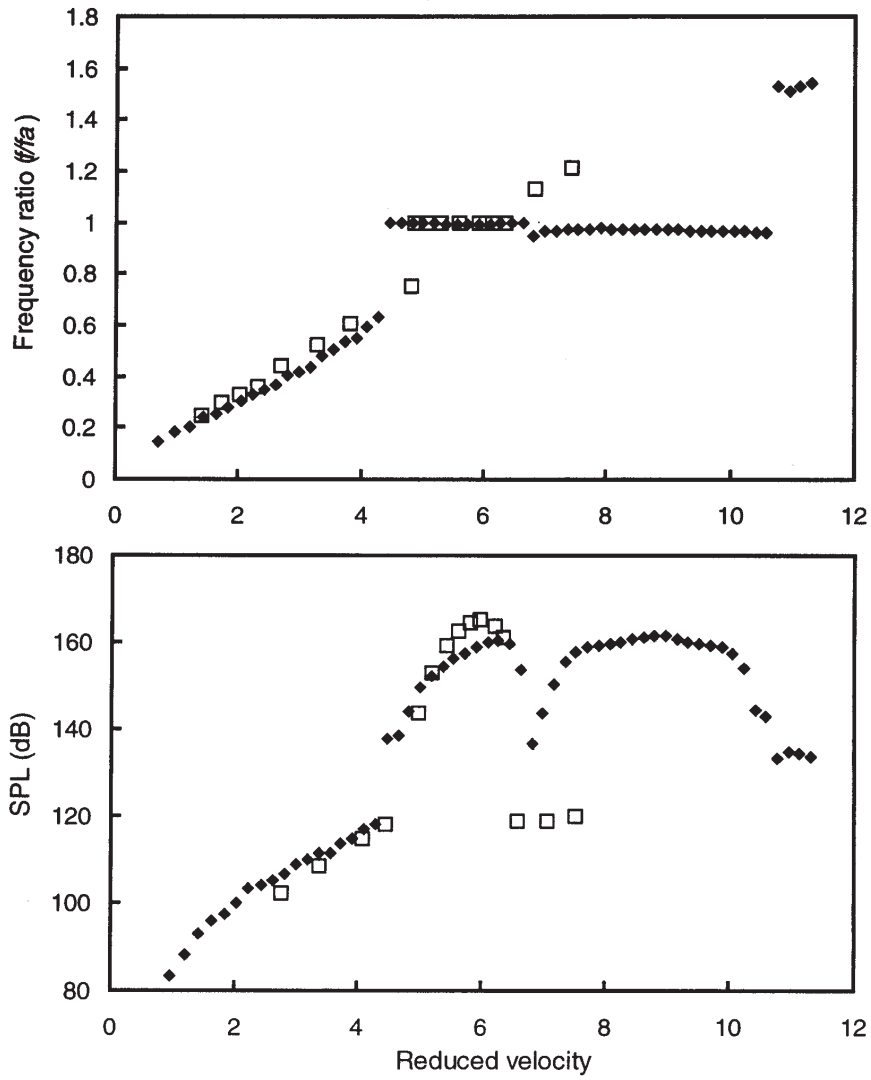

Figure 2.22: Aeroacoustic response of two tandem cylinders compared with an inline tube bundle. ♦ $P/D = 2.5$; □ $P/D = 2.6$, $L/D = 3$ inline tube bundle from Ziada and Oengören [23], Mohany [4].

the cylinders [31]. As the spacing increases into the wake interference region (where a vortex street tends to form behind the upstream cylinder), resonance only occurs over a single range of velocities and is triggered at acoustic-Strouhal coincidence [4]. Thus the two tandem cylinders effectively act like a single cylinder [5, 4, 31].

These studies have highlighted substantial differences between the mechanisms generating noise in these structures. However, they have not provided any insight into the location of the dominant sources in the flow field. Fitzpatrick [32] addressed this by completing roving hot film anemometer and microphone tests for two tandem cylinders with $P/D > 3$. He found that the sound generated from the cylinders had two frequency components, a dominant component at the vortex shedding frequency and a secondary component at its first harmonic. He reported that the sound due to vortex shedding was strongest at the mid-point between the cylinders and at the downstream cylinder. The harmonic component generated by the non-linear flow-acoustic interactions was strongest at the downstream cylinder. Fitzpatrick [32] related the key mechanism generating the noise to a feed-back loop caused by the impingement of the vortices on the downstream cylinder. When the vortex impinges on the downstream cylinder, the pressure fluctuations radiate back upstream at the local speed of sound causing further pressure disturbances at the separation point on the upstream cylinder. If the radiated pressure is in-phase with the unsteady fluctuating pressure at the upstream cylinder, a positive feed-back loop is set up and there is a possibility of enhanced noise generation [32]. The description of the feed-back loop between the two cylinders is analogous to the feed-back loop set up between the upstream and downstream edges of a deep cavity resonator for fluid-dynamic oscillations as described by Rockwell and Naudascher [33]. The work of Fitzpatrick [32] gave good insight into the local identification of acoustic sources, however, nothing could be said about the global distribution of acoustic sources in the flow field.

2.3.3 Acoustic resonance of an inline tube bundle

Acoustic resonance is one of the four excitation mechanisms of vibration that can occur in a heat exchanger tube bundle [20]. The others are turbulent buffeting, fluid elastic instability and vortex shedding, which was already discussed extensively. Acoustic resonance occurs in tube bundles exposed to high velocity cross flows and as with the other

P/D	1.5	3	2	1.5	3	1.5	6	Incorrect
L/D	1.5	3	2	3	1.5	6	1.5	Predictions
Grotz and Arnold [35]	Y	Y	Y	Y	Y	Y	Y	2
Chen and Young [36]	Y	Y	Y	Y	Y	Y	Y	2
Fitzpatrick and Donaldson [37]	N	Y	Y	Y/N	Y	N	Y	0
Ziada *et al.* [38]	Y	Y	Y	Y	Y	Y	Y	2
Actual Resonance [28]	N	Y	Y	Y	Y	N	Y	

Table 2.1: Comparison of the damping criteria for prediction of acoustic resonance of inline tube bundles developed by various against some experimental observations, Blevins and Bressler [28]

cylinder geometries, is associated with standing acoustic waves at right angles to the tubes' axis and the mean flow. A system's ability to resonate depends very much on its acoustic damping [34]. Many authors have formulated damping criteria for the prediction of acoustic resonance. These include Grotz and Arnold [35], Chen and Young [36], Fitzpatrick and Donaldson [37], Ziada *et al.* [38]. A comprehensive summary and a comparative performance of these authors' damping criteria against actual resonant cases can be found in Blevins and Bressler [28]. Table 2.1 summarises some of the findings of Blevins and Bressler [28] for inline tube arrays. This table was used as an initial reference guide when selecting exactly which tube bundles to investigate in the current study. The damping criteria in Tab. 2.1 encapsulates many important parameters and it is clear that the cylinder spacing is one of them.

Oengören and Ziada [34] completed an in depth study of acoustic resonance in intermediately spaced arrays. Figure 2.23 shows the aeroacoustic response of a hotwire and a microphone measured behind the second row of tubes for their configuration. Resonance is initiated before acoustic-Strouhal coincidence and a "lock-in" occurs where the shedding frequency becomes entrained to the acoustic frequency f_1. This is accompanied by a significant increase in the sound pressure level. The resonance subsides at the coincidence between the vortex shedding and f_1. The corresponding resonant flow structure through the array can be seen in Fig. 2.24. If compared to Fig. 2.14, which shows the off-resonant flow structure for the same configuration, it is clear to see that the symmetrical jet instability described earlier has been replaced by an anti-symmetric mode. The main difference being that the vortices formed behind the cylinders are synchronised and in-phase.

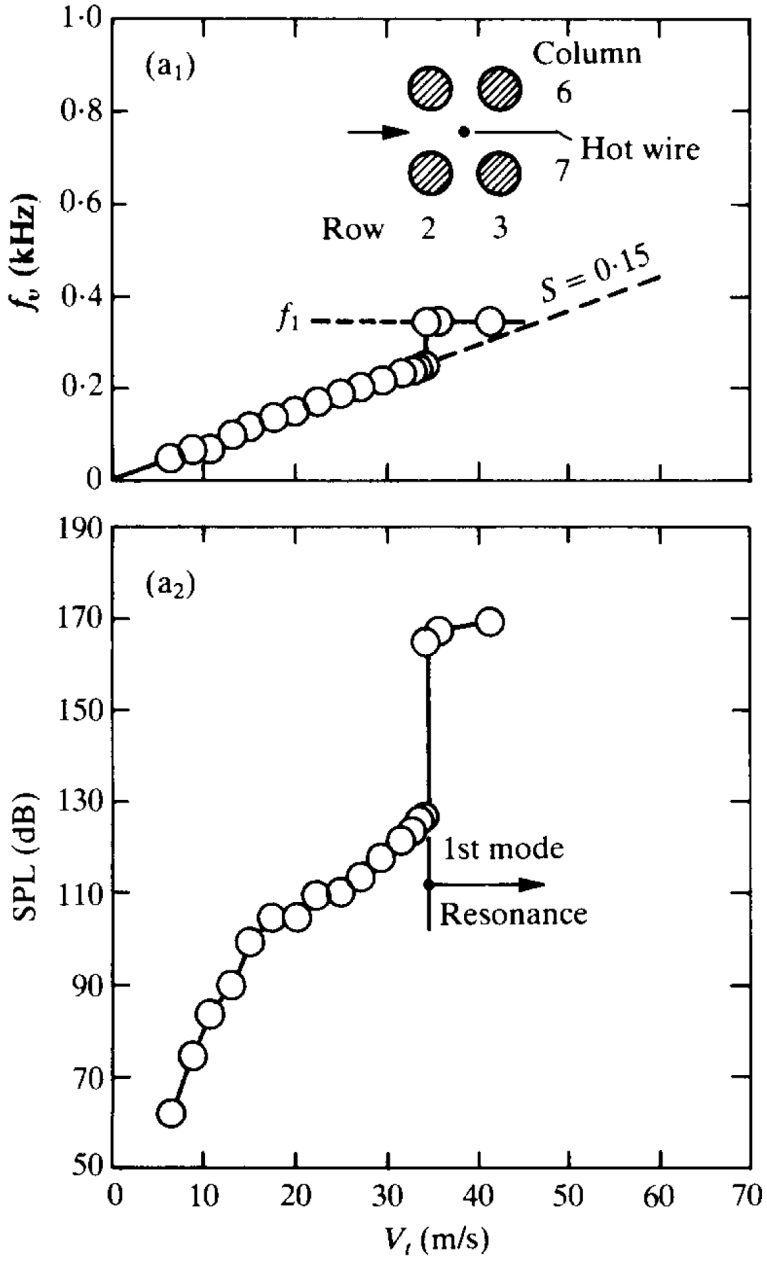

Figure 2.23: The aeroacoustic response of an intermediately spaced inline array, Oengören and Ziada [34].

Oengören and Ziada [34] called this different flow structure a shear layer mode as they attributed it to the triggering and synchronisation of instabilities in the shear layers with the resonant modes of the duct. Moreover, because this new flow structure is completely suppressed at off-resonant conditions, they suggested that the vortex shedding excitation mechanism in the tube bundles is not the cause of acoustic resonance. This suggestion was supported by their argument that the nature of the flow field due to vortex shedding

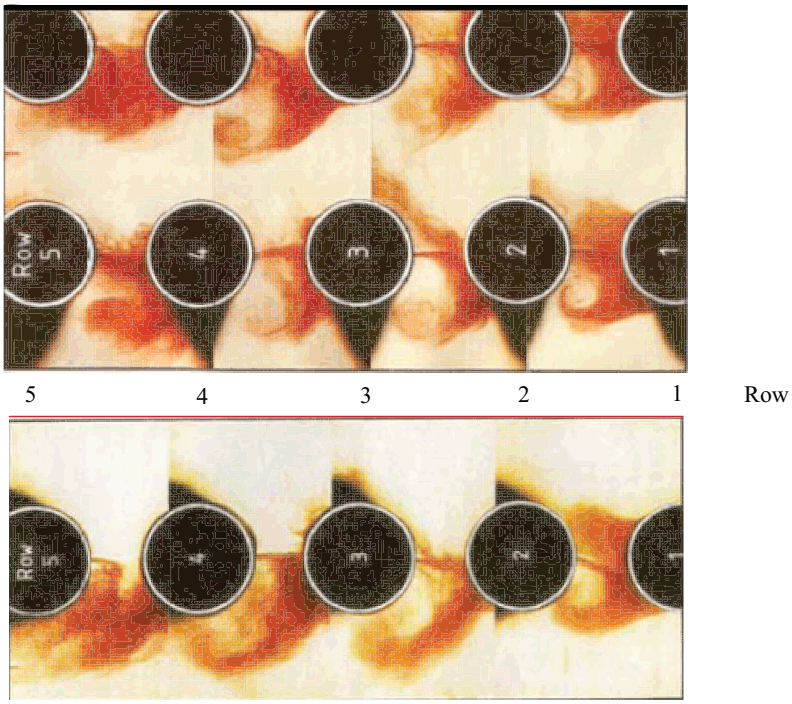

Figure 2.24: The flow structure through an intermediate array under resonant conditions. The top image shows the flow lanes while the bottom image shows the wakes behind the cylinders. Note the difference in the flow structure compared to Fig. 2.14, Ziada and Oengören [23].

(Fig. 2.14) is not conducive to coupling between the flow field and the sound field. Thus the resonance mechanism is not related to the vorticity shedding excitation mechanism which dominates intermediately spaced arrays at off-resonant conditions [34]. They concluded that the ability for the system to switch from the jet mode to the shear layer mode is dependent on the level of turbulence and acoustic damping in the system.

For arrays with large spacing ratios ($P/D > 2.7$), Ziada and Oengören [23] found a rather different acoustic response to that of intermediate arrays ($1.75 < P/D < 2.7$). Figure 2.25 shows the aeroacoustic response for an inline bundle with $P/D = 3.25$ and $L/D = 3.75$. Here acoustic resonance occurs just before acoustic-Strouhal coincidence and remains "locked-in" for a certain range of velocities afterwards. This response is different from that shown in Fig. 2.23. Ziada and Oengören [23] deduced that for arrays with large spacing ratios, resonance is initiated by vortex shedding excitation in the array. Remember that for largely spaced arrays, two different flow structures can occur, namely jet instability and wake instability [21]. Ziada and Oengören [23] found that the acoustic

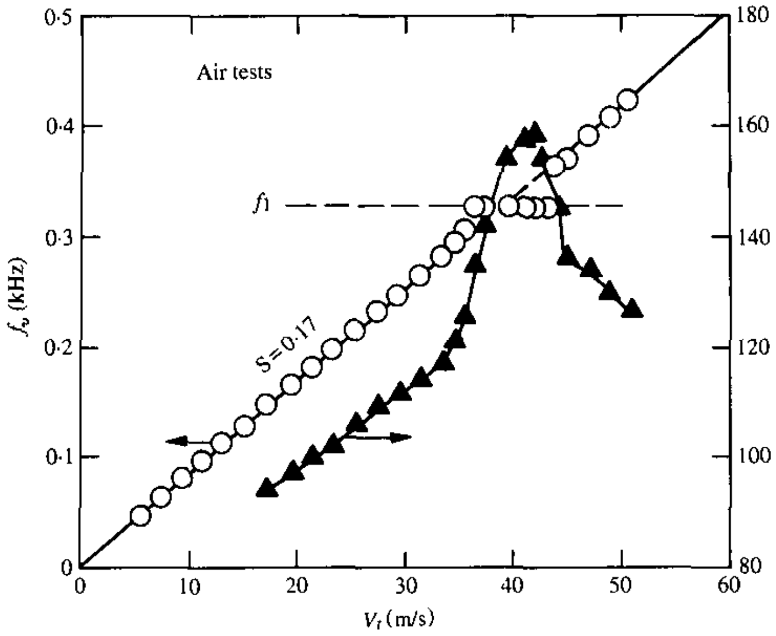

Figure 2.25: The aeroacoustic response of a largely spaced inline array, Ziada and Oengören [23].

resonance was initiated by the wake instability mode. This makes sense given that, as with intermediately spaced arrays, the jet instability mode is not conducive to flow-acoustic coupling. Moreover, as resonance occurs at higher flow velocities, the turbulence level in the duct is likely to be higher than that at low flow velocities and thus wake instability will be the dominant mode. For arrays with small spacing ratios ($P/D < 1.5$), Ziada *et al.* [22] found that resonance of a duct mode is triggered by shear layer instability and not by vortex shedding.

It is clear from the above discussion that the mechanism of acoustic resonance for inline tube bundles is quite complex and highly dependent on the spacing ratio. For this reason, Ziada [24] discussed how Strouhal numbers at resonant conditions tend to be different from those at off-resonant conditions. In this review of vortex shedding and acoustic resonance in all tube bundle patterns, he suggested that an acoustic Strouhal number, St_a should be used in the design stage rather than St_u or St_g, especially for arrays with intermediate and small spacing ratios. Figure 2.26 shows a Strouhal number chart for acoustic resonance of inline tube arrays with various spacing ratios and is different from that shown in Fig. 2.15(b). The acoustic Strouhal number in this chart is based on the first acoustic mode of the duct and the streamwise pitch (not the cylinder diameter). His

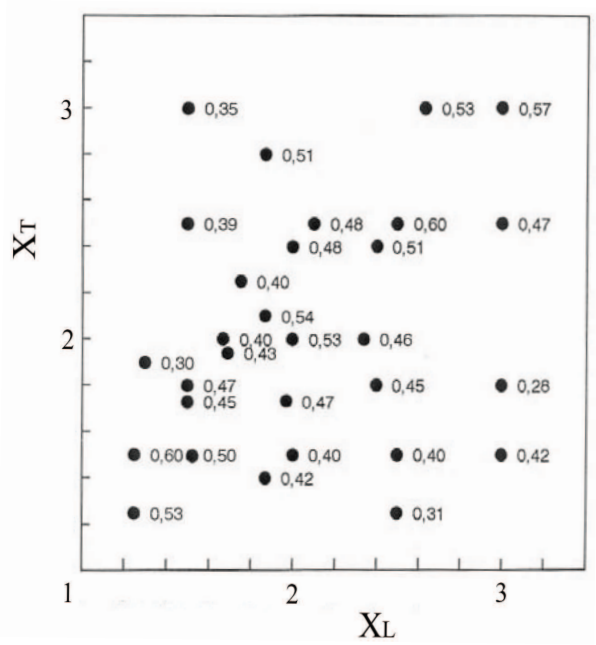

Figure 2.26: Strouhal number of acoustic resonance, St_a for an inline array based on the first acoustic mode of the duct and the streamwise pitch between the cylinders, $X_L \equiv P/D$ and $X_t \equiv L/D$, Ziada [24].

logic for this was that the mechanism of resonance for intermediate inline arrays is similar to that of deep cavities and so a similar characteristic length should be used. However, he conceded that because largely spaced arrays resonant due to vorticity shedding excitation, the Strouhal map in Fig. 2.15(b) should be used.

2.4 Theoretical basis of aeroacoustics

In classic acoustics, sources, dipoles and quadrupoles are the three basic mechanisms of sound generated by small disturbances to a gas at rest. They are properties of the solutions to the equations of motion and describe radiation generated at a point singularity. An overview of their characteristics can be found in Appendix D.

2.4.1 Lighthill's acoustic analogy

Lighthill [39] initiated a theory based on the equations of motion of a gas to describe the sound generated aerodynamically. Here the sound sources are strictly due to aerodynamic motions in a turbulent flow rather than externally applied forces causing vibration of an actual body [40]. Lighthill [39] argued that in a fluctuating flow occupying a limited

portion of a very large volume of fluid (of which the remainder is at rest), the density fluctuations of the real fluid are comparable to those of a uniform acoustic medium at rest coinciding with the real fluid outside of the flow. The exact equations of motion for gas are:

$$\frac{\partial \rho}{\partial t} + \frac{\partial}{\partial x_i}(\rho v_i) = 0 \tag{2.8}$$

$$\frac{\partial}{\partial t}(\rho v_i) + \frac{\partial}{\partial x_j}(\rho v_i v_j + p_{ij}) = 0 \tag{2.9}$$

where Eqn. 2.8 is the exact equation of continuity and Eqn. 2.9 is the (exact) Reynolds momentum equation [39]. According to Lighthill [39], the physical meaning of Eqn. 2.9 is that the momentum of a gas changes at exactly the same rate as if it were at rest under the combined influence of a stress p_{ij} and a fluctuating Reynolds stress $\rho v_i v_j$. The term p_{ij} is the stress between two adjacent fluid elements and consists of a pure pressure $p\delta_{ij}$ and viscous term [41]. The term $\rho v_i v_j$ represents the convection of the momentum ρv_i by the velocity v_j [41]. According to Lighthill [39], a uniform acoustic medium at rest only experiences a stress field of hydrostatic pressures whose fluctuations are proportional to changes in the density, i.e., $p\delta_{ij} \propto c^2\rho\delta_{ij}$ where c^2 is the constant of proportionality. Since the acoustic medium and flow medium exhibit a common stress, Lighthill [39] stated that the sound produced by the flow must be exactly that as produced by an acoustic medium subjected to an external stress field. The stress field is given by

$$T_{ij} = \rho v_i v_j + p_{ij} - c^2\rho\delta_{ij} \tag{2.10}$$

and is called the Lighthill stress tensor. T_{ij} describes the difference between the real stresses in a flow and the stresses in a uniform acoustic medium at rest. To derive Lighthill's acoustic analogy one can use the same procedure described by Rienstra and Hirschberg [42] to form the homogeneous wave equation from the equations of motion. Firstly, take the time derivative of Eqn. 2.8

$$\frac{\partial^2 \rho}{\partial t^2} + \frac{\partial^2}{\partial t \partial x_i}(\rho v_i) = 0, \tag{2.11}$$

and then the divergence of Eqn. 2.9

$$\frac{\partial^2}{\partial x_i \partial t}\left(\rho v_i\right) + \frac{\partial^2}{\partial x_i \partial x_j}\left(\rho v_i v_j + p_{ij}\right) = 0. \tag{2.12}$$

Next, combine the equivalent terms to eliminate the momentum term ρv_i from the resulting equations

$$\frac{\partial^2 \rho}{\partial t^2} = \frac{\partial^2}{\partial x_i \partial x_j}\left(\rho v_i v_j + p_{ij}\right). \tag{2.13}$$

Since Eqn. 2.10 can be rearranged in the form

$$\rho v_i v_j + p_{ij} = T_{ij} + c^2 \rho \delta_{ij}, \tag{2.14}$$

Eqn. 2.13 can be rewritten as

$$\frac{\partial^2 \rho}{\partial t^2} = \frac{\partial^2}{\partial x_i \partial x_j}\left(T_{ij} + c^2 \rho \delta_{ij}\right) \tag{2.15}$$

$$\Rightarrow \frac{\partial^2 \rho}{\partial t^2} - \frac{\partial^2}{\partial x_i \partial x_j}\left(c^2 \rho \delta_{ij}\right) = \frac{\partial^2}{\partial x_i \partial x_j}\left(T_{ij}\right) \tag{2.16}$$

$$\Rightarrow \frac{\partial^2 \rho}{\partial t^2} - c^2 \nabla^2 \rho = \frac{\partial^2 T_{ij}}{\partial x_i \partial x_j} \tag{2.17}$$

which is the Lighthill's equation for radiation aerodynamic sound. As can be seen, it is similar to the homogeneous wave equation in that the propagation terms are on the left of the equation. The difference is that in Eqn. 2.17, a source exists on the right. This term represents the external stress field applied to the fluid and is equivalent to a static distribution of quadrupoles over the whole space with instantaneous strength per unit volume T_{ij}. The term δ_{ij} in the above equations is a delta function, and so allowed

$$c^2 \nabla \rho \equiv c^2 \frac{\partial^2 \rho}{\partial x_i^2} = \frac{\partial^2 (c^2 \rho \delta_{ij})}{\partial x_i \partial x_j} \tag{2.18}$$

to be used in the final step. The term δ_{ij} is 1 when $i = j$ and 0 otherwise [41]. In formulating his theory, Lighthill [39] not only accounted for the generation of sound, but also its self-modulation due to acoustic non-linearity, its convection within the flow, its propagation with variable speed and its attenuation due to both conduction and viscosity [43]. He also considered the relative importance of each term in T_{ij} for low Mach number flows

with uniform temperature distributions. He argued that the effects of viscosity and conduction can be ignored in these cases and that the Lighthill stress tensor can be simplified as

$$T_{ij} \simeq \rho_0 v_i v_j. \tag{2.19}$$

This means that for low velocity flows without any solid boundaries, the Reynolds stresses in the flow are the main generators of turbulent sound.

2.4.2 Influence of solid boundaries on sound

Lighthill's aeroacoustic theory describes the conversion of kinetic energy into acoustic energy in an unbounded flow in the absence of any solid boundaries. Curle [27] extended this theory by including solid boundaries in the flow. In their presence, he found that the sound generated by Lighthill's quadrupoles are reflected and diffracted at the boundaries and are no longer distributed over the whole space but rather throughout the region external to the boundaries [27]. He formulated a new solution to Eqn. 2.17 which takes the form

$$\rho - \rho_0 = \frac{1}{4\pi c^2} \frac{\partial^2}{\partial x_i \partial x_j} \int_V \frac{T_{ij}(\mathbf{y}, t - \frac{r}{c})}{r} \mathrm{d}\mathbf{y} - \frac{1}{4\pi c^2} \frac{\partial}{\partial x_i} \int_S \frac{F_i(\mathbf{y}, t - \frac{r}{c})}{r} \mathrm{d}S(\mathbf{y}) \tag{2.20}$$

where F_i is the strength per unit area of a dipole. F_i is exactly the force per unit area exerted on the fluid by the solid boundaries in the x_i direction [27]. If compared to Eqn. D.5 one can see that there is an additional surface integral term in Eqn. 2.20. This surface integral represents Curle's modification to Lighthill's theory and is exactly equivalent to the sound generated in a medium at rest by a distribution of dipoles of strength F_i. The volume integral represents the distribution of quadrupoles in the region external to the solid boundaries [27]. Thus, the sound generated by a perfectly rigid solid boundary in a flow is due to a combination of dipoles along the surface of the solid boundary and quadrupoles in the volume surrounding the region beyond the body [27]. Similar to Lighthill [39], Curle [27] used the exact equations of motion and so encapsulated not only viscous, thermal and convection effects (accounted for by T_{ij}), but also included the effects of reflection and diffraction (accounted for by F_i) [27].

Lighthill [39] used dimensional analysis to determine that the intensity of the sound field generated by the quadrupoles is

$$I_Q \propto \rho V_\infty^8 c^{-5} \left(\frac{l}{\mathbf{x}}\right)^2 \tag{2.21}$$

where l is characteristic length of the body and $\mathbf{x}$ is the distance of the observer from the source. Using a similar analysis, Curle [27] determined that the intensity of the sound field generated by the dipoles in Eqn. 2.20 is

$$I_D \propto \rho V_\infty^6 c^{-3} \left(\frac{l}{\mathbf{x}}\right)^2 . \tag{2.22}$$

As above, l and $\mathbf{x}$ are dimensional quantities and it should be noted that $\mathbf{x}$ must be larger than the wave length of the generated sound. Curle [27] compared the relative influences of the quadrupoles and the dipoles. He found that for low Mach numbers, the contribution made by the dipoles in Eqn. 2.20 should be greater than the quadrupoles. Moreover, he discussed how the frequency of the quadrupoles tend to be double that of the dipoles, particularly for flows that impinge on a circular cylinder and induce a vortex street.

A common example of sound generated by solid bodies in a flow is aeolian tones, which can be heard with the whistling of telephone wires in the wind. Phillips [44] used the theory developed by Curle [27] to estimate the intensity of the sound radiated from a circular wire in terms of the fluctuating forces acting on the wire. He found that the sound was generated by a dipole field. As the radiation pattern of the dipole was normal to the axis of the wire, Phillips [44] deduced that the sound must be generated by the fluctuating lift force [44]. Assuming an incompressible, low Mach number flow, he estimated the intensity of the sound between $100 \leqslant Re \leqslant 160$ to be

$$I(x) \sim 0.27 \cos^2\theta \frac{\rho^2 l D V_\infty^6 S t^2}{c^2 x^2} \tag{2.23}$$

where θ is the angle between the observer and the main flow. For higher Reynolds numbers, where the wake of the cylinder is turbulent, he found a similar expression for the radiated sound intensity except with a smaller numerical constant, roughly 0.037. Importantly, Phillips [44] observed that the intensity of the sound strongly depends on the correlation of the fluctuating lift force along the length of the wire. He found that an

increase in the correlation provides a much more powerful radiation into the far field. This is due to the fact that a correlated fluctuating lift force induces vortex shedding that is more two-dimensional than an uncorrelated fluctuating lift force. Phillips [44] suggested that this is why the intensity of the sound generated in a turbulent wake is smaller than the sound generated in a laminar wake.

2.4.3 Vortex sound

Powell [45] examined the connection between vortex motion and acoustic generation. He identified vortex formation to be a fundamental mechanism. The connection between vortex motion and sound generation is highlighted by Powell's equation, which is an inhomogeneous wave equation for a low speed flows. Expressed as

$$\frac{\partial^2 p}{\partial t^2} - c^2 \nabla^2 p = \nabla \cdot \left(\rho(\omega \times \widehat{v}) + \nabla \frac{1}{2} \rho \widehat{v}^2 \right), \tag{2.24}$$

ω is the vorticity and $\widehat{v}$ is the incompressible velocity. A solution can be found in Powell [45] where it is shown that the pressure perturbation is attributable to the sum of four parts. The dominant component is a volume distribution of dipoles whose strength is proportional to the term $(\omega \times \rho)$ which describes the vortex motion due to the fluctuating velocity [4]. The rest of the sound is generated by contributions from a volume distribution of non-directional sources in the flow, a surface distribution of dipoles and a surface distribution of monopoles on the solid body itself.

Howe [46] also examined the contribution made by vorticity in the generation of acoustic energy. He recast Lighthill's equation using the total enthalpy as the acoustic wave operator instead of the acoustic pressure. The total enthalpy describes the total thermodynamic energy in the system and by using it instead of pressure, he accounted for interactions with solid boundaries [47]. Howe [46] used the Crocco's form of the momentum equation when formulating his inhomogeneous wave equation. The Crocco's form of the momentum equation for an incompressible fluid can be expressed as

$$\frac{\partial \widehat{v}}{\partial t} + (\omega \times \widehat{v}) + \nabla B = -\nu \nabla \times \omega \tag{2.25}$$

where B is the total enthalpy and ν is the viscosity [48]. As can be seen, by using this

form of the momentum equation, the contribution made by vorticity is introduced. Using the same approach to formulate Lighthill's equation (taking the time derivative of the continuity equation, the divergence of the momentum equation and subtracting the two), Howe [46] formulated his inhomogeneous to take the form

$$\frac{\partial^2 B}{\partial t^2} - c^2 \nabla B = \nabla \cdot (\omega \times \widehat{v}) \tag{2.26}$$

where $\widehat{v}$ is the total velocity comprising of a hydrodynamic component and an irrotational unsteady component [49]. Howe [48, 50] approximates the acoustic pressure in the far field as $p \approx \rho B$, which allows Eqn. 2.26 to be rewritten as

$$\frac{\partial^2 p}{\partial t^2} - c^2 \nabla p = \rho \nabla \cdot (\omega \times \widehat{v}) \tag{2.27}$$

The implication of which is that the acoustic sources generating sound are associated with those regions of the flow where the vorticity is non-vanishing [46]. It should be noted that Eqn. 2.26 and Eqn. 2.27 assumes the flow is isentropic, homentropic and has a low Mach number [42, 46, 48, 50]. The term $\rho\,(\omega \times \widehat{v})$ appears in both Eqn. 2.24 and Eqn. 2.27. This term is the Coriolis force and seems to be the mechanism generating the sound because it exerts an external force on the acoustic field [42].

2.5 Summary

As can be seen, much effort has been expended in understanding the fluid dynamic and acoustic resonant characteristics of systems found in common industrial engineering settings. While it is clear that much is understood about "lock-in", a qualitative and quantitative understanding of the acoustic energy transfer between the flow field and the sound field is largely absent. To this end, the current work is focused on investigating the flow sound-interaction for the bluff body configurations discussed above. The next chapter describes the conceptual approach developed as part of this work.

Chapter 3

Localising Resonant Aeroacoustic Sources

3.1 Introduction

This chapter describes the conceptual approach used to study the energy transfer mechanism between the flow field and the sound field of a ducted bluff body flow. The theory of vortex sound developed by Howe [1, 46] forms the basis of these experiments and the methodologies used to resolve the hydrodynamic and acoustic characteristics in the current work are set out.

3.2 Howe's integral

The work of Powell [45] and Howe [46] discussed in the last chapter have shown the prominence that vorticity plays in the generation of sound. Extending his work, Howe [1] developed an equation for the dissipation of sound from a sharp edge in low subsonic, isentropic mean flow. It can be used to determine the energy transfer between the hydrodynamic flow field and the acoustic field. This equation is named the Howe's integral and takes the form

$$\Pi_{abs} = \rho_0 \int U_a \cdot (\omega \times V) d\Re. \tag{3.1}$$

Howe's equation is the integral of the triple product between the vorticity, ω, the hydrodynamic velocity, V and the acoustic particle velocity, U_a in volumetric flow field $\Re$ with mean density ρ_0. With reference to the work of Howe [1, 50], Rienstra and Hirschberg [42]

and Dequand *et al.* [49], Eqn. 3.1 is derived below.

The incompressible velocity field $\widehat{v}$ is comprised of two components, namely the unsteady hydrodynamic velocity V and the unsteady irrotational velocity $\nabla\Phi$ [49]. That is to say

$$\widehat{v} = V + \nabla\Phi. \tag{3.2}$$

As the term $\nabla\Phi$ is non-zero when the fluid is incompressible, it can be considered as the acoustic particle velocity U_a. According to Howe [1, 50] the unsteady hydrodynamic component (V) solely contains kinetic energy. This energy is supplied to the flow field at a rate

$$\Pi = \rho_0 \frac{\partial}{\partial t} \int \frac{1}{2} V^2 \mathrm{d}^3\mathrm{x}. \tag{3.3}$$

In ducted flows, this kinetic energy will be much stronger than any of the kinetic energy contained in U_a [50]. Since the vortices in the flow will cause the energy to fluctuate, the momentum equation can be used to determine its variation. Howe [1, 50] used the Crocco's form of the momentum equation which can be expressed in a form similar to Eqn. 2.25 as

$$\frac{\partial V}{\partial t} + \nabla B = -\left(\omega \times \widehat{v}\right). \tag{3.4}$$

Here, the incompressible velocity field, $\widehat{v}$ in the first term on the left has been replaced by V as we are only interested in the hydrodynamic component, whilst the viscosity term ν has been discarded as viscous effects were ignored [1]. Substituting in for the incompressible velocity field $\widehat{v}$, Eqn. 3.4 can be recast as:

$$\frac{\partial V}{\partial t} + \nabla B = -\left(\omega \times (V + U_a)\right) \tag{3.5}$$

$$\Rightarrow \frac{\partial V}{\partial t} + \nabla B = -\left(\omega \times V\right) - \left(\omega \times U_a\right). \tag{3.6}$$

Howe [1, 50] subsequently takes the scalar product between V and Eqn. 3.6 which obtains

$$V \cdot \frac{\partial V}{\partial t} + V \cdot \nabla B = -V \cdot \left(\omega \times V\right) - V \cdot \left(\omega \times U_a\right). \tag{3.7}$$

This can be rearranged in the form

$$V \cdot \frac{\partial V}{\partial t} + V \cdot \nabla B = -\omega \cdot (V \times V) - V \cdot (\omega \times U_a) \tag{3.8}$$

and simplified as

$$\frac{\partial}{\partial t}\left(\frac{1}{2}V^2\right) + \nabla \cdot (VB) = -V \cdot (\omega \times U_a) \tag{3.9}$$

using the mathematical identities

$$\underline{A} \cdot \frac{\partial \underline{A}}{\partial t} \equiv \frac{1}{2}\frac{\partial}{\partial t}\left(\underline{A} \cdot \underline{A}\right) \equiv \frac{1}{2}\frac{\partial}{\partial t}\left(\underline{A}^2\right)$$

$$\underline{A} \cdot (\underline{A} \times \underline{B}) = \underline{B} \cdot (\underline{A} \times \underline{A}) = 0.$$

Since the flow is assumed to be incompressible, $\nabla \cdot V = 0$ and the divergent term vanishes from Eqn. 3.9. Integrating over a complete volume and back substituting in Eqn. 3.3, one obtains the Howe's integral. That is to say

$$\frac{\partial}{\partial t}\int \left(\frac{1}{2}V^2\right) \mathrm{d}^3\mathrm{x} = \int -U_a \left(V \times \omega\right) \mathrm{d}^3\mathrm{x} \tag{3.10}$$

$$\Rightarrow \Pi_{abs} = \rho_0 \frac{\partial}{\partial t}\int \frac{1}{2}V^2 \mathrm{d}^3\mathrm{x} = \rho_0 \int U_a \left(\omega \times V\right) \mathrm{d}^3\mathrm{x} \tag{3.11}$$

which is exactly Eqn. 3.1. The identity $\underline{A} \cdot (\underline{B} \times \underline{C}) = -\underline{A} \cdot (\underline{C} \times \underline{B})$ was used in the final step. It is important to note that Howe's integral describes the *dissipation* of acoustic energy. Moreover, it should also be noted that in this study only two dimensional components of the hydrodynamic flow field were resolved. This means, the vorticity is actually a scalar and not a vector in this case. To use Howe's integral for determining the *generation* of acoustic power, firstly change the polarity of Eqn. 3.1. Secondly, rearrange it using the same vector identity as Eqn. 3.11 as well as the identity $\underline{A} \cdot (\underline{B} \times \underline{C}) = \underline{B} \cdot (\underline{C} \times \underline{A})$ so that vorticity is not part of the cross product. Thus, the generation of acoustic power in a low Mach number isentropic mean flow can be determined using the formula

$$\Pi_{gen} = \rho_0 \int \omega \cdot (U_a \times V) d\Re. \tag{3.12}$$

Equation 3.12 calculates the instantaneous acoustic power generated by fluctuating vorticity embedded in an acoustic field. Integrating this instantaneous power over a whole acoustic wave cycle determines the net acoustic energy and identifies regions in the flow where sound is either generated (a source) or absorbed (a sink). Acoustic sources occur in regions where energy is transferred from the flow field to the sound field whilst acoustic sinks occur in regions where energy is transferred from the sound field to the flow field [4].

To understand this energy transfer mechanism, two points should be made about Howe's integral and in particular, the triple product. First, there must be some angular dimension between each of the three of the components ω, V and U_a. If any of the components have a zero angle between them, no acoustic energy can be generated. Second, only in cases where the integral of the triple product is non-zero, can the vorticity field represent an acoustic source or sink [4]. That is to say, the amplitude of the hydrodynamic quantities must not remain constant over an acoustic wave cycle. This is due to the fact that the mean of U_a equals zero because of its oscillatory nature. If the hydrodynamic quantities do retain constant amplitude over whole cycle, the total transfer of energy would be zero.

3.3 Conceptual approach

Figure 3.1 shows an organisational tree of the conceptual approach used to implement Eqn. 3.12 and employs predominantly experimental techniques. A key assumption used in this approach is that the flow field can be decoupled from the sound field and resolved separately. According to Tan *et al.* [51], at low Mach numbers (where the fluid can be considered incompressible), it is reasonable to do this when the source regions are compact compared the wavelength of the acoustic wave. The geometry of the test section used in these experiments (see Ch. 4) facilitated a long acoustic wavelength compared to the size of a vortex, which meant it was compact. As can be seen in Fig. 3.1, the hydrodynamic flow field (V and ω) was resolved using phased averaged PIV whilst the acoustic particle velocity (U_a) was resolved by combining a FEA model of the duct's resonant acoustic mode with a point measurement of the acoustic pressure. Using PIV to experimentally

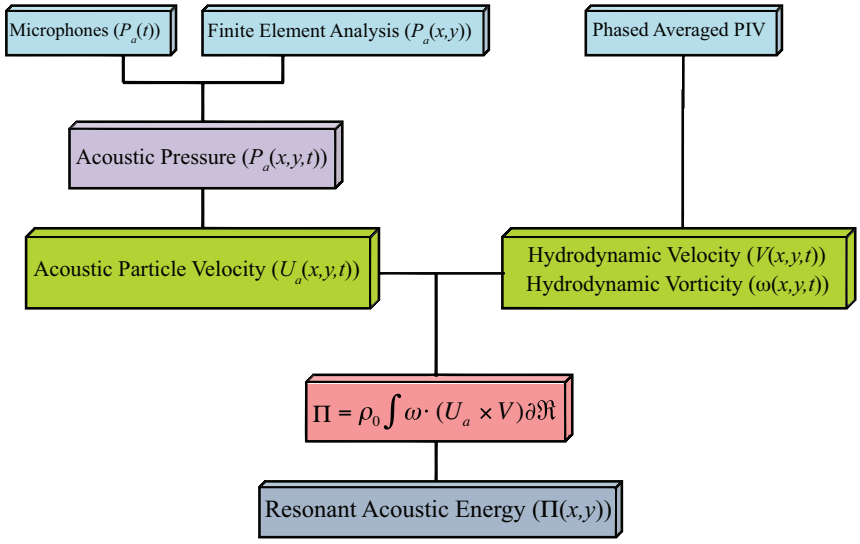

Figure 3.1: Conceptual approach used to experimentally investigate flow-acoustic coupling of resonant ducted bluff body flows.

resolve the "locked-in" flow field meant that feedback mechanism generating the resonance did not have to be simulated.

Many other authors have adopted a similar approach (by decoupling the flow field and the sound field) when evaluated Howe's integral. Some of these authors include Welsh *et al.* [52], Stoneman *et al.* [53], Tan *et al.* [51], Hourigan *et al.* [54], Oshkai and Yan [55], Dequand *et al.* [49] and Mohany and Ziada [56]. Welsh *et al.* [52], Stoneman *et al.* [53] and Tan *et al.* [51] investigated the acoustic resonance of flat plates in duct whilst Hourigan *et al.* [54] studied the sound generated by baffles. Oshaki and Yan [55] and Dequand *et al.* [49] studied co-axial side-branch resonators whilst Mohany and Ziada [56] simulated the resonance of single and two tandem cylinders.

Apart from Oshkai and Yan [55], all of these authors have used numerical or analytical means to resolve the hydrodynamic quantities in Eqn. 3.12. Whilst there were experimental elements in all of these studies, validation of the acoustic source mechanisms were limited to qualitative techniques such as flow visualisation. The main difficulty in using a numerical technique is coupling the flow field with the sound field so that it induces a "locked-in" flow structure. This is usually done by introducing a small oscillatory perturbation onto the boundaries of the flow field simulation. However, as Reyes *et al.* [57] discussed, the type of oscillatory perturbation, which represents the feedback mechanism,

has a significant effect on the acoustic source distribution. This means that simulating the true flow-acoustic coupling mechanism is not trivial and is a significant disadvantage to using numerical techniques for studying flow-sound interaction in ducted bluff body flows.

3.4 Resolving acoustic particle velocity

The acoustic particle velocity is a key component in the transfer of energy between the flow field and the sound field. Normally, to measure a temporal, spatial distribution of the acoustic particle velocity, an array of microflowns (acquiring simultaneous measurements of the acoustic field characteristics) could be used. However, because the amount of microflowns needed to achieve a high spatial resolution of U_a would be impractical, this approach was not explored. Alternatively, an array of microphones could have been used to directly measure the acoustic pressure over the whole flow field which could then be converted in to acoustic particle velocity. However, as with microflowns, the number of microphones needed in the array to obtain a high spatial resolution would be impractical. Rather than directly measuring the acoustic particle velocity or the acoustic pressure experimentally, it was decided to use a different approach that decoupled the acoustic pressure field into a temporal component and a spatial component as shown in Fig. 3.1. It was decided to do this because the spatial component and the temporal component were easy to determine individually. Figure 3.1 shows that the spatial component of the resonant acoustic pressure, also known as the mode shape, was calculated by solving a finite element analysis (FEA) of the system whilst the temporal component was measured with a single point microphone measurement of the acoustic pressure.

Using ANSYS Multiphysics 11.0 software, a quiescent flow finite element model of the test section was simulated in order to determine the mode shapes of the system with the cylinders *in situ*. For low Mach numbers, the Navier-Stokes (momentum) equations and continuity equation can be reduced to the acoustic wave equation. This governs the acoustic pressure in the system and can be expressed as

$$\frac{1}{c^2}\frac{\partial^2 \widehat{P}_a}{\partial t^2} - \nabla^2 \widehat{P}_a = 0 \tag{3.13}$$

where c is the speed of sound, $\widehat{P}_a$ is the acoustic pressure and t is the time. This equation assumes that the flow is compressible and inviscid and that the mean density and pressure are uniform throughout the fluid [58]. It also assumes that there is no mean flow of the fluid itself and is called a lossless wave equation as it neglects viscosity [58]. Resonant acoustic modes in a duct fluctuate with simple harmonic motion. Thus, the acoustic pressure in the test section can be expressed as a standing-wave solution

$$\widehat{P}_a = P_a e^{i2\pi f_a t} \tag{3.14}$$

where P_a is the time independent amplitude of the resonant acoustic pressure and f_a is the mode's frequency of oscillation. Substituted into Eqn. 3.13, the wave equation reduces to Eqn. 3.15, which is the Helmholtz equation

$$k^2 P_a + \nabla^2 P_a = 0 \tag{3.15}$$

where $k = \frac{2\pi f_a}{c}$ is the wave number. The Helmholtz equation is discretized and solved using appropriate matrix reduction. The finite element type chosen to model the fluid in the duct field was ANSYS "Fluid29". This is a 2-dimensional element, with four corner nodes and 3 degrees of freedom per node. These degrees of freedom include translations in the nodal x and y directions and pressure. "Fluid29" is a quadrilateral element with a triangular option. However, only quadrilateral elements were used in the model as they are more accurate than triangular elements. The boundary condition applied at the inlet and outlet of the test section was

$$P_a = 0, \tag{3.16}$$

which is a Dirichlet boundary condition. The boundary condition applied to the walls and cylinders was

$$\underline{n} \nabla P_a = 0, \tag{3.17}$$

which is a Neumann boundary condition. The walls and cylinders were also assumed to be rigid ideal acoustic media. These boundary conditions were selected in order to simulate an open ended duct facilitating the extraction of the β-mode [59] and followed

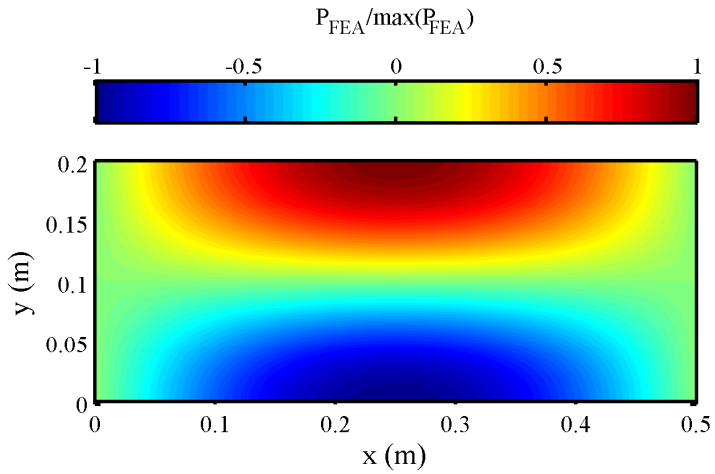

Figure 3.2: Pressure distribution of the β-mode for a simple rectangular duct.

the work of Stoneman *et al.* [53], Hourigan *et al.* [54], Tan *et al.* [51] and Mohany and Ziada [56]. A key feature of the β-mode is that the pressure along the wall of the duct decays exponentially away from the bluff bodies. Another key feature is that it exhibits a half wavelength across the duct with an acoustic pressure node at the midpoint and acoustic pressure anti-nodes at the walls. The anti-nodes are of equal magnitude and opposite polarity.

An example of a β-mode for a simple rectangular duct without any obstructions can be seen in Fig. 3.2 whilst profiles of the pressure across the width of the duct and along the length of the duct can be seen in Fig. 3.3 and Fig. 3.4 respectively. It should be noted that even though the boundary conditions which satisfy the β-mode normally assume that the inlet and outlet of the duct are infinitely far away from the area of interest, the test section geometry was modelled exactly and the contraction and diffuser sections were not considered in the analysis.

The output from the finite element analysis is a series of nodal pressures which when combined with their coordinates can be used to form a spatial distribution of the resonant acoustic pressure. However, because no acoustic source was defined in the model, the magnitude of the spatial pressure distribution, $P_{FEA}(x, y)$ was arbitrary and needed to be scaled. If the location of a reference microphone (say $M1$ in Fig. 4.2) is specified, the arbitrary pressure at that location in the model can be used to normalise the entire pressure field. It is preferable to have M1 located near the region of maximum acoustic

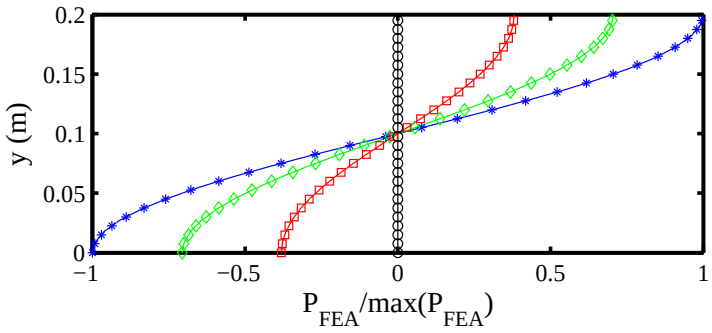

Figure 3.3: Pressure profile of the β-mode across the duct at various streamwise locations. $*$ $x = 0.25$ m; $\diamond$ $x = 0.15$ m; $\square$ $x = 0.05$ m; $\circ$ $x = 0$ m

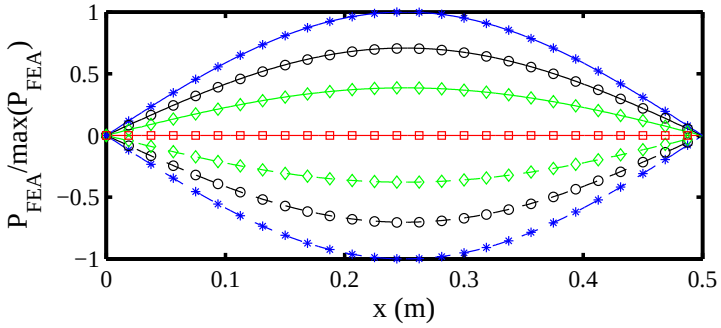

Figure 3.4: Pressure profile of the β-mode across along the length of the duct at various transverse locations. $*$ $y = 0.2$ m ($y = 0$ m); $\circ$ $y = 0.15$ m ($y = 0.05$ m); $\diamond$ $y = 0.125$ m ($y = 0.075$ m); $\square$ $y = 0.1$ m. The bracketed distances correspond to the dashed lines which have been included to highlight the symmetry of the β-mode about the mid-plane of the duct.

pressure. This normalised pressure field can then be simply scaled by the actual pressure measured at the reference microphone under experimental conditions to obtain the real resonant acoustic pressure distribution in the flow field. Expressed mathematically as

$$\widehat{P}_{FEA}(x,y) = P_{FEA}(x,y)P_{M1}, \tag{3.18}$$

this equation is the average spatial distribution of the acoustic pressure under resonant conditions. Since the resonant mode of interest is a β-mode, the acoustic pressure propagates across the duct in plane waves. Thus, the temporal acoustic pressure measured by microphone $M1$ can be expressed as

$$P_{M1}(t) = P_a sin(2\pi f_a t) \tag{3.19}$$

where P_a is the amplitude of the pressure signal and f_a is the resonant frequency. Equation. 3.18 can now be expressed as

$$\widehat{P}_{FEA}(x,y,t) = P_{FEA}(x,y)P_a sin(2\pi f_a t) \tag{3.20}$$

which is the temporal, spatial distribution of the acoustic pressure used to derive the acoustic particle velocity at every location in the duct at any phase in the acoustic wave cycle. The relationship between the acoustic pressure and the acoustic particle velocity, U_a was determined by solving the Euler equation,

$$\rho\frac{\partial U_a(x,y)}{\partial t} = -\nabla\widehat{P}_{FEA}(x,y,t). \tag{3.21}$$

Substituting Eqn. 3.20 into the Eqn. 3.21, the full Euler equation may be expressed as

$$\rho\frac{\partial U_a(x,y)}{\partial t} = -\nabla(P_{FEA}(x,y)P_{M1}(t)). \tag{3.22}$$

After some simple integration, it follows that the acoustic particle velocity, U_a can be quantified as

$$U_a(x,y,t) = \frac{P_a}{2\pi f_a \rho} cos(2\pi f_a t)\nabla P_{FEA}. \tag{3.23}$$

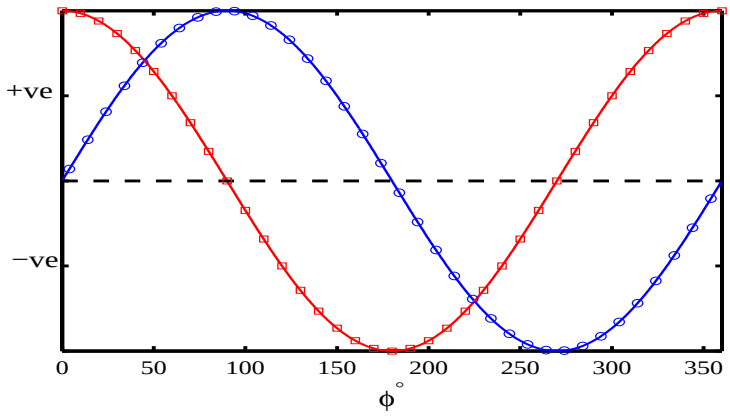

Figure 3.5: Relationship between the acoustic pressure measured at microphone $M1$ and the acoustic particle velocity adopted in the current work. ○ Pressure; □ Acoustic particle velocity.

The acoustic particle velocity is a cosine dependent variable which means it leads the acoustic pressure by 90°. Figure 3.5 highlights the relationship between the acoustic pressure measured at $M1$ and the acoustic particle velocity adopted in the current work. This becomes important with regard to phasing between the vortices shed from the cylinders and the acoustic particle velocity propagating across the duct. At phase $\phi = 0°$ there is zero acoustic pressure but maximum positive acoustic particle velocity whilst at $\phi = 180°$, there is maximum acoustic pressure but zero acoustic particle velocity. It should be noted that in all that follows, any reference to the phase, ϕ, refers to the phase of the acoustic pressure and not the acoustic particle velocity.

3.5 Resolving velocity and vorticity

The vorticity convecting in the flow field, which Howe [46] pointed out as being the main contributor to the generation of sound in low Mach number mean flows, and the hydrodynamic velocity was resolved by using particle image velocimetry (PIV). PIV is a non-intrusive optical flow measurement technique that is based on the very simple principle that if the displacement of a particle in the fluid over a known period of time can be measured, then its velocity can be calculated. It provides both qualitative and quantitative characteristics of the flow. The major advantage of PIV over other flow measurement techniques is that it can resolve velocities over the whole flow field instantaneously rather

than just at a single point. A brief discussion on the PIV technique will be outlined below but a more in depth synopsis on some of its intricate technical details can be found in Raffel *et al.* [60].

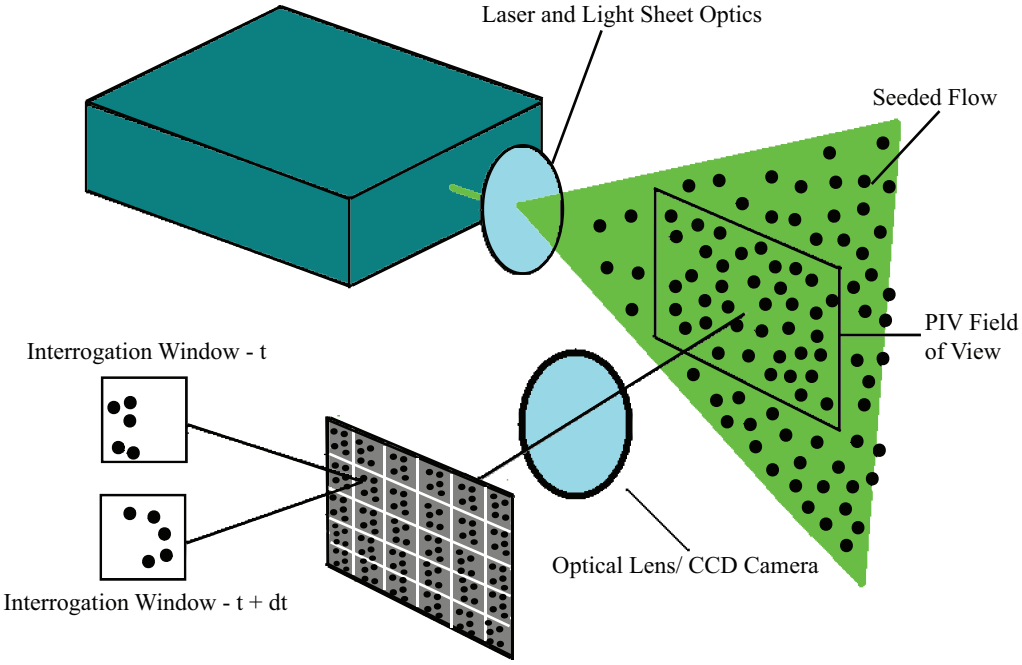

Figure 3.6: General setup of a two dimensional, two component PIV system.

Figure 3.6 shows the general setup of a two dimensional, two component PIV system that can resolve velocities in the x and y directions (u and v, respectively). The flow field is seeded with small tracer particles generated by a lasken nozzle and distributed into the duct using a seeding box. The particles have a diameter of 1 μm so that they follow the flow of the fluid but are not large enough to alter it. These particles are then illuminated by a high repetition laser and an image of the flow field is taken with a camera at a certain time t. A second image of the flow is then taken at a later time, $t+dt$ such that the particles recorded in the first image have moved to different positions in the second image. These two images of the flow are then split into regular grid cells, or interrogation windows, and a spatial cross-correlation is calculated between them in order to determine the statistically most probable particle displacement for each window. The spatial cross-correlation is defined as

$$R_{I1I2_i}(s) = \iint I1(x)I2(x+s)d^2x \tag{3.24}$$

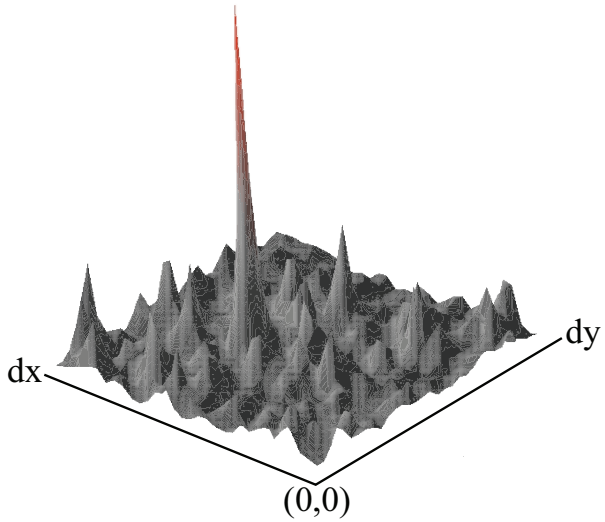

Figure 3.7: A typical cross-correlation map between two interrogation windows of the first and second images. The largest peak corresponds to the most probable particle pixel displacement.

where $I1$ and $I2$ represent the intensities of the particles measured by the camera in the first and second images respectively. The physical spatial coordinate is x whilst s is the spatial coordinate in the correlation plane [61]. A cross correlation is calculated between the first and second images for each interrogation window in the field of view. This results in a correlation map being generated for each interrogation window, similar to that shown in Fig. 3.7. As can be seen, the correlation map consists of a number of peaks. The largest of these peaks corresponds to the most probable particle displacement and is determined using a peak-searching algorithm.

The correlation map in Fig. 3.7 has a high signal-to-noise ratio, that is, the highest peak (the most probable particle displacement) is much higher than the rest of the peaks in the interrogation window. Having a high signal-to-noise ratio in every interrogation window is desirable and it ensures that there is a high level of confidence in the calculated velocity vector. The quality of the cross correlation (signal-to-noise ratio) between the first and second images is dependent on many factors including the quality of the images (which in-turn depends on various factors such as the seeding density, the seeding uniformity and the illumination), the interrogation window size, the algorithms used to solve the cross correlation and the uniformity of the velocity field within the interrogation window.

The pixel displacement values of the particle corresponding to the largest correlation

peak from the origin of the map in the x and y directions are dx and dy respectively. These are combined with the time separation between the two images, dt to determine most probable velocity vector components u and v in the interrogation window. The velocity component in the x direction is $u = dx/dt$ whilst the velocity component in the y direction is $v = dy/dt$. The most probable particle displacement and hence the most probable velocity vector are calculated for each interrogation window in the image plane and when assembled together, form a velocity vector map of the entire flow field. The magnitude of the individual velocity components u and v can then simply be expressed as

$$V(x,y) = \sqrt{u(x,y)^2 + v(x,y)^2} = \frac{\sqrt{dx(x,y)^2 + dy(x,y)^2}}{dt} \tag{3.25}$$

which is generally plotted as a contour map when presenting the results.

The underlying structure of a "locked-in" flow is strongly periodic. However, because the Reynolds numbers at which resonance occurs are usually high enough for the flow regime to be turbulent, ensemble averaging is needed to obtain the mean periodic variation. There are two approaches to ensemble averaging PIV data. The first way, which is referred to herein as conventional PIV (or standard PIV) uses Eqn. 3.24 and Eqn. 3.25 to first calculate velocity vector maps for every realisation in the data sequence which are then averaged. The second way, which can be referred to either as ensemble correlation PIV or sum of correlation PIV uses Eqn. 3.26 but averages all of the correlation maps in the data sequence and not the velocity vector maps.

$$\overline{R}_{I1I2B}(s) = \iint \overline{I1(x)I2(x+s)} d^2x \tag{3.26}$$

Doing this forms an ensembled correlation map which can then be used to determine the most probable particle displacement and velocity vector as before. The key difference between the two methods is that averaging occurs at different stages in the algorithm. Figure 3.8(a) shows a flow chart of the algorithm employed for conventional PIV whilst Fig. 3.8(b) shows the same for ensemble correlation PIV. It should be noted that the peak searching algorithms used to determine the velocity vectors for ensemble correlation PIV and conventional PIV are the same. The advantage of the ensemble correlation algorithm

is that it can increase the signal-to-noise ratio of the data because the noise due to the random pairing of particles is averaged out leaving only the true displacement of the particle in the interrogation window. This is particularly important because the non-linear peak searching algorithm used to determine the most probable particle displacement is prone to producing erroneous results from low signal-to-noise ratio correlations [61]. The ensemble correlation PIV algorithm is most useful when the flow is periodic and when quality of the data may be compromised due to velocity gradients in the flow, poor seeding and large reflections from the flow area boundaries.

Meinhart *et al.* [61] compared the performance of the conventional PIV algorithm with that of the ensemble averaged PIV algorithm under challenging micro-channel flow conditions. They found that ensemble correlation algorithm greatly outperformed the conventional PIV algorithm. The results of their study is given in Fig. 3.9 which plots the percentage of valid measurements against the number of realisations in the measurement. There is a stark difference in the number of valid measurements recorded between the two algorithms. In fact, after only just 5 averages, the ensemble correlation PIV algorithm produces 20% more valid vectors than the conventional PIV algorithm. Another advantage of the ensemble correlation PIV algorithm in challenging experimental conditions is that there is no penalty for the number of measurements used in the average. This is evident in Fig. 3.9 as the fraction of valid measurements remains constant as the number of averages increases. The same cannot be said for the conventional PIV algorithm as increasing the number of averages actually lowers the fraction of valid measurements.

Meinhart *et al.* [61] also studied the performance of a third PIV algorithm called the "average image technique". This PIV algorithm takes the average of all the images in the sequence, calculates the cross-correlation of the averaged image and then applies peak detection to determine the mean velocity vector. As can be seen, in challenging PIV conditions this technique out performs the conventional PIV algorithm but is still not reliable compared to the ensemble correlation PIV method.

For its advantages, ensemble correlation PIV should only be used in steady periodic flow applications where only phase averaged velocity measurements are desired. This can make its application quite limited and highlights its inability to calculate instantaneous velocity measurements. This means that higher order statistics such as turbulence energy

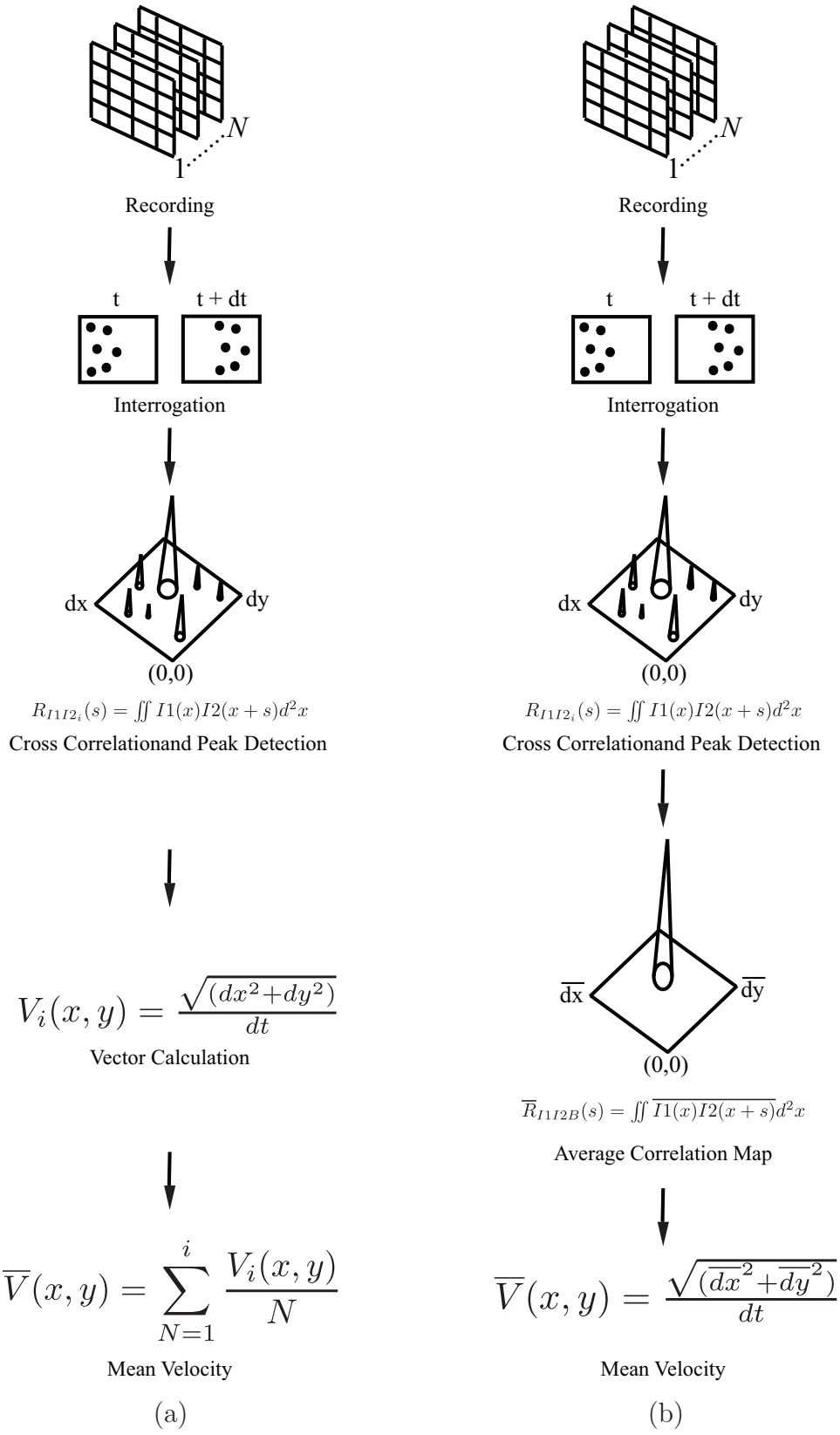

Figure 3.8: The conceptual approach of two different PIV algorithms. (a) Conventional PIV algorithm; (b) Ensemble correlation PIV algorithm.

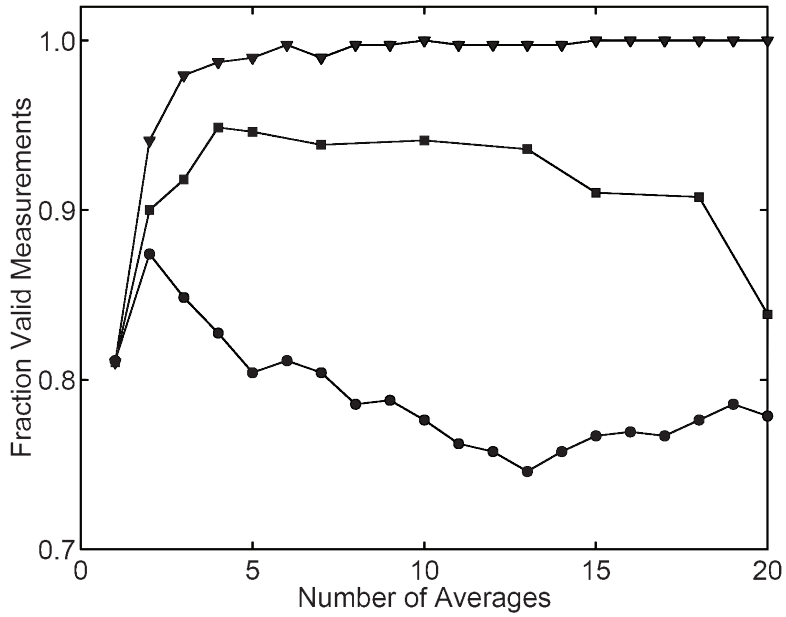

Figure 3.9: The performance of various PIV algorithms under challenging PIV conditions. • - conventional PIV; ■ - average image PIV; ▼ - ensemble correlation PIV. Meinhart *et al.* [61].

(which would be of interest in jet applications) cannot be explored and is a significant disadvantage. Notwithstanding this, it was decided to use the ensemble correlation PIV algorithm as the cylinder configurations had very complex geometries and flow patterns. A comparison of the results obtained from conventional PIV and ensemble correlation PIV can be found in Appendix. B. It is also interesting to note that the conventional PIV algorithm and the ensemble correlation PIV algorithm can both achieve sub-pixel accuracy when calculating the particle displacements. This means they can both achieve a high level of accuracy. In fact, the software used in the present experiments, Davis 7.2 by LaVision, can achieve a pixel displacement accuracy as high as 0.05 px [62]. This is a major advantage of the PIV technique, especially when you consider the high spatial resolution that can be achieved with the correct setup.

Another major advantage of PIV over other flow field measurement techniques is that the data can be easily organised. Regardless of what algorithm is actually used to calculate the velocity vectors, the results are always placed on regular, uniform grids. These meshes are inherently two dimensional (with a spatial resolution of Δx and Δy) which means differential field quantities, such as the vorticity (ω) can be computed. For a

two dimensional, two component PIV system, the out-of-plane vorticity can be expressed as

$$\omega = \frac{\partial v}{\partial x} - \frac{\partial u}{\partial y}. \tag{3.27}$$

According to Westerweel [63] and Raffel *et al.*[60] this can be estimated from a first-order central difference scheme of the measured data to be

$$\omega_{i,j} = \frac{v_{i+1,j} - v_{i-1,j}}{2\Delta x} - \frac{u_{i,j+1} - u_{i,j-1}}{2\Delta y} \tag{3.28}$$

where i and j are the indices of the mesh points of interest in the x and y directions respectively. Davis 7.2 incorporates the central difference scheme into its post-processing operations and calculates the vorticity any point in the mesh based on the velocity components of its four closest neighbours.

An alternative algorithm based on Stokes' theorem was proposed by Raffel *et al* [60]. Stokes' theorem relates the vorticity in a flow to the circulation using the expression

$$\Gamma = \oint \mathrm{U} \cdot \mathrm{d}\mathbf{l} = (\nabla \times V) \cdot \mathrm{d}\mathbf{S} = \int \omega \cdot \mathrm{d}\mathbf{S} \tag{3.29}$$

and states that the circulation around a closed contour is equal to the sum of vorticity enclosed within that contour. When applied to a regularly spaced PIV grid, Eqn. 3.29 can be rearranged as

$$\overline{\omega}_{i,j} = \frac{1}{A}\Gamma_{i,j} = \frac{1}{A}\oint_{\mathbf{l}(x,y)} (u, v) \cdot \mathrm{d}\mathbf{l} \tag{3.30}$$

where $(\overline{\omega}_{i,j})$ is the average vorticity within the area A. To implement Eqn. 3.30 on a mesh of velocity vectors, a small contour of data points (similar to that shown in Fig. 3.10) is selected and the circulation around the boundaries of this square is calculated using a standard integration scheme. The average vorticity can then be calculated by dividing the total circulation around the contour by its area. Expressed mathematically as

$$\overline{\omega}_{i,j} \approx \frac{\Gamma_{i,j}}{4\Delta x \Delta y}, \tag{3.31}$$

Δx and Δy are the grid spacings of the in Fig. 3.10. The constant 4 indicates that the contour spans four cells. Raffel *et al.* [60] used the trapezoidal rule to integrate around

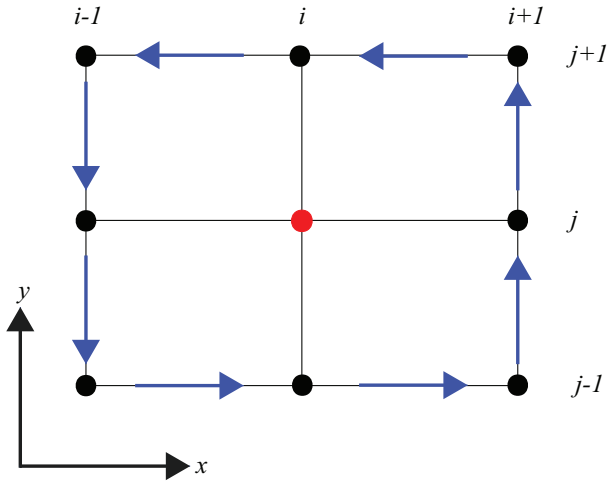

Figure 3.10: Definition of the grid used to calculate vorticity with Eqn. 3.31 and Eqn. 3.32.

the path of the contour in Fig. 3.10. Based on its two mesh point height and two mesh point width, the estimation of the circulation can be expressed as

$$\begin{aligned}\Gamma_{i,j} = \quad & \tfrac{1}{2}\Delta x(u_{i-1,j-1} + 2u_{i,j-1} + u_{i+1,j-1}) \\ & + \tfrac{1}{2}\Delta y(v_{i+1,j-1} + 2v_{i+1,j} + v_{i+1,j+1}) \\ & - \tfrac{1}{2}\Delta x(u_{i+1,j+1} + 2u_{i,j+1} + u_{i-1,j+1}) \\ & - \tfrac{1}{2}\Delta y(v_{i-1,j+1} + 2v_{i-1,j} + v_{i-1,j-1}).\end{aligned} \tag{3.32}$$

Equation 3.32 uses 12 separate velocities over 8 different data points. Substituting this estimation of the circulation into Eqn. 3.31, the vorticity at any point (i, j) on a velocity field grid can be calculated from the velocity vector components of the flow. Westerweel [63] found that applying Eqn. 3.31 to a regularly spaced PIV mesh was equivalent to applying a central difference scheme over a smoothed (3-point) velocity field. That is to say, $\overline{\omega}_{i,j} \equiv \omega_{i,j}$. However, because the Eqn. 3.28 only uses 4 neighbouring data points to estimate the vorticity (compared to the 8 used by Eqn. 3.31), the uncertainty in the estimate of the vorticity using the central difference scheme is much higher [60]. Westerweel [63] compared the performance of Eqn. 3.31 with that of the central difference scheme on a set of well controlled data and found the circulation method to be more accurate than the central difference scheme. For this reason, Eqn. 3.31 and Eqn. 3.32 were used to estimate the vorticity and were implemented as post-processing regimes in Matlab.

3.6 Summary

This chapter has presented a conceptual approach that can be used to experimentally investigate flow-sound interaction between ducted bluff bodies and their surroundings in a low Mach number isentropic mean flow. The specific application of this conceptual approach was to predict the resonant acoustic sources generated by groups of cylinders subject to cross flow. However, the application can be easily extended to other engineering applications. PIV, FEA and a single microphone are used to calculate acoustic power generated by these groups of cylinders and the work really only boils down to four equations, namely Eqn. 3.33, Eqn. 3.34, Eqn. 3.35 and Eqn. 3.36. It should be noted here that the temporal term, t is replaced by the phase of the acoustic pressure wave cycle, ϕ. The next chapter describes the experimental facilities and instrumentation used to resolve these equations.

$$\pi(x,y,\phi) = \rho_0 \int \omega(x,y,\phi) \cdot (U_a(x,y,\phi) \times V(x,y,\phi) d\Re \tag{3.33}$$

$$\omega(x,y,\phi) \approx \frac{\Gamma(x,y,\phi)}{4\Delta x \Delta y} \tag{3.34}$$

$$U_a(x,y,\phi) = \frac{P_a}{2\pi f_a \rho} cos(2\pi f_a \phi) \cdot \nabla P_{FEA} \tag{3.35}$$

$$\overline{V}(x,y,\phi) = \frac{\sqrt{(\overline{dx}^2(x,y,\phi) + \overline{dy}^2)(x,y,\phi)}}{dt} \tag{3.36}$$

Chapter 4

Experimental Facilities and Instrumentation

4.1 Experimental facility

This chapter describes the experimental facility and instrumentation employed in the current study. An explanation of the experimental facility and its constituent parts precedes a discussion of the instrumentation used.

4.1.1 Wind tunnel

The wind tunnel in the current work was an open loop draw down tunnel and utilised air as the working fluid. An isometric schematic of the tunnel is shown in Fig. 4.1. It was approximately 3.5 m long and consisted of four components, namely the test section, the intake, the diffuser and the fan.

The cross sectional area of the test section was 125 mm $\times$ 125 mm and spanned 330 mm. The top and bottom walls onto which the cylinder configurations were mounted were removable. On the side walls, there were two circular co-axial side-branches attached at the mid-span. They had a diameter $L_c = 127$ mm and depth $D_c = 220$ mm and were orientated perpendicular to the axis of the cylinders. A plan view of the test section can be seen in Fig. 4.2(a). HW1 and HW2 correspond to locations where a roving hotwire was installed to measure the flow field characteristics across the width of the duct both upstream and downstream of the side-branches. M1 corresponds to the location at the end of a side-branch where a microphone was flush mounted to measure the acoustic pressure. The main duct walls were made from 10 mm thick perspex whilst the round

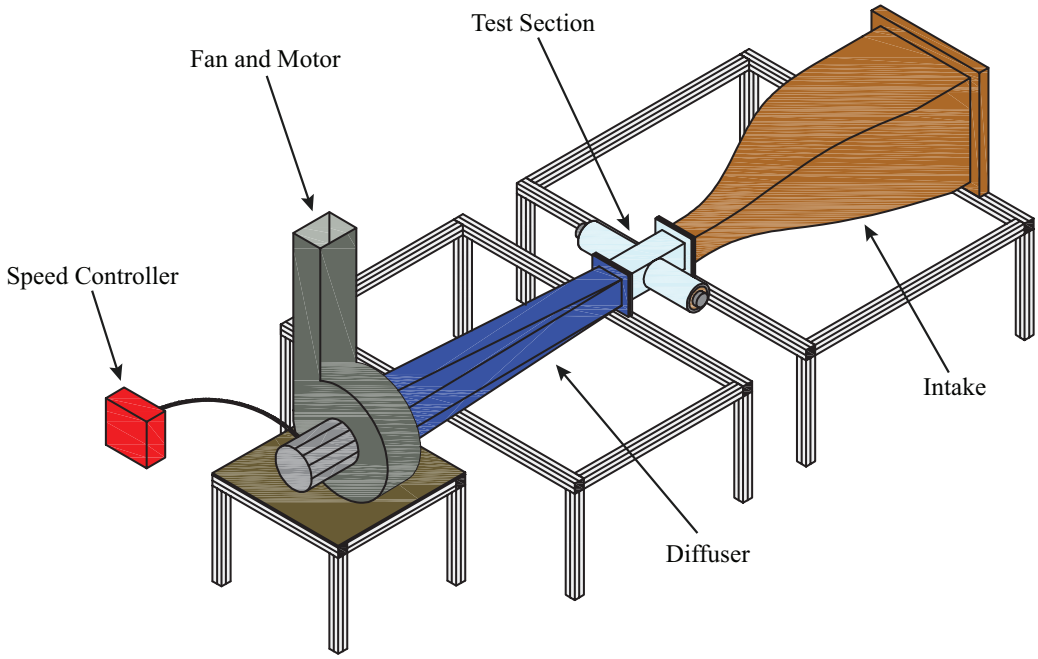

Figure 4.1: Schematic of the wind tunnel.

side-branches were made from 3.5 mm thick perspex and UV-welded to the outer face of the walls. Perspex was used as the working material because it allowed good optical access for PIV yet was easily machinable. This facilitated the installation of any type of cylinder configuration. Figure 4.2(b) shows a photograph of the test section.

The flange of the intake was bolted to the flange of the test section and a sheet of neoprene was used to ensure there were no gaps at the joints which could act as a bleed and hence affect the flow in the test section. The test section and the diffuser were attached in a similar manner. A square-octagon diffuser was employed to accommodate the circular profile of the fan mouth and a flexible seal made from dingy sail material connected the diffuser to the inlet of the fan. The use of sail material minimised the losses in the wind tunnel at the fan inlet because it provided a good air tight seal yet prevented transmission of vibration. The flow in the test section was provided by a centrifugal fan driven by an English Electric Company 1HP three phase induction motor. Initially, the motor ran at a constant speed and the flow velocity in the duct was varied by sliding a baffle plate across the exhaust of the fan. However this set-up could not ensure an accurate and repeatable measurement of the velocity. Thus, the sliding baffle was replaced by an Allen-Bradley Power Flex 40 AC speed controller which controlled the flow velocity by varying the

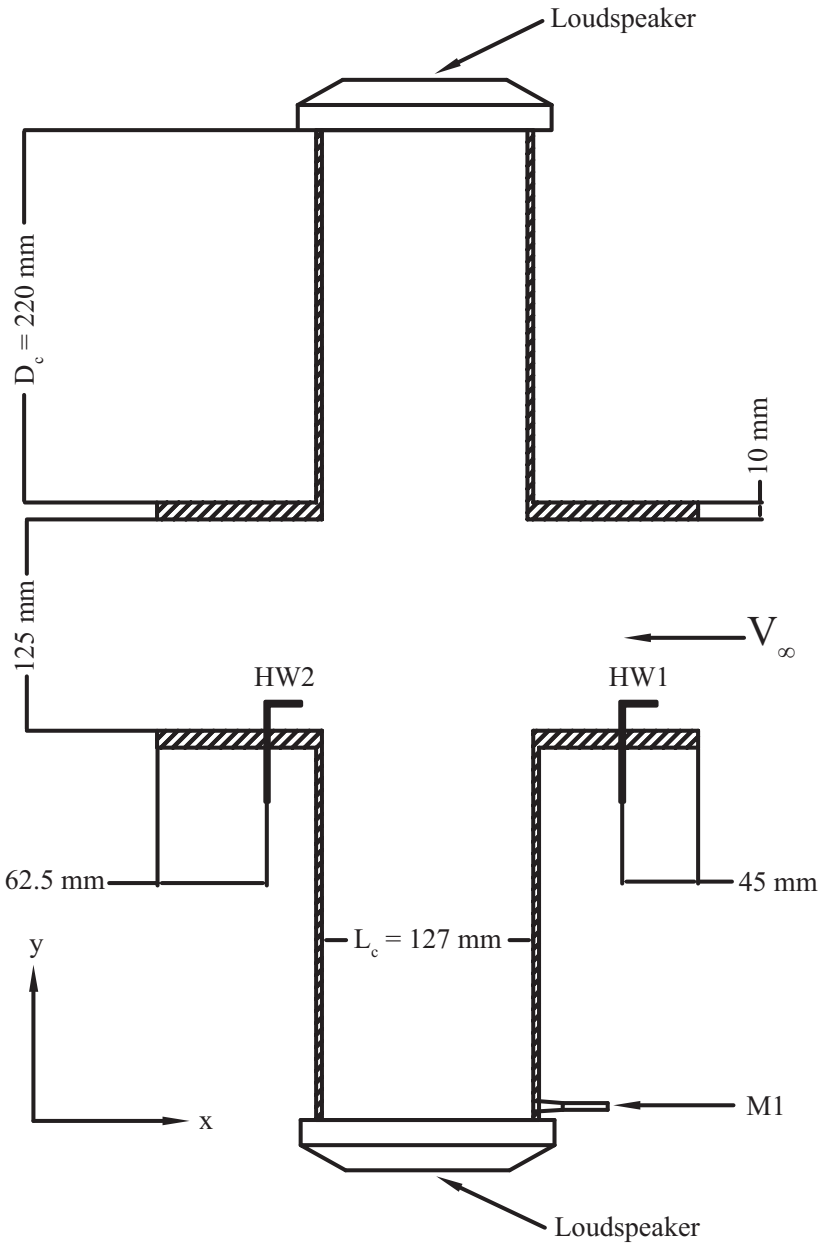

(a) Schematic

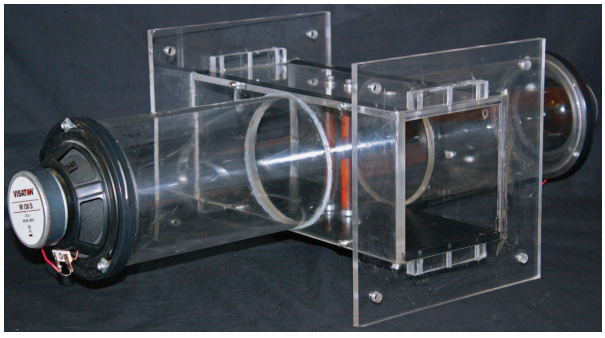

(b) Photo

Figure 4.2: The test section.

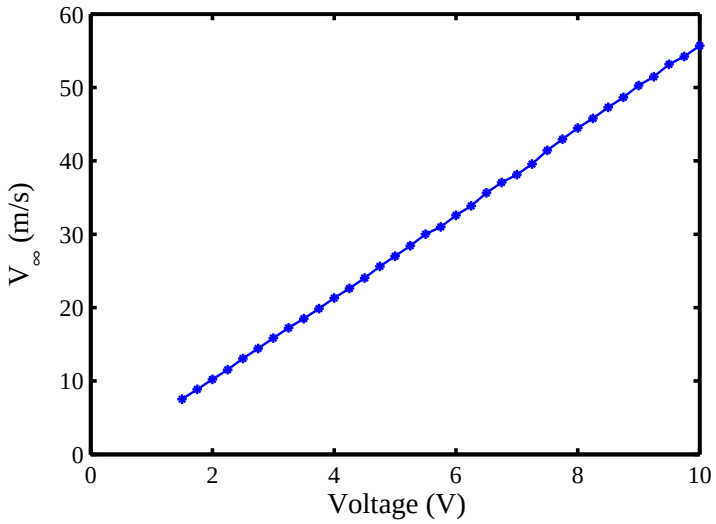

Figure 4.3: The relationship between speed controller voltage and the mainstream velocity.

frequency at which the motor operated. Using Labview software, a constant voltage output was sent to the speed controller. The value of this load determined the frequency at which the motor operated and hence determined the velocity in the tunnel. Figure 4.3 shows the velocity measured at the midspan of the tunnel with a pitot tube against the applied voltage when there was no blockage. The pitot tube was located near the inlet of the test section. As can be seen, the relationship between the applied voltage and the flow velocity in the duct was linear and ranged from 7.5 m/s to 55 m/s. It should be noted that Fig. 4.3 was not constructed by simply incrementing the applied voltage to the fan from 1.5 V to 10 V (in increments of 0.25 V) and then measuring the corresponding velocity. Instead, the order of the voltages from 1.5 V to 10 V was randomised which meant that the flow velocity in the duct could either increase or decrease before a measurement was taken. Adopting this approach ensured that any unknown bias or hysteresis in the flow field could not contaminate the measurements.

The intake of the wind tunnel had an opening of 500 mm $\times$ 500 mm and contracted elliptically to a working section of 125 mm $\times$ 125 mm giving a contraction ratio of 16 : 1 over a span of 1.5 m. The intake also featured honeycomb and turbulence mesh. A profile of the percentage turbulence intensity as well as the velocity profile across the width of the duct at position HW1 for three different mean flow velocities can be seen in Fig. 4.4(a). The turbulence intensity, measured using a roving hotwire can be defined as

Position	Fan Voltage (V)	$V_\infty(m/s)$	$\%T_u$
HW1	3	15.86	0.18
	5	26.98	0.19
	7.5	40.42	0.35
HW2	3	15.94	0.32
	5	26.84	0.33
	7.5	40.66	0.44

Table 4.1: Flow characteristics measured at the midspan of the test section at position ($y = 62.5$ mm).

$$T_u = \frac{\sqrt{\overline{u'^2}}}{\overline{u}} = \frac{\sigma_u}{\overline{u}}, \tag{4.1}$$

where σ_u is the standard deviation of the fluctuating velocity and $\overline{u}$ is the mean velocity. For these tests, no cylinders were mounted. Near the walls, there were relatively high turbulence intensities due to the boundary layer. However, in the freestream where the velocity profiles were much flatter, the turbulence intensities were much lower. The effect of the side-branches on the flow characteristics can be seen in Fig. 4.4(b), which plots the turbulence intensities and velocity profiles across the width of the duct at the downstream location HW2 for the same mainstream velocities. The turbulence intensities close to the walls were very high but in the freestream (which was the predominant area of interest), there were good flow characteristics.

Table 4.1 compares the percentage turbulence intensity and the velocity measured at the midspan of the test section ($y = 62.5$ mm) at position HW1 and HW2. Slightly higher turbulence intensity levels were measured downstream of the side-branches. The average increase in the turbulence intensity between HW1 and HW2 was 0.12%. This small increase is to be expected considering the large pressure variations in the flow field created by the vortices in the side-branch mouths.

One stark difference in the flow characteristics measured at HW1 and HW2 is the thickness of the boundary layer. For the upstream cases (HW1) the freestream velocity occurs approximately 5 mm away from the walls whilst for the downstream cases (HW2) this occurs almost 15 mm away from the walls. The thicker boundary layers downstream of the side-branches are pressumably due to the complex vortex structures that form across the mouths of the circular side-branches.

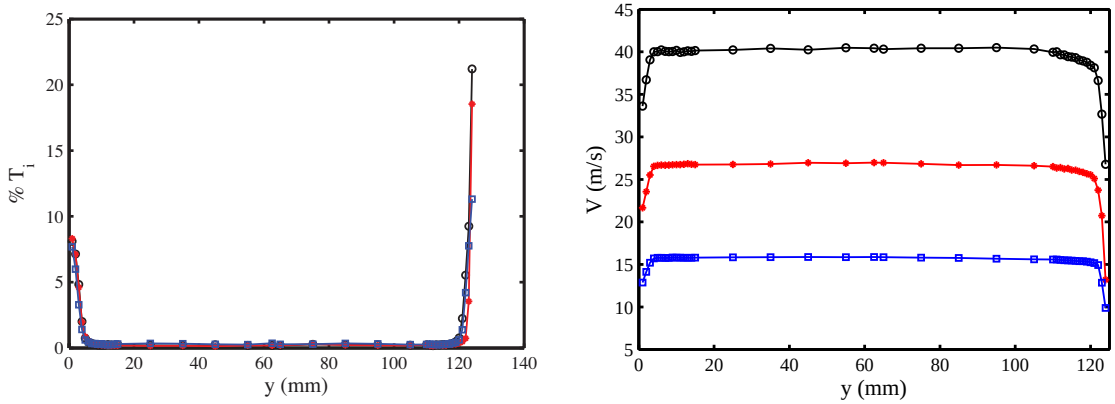

(a) HW1 - Upstream flow characteristics

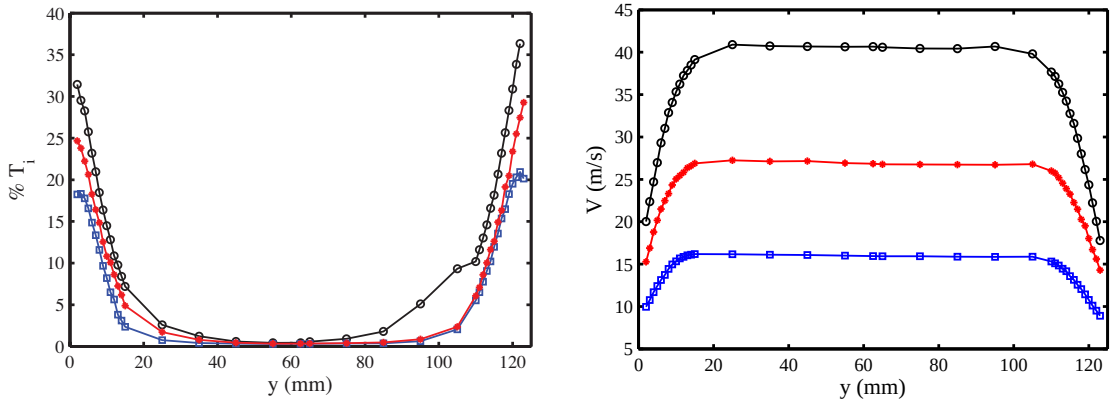

(b) HW2 - Downstream flow characteristics

Figure 4.4: Turbulence intensity profiles measured across the width of the duct at HW1 and HW2. □ $V_\infty \approx 16$ m/s; $*$ $V_\infty \approx 26$ m/s; ∘ $V_\infty \approx 40$ m/s.

Evidence of vortex shedding from the mouths of the side-branches can be seen in Fig. 4.5(a) which shows a contour plot of the acoustic pressure measured by M1 over a range of flow velocities when there were no cylinders installed in the test section. Two Strouhal dependencies were recorded by the microphone and are denoted by lines L1 and L2. Figure 4.5(b) shows a contour plot of the acoustic pressure measured by M1 over the same range of flow velocities when there were no cylinders installed in the test section and when a sheet of gauze was placed over the mouths of each branch. With the gauze is installed, the Strouhal dependencies L1 and L2 are no longer visible. The mean Strouhal numbers, based on the mainstream velocity and side-branch diameter were 0.596 for L1 and 1.09 for L2. $St_{L_c} = 0.596$ almost exactly agrees with the Strouhal numbers measured by Ziada and Bühlmann [64] and Ziada and Shine [65] for the first mode of vortex shedding from circular co-axial side-branches.

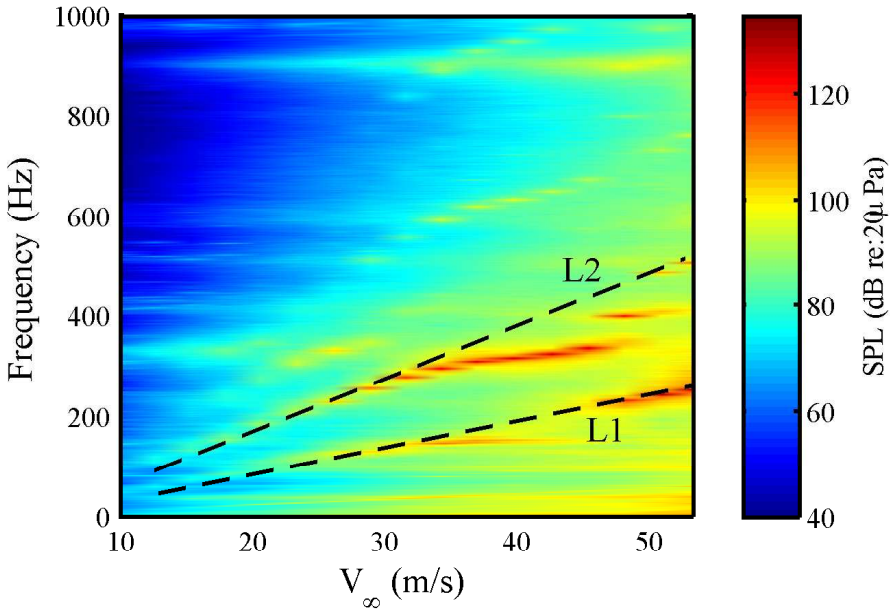

(a) Open mouthed side-branches

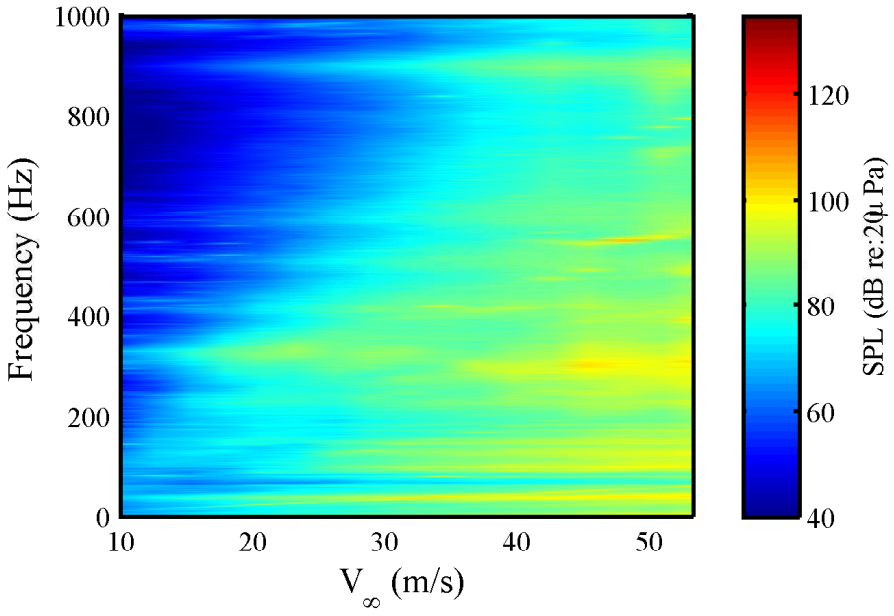

(b) Closed mouth side-branches

Figure 4.5: Aeroacoustic characteristics of the test section measured by microphone M1 without any cylinders installed.

As the Strouhal number of L2 is a close multiple of L1, it is likely to be the second hydrodynamic mode of vortex shedding across the side-branches. It should be noted that the second hydrodynamic mode of vortex shedding from the side-branches dominates the first mode at medium flow velocities whilst the first mode dominates the second at much higher velocities. This is because the second mode "locks-in" with the first acoustic mode of the duct at around $V_\infty = 30 - 35$ m/s and remains "locked-on" until about $V_\infty = 48$ m/s after which the "lock-in" is broken. The influence that vortex shedding across the side-branches has on the flow field around the cylinders will be discussed in Ch. 5.

4.1.2 Cylinder configurations

The objective of the current work was to determine the resonant acoustic sources in a tube bundle akin to what might be found in a heat exchanger. Thus, the cylinder configurations were carefully selected. It was known that resolving the different quantities of Howe's integral in a tube bundle straight from the outset would be difficult. Therefore it was decided to initially study less complex configurations to test the performance of the conceptual approach before gradually increasing the geometric complexity. In this way, the various issues that make studying flow-sound interaction of ducted bluff bodies in air difficult could be hurdled much easier.

Figure 4.6 summarises the different cylinder configurations that were studied. Three distinct groups were investigated, namely two tandem cylinders, four cylinders, and inline tube bundles. Each configuration represents a separate test campaign that was undertaken and so the results from each one will be presented separately in Ch. 5, 6 and 7. The variable P is the centre-to-centre pitch between adjacent cylinders in the streamwise (x) direction whilst the variable L is the centre-to-centre pitch between adjacent cylinders in the transverse (y) direction based on the coordinate system given in Fig. 4.2. When divided by the cylinder diameter, D, these quantities become the streamwise and transverse pitch ratios which were important non-dimensional quantities used to differentiate between the various cylinder configurations studied.

The diameter of cylinders was 13 mm which meant they had an aspect ratio ≈ 9. They were made from hollow perspex tubing and had a nominal wall thickness of 2 mm, which

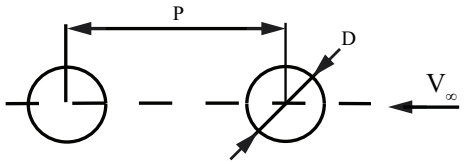

(a) 2TC - Two tandem cylinders

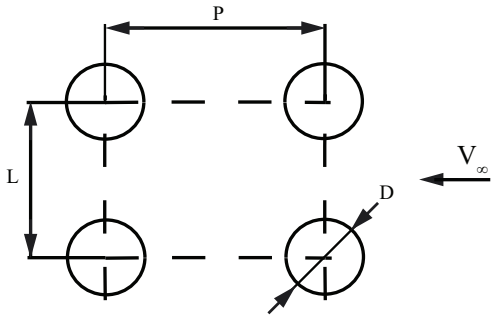

(b) 4C - Four cylinders

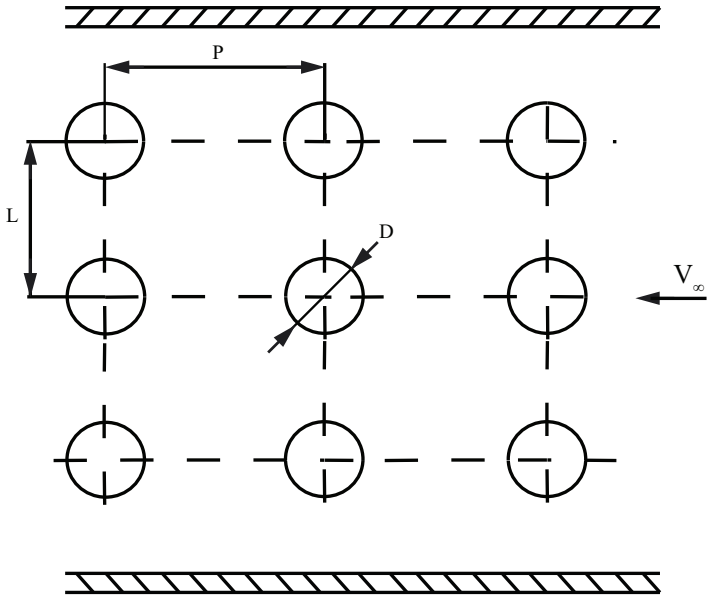

(c) ITB - Inline tube bundle

L/D / P/D	0	1.5	1.75	2.0	2.25	2.5	2.75	3.0
2.5	2TC	4C	4C	4C	4C	4C/ITB	4C	4C
3.0	-	4C/ITB	4C	4C	4C	4C	4C	4C/ITB

Figure 4.6: Summary of the three different configurations that were tested.

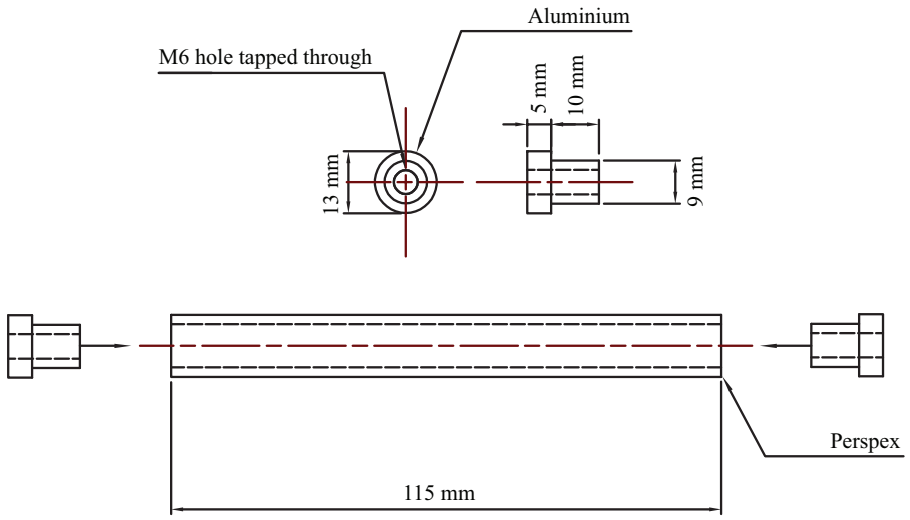

Figure 4.7: Schematic of a cylinder and the aluminium bushing mounts.

was the thinnest that could be sourced for that diameter. Figure 4.7 shows a schematic of a typical cylinder. Hollow perspex tubing was selected due to its rigidity and good optical properties. Having good optical properties allowed the laser light sheet to pass through the cylinders and illuminate particles on the far side, which was very important. The issues surrounding the illumination of the flow field for PIV will be discussed further in Ch. 5, 6 and 7. Being made from hollow tubing, the cylinders could not be mounted directly to the test section walls. Therefore a set of top hat bushings were machined with the same outside diameter as the tubes. The inner diameter of the top hat bushings slotted into the tube and were tapped for an M6 bolt. Figure 4.7 also shows a schematic of the bushing. The nominal length of the tube was 115 mm whilst the length on the bushings (along the outside diameter) were 5 mm each. Thus, the nominal length of the assembled cylinder was 125 mm.

4.1.3 Acoustic excitation

The reason for attaching the side-branches to the walls of the test section was so that the maximum flow velocity in the duct with two tandem cylinders installed was $V_\infty \approx 50\ m/s$. This was insufficient to excite the first transverse acoustic mode of the duct when it had an entirely square cross section. Based on Strouhal numbers published in literature for the tandem cylinder configuration, a mainstream velocity of about 118 m/s would have been needed to achieve acoustic-Strouhal coincidence. Adding the side-branches to

the midspan of the test section increased the acoustic length of the duct in the region where the cylinders were mounted and hence effectively lowered the natural frequency of the test section. A major advantage of lowering the natural frequency was that it brought the acoustic "lock-in" range in-line with the capability of the fan. An additional significant advantage of installing the side-branches was that the corresponding acoustic modes became trapped modes with vanishing radiation into the main duct [66, 67]. For a trapped mode, the acoustic flux becomes concentrated between the opening of the branches and the maximum acoustic particle velocity occurs in the centre of the duct where the cylinders are mounted. This was advantageous as according to Blevins [29], the entrainment of a flow field by a sound field is induced by the velocity of the sound wave rather than the pressure of the sound wave.

Two tandem cylinders with a centre-to-centre pitch ratio of $P/D = 2.5$ were initially explored but did not resonate naturally. Therefore a loudspeaker was installed at the closed ends of side-branch and the excitation of the resonance mode at high sound pressure levels was artificially induced. Labview software was used to generate an analogue output sinewave that was amplified before reaching the loudspeakers. Using Labview facilitated the manipulation of acoustic wave's amplitude (SPL) and frequency. The resonant mode of interest was the fundamental first acoustic mode of the duct. Therefore, the loudspeakers were wired 180° out-of-phase which also meant that only odd harmonics could be excited. The frequency that was applied to the loudspeakers always corresponded to the first acoustic mode of the duct and was always determined before each by using white noise.

4.2 Instrumentation

Measurements of the fluctuating resonant acoustic pressure coupled with the velocity measurements in the flow field were conducted in this study. The instrumentation used to measure these quantities is described below.

4.2.1 Microphones

The unsteady acoustic pressure was measured using a single microphone, labelled M1 in Fig.4.2. M1 was a G.R.A.S Type 40BH $\frac{1}{4}$" High Pressure microphone with a nominal

Test duration (s)	30
Sampling frequency (Hz)	4096
FFT block length (samples)	4096
FFT % overlap	0
Window type	Hanning
Number of averages	30
Spectral resolution (Hz)	1

Table 4.2: Signal processing parameters used to measure the resonant acoustic pressure at M1 and determine its frequency components.

sensitivity of 0.518 mV/Pa. This sensitivity was determined from the manufacturers documentation and verified to within 2.7% with a Brüel and Kjaer Sound Level Calibrator Type 4231 at a frequency of 1000 Hz and a pressure of 1 Pa (94 dB). M1 had an upper SPL limit of 194 dB with a distortion of 3% and was connected to a Preamplifier Type 26AC via a Power module Type 12AN (both G.R.A.S).

The microphone, which was flush mounted at the end of one of the side-branches was primarily used to measure the amplitude of the applied acoustic signal and to detect if "lock-in" occurred. The amplitude of the acoustic signal was determined from the RMS of the pressure in the time domain whilst spectral analysis was used to determine its frequency components. Although the pressure signal was recorded in Labview, all calculations were in Matlab. The frequency components of M1's time signal were determined by implementing the coding described by Bennett [68] and used the Welch spectral estimator. The signal processing parameters are detailed in Tab. 4.2. As previously mentioned, the time signal from microphone M1 was also used as the reference against which all PIV measurements were made. All phase angles, ϕ are referenced against the zero crossing of M1.

4.2.2 Pitot-static tube

A pitot-static tube was installed to measure the free stream velocity in the duct and was positioned upstream of the cylinder configurations near the inlet of the test section. The pressure difference between the stagnation pressure and the static pressure for a given fan voltage was recorded by a Furness Control micromanometer (model FC015) which internally calculated the velocity. During actual testing, the pitot tube was removed from

the tunnel for acoustic reasons and graphs similar to that shown in Fig. 4.3 (which were acquired for each cylinder configuration) were used to determine the mean flow velocity in the duct for a given fan setting. The drawback to this approach was that day-to-day variation in the laboratory conditions, such as temperature or atmospheric pressure (which could have had an effect on the mainstream velocity), were not accounted for. However, when there were significant shifts in temperature (say for example between summer and winter) the voltage-velocity profile was remeasured.

4.2.3 Hotwire anemometry

The primary function of the hotwire was not to measure the free stream velocity as the pitot tube was used for this. Instead, it was used predominately to characterise the test section, for example by determining velocity profiles and turbulence intensities in Fig. 4.4. Due to its high temporal resolution, a secondary use of the hotwire was to determine whether or not the flow field was "locked-in". However, it was only used to supplement the microphone M1 and not replace it when determining if the flow field was "locked-in" to the acoustic field. Using the pitot tube, a Dantec Dynamics 55P14 single probe was calibrated for velocities between 7 and 45 m/s.

4.2.4 Particle image velocimetry

Quantitative flow characterisation was completed using a low speed LaVision PIV system. A brief discussion of the PIV technique was provided in Ch. 3 and so this section describes the details of the PIV setup used.

The flow was seeded using diethylhexylsebacate (DEHS) tracer particles which have a typical diameter of 1 μm. DEHS is liquid oil that becomes vaporised when passed through a lasken-nozzle. The vaporised oil contains the seeding particles in the form of smoke. The seeding was introduced into the flow via the intake of the wind tunnel and was provided for with a seeding box. This box was placed 2 m in front of the intake and had a simple venting fan attached to a hole cut from the box. The box was filled with smoke and the fan propelled it forward, towards the intake. The mixing action caused by the fan ensured that the seeding distribution at the mouth of the intake was uniform. This afforded the best opportunity to achieve a uniform seeding distribution in the area

of interest and was critically important to obtaining good quality PIV measurements. As the seeding distribution at the mouth of the intake was uniform, "streaking" of the seeding was minimised. "Streaking" occurs when there is more seeding in one part of the flow than another and the underlying flow patterns become visible. This is desirable in flow-visualisation but not in PIV.

An advantage of having a uniform seeding distribution is that the illumination of the particles also become uniform. A double pulsed Nd:YAG-laser was used to illuminate the flow field. It had a pulse energy of 30 mJ and a repetition rate of 15 Hz. A telescopic spherical lens pair, consisting of a diverging lens and a converging lens, along with a cylindrical lens was used to transform the laser beam into a laser sheet. The cylindrical lens converted the beam into a sheet whilst the telescopic lens pair was used for focusing. The resulting light sheet had a thickness in the area of interest of 1 mm and illuminated the entire field of view of the camera. The illuminated particles were captured using a digital Flow Master CCD camera. A pair of images was recorded by the camera, one image for each pulse. The time separation between each pulse was of the order of 20 μs. For the present study a lens with a focal length of 28 mm was used in conjunction with a 1279 px $\times$ 1023 px sensor. An optical bandpass filter that only allowed green light ($\lambda = 532$ nm) to pass through was attached to the camera lens in order to protect the CCD chip from becoming over saturated by any reflections off the cylinders in the flow. The camera was calibrated using a LaVision calibration plate (Type 11). The plate was aligned so that its surface was in-plane with the light sheet at the centreline of the duct where the measurements were taken. When calibrating the camera, the cylinders were removed so that the calibration plate filled the entire field of view. When calibration was completed, the cylinders were reinstalled and a coordinate reference calibration grid was placed in the field of view to reset the coordinates.

A crucial characteristic of the low speed system was that the maximum recording rate of the camera was 4.03 Hz. This was substantially lower than the frequencies of interest. Therefore, a triggering system was implemented in order to resolve the vortex shedding regime at "lock-in". A schematic of the timing diagram can be seen in Fig. 4.8. There are three components to the timing diagram: the external trigger, the image acquisition timing and the reference time delay.

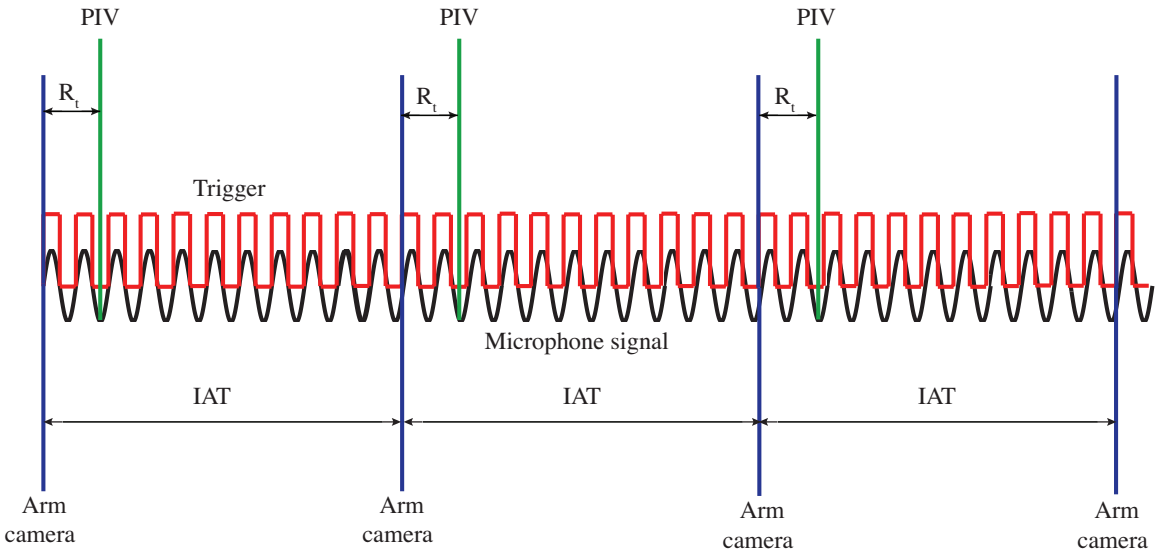

- IAT - Image acquisition timing - Lowest common multiple between the trigger and the camera's maximum recording rate
- Arm camera - Camera recieves a correct trigger and arms the camera to acquire
- Rt - Reference time delay
- PIV - PIV acquisition

Figure 4.8: The PIV timing diagram used to phase-lock image acquisitions.

The trigger was the signal which notified the camera when a particular event happened and was generated externally in Labview. It had to be a TTL signal ($0-5$V with a gate ≥ 1 μs) and was generated with the same software and hardware that provided the signal to the loudspeakers. Having the same DAC path generating the two signals ensured that they were synchronised. Synchronous signals allowed the time trace recorded by M1 to be used as the reference signal. The downside to having the signals synchronised was that only conditions that were "locked-in" could be investigated.

The next component of the timing diagram was the image acquisition timing. This was controlled by the software's programmable timing unit and essentially calculated the image acquisition rate to be a multiple of the incoming external trigger without exceeding the maximum recording rate of the camera (4.03 Hz). That way, an acquisition (an image) of the flow field could be taken exactly when a trigger occurred.

The last component of the timing diagram was the reference time delay. This was the most important part of the triggering system as it allowed for a certain time delay (between when the trigger arrived at the camera and when the actual acquisition occurred) to be set. The reference time delay was adjusted until a PIV acquisition coincided with

a zero crossing of the microphone. This was then considered to be the base reference time for all the measurements. Once this was found, the reference time delay could then be simply adjusted (in fractions of the microphone period) to acquire PIV images at the desired phase angle. As the system was in resonance, the microphone signal was strongly periodic and hence the period between zero crossings could be easily determined. This also meant that the adjustments required in the reference time delay to acquire at a certain phase could also be easily determined.

An example of how the phase angle, ϕ was calculated for a particular PIV image can be seen in Fig. 4.9 which plots simultaneous recordings of the output terminal on the PIV laser and M1. It should be noted that these signals were acquired at $f_{samp} = 32768$ Hz in order to fully resolve the laser output trigger. Moreover, the phase of the image acquisitions were not monitored during individual testing as the amount of data recorded by the acquisition system would have been impractical. Alternatively, it was decided to sample the data, under full experimental conditions, for a short period of time to determine the desired phasing. Once this was achieved, the sampling rate was then down sampled to the rate given in Tab. 4.2, and the microphone was used to monitor the acoustic pressure in a normal fashion.

In Fig. 4.9, point A corresponds to the base reference time, point B corresponds to the time of the next zero crossing and point C corresponds to the time of the first laser flash. It is very simple to determine the phase in the acoustic wave at which point C occurs. Using Matlab code that could determine the peaks and zero crossings in a signal, the phase angle of every PIV acquisition in a sequence could be determined. Figure 4.10 shows a typical example of the acquisition phases of an entire sequence of 60 recordings measuring at a nominal phase angle of $\phi = 180°$. Due to jitter and drift in the triggering signal, not all of the images were recorded at exactly $\phi = 180°$. However, the maximum deviation from the nominal phase is $\pm 3.5°$ which corresponds to only 1.96% error in the phase measurements. This ambiguity pertaining to the phase of the PIV images was within the uncertainty bounds expected for the data acquisition system, which as mentioned, simultaneously sampled the PIV trigger and the microphone signal at $f_{samp} = 32768$ Hz. Therefore, the period of the data acquisition system was $\tau = 0.000031$ s which is approximately 3.5% of the acoustic cycle period. This uncertainty error surrounding the phasing of each

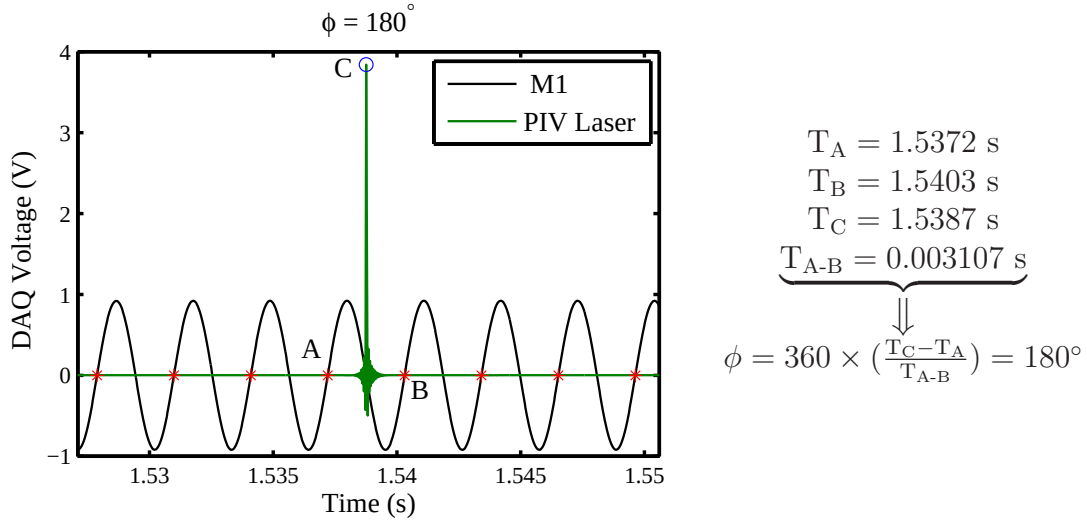

Figure 4.9: A typical time signal of M1 and the PIV laser used to determine ϕ (acquired simultaneously).

ensemble PIV calculation will tend towards zero as the number of images is increased.

For the present study, the whole acoustic cycle was split into phase steps of 22.5° and 100 images were taken at each phase. The PIV triggering system could record the flow field at any phase in the acoustic wave cycle and with this setup, hundreds of shedding cycles occurred in between a particular image acquisition and the next. However this did not matter so long as the system remained "locked-in" and the vortex shedding stayed periodic. This was ultimately the main advantage to forcing the acoustic resonance.

The images were processed using Davis 7.2 software and exported into Matlab for postprocessing. The actual parameters used to calculate the velocity vectors, such as interrogation window size, overlap and shift are dependent on many factors and were specific to each cylinder configuration. Therefore these parameters will be defined individually in later chapters. However, all images were preprocessed with a low-pass sliding background filter and a standard min-max normalisation filter in order to correct inhomogeneity in the light sheet and to help improve the overall signal-to-noise ratio. Preprocessing the images improved the quality of the data near the cylinders (where large reflections were contaminating otherwise good data). More importantly, it helped to improve the data in the shadow of the cylinders which had significantly lower intensities compared to the other regions of the flow. Finally, it was endeavoured to follow the four rules of a well designed PIV experiment. These rules, which are summarised below are a set of guide-

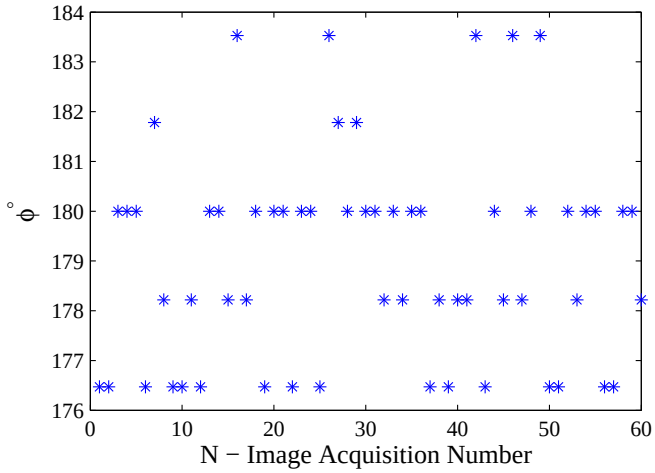

Figure 4.10: A typical example of the PIV image phases in a sequence of 60 recordings measuring data at $\phi = 180°$. The variability in the phase angle is due to jitter in the trigger signal and was within the uncertainty bounds of the acquisition system.

lines described by Tropea *et al.* [69] for achieving good PIV measurements. If the criteria are followed, at least 95% of the interrogations will return the correct particle image displacements [69].

- $N_I > 10$ Each interrogation area must have a density of at least 10 particle-image pairs
- $|\Delta x| < \frac{1}{4} D_I$ The in-plane displacement of any pixel should not be bigger than one quarter of the initial interrogation window size ("*one quarter rule*")
- $|\Delta z| < \frac{1}{4} \Delta z_0$ The out-of-plane motion should not exceed one quarter the thickness of the light sheet ("*one quarter rule*")
- $M_0 |\Delta u| dt < d_\tau$ The local variation of displacement within each interrogation window should be less than the particle image diameter

4.2.5 Data acquisition

All the data measured from the microphone, the pitot tube, the hotwire and the triggering system was recorded on a National Instruments NI PXI-100 chassis, which housed one eight channel NI PXI-4472B data acquisition card and one eight channel NI PXI-6713 analogue output card. The chassis was connected to the PC via a NI PXI-8330 serial bus and was controlled using Labview. The hardware had built-in anti-aliasing filters and all data was written to file in order to be post-processed in Matlab.

4.3 Summary

This chapter has described the experimental facilities and instrumentation used to study the energy transfer mechanism between the flow field and the sound field in ducted bluff body flows. The following three chapters describe the results of the study. Chapter 5 describes the work completed for two tandem cylinders whilst Ch. 6 and Ch. 7 presents the results for the four cylinder configuration and inline tube array respectively.

Chapter 5

Case 1 : Two Tandem Cylinders

5.1 Introduction

Chapter 3 presented a conceptual approach for investigating the flow-sound interaction of ducted bluff bodies using experimental techniques rather than numerical techniques. This chapter discusses the results obtained for two tandem cylinders, which was selected in order to test the robustness of the conceptual approach. It also acted as a stepping stone towards investigating more complex configurations. These initial experiments were similar to one of the configurations studied by Mohany and Ziada [5] so that direct comparisons could be made. As detailed in Fig. 4.6, the configuration had a $P/D = 2.5$. The response to forced acoustic resonance was studied in order to reveal the range of mainstream velocities for which the flow field became "locked-in". It was in this range of velocities that the energy transfer mechanism between the flow field and the sound field was studied. The effect of the sound pressure level (SPL) was also investigated. Installing the two tandem cylinders increased the blockage ratio in the duct and so reduced the maximum capable velocity of the fan. With the cylinders installed, the maximum velocity in the duct was $V_\infty \approx 50$ m/s.

5.2 System response : Without acoustic excitation

5.2.1 Microphone and hotwire analysis

A typical response of the two cylinders subject to cross flow can be seen in Fig. 5.1. Here the pressure spectrum measured by M1 and the velocity spectrum measured by HW2 are plotted together. The velocity spectrum was measured by fixing HW2 in the location

where the best signal was recorded. Peaks at $HW2_A$ and $M1_D$ are evident in the spectra at 261 Hz, which is the vortex shedding frequency. The higher harmonics $HW2_B$ and $HW2_C$ of the vortex shedding frequency can also be seen in the velocity spectrum. In the pressure spectrum, $M1_A$ corresponds to the blade pass frequency of the fan whilst $M1_B$ and $M1_C$ appear to be the first and second vortex shedding modes across the mouths of the side-branches as their frequencies correspond to $St_{L_c} = 0.63$ and $St_{L_c} = 1.13$ respectively. The peak at $M1_F$ has a nearly constant frequency over the whole range of velocities and so seems to be the third acoustic mode of the duct. $M1_E$ corresponds to the first acoustic mode of the duct.

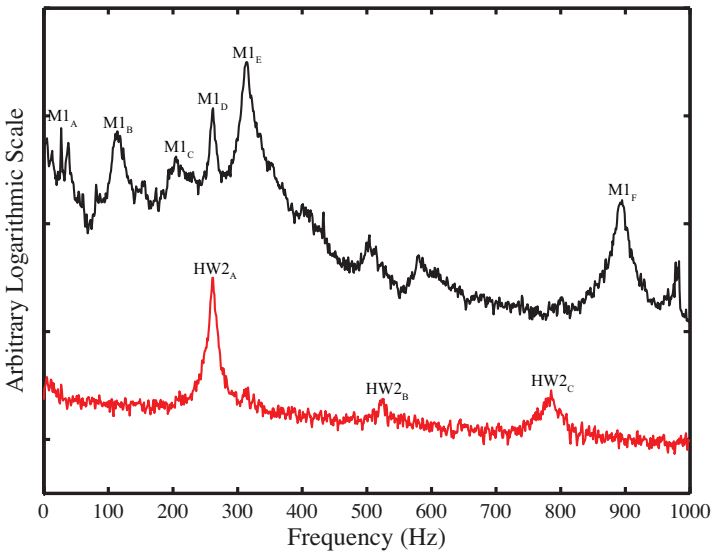

Figure 5.1: Pressure and velocity spectra measured for two tandem cylinders in the absence of acoustic excitation, $V_\infty = 22.9$ m/s.

Figure 5.2(a) presents a waterfall plot of the pressure spectra measured by M1 and shows very similar characteristics to that of Fig. 4.5(a). The major difference being that in Fig. 5.2(a) there is a clear Strouhal dependency corresponding to the vortex shedding frequency from the cylinders in Fig. 5.2(a). One may also note that the third acoustic mode is more pronounced in Fig. 5.2(a), particularly at higher flow velocities. As before, the effect of the side-branch mouths is clear to see in Fig. 5.2(b) which is the same plot as Fig. 5.2(a) except with a sheet of gauze covering each mouth. The gauze was only installed to highlight the effect that the side-branches had on the system. All discussions from here on are for cases where no gauze was attached.

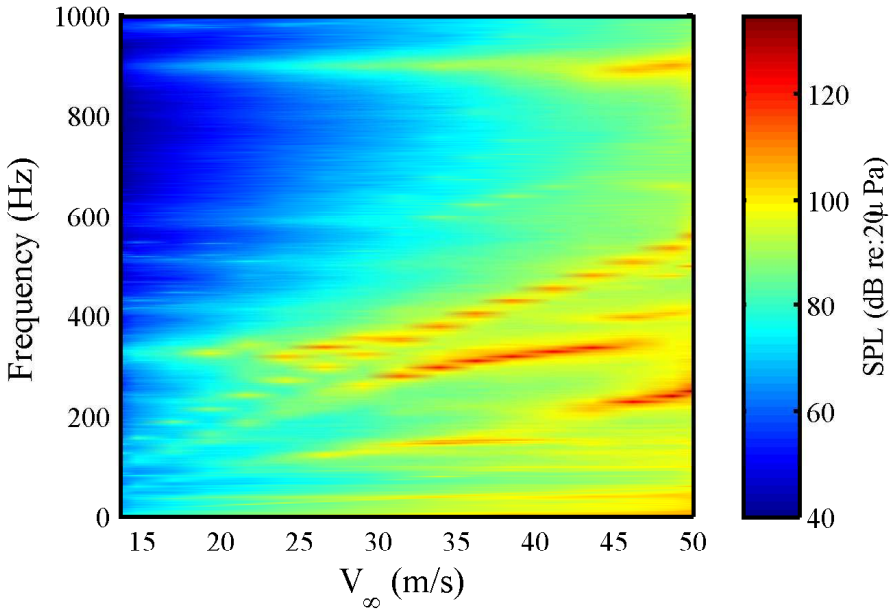

(a) Open mouthed side-branches

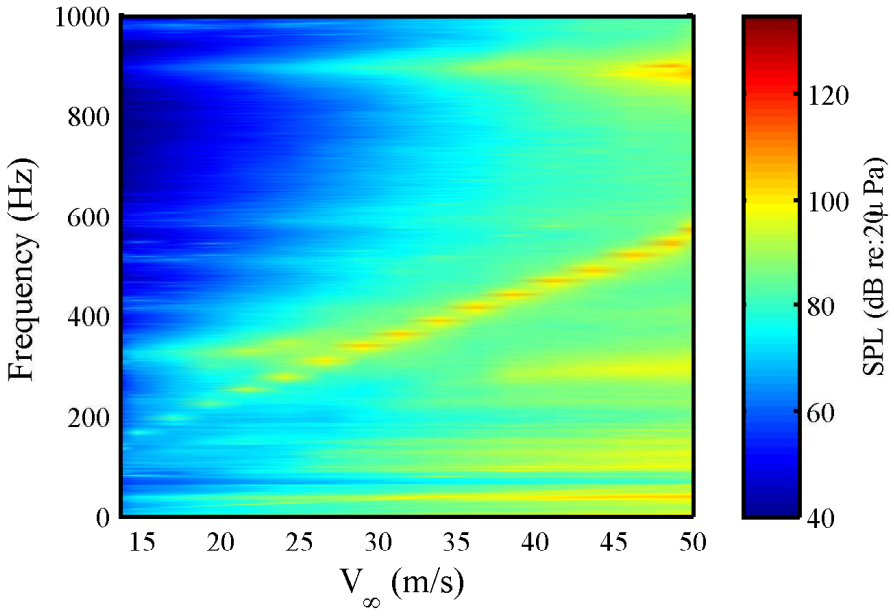

(b) Closed mouth side-branches

Figure 5.2: The aeroacoustic characteristics measured by M1 in the absence of applied sound with two tandem cylinders installed.

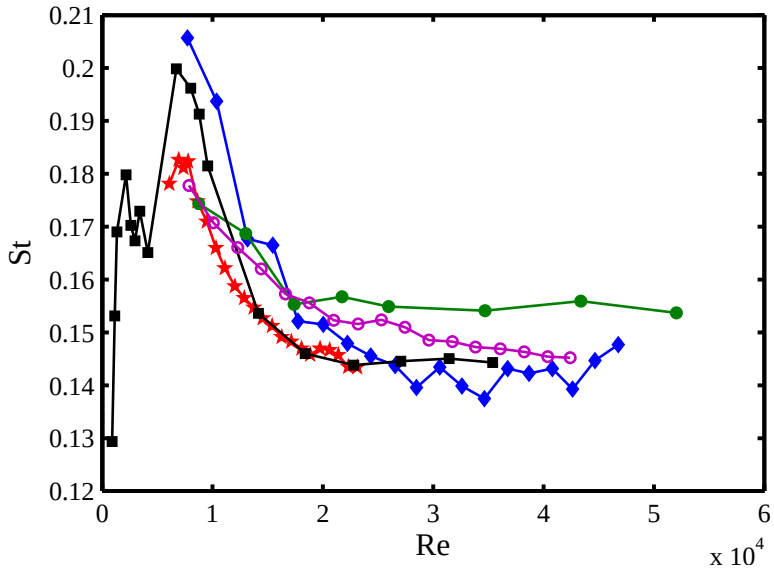

Figure 5.3: The variation of Strouhal number with Reynolds number observed for two tandem cylinders, $P/D = 2.5$. ● Igarashi [15]; ★ Hall *et al.* [2]; ■ Xu and Zhou [14]; ♦ Mohany [4]; ○ Current study.

As discussed in Ch. 2.2.2, unlike a single cylinder, the frequency of vortex shedding from two tandem cylinders in the proximity interference region does not vary linearly with flow velocity. Figure 5.3 plots the variation of the Strouhal number with Reynolds number measured by HW2. The profiles from Fig. 2.10 are reproduced for comparison. The Strouhal number for a given Reynolds number is in good agreement with the other authors' findings. It shows a slow decent as Reynolds number increases and furthermore, seems like it will flatten out as $Re \rightarrow 5 \times 10^4$. This provides good evidence that the tandem cylinders are behaving as expected and give some credence to the experimental setup.

5.2.1.1 Flow structure

The flow structure around the two cylinders at off-resonant conditions can be seen in Fig. 5.4. Contours of the velocity and vorticity measured using PIV at certain phases in the shedding cycle are plotted in Fig. 5.4(a) and Fig. 5.4(b) respectively. The flow is from right to left. In Fig. 5.4(a), the flow velocity becomes retarded as it impinges on the upstream cylinder and a boundary layer develops. Separation from the cylinders occurs approximately 120° from the upstream stagnation point and a shear layer is formed. The

velocity of the shear layer is higher than that measured by the pitot tube far upstream of the cylinders, which was $V_\infty \approx 26$ m/s.

Contours of the vorticity show that the shear layers reattach to the downstream cylinder and no that vortex shedding occurs in the gap region. There is residual vorticity between the cylinders, but this seems to be due to the impingement of the shear layers and the mixing of the stagnant flow rather than a vortex street. After reattachment, vortices form alternatively in the wake of the two cylinders. The mean flow structure over the whole shedding cycle can be seen in the bottom row of Fig. 5.4.

The observed flow structure over the different phases is as expected for a configuration with this spacing ratio and is consistent with the studies mentioned in Ch. 2. These images were acquired by applying an acoustic wave at the natural vortex shedding frequency, $f_v = 312$ Hz. This frequency was removed from the natural frequency of the duct during the test. As discussed in Ch. 2, applying an acoustic wave at f_v rather than f_a synchronises the vortices along the length of the cylinder. Moreover, it provides the PIV trigger signal. Otherwise, the phase averaged flow structure could not have been resolved with the current setup.

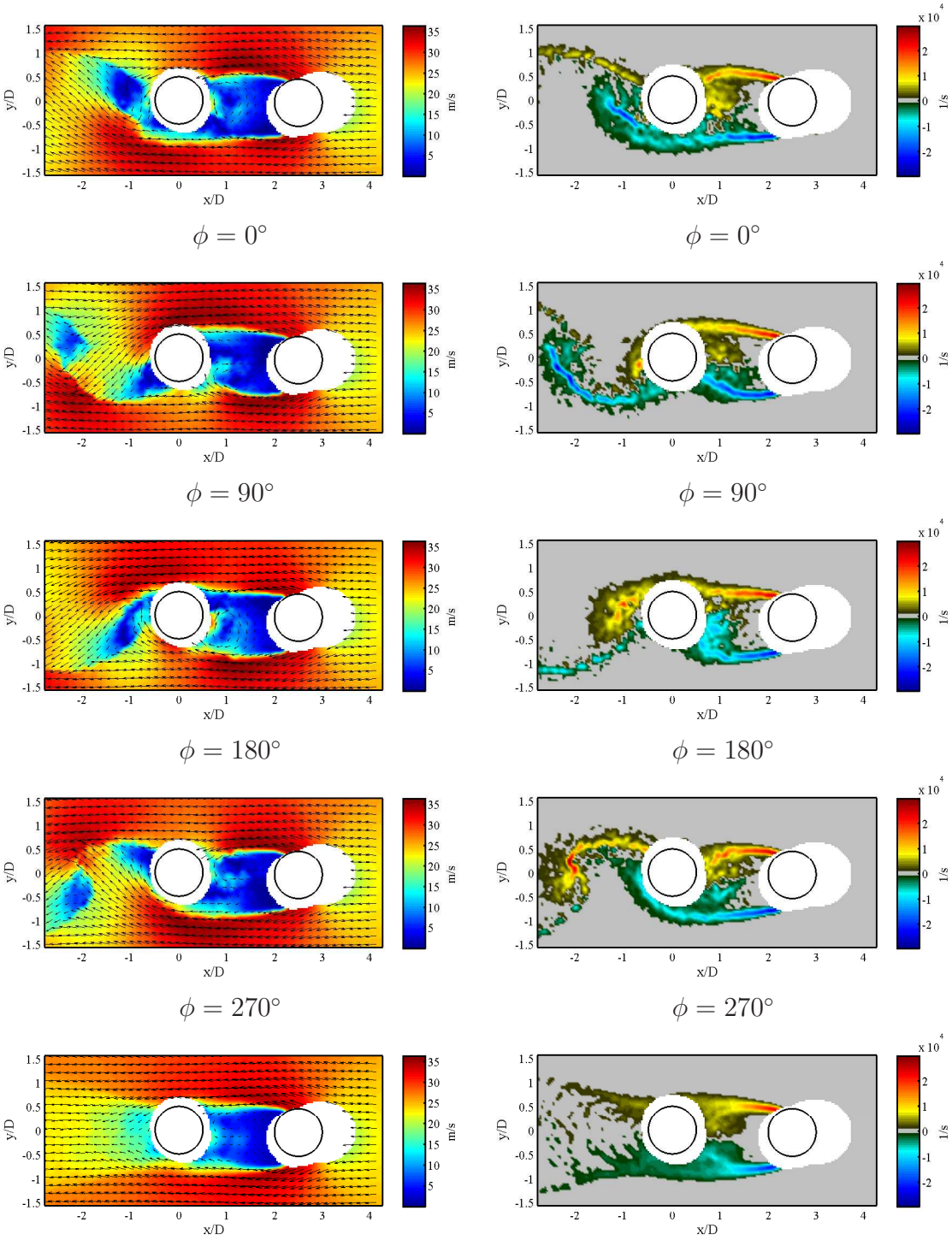

Mean velocity
(a) Velocity

Mean vorticity
(b) Vorticity

Figure 5.4: Phase averaged and mean flow structure around two tandem cylinders at off-resonant conditions. Left - velocity; Right - vorticity, $V_\infty = 26.55$ m/s, $f_v = 312$ Hz. The natural acoustic frequency was $f_a = 330$Hz on the day of the test.

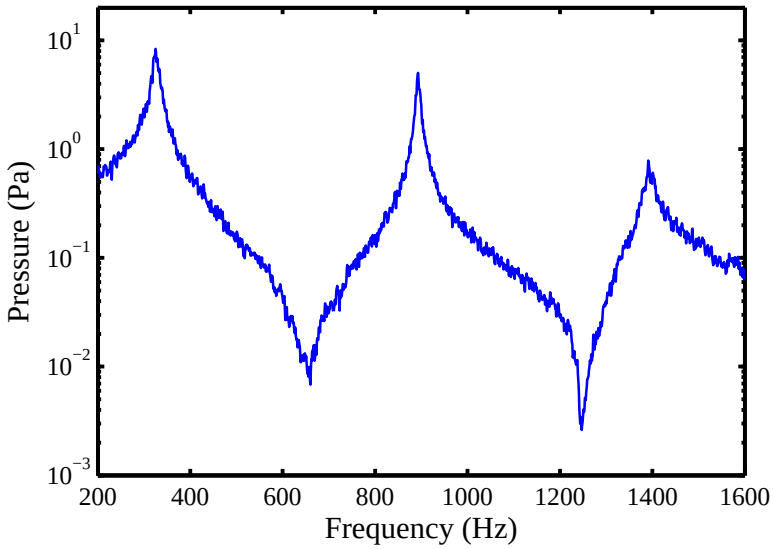

Figure 5.5: The first three acoustic mode frequencies measured by M1 with the cylinders installed and with no flow in the duct.

5.3 System response : With acoustic excitation

5.3.1 Microphone and hotwire analysis

It is clear that the flow field around the two tandem cylinders is not "locking-in" with the acoustic field. Thus resonance does not occur in the absence of acoustic excitation. One of the difficulties observed when testing the cylinders with the loudspeakers installed was determining the natural frequency of the duct. Thus, before each test, the natural frequency was determined using white noise emitted from the speakers with the cylinders installed and with no flow in the duct. A typical pressure spectrum recorded by M1 is shown in Fig. 5.5. Three distinct peaks are evident in this graph. They correspond to the first (P($\lambda/2$)), the third (P($3\lambda/2$)) and the fifth (P($5\lambda/2$)) acoustic modes of the duct. As described in Ch. 4, the wiring of the loudspeakers restricted excitation to odd numbered acoustic modes and harmonics only. This is why the signal falls out near the second and fourth mode frequencies.

The frequency of P($\lambda/2$) is 325 Hz. However this ranged between 322 Hz $< f_a <$ 330 Hz depending on the day to day variation of parameters that could not be controlled such as the laboratory temperature. This variation in the measured natural frequency was not considered to be of significant importance as the resonance could be forced at any desired frequency. Again, this always corresponded to the frequency of the first peak

in Fig. 5.5. The effect that forced excitation has on the vortex shedding frequency at $V_\infty = 25.3$ m/s can be seen in Fig. 5.6. The top plot shows the spectrum of the acoustic pressure. The black line represents the case of no applied sound and the red line represents the case of applied sound at $f_a = 325$ Hz. The acoustic velocity amplitude of the forced excitation is $\widehat{U}_a = 18\%$ of the flow velocity i.e., $\widehat{U}_a/V_\infty = 0.18$. This quantity is also called the dimensionless acoustic amplitude or the dimensionless acoustic velocity ratio. Assuming plane wave propagation, the acoustic velocity amplitude in the duct is defined as:

$$\widehat{U}_a = \frac{P_a}{\rho c} \tag{5.1}$$

where as before, P_a is the amplitude of the microphone pressure signal. The dimensionless acoustic amplitude ($\widehat{U}_a/V_\infty$) is a useful quantity as it gives an indication of the forcing applied by the loudspeakers. Figure 5.6(b) shows the response measured by HW2. In the absence of acoustic excitation, vortex shedding occurs at its natural frequency, $f_v \approx$ 283 Hz and a peak is recorded near the natural frequency of the duct. When the sound is applied, the peak at the shedding frequency becomes suppressed and "locked-in" to the applied frequency. It can also be seen that the peak of the natural acoustic frequency becomes less broadband and stronger. This is in line with the findings of Hall *et al.* [2].

One point worth mentioning from Fig. 5.6 is the fact that in the absence of applied sound, the natural frequency is at a slightly higher frequency than was determined for the duct using white noise. This was observed for every single configuration tested during this study. In fact, it has been found that the nominal natural acoustic frequency increases with velocity well beyond what was measured using white noise. However, after a certain mainstream flow velocity is reached, the natural frequency jumps back to a lower frequency which is more in line with that of Fig.5.5. This increase in the natural frequency is being attributed to the presence of the loudspeakers at the end of the side-branches. As the velocity in the duct increases, so too does the static pressure in the cavity. This causes a significant suction on the loudspeakers which shortens the acoustic length of the duct and hence increases the frequency.

The amount of suction, and the resulting displacement of the loudspeaker cone in-

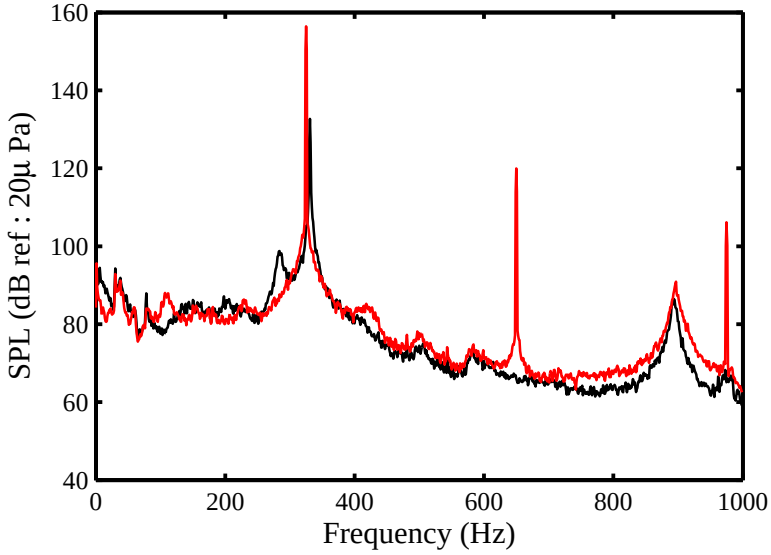

(a) Pressure spectra measured by M1

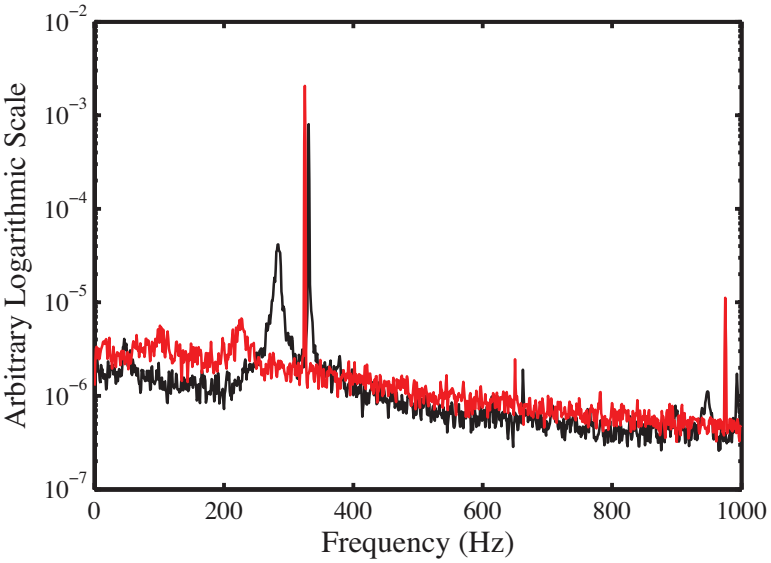

(b) Velocity spectra measured by HW2

Figure 5.6: Pressure and velocity spectra measured for two tandem cylinders, V_∞ = 25.3 m/s. − No applied sound; – $\widehat{U}_a/V_\infty = 0.18$.

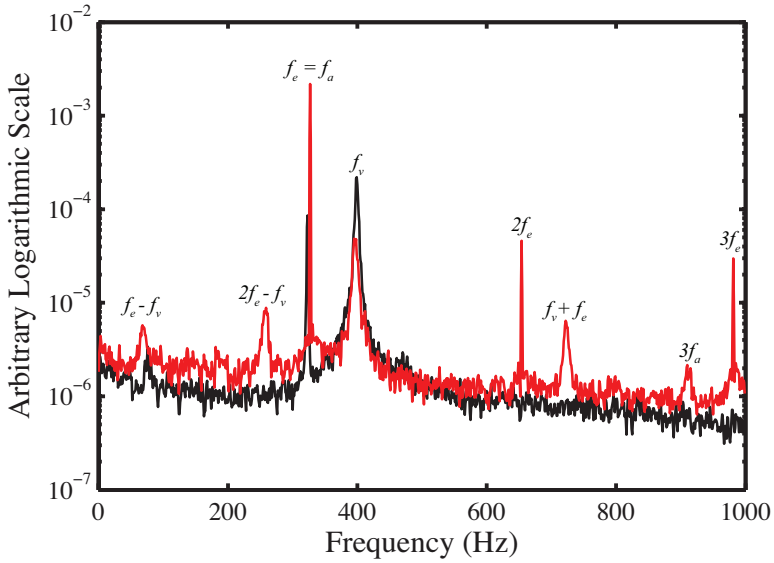

Figure 5.7: An example of a velocity spectrum that is not "locked-in", showing non-linear combinations of f_v and f_a at $V_\infty = 34.9$ m/s. − No applied sound; – $\widehat{U}_a/V_\infty = 0.05$.

creases with velocity. This may explain why the frequency increases with velocity. The jump back seems due to the fact that the vortices shed from the side-branches become "locked-in". When this occurs, the vortices will excite the acoustic field at its naturally preferred frequency. The effect of the "lock-in" is more powerful than the static pressure on the loudspeaker diaphragm and so the naturally preferred frequency becomes excited and dominant. The fact that 'lock-in" of the side-branches seems to occur also explains why the Strouhal dependency L2 in Fig. 4.5(a) and Fig. 5.2(a) becomes significantly strengthened.

For flow velocities that are not "locked-in" but still sufficiently close to the excitation frequency, Hall *et al.* [2] observed modulated frequency spectra. A modulated frequency spectra shows peaks at non-linear combinations of f_v and f_e. Mahir and Rockwell [70] also observed this behaviour and it seems to occur because excess energy in the flow provided by the excitation overwhelms the vortex shedding frequency. The shear layers have to release this excess energy and so these peaks begin to appear. An example of a velocity spectrum measured by HW2 that is not "locked-in" and shows non-linear combinations of f_v and f_a is shown in Fig. 5.7 when $V_\infty = 34.9$ m/s and $\widehat{U}_a/V_\infty = 0.05$.

Figure 5.6(a) shows that an applied sound field can "lock-in" and shift the frequency of flow field. Plots similar to this were used to determine if "lock-in" occurred over a whole

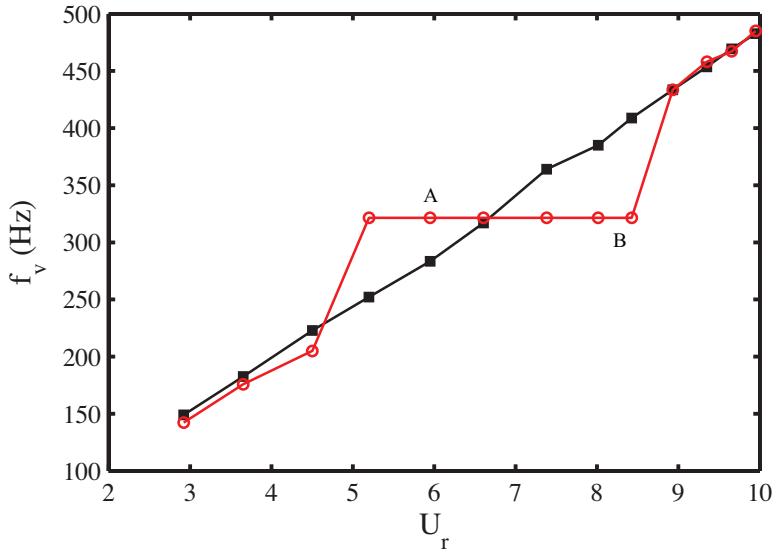

Figure 5.8: The frequency of vortex shedding measured by microphone M1 versus the reduced velocity for two tandem cylinders. ■ No applied sound; ● Applied acoustic excitation at $f_a = 322$ Hz.

range of flow velocities. Figure 5.8 shows the vortex shedding frequency versus the reduced velocity U_r without acoustic excitation and with acoustic excitation at $f_a = 322$ Hz. It should be noted that for this figure, it does not make sense to quote the strength of the applied acoustic wave. The reason for this is that the excitation level, i.e. the applied voltage to the loudspeaker was kept constant over all velocities. This subsequently meant that $\widehat{U}_a/V_\infty$ decreased with increasing velocity. $\widehat{U}_a/V_\infty$ will however be quoted when referring to individual test points.

Inspection of Figure 5.8 reveals that in the absence of applied sound, the vortex shedding frequency increases with flow velocity and does not "lock-in" with the acoustic field. However, in the presence of an applied sound wave, the vortex shedding frequency becomes "locked-in" to the acoustic natural frequency over a reduced velocity range of $5.4 < U_r < 8.4$. These reduced velocities correspond to mainstream velocities of $V_\infty = 22.6$ m/s and $V_\infty = 35$ m/s respectively and are in good agreement with those observed by Hall *et al.* [2]. Furthermore, these reduced velocities are consistent with the natural acoustic resonance range observed by Mohany [4] and Mohany and Ziada [5] for a similar configuration.

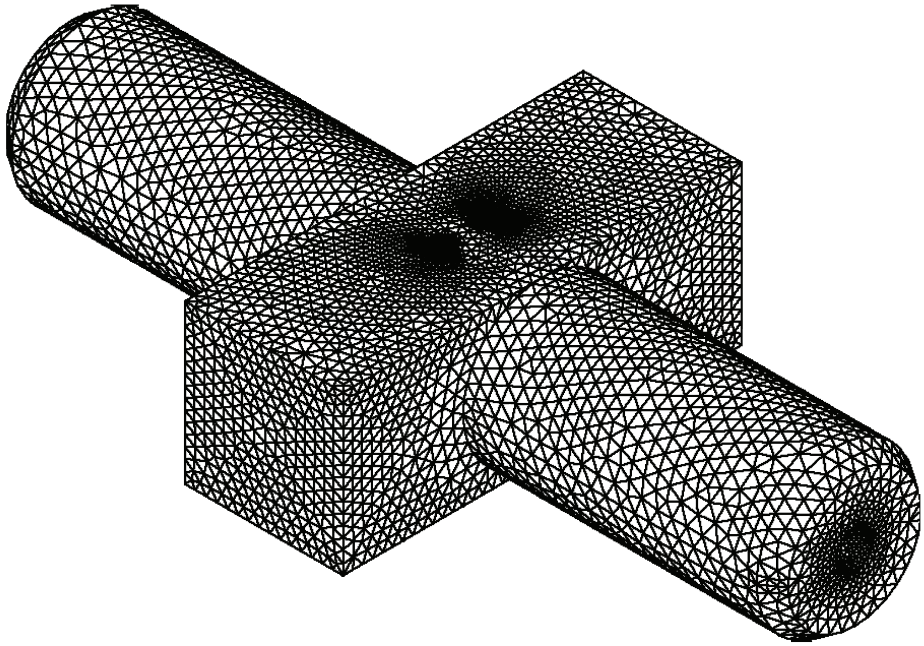

Figure 5.9: Aeroacoustic characteristics measured by M1 for two tandem cylinders. ■ - No applied sound ∘ - Applied sound at $f_a = 322$ Hz.

5.3.2 Resonant acoustic field

Figure 5.8 shows that when an external excitation simulating the natural acoustic resonant phenomenon is applied to the system, "lock-in" can occur over a wide range of flow velocities. Within this range of flow velocities, the acoustic field is expected to behave in a manner similar to that described in Ch. 3.4. A picture of the unstructured 3D mesh used in the finite element model can be seen in Fig. 5.9. A large mesh density was employed around the cylinders whilst in the regions away from the cylinders, a coarser mesh was used. Account was made for the geometry of the loudspeakers at the end of each side branch.

As the PIV measurements were made at the mid-plane of the duct, a cross-section of the 3D model was taken at its mid-plane. The pressure at each node in this unstructured FEA cross-section was reorganised onto a structured grid in Matlab. The location of M1 was identified and the corresponding pressure value was used to normalise the entire distribution. Figure 5.10 shows the spatial distribution of the normalised acoustic pressure

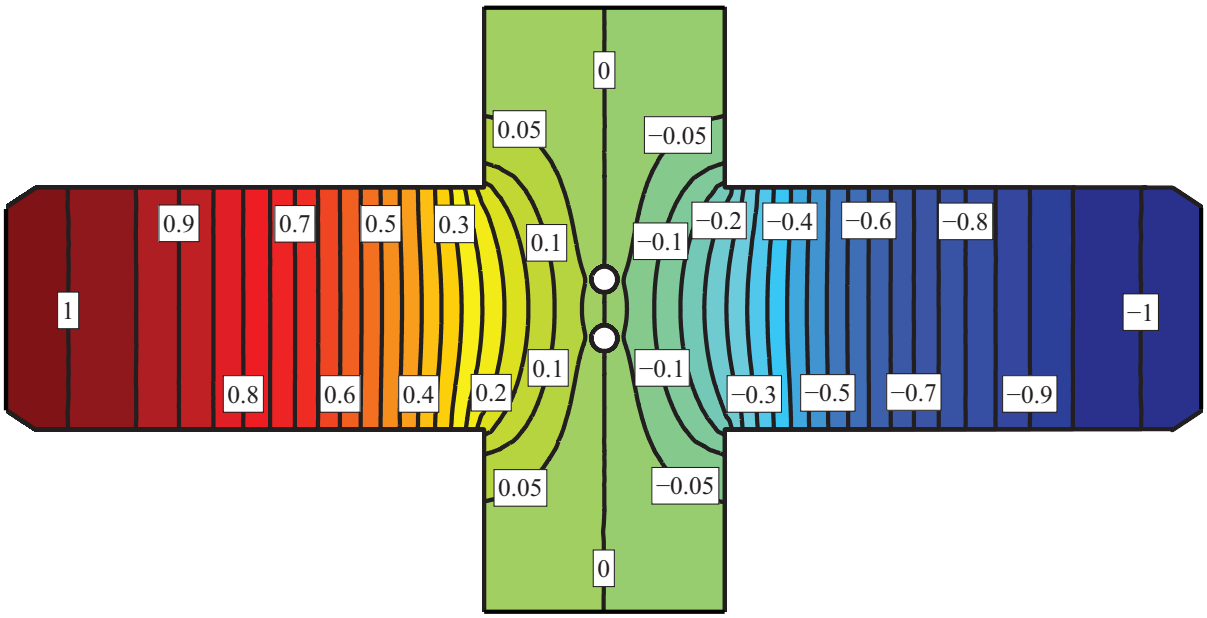

Figure 5.10: Normalised pressure contours of the first acoustic mode at the mid-plane of the finite element model.

for the first resonant acoustic mode of the duct. As expected, it displays a harmonically varying pressure wave. The natural frequency was calculated to be 301 Hz, when the speed of sound was assumed to be $c = 343$m/s. This normalised acoustic pressure field was then scaled by the actual acoustic pressure measured during a test. Finally, using Eqn. 3.23 the acoustic particle velocity was determined for any phase. The edges at the cavity junctions in Fig. 5.10 were not rounded, which meant that a singularity and hence an artificially high value of U_a existed in the model at these points. Dequand *et al.* [49] and Rienstra and Hirschberg [42] have discussed the effect of a sharp geometry on energy transfer mechanism between the flow field and the sound field. However, because the area of interest was far away from the junction of the side-branches, this effect was ignored.

Contour plots of U_a within the PIV area of interest at $\phi = 0°$, $\phi = 67.5°$, $\phi = 180°$ and $\phi = 247.5°$ can be seen in Fig. 5.11. $\phi = 0°$ and $\phi = 180°$ correspond to the maximum positive and maximum negative acoustic particle velocity respectively whilst $\phi = 67.5°$ and $\phi = 247.5°$ correspond to phases just before U_a crosses zero and changes direction. At $\phi = 67.5°$, U_a is about to change from positive to negative whilst at 247.5°, U_a is about change from negative to positive. Therefore the maximum velocities occur at the edges of the cylinders where the pressure wave must squeeze through the gap. Away from

the cylinders, U_a drops off as expected. The contours are normalised by the mainstream velocity corresponding to a pre-coincidence resonance case measured upstream of the cylinders. This highlights the spatial distribution of the dimensionless acoustic amplitude $\widehat{U}_a/V_\infty$ throughout the PIV area of interest.

Figure 5.5 shows that the natural frequency measured in this test was 325 Hz. The natural frequency numerically computed by the model was 301 Hz which is a discrepancy of 8%. Given that the measured frequency varied between 322 Hz $< f_a <$ 330 Hz, this meant the error between the measurements and the simulations ranged between 6.5% and 9.6%. A study was undertaken to determine if the boundary conditions at the inlet and outlet of the model had any influence. Changing the boundary conditions between closed-closed, open-open (the original boundary conditions) and open-closed had a negligible effect. It changed the frequency by less than 0.1%. The methodology used to build the FEA model was tested against a simple rectangular case similar to that shown in Fig. 3.2. It was found that the length to width ratio of the model had significant influence on the predicted frequencies. In particular, the longer the pipe, the better model predicted the theoretical natural frequency. This makes sense given the boundary conditions used to simulate a β-mode assume the pipe is infinitely long. However, when additional length was included at the inlet and outlet of the test section, there was no change in the predicted frequency. Thus, the discrepancy between the measured and simulated frequencies has been attributed to the presence of the loudspeakers and discrepancies in the true speed of sound between the model and the test facilities. The main contributor is assumed to be the presence of the loudspeakers which were modelled as hard walls in the simulation.

The measured and simulated frequency may show some variability. However, the predicted frequency of the first acoustic mode is not overly important. What is more important for this study is the actual mode shape. Figure 5.12 shows the acoustic pressure and phase measured at the centre-plane of the branches across the width of the duct by a roving microphone. It highlights the first acoustic mode shape of the duct when one of the speakers was installed and operating. The other loudspeaker was replaced by a hard wall blank to facilitate the installation of the roving microphone. It should be noted that there was no flow in the duct during the test and that the phase difference was calculated between the roving microphone and microphone M1. The profile of the acoustic pressure

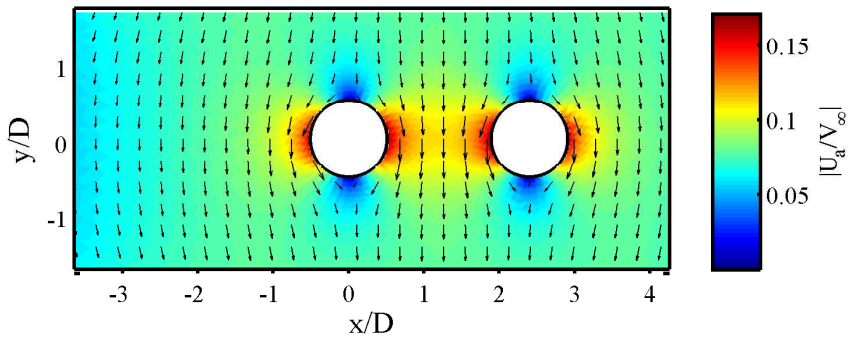

$\phi = 0°$

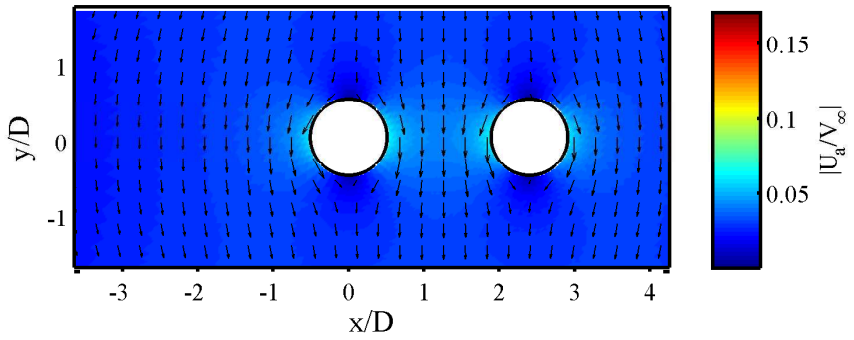

$\phi = 67.5°$

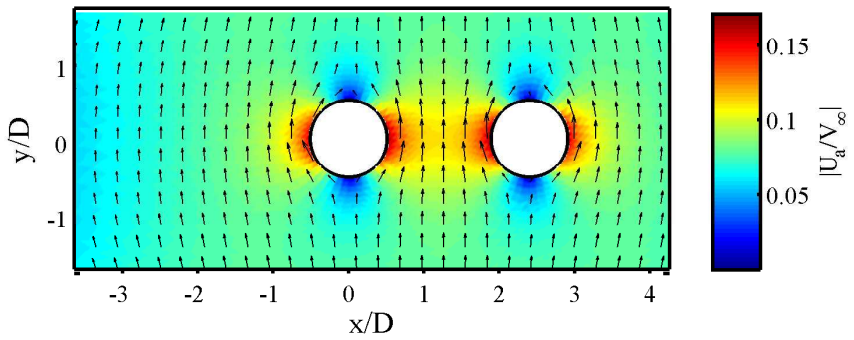

$\phi = 180°$

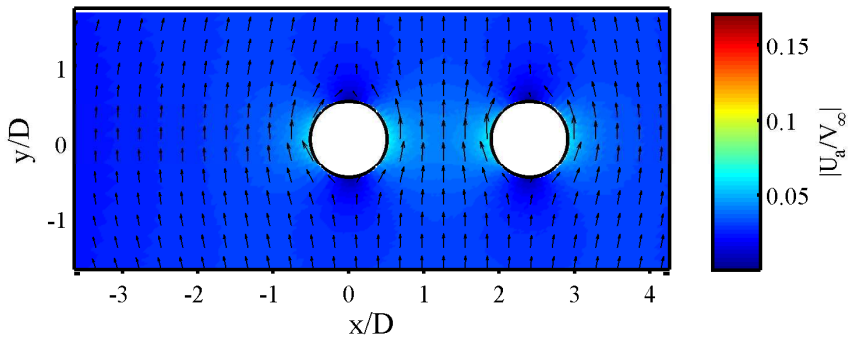

$\phi = 247.5°$

Figure 5.11: Phase averaged acoustic particle velocity during a pre-coincidence resonance condition, $V_\infty = 25$ m/s

determined from the FEA model along the path of the roving microphone is plotted for comparison. As can be seen, the simulated mode shape and the measured mode shape show good agreement; the mean error in the pressure between the roving microphone and the simulation is 0.55%.

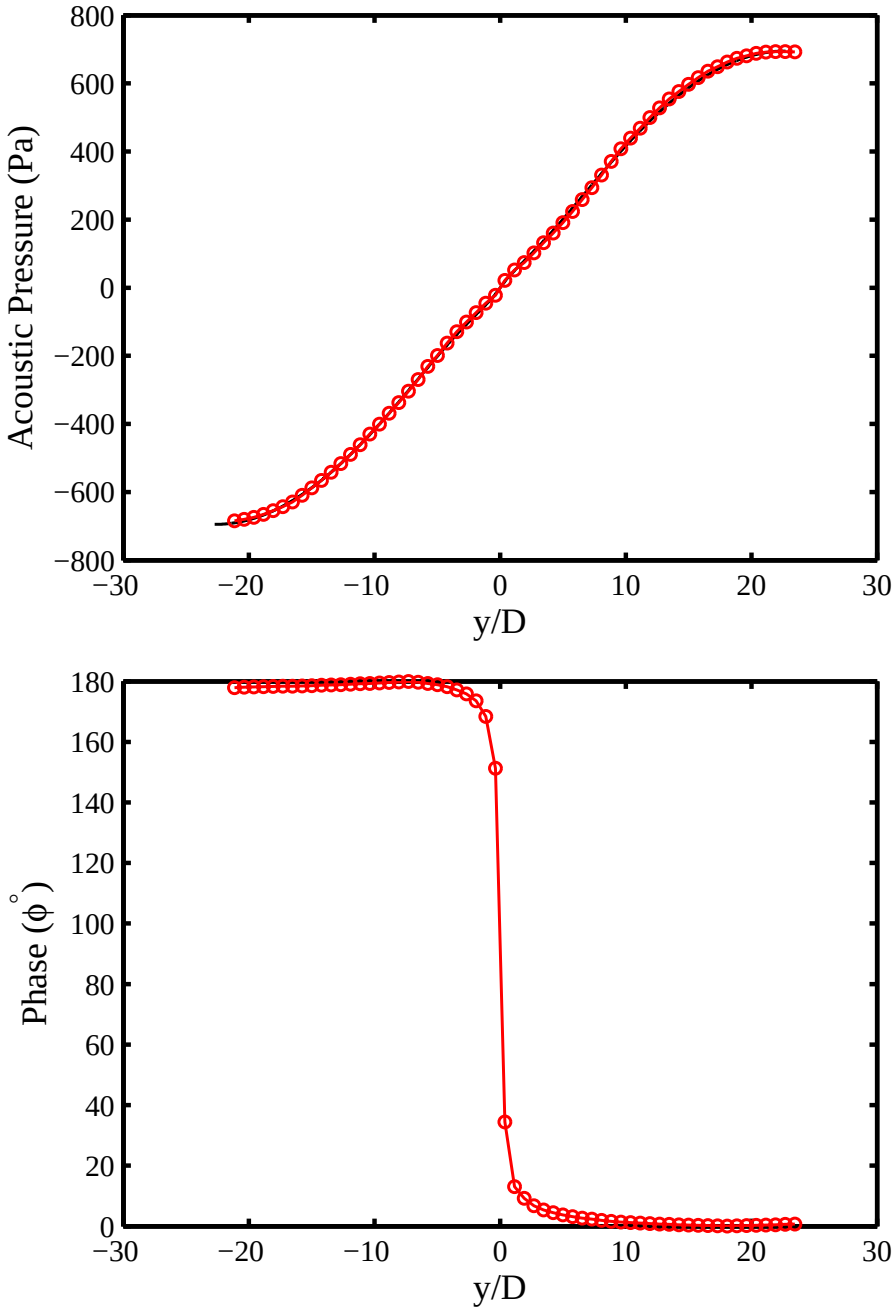

Figure 5.12: Validation of the FEA model across the width of the duct at the centre-plane of the side-branches using a roving microphone. ○ Roving microphone; − FEA model.

5.3.3 Flow structure

Figure 5.8 shows that the flow field becomes "locked-in" to the acoustic field over a wide range of flow velocities when acoustic excitation is applied. It is the coupling between the flow field and sound field within this range of velocities that is of interest. The frequency of the applied sound wave in Fig. 5.8 was 322 Hz. Inserted on the graph are two points, A and B. These correspond to the two reduced velocities that were selected for detailed testing. Point A is at the lower reduced velocity, $U_r = 5.97$ and is in the pre-coincidence resonance regime. The mainstream flow velocity for this case was $V_\infty = 25$ m/s and corresponded to a Reynolds number of $Re = 22,308$. The frequency ratio between the applied frequency and the vortex shedding frequency was $f_a/f_v = 1.2$ and the dimensionless acoustic velocity ratio was $\widehat{U}_a/V_\infty = 0.13$. Point B occurs at a higher reduced velocity, $U_r = 8.4$ and is in the coincidence acoustic resonance regime. The mainstream flow velocity for this case was $V_\infty = 35$ m/s and corresponded to a Reynolds number of $Re = 33,462$. The frequency ratio between the applied frequency and the vortex shedding frequency was $f_a/f_v = 0.8$ and the dimensionless acoustic velocity ratio was $\widehat{U}_a/V_\infty = 0.08$. The frequency ratios at points A and B correspond to the values used by Mohany and Ziada [56] to simulate pre-coincidence and coincidence resonances for a similar configuration.

Figure 5.13(a) shows the phase averaged velocity at $\phi = 45°$, 135°, 225°, and 315° for pre-coincidence resonance case A. Figure 5.13(b) shows the corresponding vorticity calculated using Eqn. 3.31. The red contours represent positive anti-clockwise vorticity whilst blue contours represent negative clockwise vorticity. As previously seen for the non-resonant case, the velocity at the outer edges of the shear layers is higher than the mainstream velocity. Furthermore, if Fig. 5.13(b) is compared to the off-resonant case (Fig. 5.4(b)), one can see that the separated shear layers from the upstream cylinder no longer reattach to the downstream cylinder. Instead, they roll up in the gap region and form strong vortices in an alternative fashion. These vortices then impinge on the downstream cylinder before shedding again into the wake. Inspection of Fig. 5.13(b) reveals that the vortices shed from the upstream cylinder are in-phase with the vortices shed from the downstream cylinder. Thus, they have become synchronised. This is also what happens in an intermediately spaced inline array during acoustic resonance [34].

This synchronisation implies that the acoustic power generated by a vortex shed from the same side of both the upstream and downstream cylinders will have the same polarity at any point in the acoustic cycle. That is to say, they will both either generate or absorb acoustic power. The vorticity maps at $\phi = 45°$ and $\phi = 225°$ are nearly mirror images of each other suggesting that they are indeed 180° out-of-phase.

Figure 5.14 shows the phase-averaged hydrodynamic flow field characteristics around the two cylinders for coincidence resonance case B. As above, Fig. 5.14(a) and Fig. 5.14(b) show phase averaged velocity and vorticity for $\phi = 45°$, 135°, 225° and 315°. Inspection of the vorticity shows that well defined vortices do not form in the gap region between the cylinders. In fact, any roll up of the shear layers tends to be elongated compared to pre-coincidence resonance and the structures are not as well defined. Instead, the shear layers reattach directly onto the downstream cylinder and fully developed vortices are triggered in the wake region only. This type of flow structure seems to indicate that the cylinders are acting like a single bluff body. This is consistent with the findings of Mohany and Ziada [5]. As the flow structure is quite different from that observed during pre-coincidence resonance, it is expected that the mechanisms driving coincidence resonance will be quite different as well.

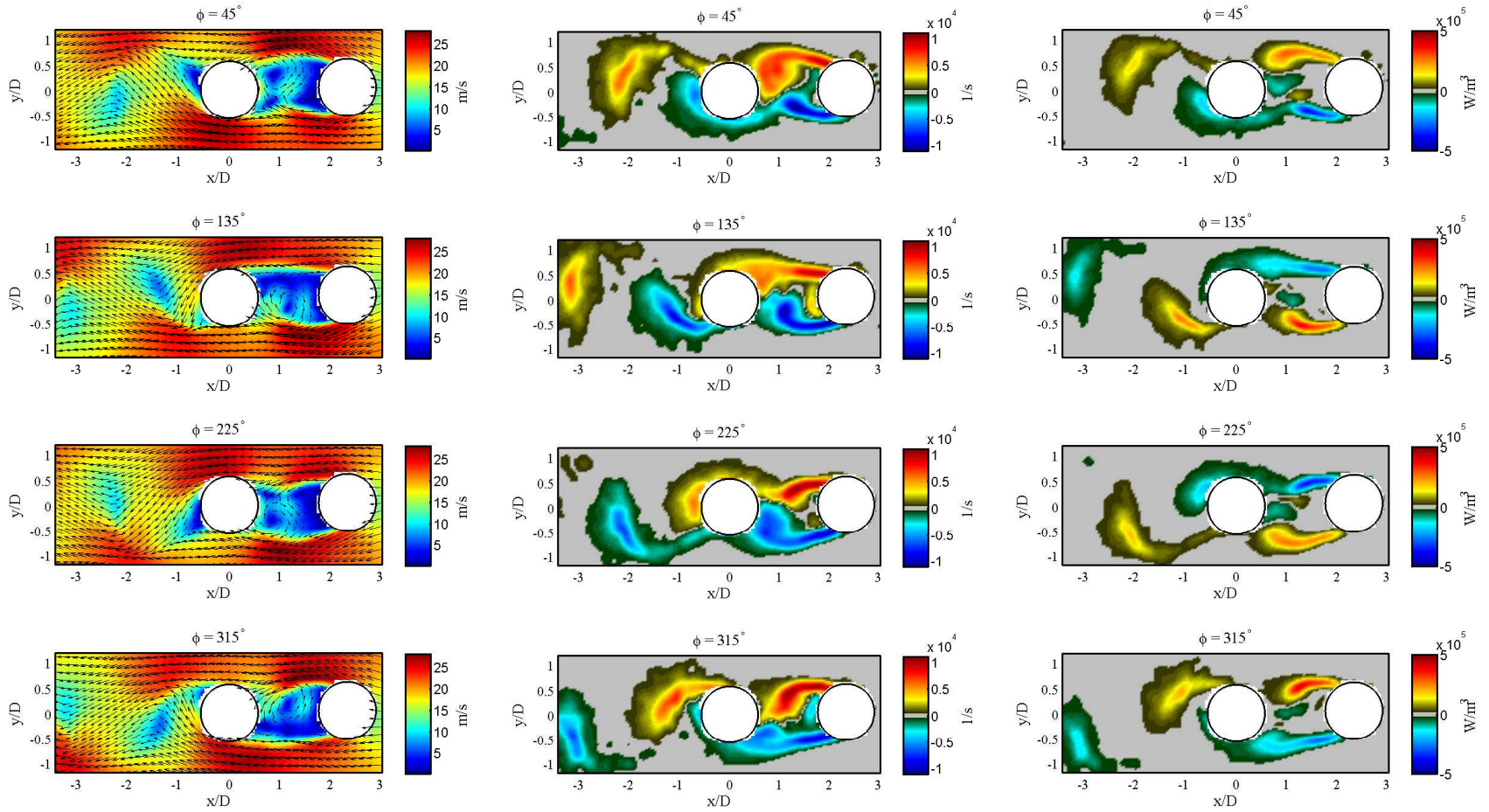

(a) Velocity (b) Vorticity (c) Acoustic power

Figure 5.13: Contours of the velocity, the vorticity and the acoustic power at various phases in the acoustic wave cycle for pre-coincidence resonance case A, $f_a/f_v = 1.2$, $Re = 22,308$.

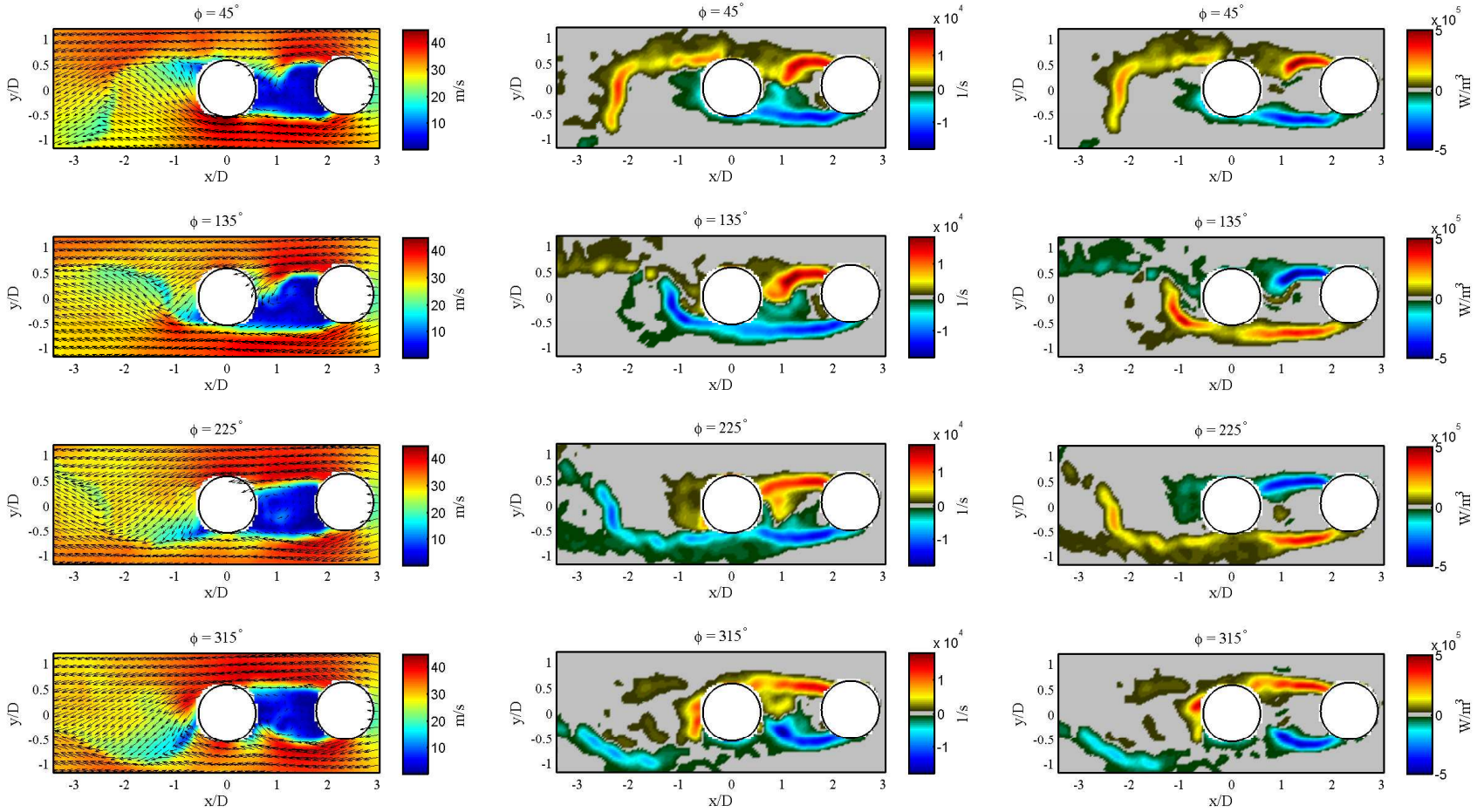

(a) Velocity (b) Vorticity (c) Acoustic power

Figure 5.14: Contours of the velocity, the vorticity and the acoustic power at various phases in the acoustic wave cycle for coincidence resonance case B, $f_a/f_v = 0.8$, $Re = 33,462$.

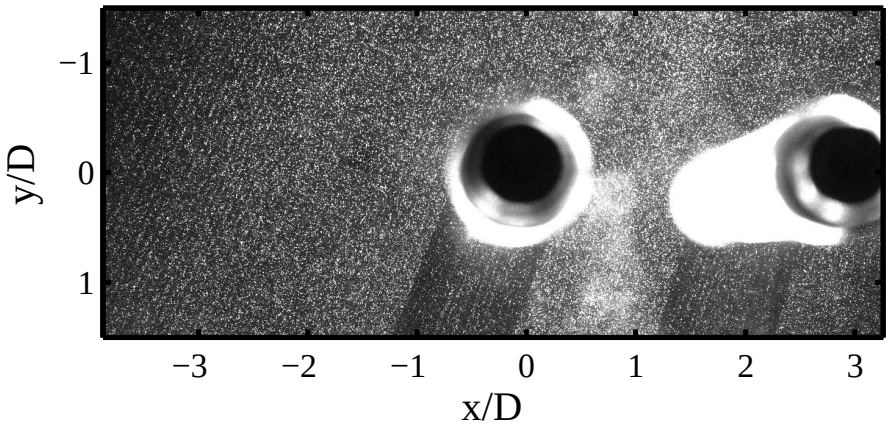

Figure 5.15: A typical raw PIV image.

5.3.3.1 PIV uncertainty

The accuracy of any PIV measurement is dependent on many factors including the seeding density, the homogeneity of the seeding distribution, the illumination, the calibration of the camera and the processing parameters. Figure 5.15 shows a typical raw PIV image. This image shows good, homogeneous seeding density throughout the flow field as the underlying flow structure is not visible. The illumination is fairly homogeneous except for those regions in the shadows of the cylinders. Nonetheless, particles are still visible. At the edges of the cylinders, there are some reflections. These reflections tend to saturate the CCD in these areas. Normal practice is to mask out these areas of the flow so they cannot contaminate the vector calculation. However, valid particles may still exist in the reflections which means perfectly good data might be discarded. This highlights the constant trade off between accuracy and resolution in PIV measurements. Figure 5.15 is considered a good PIV image, but the high reflections and loss of illumination in the shadows makes these PIV conditions very challenging. This is why the sum of correlation PIV algorithm was used to calculate the velocity vectors.

The vector fields in Figs. 5.4, 5.13 and 5.14 were calculated using a multi-pass reducing window of 32 px × 32 px → 8 px × 8 px with 0% overlap and no initial window shift. This processing regime was adopted after several iterations of different parameter settings and was found to give the highest number of accepted vectors. Removed vectors were interpolated for and replaced as the average number of rejected/missing vectors was less than 5%.

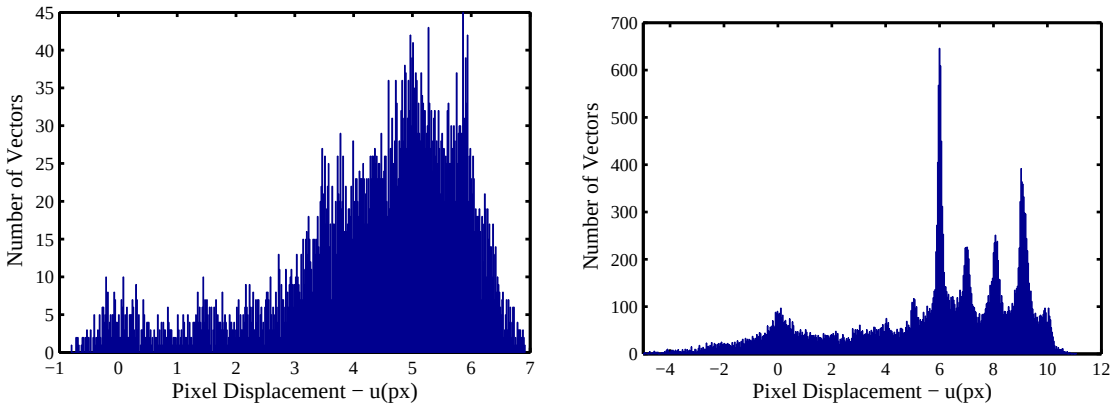

(a) No "peak-locking" - $\zeta = 0.015$ (b) Strong "peak-locking" - $\zeta = 0.18$

Figure 5.16: Histograms of the u component particle displacements. (a) A typical histogram; (b) Not a typical histogram.

Systematic errors in the flow field calculations can be assessed by inspecting a histogram of the seeding particle displacements. Bias in the calculated vectors is referred to as "peak-locking" which is a term used to describe displacement bias error that has periodic pattern at pixel intervals [60]. "Peak-locking" of a PIV calculation occurs when the particles captured on the CCD chip are smaller than 3 px. Thus, the size of the particles was checked at the beginning of every test. If a lens with a zoom function is not available, the only way to enlarge the images on the CCD chip is to move the camera closer. However, this reduces the field of view and hence the area in which one can resolve vectors. This is another example of the trade off between accuracy and resolution in PIV measurements. Histograms that show bias towards integer values are said to be "peak-locked". Figure 5.16(a) shows a typical histogram of the particle displacements in the direction of the u velocity component. The histogram shows no strong indication of "peak-locking" which suggests that any systematic bias in the system is smaller than the random variation in the data. The histogram is accompanied by a "peak-locking" coefficient, $\zeta = 0.015$. This was calculated within the Davis 7.2 software and is below the acceptable limit of 0.1 suggested by LaVision. Figure 5.16(b) shows a histogram of an image that was specifically set up to induce "peak-locking" for comparison. Every PIV calculation was checked to ensure there was no "peak-locking" effect. As such, there can be confidence in the vector processing regime.

Uncertainty error of the LaVision PIV algorithm can be estimated between 0.05 px

and 0.06 px [62]. However, this estimate is generally for simulated data only and is a best-case scenario for experimental data. A more conservative estimate of 0.1 px for the PIV algorithm error is appropriate for the current setup. This is based on the average error achieved by numerous PIV manufacturers to experimental data in Stanislas *et al.* [62]. Using the "*one quarter rule*", a pixel shift in the initial interrogation window between image pairs was defined to be $5-7$ px. Based on the fact that the calibration error of the camera was always within the recommended levels suggested by LaVision and assuming the error estimate of 0.1 px, the PIV calculations were estimated to have a worst case uncertainty error of 2%. Ambiguity pertaining to the phasing of the images has already been discussed.

5.3.4 Flow/sound interaction

5.3.4.1 Phase averaged acoustic power

Contours of the phase averaged acoustic power generated during pre-coincidence and coincidence resonance can be seen in Fig. 5.13(c) and Fig. 5.14(c) respectively. The red contours represent regions of energy transfer from the flow field to the sound field (acoustic sources) whilst the blue contours represent regions of energy transfer from the sound field to the flow field (acoustic sinks). It is clear that the formation and propagation of the acoustic sources are related to the shedding and propagation of the vortices from the cylinders. However, the distribution and amplitude of the sources are quite different between pre-coincidence and coincidence acoustic resonance. Furthermore, the generation and absorption of acoustic power is not constant over time. This is a direct consequence of U_a, which changes in amplitude and polarity with phase angle. As previously discussed, well defined vortices form in the gap region between the cylinders for pre-coincidence resonance whilst for coincidence resonance, the shear layers tend to reattach to the downstream cylinder. This explains why well defined sources (and sinks) exist in the gap for pre-coincidence resonance and why sources tend to buffer the shear layers in the gap region for coincidence resonance. The total acoustic power at each phase is plotted in Fig. 5.17(a) and Fig. 5.17(b) for pre-coincidence and coincidence resonance respectively[1].

[1]In Fig. 5.17(a) and Fig. 5.17(b), there is an asymmetry in the amount of acoustic power generated between $\phi = 0° - 180°$ and between $\phi = 180° - 306°$ because of parallax in the PIV measurement.

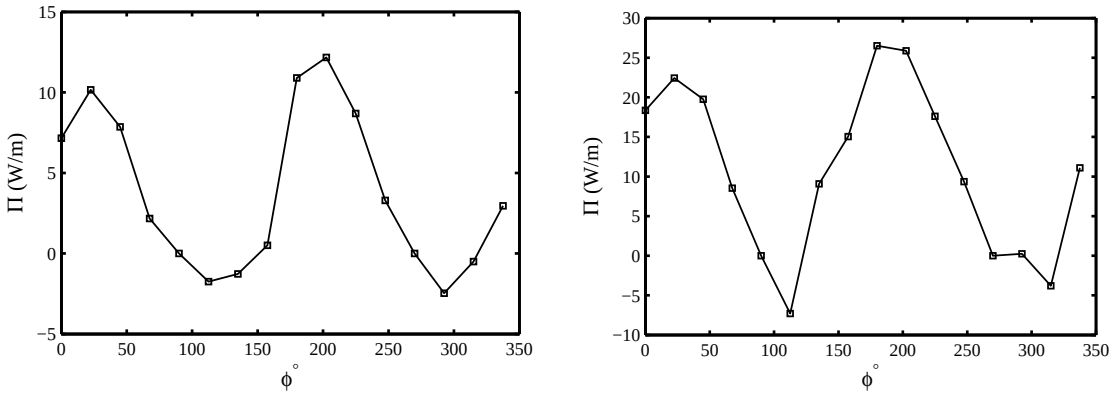

(a) Pre-coincidence resonance case A (b) Coincidence resonance case B

Figure 5.17: The total acoustic power generated at a given phase for pre-coincidence and coincidence acoustic resonance.

For pre-coincidence resonance, acoustic power is generated between $\phi = 0° - 90°$ and between $\phi = 157.5° - 270°$. Observation of Fig. 5.13(b) and Fig. 5.13(c) at $\phi = 45°$ shows that the acoustic sources are generated by the vortices shed from the top sides of the cylinders. A closer look reveals that for this phase, two distinct vortices form in the field of view. One is propagating in the wake of the cylinders and the other is impinging on the downstream cylinder. Acoustic power is generated at this phase because the vortices absorbing energy are still developing and hence have a smaller contribution. At $\phi = 225°$ the converse is true. Figure 5.13(c) indicates that the acoustic sources are associated with vortices shed from the bottom sides of the cylinders. As with $\phi = 45°$, the vortices at this phase are impinging on the downstream cylinder and propagating in the wake.

Further inspection of the vorticity and acoustic power plots during pre-coincidence for the other phases has revealed that as the vortices travelling in the wake between $x/D \approx -1$ and $x/D \approx -2$ always act as acoustic sources. That is to say, for pre-coincidence resonance, acoustic power will have a strong net positive contribution in the near wake region just downstream of the two tandem cylinders. This observation is easily justified using a similar rationale to that of Tan *et al.* [51]. At $\phi = 45°$, positive (counter clockwise) vorticity is dominant at $x/D = -2$. As shown by the sketch in Fig. 5.18, the acoustic particle velocity is travelling in the negative j direction at this phase and combines with the positive vorticity to generate positive acoustic power and hence an acoustic source according to Eqn. 3.12. By a similar argument, at $\phi = 225°$, negative

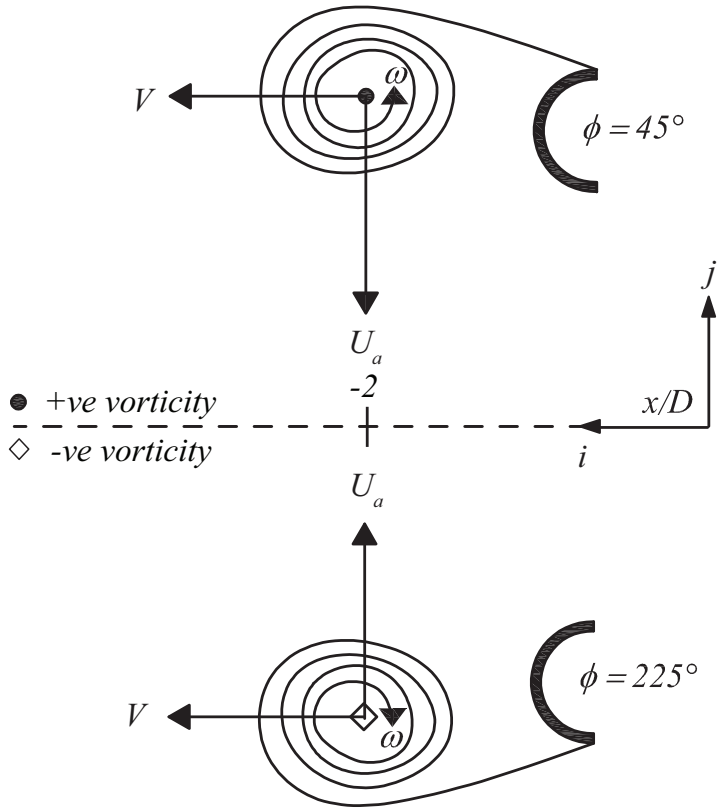

Figure 5.18: Interpretation of why vortices in the wake of the tandem cylinders between $x/D \approx -1$ and $x/D \approx -2$ always act as acoustic sources.

(clockwise) vorticity is dominant in the region $x/D = -2$. However, because at this phase, U_a is in the positive j direction, Eqn. 3.12 predicts positive energy transfer between the flow field and the sound field. Similar arguments can be made for other phases.

Absorption of acoustic power at $\phi = 135°$ and $\phi = 315°$ seems to be related to the fact that after the vortex impinges on the downstream cylinder, it still remains part of the shear layer from which it was formed. This spreads the vorticity over a large area compared to the compact vortices forming on the other side of the upstream cylinder. The phasing of this event is such that the sinks associated with this large area of vorticity are stronger than the sources associated with compact vortices and hence absorption occurs. It would be interesting to see if this occurs for configurations with larger spacing ratios where an independent vortex street can form instead of a reattached shear layer following vortex impingement.

For coincidence resonance, Fig. 5.17(b) shows that acoustic power is generated between $\phi = 0° - 90°$, between $\phi = 135° - 270°$ and at $\phi = 337.5°$. Looking at Fig. 5.14(b) for

$\phi = 45°$, there is only 1 vortex (with positive vorticity) present in the flow. Figure 5.14(c) indicates that this vortex corresponds to a very strong acoustic source. At $\phi = 225°$, the same is true as only 1 vortex (now with negative vorticity) is present in the flow. This vortex also corresponds to a strong acoustic source. Given that the plots of the acoustic power indicate the magnitudes and distributions of the sources/sinks generated in the gap region from both sides of the upstream cylinder are comparable, it is reasonable to suggest that they will effectively negate each other and that the main contributor to acoustic power generation is the single vortex propagating in the wake. Figure 5.17(b) shows that absorption of acoustic power occurs at $\phi = 112.5°$ and $\phi = 315°$. These sinks, which will have a negative net contribution to the acoustic resonance are also associated with vortices shed in the wake of the cylinders.

For both pre-coincidence and coincidence resonance, peak values of power generation occur at $\phi = 22.5°$ and $\phi = 202.5°$. Figure 5.19(a) plots the vorticity and acoustic power at these phases for pre-coincidence case A. At $\phi = 22.5°$ the vortex shed from the upstream cylinder is just about to impinge on the downstream cylinder. At the same time, the vortex in the wake of the cylinders is just about to be separated from the shear layer which is feeding it circulation. As mentioned in Ch. 2.2.1.1, separation of a vortex from its shear layer occurs when the opposite shear layer gets drawn across the wake and effectively "cuts-off" the vortex. According to Gerrard [7], at this point in the formation, a vortex is at its strongest. Since the upstream and downstream flow structures are synchronised, it is expected that the vortex in the gap region will also be at its strongest. Thus, the vortex pair will have its maximum influence on the generation of acoustic power even though $\phi = 22.5°$ is not a phase where U_a has maximum amplitude. The peak at $\phi = 202.5°$ corresponds to when the vortices shed from the bottom sides of the cylinders are at their maximum strength. Figure 5.19(b) shows the vorticity and the acoustic power generated at $\phi = 22.5°$ and $\phi = 202.5°$ for coincidence case B. It is a little more difficult to tell than with the pre-coincidence case, but it seems as if these phases also correspond to when the vortices shed from the top and bottom sides of the downstream cylinder are about to separate from their shear layers.

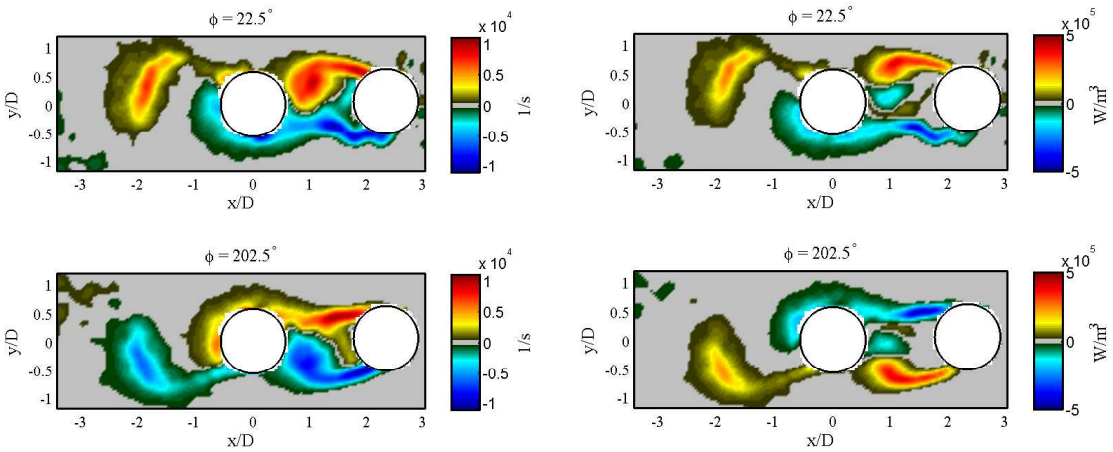

Vorticity Acoustic power

(a) Pre-coincidence resonance case A, $f_a/f_v = 1.2$, $Re = 22,308$

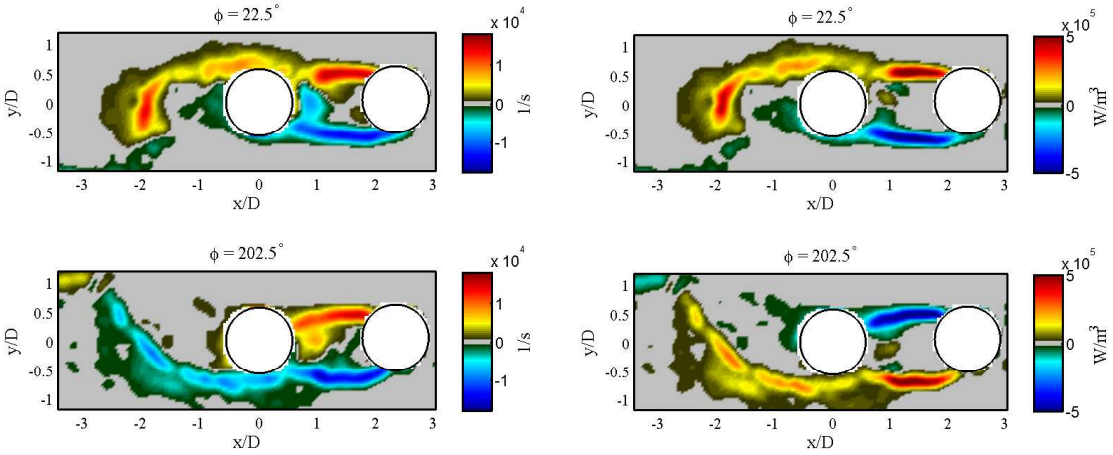

Vorticity Acoustic power

(b) Coincidence resonance case B, $f_a/f_v = 0.8$, $Re = 33,462$

Figure 5.19: Vorticity and acoustic power generated by the two tandem cylinders at $\phi = 22.5°$ and $\phi = 202.5°$ for both pre-coincidence and coincidence acoustic resonance. These phases correspond to the peak acoustic power generation.

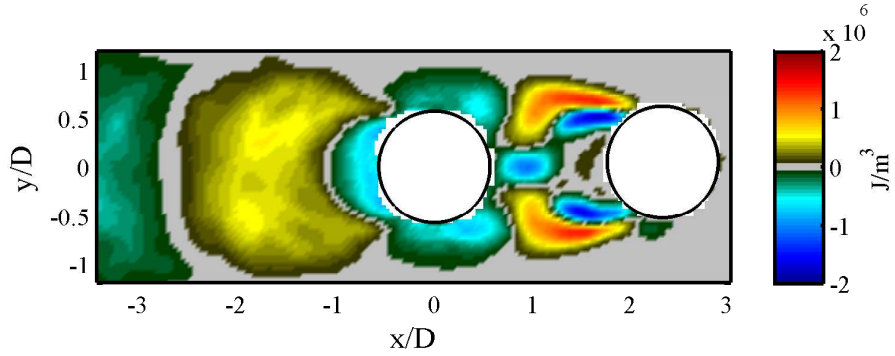

Figure 5.20: The net acoustic energy per cycle for pre-coincidence resonance case A, $f_a/fv = 1.2$ and $Re = 22,308$.

5.3.4.2 Net acoustic energy

Integrating the phase averaged acoustic power over an entire wave cycle determines which regions of the flow have an overall positive and overall negative contribution towards acoustic resonance. Figure 5.20 shows the spatial distribution of the net acoustic energy for the pre-coincidence resonance case A. It is notable that the sources and sinks are symmetric about the centreline of the cylinders which is obviously due to the periodicity of Karman vortex shedding. In the gap region between the cylinders, intense acoustic sources lie in the outer shear layers, hugging two very intense sinks located in the inner shear layers. In the wake region, an acoustic sink surrounds the immediate vicinity of the downstream cylinder but is dominated by a very large acoustic source farther downstream located near $x/D = -2$. For reasons discussed in the last section, the flow field in this region provides an overall positive contribution to the energy transfer between the flow field and the sound field. As the scale suggests, the most intense sources are located in the middle of the shear layers between the cylinders. This is consistent with the simulations of Mohany and Ziada [56] for a similar geometry. However, the most intense sinks are also located here. These intense sources and sinks are due to the high concentration of vorticity in the shear layers and the high acoustic particle velocity in these regions.

Figure 5.21 shows the spatial distribution of the acoustic energy generated over a whole acoustic cycle for the coincidence resonance case B. It also shows good agreement with the simulations of Mohany and Ziada [56]. The distribution of acoustic sources is quite different compared to the pre-coincidence case. Acoustic sources dominate the

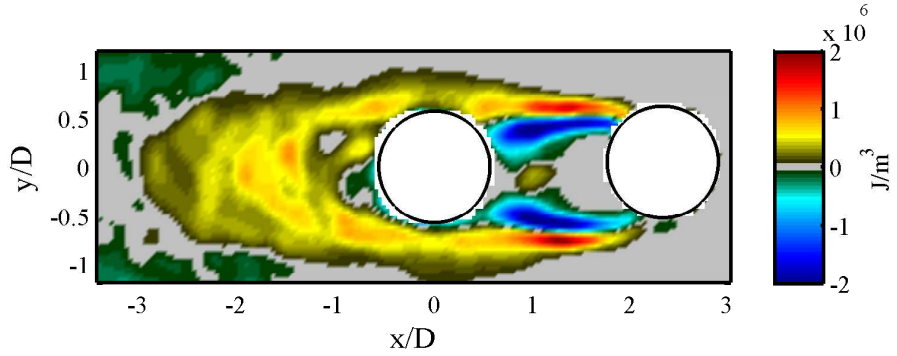

Figure 5.21: The net acoustic energy per cycle for coincidence resonance case B, $f_a/fv = 0.8$ and $Re = 33,462$.

outer shear layers, hugging two very intense sinks in the inner shear layers. The size and intensity of the sinks in the shear layers compared to the sources suggest that acoustic energy is absorbed in this region. The effect of the elongated vortices/reattached shear layers is clear to see as the acoustic sources engulf the downstream cylinder and dominate the immediate and far wake region.

Figure 5.22 compares the net acoustic energy transfer per streamwise location per cycle for the two resonant conditions A and B. The net energy transfer per streamwise location per cycle is simply the total energy generated by the system at a given x/D location. The differences between pre-coincidence and coincidence resonance are clear to see. In the gap region between the cylinders for coincidence resonance a strong net sink exists, implying that energy is being removed from the sound field and lost to the flow field by viscous damping. At the downstream cylinder ($x/D = 0$) a positive transfer of acoustic energy between the flow field and the sound field occurs and continues well into the wake region. The opposite is observed for pre-coincidence resonance as strong net sources exist in the gap region between the cylinders whilst strong net sinks exist at the downstream cylinder. The wakes for both regimes generate positive acoustic energy. The existence of net positive acoustic energy in both the gap region and wake for pre-coincidence resonance seems to be a consequence of the fact that vortices shed from the same side of both cylinders are synchronised and in-phase with each other during "lock-in". Figure 5.22 supports the postulations made Mohany and Ziada [5] that coincidence resonance is generated by vortex shedding in the wake. Moreover, it supports the suggestion that pre-coincidence

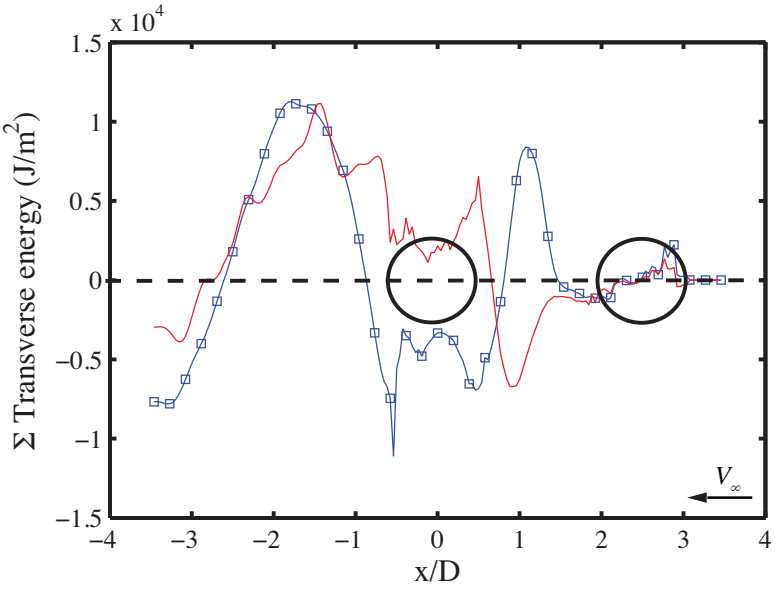

Figure 5.22: The total net energy transfer per streamwise location per cycle for the two tandem cylinders. □ Pre-coincidence acoustic resonance case A; – Coincidence acoustic resonance case B.

resonance is driven, or at least triggered, by the instability of the shear layers between the cylinders. However, the strong acoustic source just downstream of the cylinders implies that the immediate wake of the cylinders is influential as well.

5.3.4.3 Comparison with literature

Figure 5.23 plots the results simulated by Mohany and Ziada [56] for the net energy transfer per streamwise location alongside those presented here. The overall energy transfer mechanisms for the coincidence resonance case show good agreement. The overall energy transfer mechanisms for the pre-coincidence case also show good agreement. However some differences are apparent. The first is the location of the net sink near the downstream cylinder. In the current study this was located at the downstream cylinder and just in its immediate wake. Mohany and Ziada [56] observed that it formed in the wake region behind the cylinder for $-4 < x/D < 0$. This difference has been attributed to the fact that in their simulations of pre-coincidence resonance, the vortex shedding between the upstream and the downstream cylinders was out-of-phase whereas here, they are strongly in-phase. A sensitivity analysis was completed to determine if the estimated uncertainty with regard to phasing was responsible for this difference. The PIV images

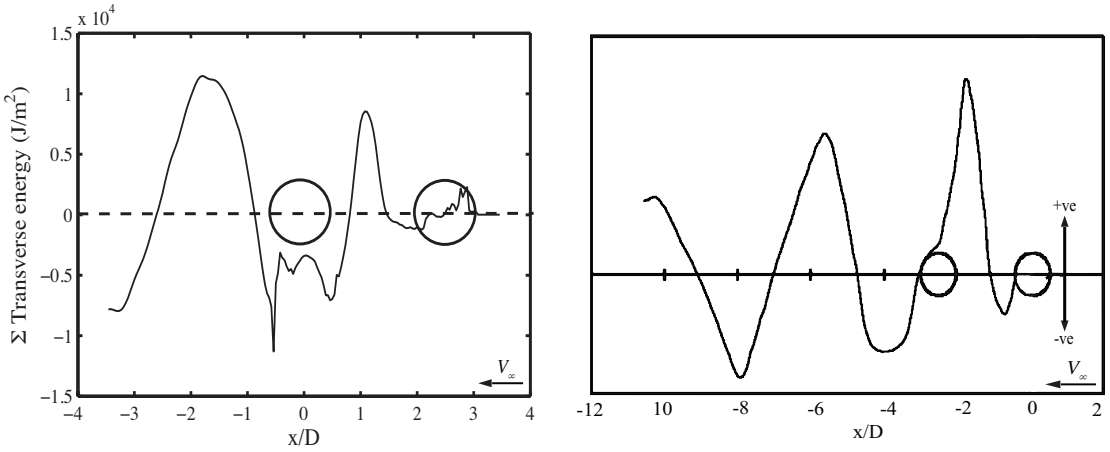

(a) Pre-coincidence acoustic resonance

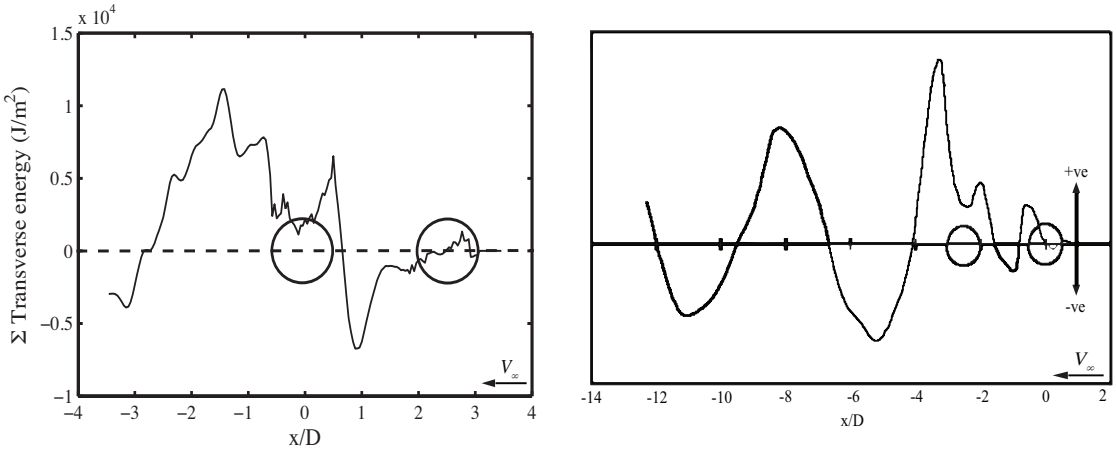

(b) Coincidence acoustic resonance

Figure 5.23: Comparison of the tandem cylinder results with simulations completed in literature. Left - Current Results; Right - Mohany and Ziada [56].

were phase shifted ±5° (which is larger than the estimated phase error limit of ±3.5°) to account for any other unknown sources of bias. Altering the phasing was found to have negligible effect on the magnitude of the sources and their distribution.

The other difference is the amount of energy generated in the wake of the cylinders compared to energy generated in the gap region. The dimensionless acoustic amplitudes applied by the loudspeakers in order to achieve "lock-in"' at pre-coincidence and coincidence acoustic resonance in the current experiments were $\widehat{U}_a/V_\infty = 0.13$ and $\widehat{U}_a/V_\infty = 0.08$ respectively. These were comparable to those applied by Mohany and Ziada [56] who needed to apply $\widehat{U}_a/V_\infty = 0.15$ to induce pre-coincidence resonance and $\widehat{U}_a/V_\infty = 0.10$ to achieve coincidence resonance. Nonetheless, the amount of positive net

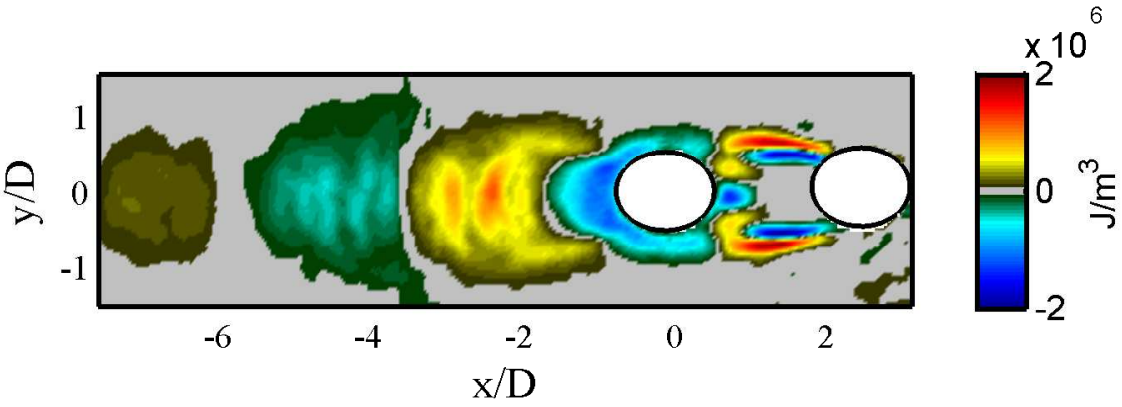

Figure 5.24: Contours of the net acoustic energy per cycle generated in the gap region and the far wake of the tandem cylinders during pre-coincidence resonance case A.

acoustic energy generated in the near wake relative to the gap region, for the experiments is far less than that observed by Mohany and Ziada [56]. This is likely due to the fact that their simulations were two dimensional and so may have underestimated the dissipation of vorticity as it propagates in the gap. If this is so, the acoustic power production/absorption is likely to be overestimated compared to the experiments and may explain this difference between the relative contributions of the wake and gap.

Another consequence of using two dimensional simulations is that a cyclical production/absorption of energy will occur in the wake of the cylinders. The simulations of Mohany and Ziada [56] modelled a two dimensional resonant duct. They observed cyclical production/absorption of acoustic energy ∼10 diameters downstream of the cylinders for both regimes. Additional tests were undertaken to investigate if this occurred in the present study. However, on this occasion images were acquired in the gap region and in the wake ∼8 diameters downstream of the cylinders. This study used nominally the same parameters as those in the pre-coincidence case described above and essentially tested the repeatability of the conceptual approach. Figure 5.24 and Fig. 5.25 show contours of the net acoustic energy per cycle and the net energy transfer per streamwise location per cycle respectively. The distribution of sources are similar those already presented and acoustic energy is indeed generated and absorbed in a periodic fashion downstream. However, the fall off in magnitude of the sources/sinks in the wake is much more substantial than that observed by Mohany and Ziada [56].

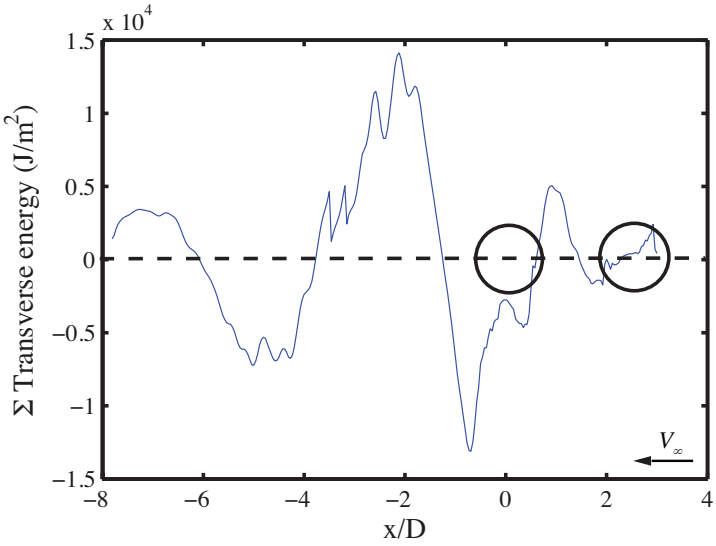

Figure 5.25: The net energy transfer per streamwise location per cycle generated in the gap region and the far wake of the tandem cylinders during pre-coincidence resonance case A.

This can be attributed to two factors. Firstly, the vorticity concentration weakens as it dissipates downstream. Hence, its contribution in Howe's integral diminishes (as previously discussed above, two dimensional simulations may underestimate this dissipation). Secondly, as the acoustic mode of the duct is a trapped mode, the acoustic particle velocity decays rapidly in the wake of the cylinders beyond the PIV field of view. Figure 5.26 shows the profile of the simulated acoustic particle velocity along the centreline of the duct in the streamwise direction both upstream and downstream of the cylinders for the same experimental parameters as those in Fig. 5.11. The acoustic particle velocity is maximum at the cylinders and decays rapidly in both the upstream and downstream directions. This means it will have a weakened contribution in Howe's integral the as the distance from the cylinders increases. In the simulations of Mohany and Ziada [56], the downstream decay of the acoustic particle velocity was more gradual than in the present experiments because it was a duct mode.

5.3.5 The effect of sound pressure level

Ziada [66] discussed how the amplitude of the acoustic wave across the mouth of a side-branch can have a substantial influence on both the formation length and path of the vortex across it. Given that the acoustic energy generated here is due to vortex shedding,

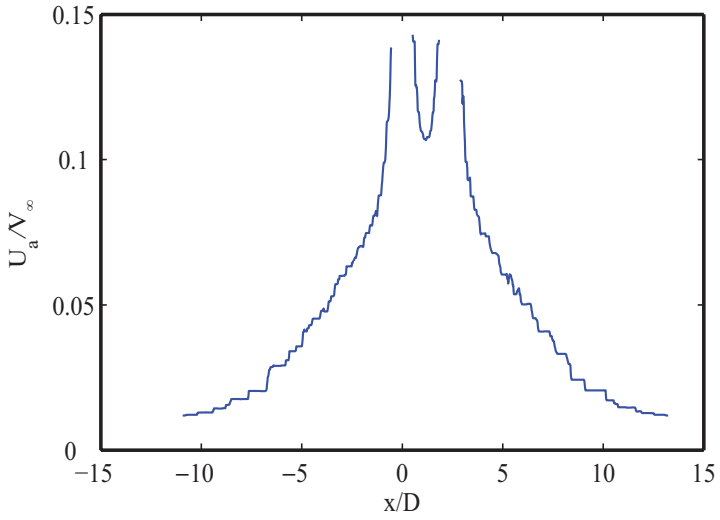

Figure 5.26: Decay of the acoustic particle velocity away from the tandem cylinders in the normalised x direction, $f_a/f_v = 1.2$, $\phi = 180°$, $V_\infty = 25$m/s.

it is quite conceivable that the spatial distribution and strength of the resonant acoustic sources may change with excitation amplitude. To this end, a set of tests were undertaken to investigate the effect of the sound pressure level (SPL) and hence the acoustic particle velocity on the flow structure around the two cylinders.

The sound pressure level in the duct was altered by varying the applied voltage to the input of the loudspeakers. Three voltage settings were selected. They were 212.5 mV, 300 mV and 425 mV. Figure 5.27 shows the vortex shedding frequency versus reduced velocity measured by M1 when the three input voltages were applied. Increasing input voltage to the loudspeakers (and hence the SPL in the duct) increases the width of the "lock-in" range both before and after acoustic-Strouhal coincidence. That is to say that increasing the SPL promotes a larger shift away from the natural vortex shedding frequency. These findings agree well with those of Hall *et al.* [2]. One observation that can be made from Fig. 5.27 is that increasing the SPL from high to very high levels only increases the width of the "lock-in" range in the coincidence resonance regime and not the pre-coincidence resonance regime. Blevins [29] observed a similar behaviour for single cylinders and this is likely due to the hysteresis effect which often appears at the high end of the "lock-in" range of self-excited acoustic resonances.

As the effect of the SPL amplitude on the spatial distribution of acoustic sources was the focus of this study, the flow field needed to be "locked-in" for all three sound pressure

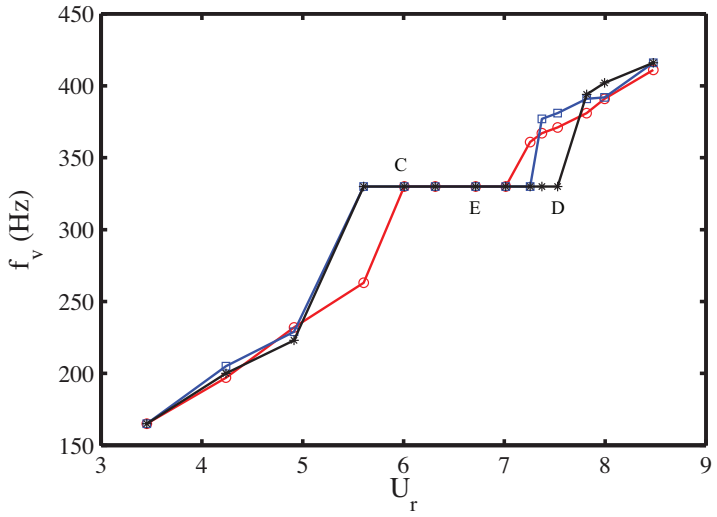

Figure 5.27: Aeroacoustic characteristics measured by M1 for varying speaker input voltages. ∗ 425 mV, □ 300mV, ○ 212.5mV.

levels. Two velocities, one in the pre-coincidence range and one in the coincidence range were selected. They are labelled C and D respectively in Fig. 5.27. For pre-coincidence case C, all the applied voltages induced "lock-in" whilst for coincidence case D, only the 425 mV setting could induce 'lock-in". Thus, the applied voltage was increased to 525 mV, but only for this velocity. Table 5.1 summarises the experimental parameters measured for cases C and D. It should be noted that the natural frequency of the duct measured during this test was $f_a = 330$ Hz. Although not shown in the graph, for the case of no applied sound, acoustic-Strouhal coincidence occurred at $U_r = 6.6$. Moreover, the frequency ratio was $f_a/f_v = 1.12$ for pre-coincidence resonance C and $f_v/f_v = 0.86$ for coincidence case D. A third velocity was also investigated and is labelled E in Fig. 5.27. This point corresponds to a flow velocity just after acoustic-Strouhal coincidence where $f_a/f_v = 0.97$. It was selected to investigate the energy transfer mechanism when the resonance subsides at acoustic-Strouhal coincidence as reported by Mohany and Ziada [5]. Its parameters are also listed in Tab. 5.1.

Contours of the phase averaged vorticity for cases C, D and E at $\phi = 270°$ are shown in Fig. 5.28. Reading from top to bottom, the sound pressure level increases between rows from the minimum applied voltage to the maximum voltage for each velocity. Reading from left to right, the flow velocity increases between columns. For pre-coincidence resonance case C, distinct vortices form in the gap and wake of the cylinders. Similar to

Case	V_∞ (m/s)	U_r	f_a/f_v	Speaker voltage (mV)	P_a (Pa)	$\widehat{U}_a/V_\infty$
Pre-coincidence case C	25.62	5.9	1.12	212.5	768	0.07
	25.62	5.9	1.12	300	1030	0.09
	25.62	5.9	1.12	425	1276	0.12
Coincidence case D	32.9	7.7	0.86	425	947	0.067
	32.9	7.7	0.86	525	1051	0.075
Coincidence case E	29.28	6.8	0.97	212.5	212	0.016
	29.28	6.8	0.97	300	386	0.03
	29.28	6.8	0.97	425	628	0.05

Table 5.1: Summary of the experimental parameters to investigate the effect of SPL on the distribution of acoustic sources around two tandem cylinders, $f_a = 330$ Hz.

that seen in Fig. 5.13, they are synchronised and in-phase with each other. For coincidence resonance case D, the shear layers of the upstream cylinder tend to reattach to the downstream and only one distinct vortex exists in the wake. Interestingly, differences in the flow structure of coincidence resonance case E with pre-coincidence case C seem to be negligible. The main observation to take from Fig. 5.28 is that increasing the dimensionless acoustic particle velocity across the cylinders has no obvious effect on the magnitudes or distributions of the vortices.

Figure 5.29 shows spatial distributions of the net acoustic energy per cycle for the three resonant cases at each SPL. In all cases, the sources and sinks are symmetric about the centreline of the cylinders. For pre-coincidence case C and coincidence case D, the distribution of the sources are almost identical to those shown in Fig. 5.20 and Fig. 5.21 for all SPL. However, the magnitudes clearly increase with $\widehat{U}_a/V_\infty$. Concentrating on Fig.5.29(b), which shows the coincidence case E, one can see a hybrid type distribution of acoustic energy which shows traits of both case C and case D. For example, the sinks forming around the downstream cylinder coupled with the sources in the far wake resemble pre-coincidence whilst the fact that sinks forming in the shear layers completely engulf the downstream cylinder resembles coincidence resonance. This suggests the possibility of a transitional type of regime in the changeover between pre-coincidence and coincidence resonance.

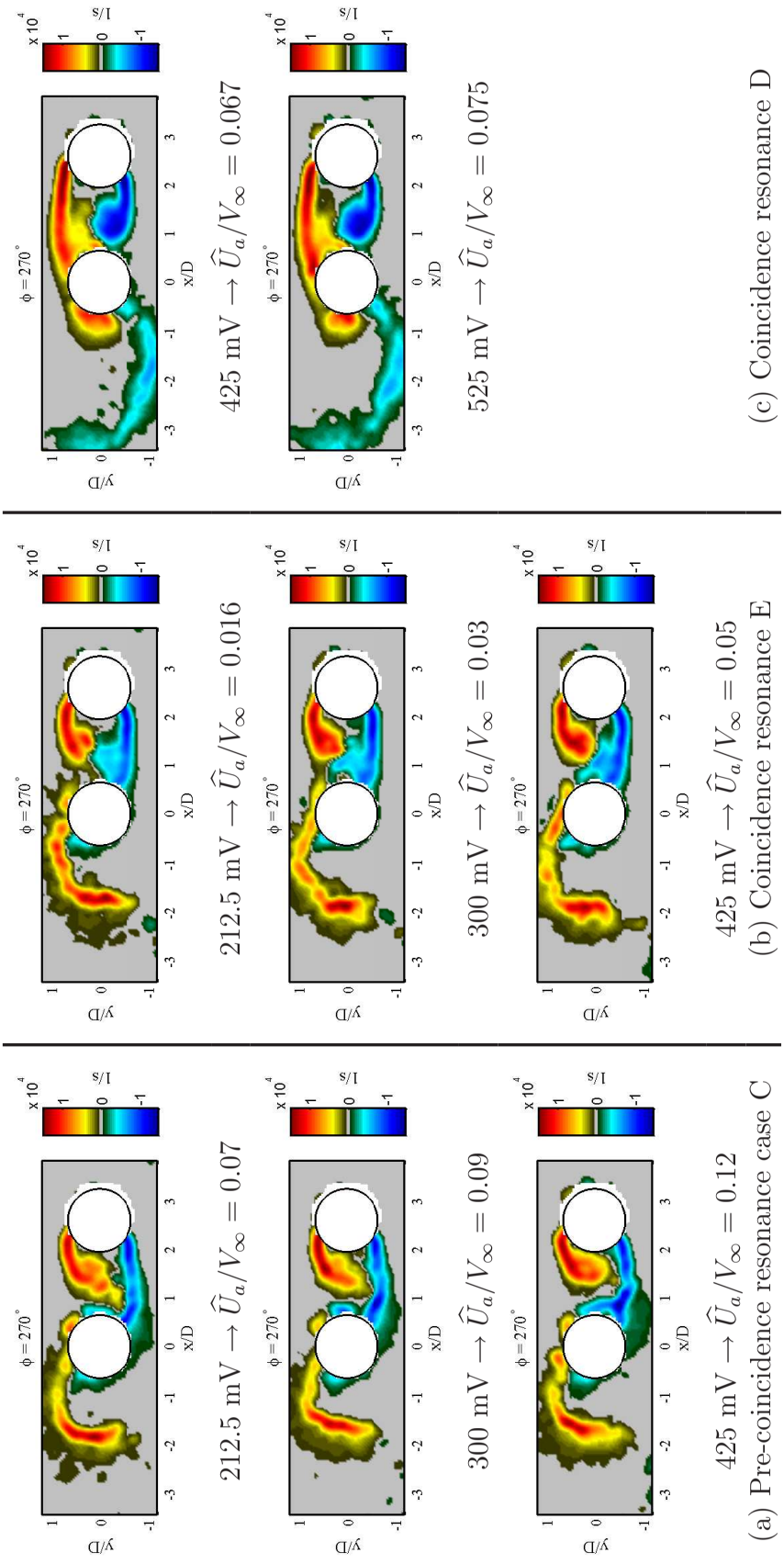

(a) Pre-coincidence resonance case C

(b) Coincidence resonance E

(c) Coincidence resonance D

Figure 5.28: Vorticity contours of the flow field at the three selected velocities for the tested sound pressure levels, $\phi = 270°$.

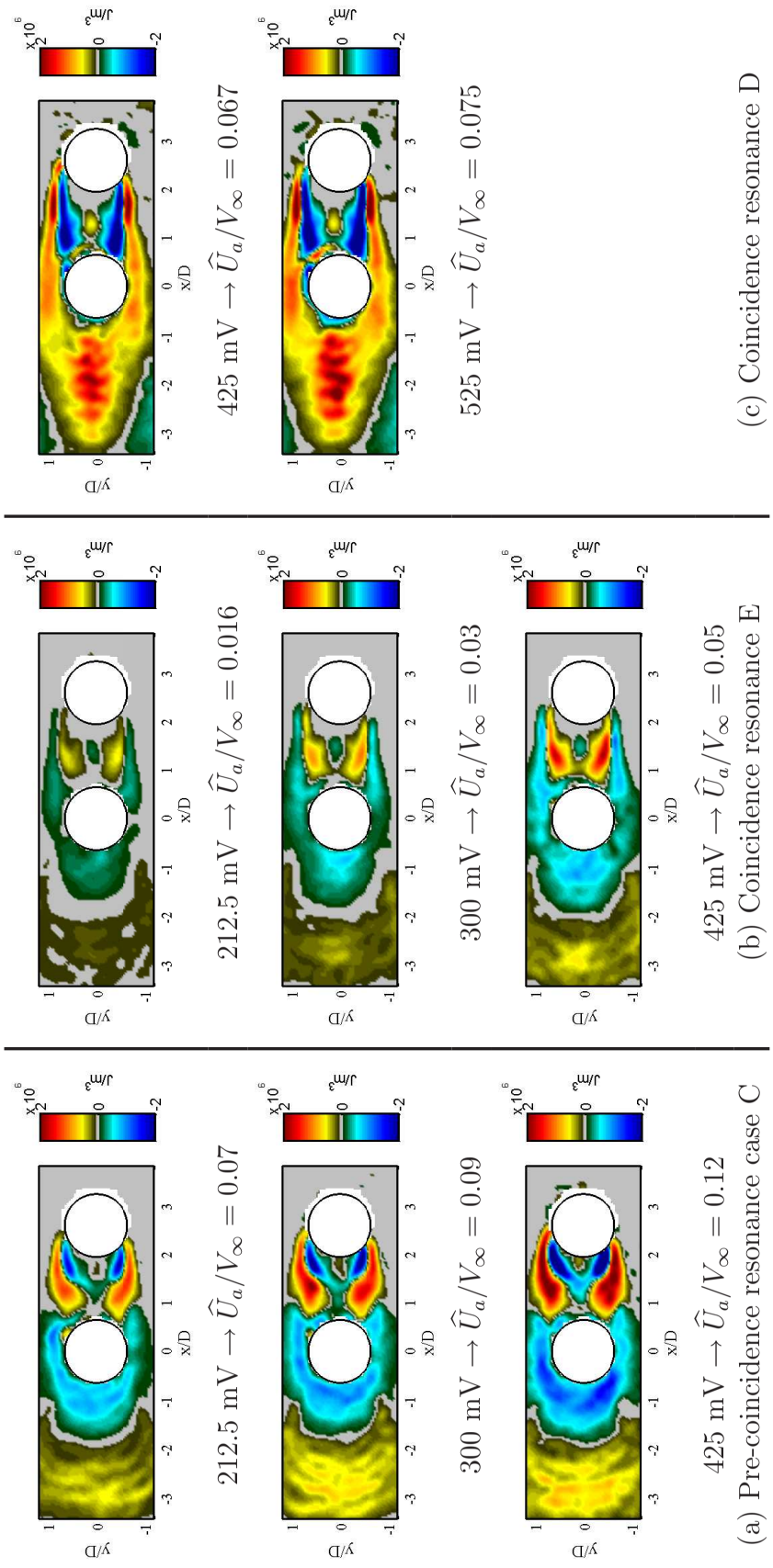

(a) Pre-coincidence resonance case C (b) Coincidence resonance E (c) Coincidence resonance D

Figure 5.29: Contours of the net acoustic energy at the three selected velocities for the tested sound pressure levels.

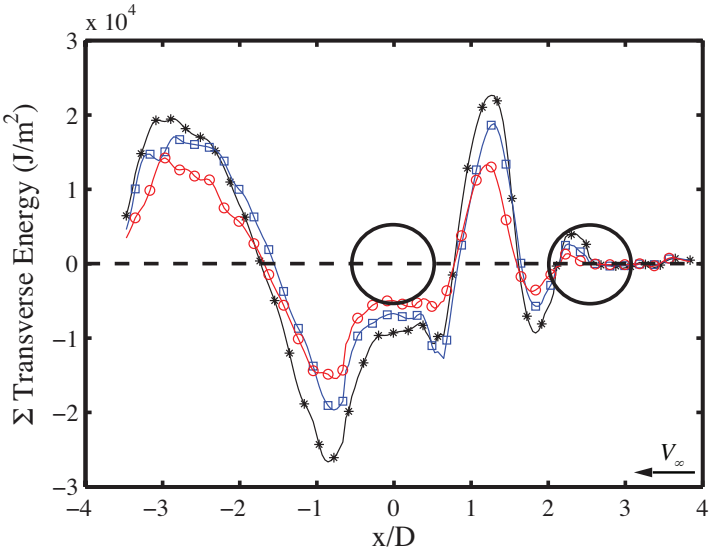

Figure 5.30: Net acoustic energy transfer per streamwise location per cycle for pre-coincidence case C. ○ 212.5 mV ($\widehat{U}_a/V_\infty = 0.07$) ; □ 300 mV ($\widehat{U}_a/V_\infty = 0.09$), ∗ 425 mV ($\widehat{U}_a/V_\infty = 0.12$).

Figure 5.30 shows the total acoustic energy transfer per streamwise location per cycle, E (J/m^2), at pre-coincidence resonance case C for the three tested SPL amplitudes. In this plot, varying the dimensionless acoustic velocity ratio seems to only increase the magnitude of the sources and sinks. Considering Howe's integral (Eqn. 3.12) and the definition of acoustic particle velocity (Eqn. 3.23), varying the acoustic pressure across the cylinders simply acts as a scalar because $U_a \propto P_a$. To properly observe the effect of the SPL amplitude on the acoustic sources, it should be taken out of consideration. A dimensional analysis revealed that the energy per streamwise location per cycle, E, can be normalised by the product of acoustic pressure (measured by M1) and the cylinder diameter. That is to say,

$$E^* = \frac{E}{P_a D}. \tag{5.2}$$

As shown in Fig. 5.31(a), by normalising the net energy transfer per streamwise location using Eqn. 5.2, the variation in the data for pre-coincidence resonance case C is greatly reduced. Since this normalisation causes the curves to collapse, it provides a good metric for the aeroacoustic source distribution at low flow velocities. Moreover, this normalisation seems valid because even though the pressure has been removed from the calculation of

the acoustic power and energy, its effect is still present when the PIV measurements are being made. Figure 5.31(b) and Fig. 5.31(c) plots E^* for coincidence cases D and E. For all cases, increasing the normalised acoustic velocity ratio ($\widehat{U}_a/V_\infty$) seems to have a negligible effect on the strength and distribution of the sources. This leads to the conclusion that when the system becomes "locked-in", it behaves linearly. Given that the "lock-in" phenomenon is inherently non-linear, this is an interesting result. Any changes to the vortex formation that do occur with varying SPL are certainly not of the same magnitude observed by Ziada [66]. This is more than likely due to the fact that the range of excitation in the present experiments was relatively small compared to his. He used a range of excitation between 5% and 50% of the mean flow velocity. Derivation of E^* can be found in Appendix A.

5.3.6 Forced resonance versus natural resonance

As resonance was forced, a question remains of how well the experiment simulates natural resonance. The loudspeakers were initially installed as the flow could not induce acoustic resonance in their absence. This condition was tested again towards the end of the study as hard wall blanks were installed instead of the loudspeakers. Figure 5.32(a) shows a spectra measured by HW2 over a range of flow velocities. Figure 5.32(b) plots the corresponding pressure. Natural acoustic resonance is induced at $V_\infty \approx 20$ m/s as a sudden increase in SPL is accompanied by a significant shift in the vortex shedding frequency. It is interesting to note that "lock-in" occurs approximately 3 m/s lower than that which was observed for the forced case. Near acoustic-Strouhal coincidence, the "lock-in" is broken. In other words, no coincidence resonance is observed. However, the microphone plot clearly shows that the first acoustic mode of the duct remains strongly excited well beyond acoustic-Strouhal coincidence.

As discussed in Fig.4.5 and Fig. 5.2, it seems that the second hydrodynamic mode of vortex shedding from the mouths of the side-branches coincides with the natural acoustic frequency of the duct around these flow velocities. Since the vortices shed from the side-branch mouths are stronger than those shed from the cylinders, it is expected that their interaction with the sound field will be far stronger as well. Therefore, it is not unreasonable to assume that the acoustics will naturally select to interact with the unsteady flow of

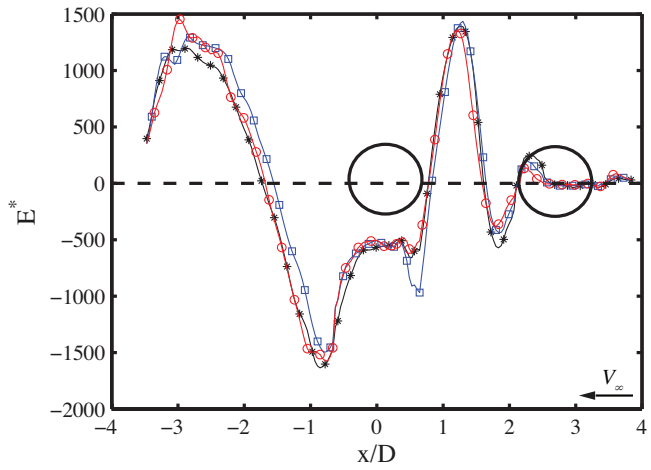

(a) Pre-coincidence resonance case C

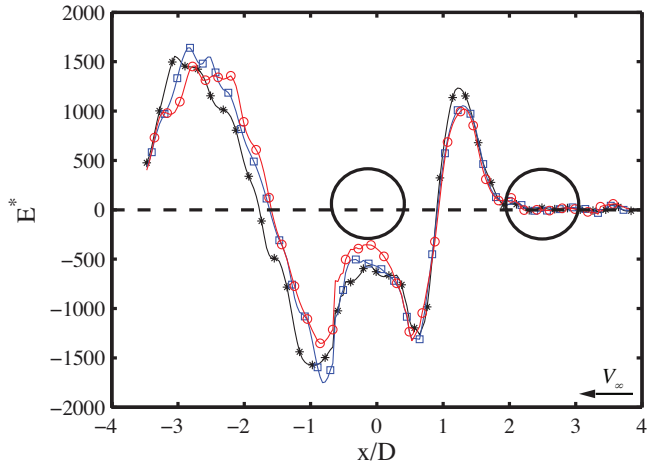

(b) Coincidence resonance case E

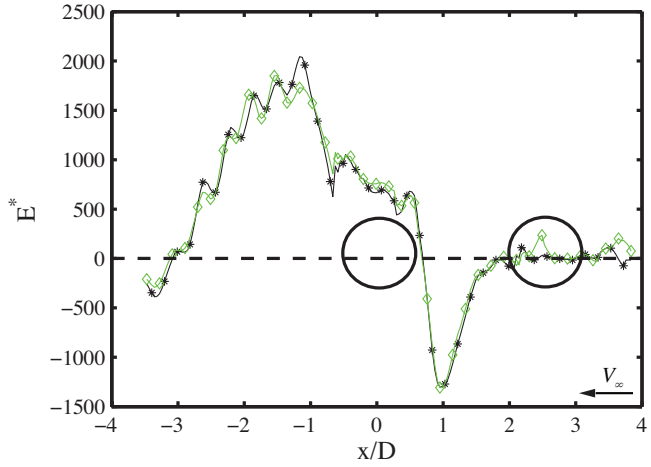

(c) Coincidence resonance case D

Figure 5.31: The normalised acoustic energy per streamwise location per cycle for all the tested velocities and loudspeaker voltages. ○ 212.5 mV; □ 300 mV; ∗ 425 mV; ◇ 525 mV.

the side-branches instead of the cylinders. Thus, acoustic energy concentrates on feeding the vortices of the side-branches and not the cylinders which may explain why "lock-in" of the cylinders is not sustained after acoustic-Strouhal coincidence. The fact that "lock-in" is observed after acoustic-Strouhal coincidence in the forced resonance cases is due to the presence of the loudspeakers as the acoustic field cannot naturally select which mechanism to excite to the same extent.

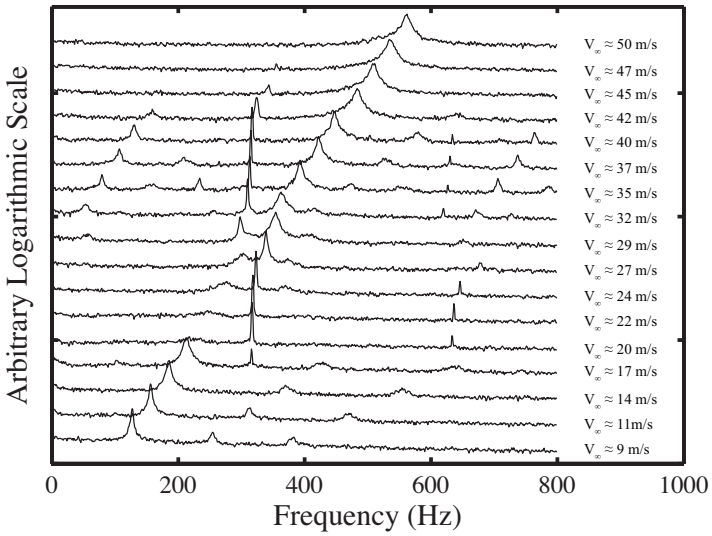

(a) Velocity spectra measured by HW2

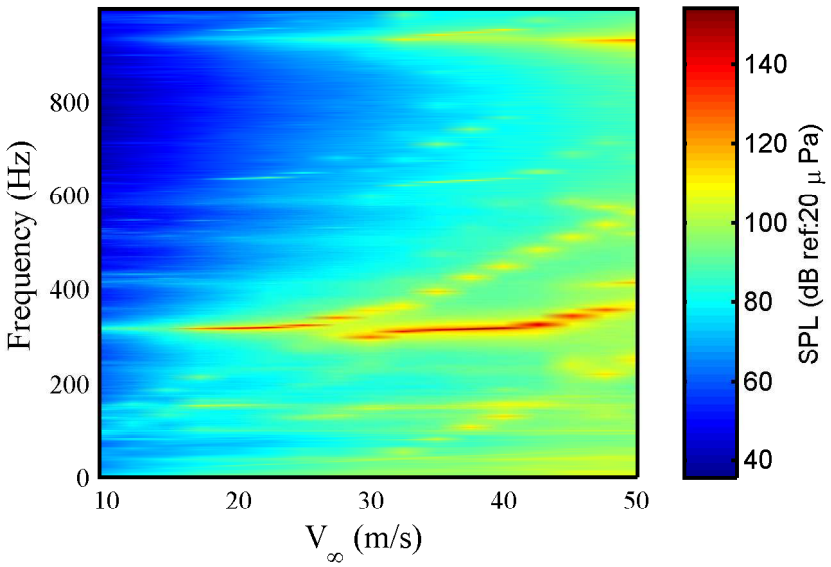

(b) Pressure spectra measured by M1

Figure 5.32: Aeroacoustic response of the two tandem cylinders when the loudspeakers are replaced with hard wall blanks.

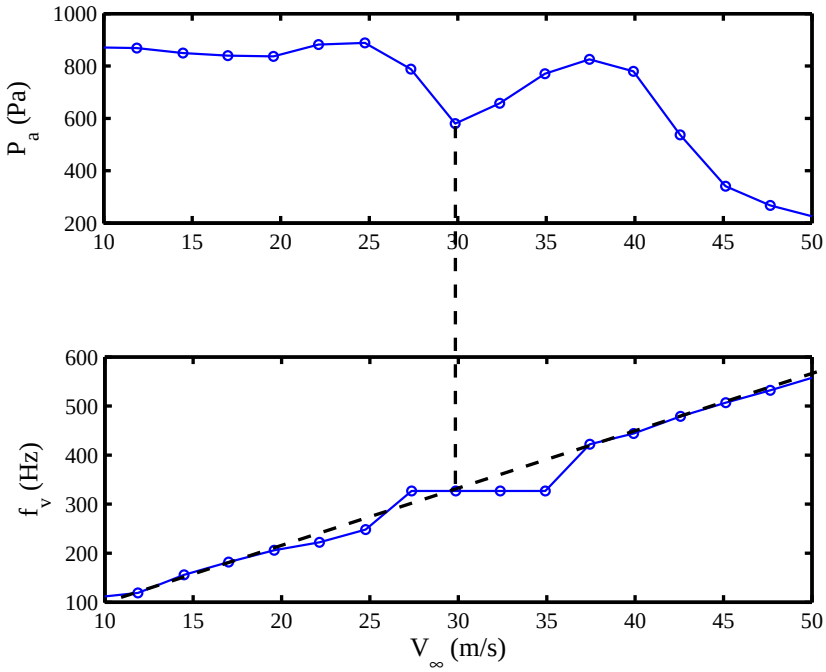

Figure 5.33: Aeroacoustic response of the tandem cylinders in the presence of an applied acoustic wave at $f_a = 327$ Hz. The top plot show the pressure measured by M1 at f_a whilst the bottom plot shows the vortex shedding frequency.

Mohany and Ziada [5] reported that acoustic pressure subsides at acoustic-Strouhal coincidence and that no resonance occurs. However, positive net acoustic energy was observed for coincidence resonance case E. Figure 5.33 shows the aeroacoustic characteristics of the cylinders when the resonance was forced at $f_a = 327$ Hz. The top plot shows the acoustic pressure measured by M1 at the frequency of excitation whilst the bottom plot shows the vortex shedding frequency. As can be seen, the acoustic pressure drops away near acoustic-Strouhal coincidence before increasing again in the coincidence resonance regime. This behaviour is also evident in Tab. 5.1. Here the highest value of acoustic pressure measured for coincidence resonance case E is lower than the lowest pressure measured for either of the other two cases. So it seems that for this setup, forced resonance mimics natural resonance fairly well, at least during "lock-in".

The fact that positive energy generation occurred during coincidence resonance case E is probably due to the presence of the loudspeakers. Even though the acoustic pressure drops out in a similar fashion to that of Mohany and Ziada [5], the speakers will still

excite the system. This is the nature of forced resonance experiments. The pressure that was recorded for the lowest applied voltage to the speakers (212.5 mV) was 212 Pa. This corresponds to a SPL of 140 dB. Blevins [29] reported that at least 130 dB was required to correlate the vortices along the span of a single cylinder and Hall *et al.* [2] concluded that two tandem cylinders are more susceptible to "lock-in" than single cylinders. Thus it is not unreasonable to infer that the residual pressure measured by M1 after the fall out is sufficiently high to organise the flow structure so that its phasing is conducive to generating net acoustic energy.

5.4 Summary

In this chapter, a study of the flow-acoustic coupling of a pair of tandem cylinders subject to ducted flow has been presented. Two cylinders were selected in order to act as a stepping stone towards investigating more complex configurations akin to a heat exchanger tube bundle. Resonance was forced via two loudspeakers at the closed ends of each side-branch rather than naturally generated. Nonetheless, the results indicate that the characteristics of the system are broadly in line with those previously completed by other authors for a similar configuration. To that end, the system seems to adequately simulate the acoustic resonance mechanism. The main conclusions to be drawn from the study are:

- An applied acoustic sound wave can shift the vortex shedding process away from its naturally preferred frequency. This shift can occur over a range of flow velocities before and after acoustic-Strouhal coincidence.
- The amount of shift achievable by the acoustic wave increases with the degree of forcing. That is to say, increasing the SPL in the duct increases the acoustic "lock-in" range. However, increases from high to very high SPL only induce wider "lock-in" ranges after acoustic-Strouhal coincidence.
- At off-resonant conditions before acoustic-Strouhal coincidence, vortex shedding only occurs in the wake of the cylinders as the shear layers in the gap region reattach to the downstream cylinder.

- The flow structure around the two cylinders during resonance is dependent on the oncoming flow velocity in the duct and thus the acoustic-resonance regime. During pre-coincidence acoustic resonance, strong vortices form in both the gap region and the wake of the cylinders. The vortices shed from a particular side of the cylinders are synchronised and in-phase. Together, they form an anti-symmetric vortex shedding regime which is similar to that of an intermediately spaced inline array. For coincidence resonance, only one vortex was shed from the two cylinders as the shear layers reattach to the downstream cylinder. The different flow structures lead to a different distribution of acoustic sources between pre-coincidence and coincidence acoustic resonance.

- The suggestion by other authors that pre-coincidence acoustic resonance is driven or at least triggered by shear layer instability in the gap region seems valid. However, the near wake also has a significant contribution in the generation of acoustic energy. The suggestion by other authors that coincidence resonance is induced by vortex shedding in the wake of the cylinders is confirmed as a strong net sink is found to lie in the gap between the cylinders.

- Even though the SPL can vary the range of flow velocities at which "lock-in" occurs, it has a negligible effect on the distribution of the sources during both pre-coincidence and coincidence acoustic resonance. Its effect is to change the magnitude of the sources/sinks in a linear fashion.

- The use of PIV to resolve the quantities in Howe's integral is robust. The fact that accurate vectors could be resolved in challenging PIV conditions where there were high flow gradients and inhomogeneous illumination means the method is well suited to investigate more extreme conditions.

Chapter 6

Case 2 : Four Cylinders

6.1 Introduction

In the previous chapter it was shown that the conceptual approach described in Ch. 3 is an effective way of investigating the energy transfer mechanism between the flow field and the sound field in ducted bluff body flows. Studying two tandem cylinders acted as a base from which more complex systems could be studied. The configuration considered in this chapter is that of four cylinders in a group and poses a significant increase in the complexity of the system, particularly regarding the PIV conditions. As previously discussed in Ch. 2, the four cylinder configuration is defined by its streamwise pitch ratio P/D, its transverse pitch ratio L/D and its angle of orientation α to the oncoming flow. The configurations studied in the present work all had $\alpha = 0°$ which means that they can effectively be considered as two pairs of two tandem cylinders or one cell in an inline tube array. The majority of the work was completed on a square configuration where $P/D = L/D = 2.5$. However, the effect of varying the sound pressure level, the transverse spacing and the streamwise spacing was also investigated. To facilitate the larger field of view that needed to be illuminated with the laser, one of the loudspeakers was removed and replaced with a hard wall blank. The other speaker was totally encased within a pressure equalising chamber. The side of the chamber exposed to the duct had holes drilled in concentric circles to maximise the acoustic transparency whilst simulating a hard walled boundary condition. The pressure on both sides of the loudspeaker cone was equalised via a small bleed line.

6.2 Four cylinders orientated in a square

6.2.1 Microphone and hotwire analysis

The addition of extra cylinders causes the blockage to increase which results in a lower velocity for a given fan voltage compared with the two tandem cylinder case. The mainstream velocity when the cylinders were installed ranged from 10 m/s to 44 m/s. The aeroacoustic characteristics of the four cylinders can be seen in Fig. 6.1 which shows a plot of the vortex shedding frequency measured by M1 versus the reduced velocity. Three loudspeaker voltages were tested for this configuration. The first was the case of no applied sound (0 mV) which is represented by the blue line. As can be seen, the vortex shedding frequency increases linearly with velocity but does not "lock-in". Figure 6.2 plots the variation of the Strouhal number with Reynolds number measured by hotwire in the wake of the cylinders. It shows a similar trend to that observed for the two tandem cylinders in that it decreases with Reynolds number. Lam and Lo [18] observed that the Strouhal number of vortex shedding varies from cylinder to cylinder. In these tests, HW2 was positioned in a similar location to that of cylinder 4 in Fig. 2.12. For $P/D = 2.5$, Lam and Lo [18] measured $St \approx 0.195$ behind cylinder 4 at $Re = 2100$. The lowest Reynolds number tested here was $Re = 7099$. However, Fig. 6.2 suggests that the data would be in good agreement for lower Reynolds numbers. The other two loudspeaker voltages were 212.5 mV and 425 mV. These corresponded to sound pressures of 155 dB and 158 dB when there was no flow in the duct. The natural frequency measured for these tests was $f_a = 329$ Hz. The applied sound wave can "lock-in" in the system. Resonance was initiated at $U_r = 4.85$ for each speaker setting and was sustained over a range of reduced velocities through acoustic-Strouhal coincidence. "Lock-in" subsides at $U_r = 6.2$ for the 212.5 mV case and at $U_r = 6.44$ for the 425 mV case. The aeroacoustic behaviour of the four cylinders is similar to that observed for two tandem cylinders in that "lock-in" was sustained over a range of flow velocities before (pre-coincidence resonance) and after acoustic-Strouhal coincidence (coincidence resonance). The behaviour of the four cylinders is also similar to the two tandem case because increasing the SPL in the duct seems more influential on the width of the "lock-in" range after acoustic-Strouhal coincidence. As before, this is probably due to hysteresis.

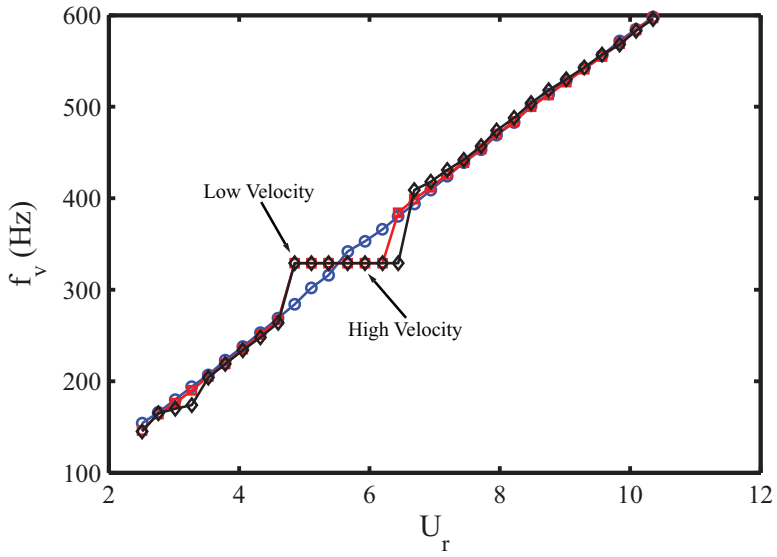

Figure 6.1: Aeroacoustic characteristics of four cylinders in a square measured by M1. ○ No applied sound; □ 212.5mV; ◇ 425mV.

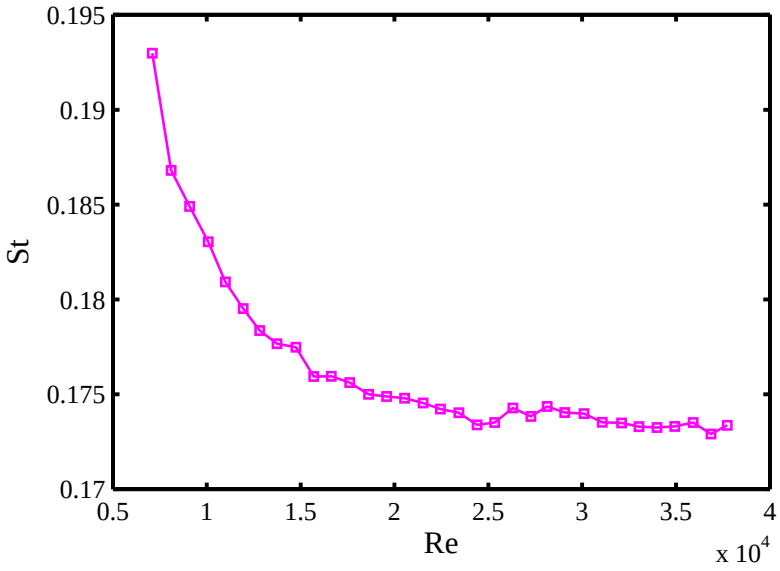

Figure 6.2: Variation of Strouhal number with Reynolds number for four cylinders in a square measured by HW2.

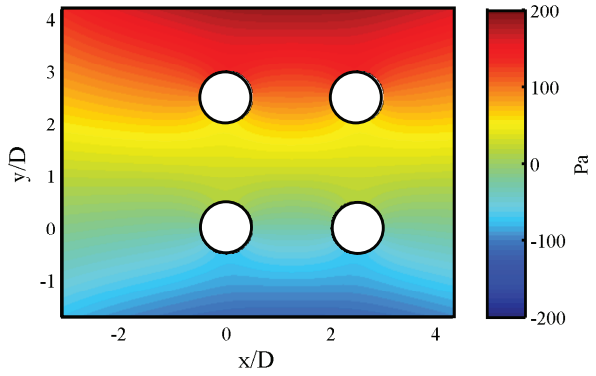

(a) Acoustic pressure

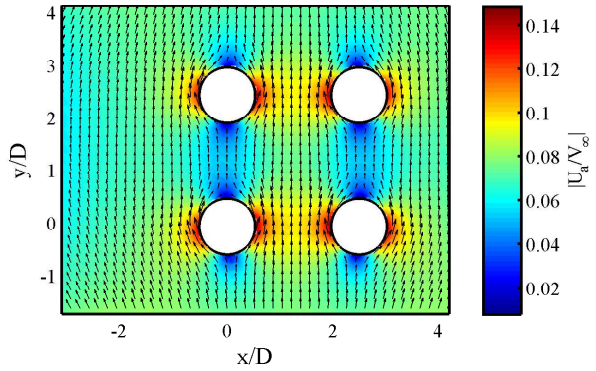

(b) Acoustic particle velocity

Figure 6.3: Resonant acoustic mode around the four cylinders (within the PIV field of view) calculated by FEA.

6.2.2 Resonant acoustic field

The simulated acoustic mode shape calculated from Eqn. 3.13 and the induced acoustic particle velocity calculated from Eqn. 3.23 can be seen in Fig. 6.3. Similarly to what was seen before, the highest acoustic particle velocity occurs at the cylinders. The contours are normalised by the mainstream flow velocity $V_\infty = 25.4$ m/s. The simulated natural frequency was 304 Hz. The natural frequency measured by M1 during the test was 329 Hz. This gave a discrepancy of 8.2% between the numerically computed value and measured value. However, as was shown in Ch. 5, this discrepancy in the resonant frequency should not affect the mode-shape itself as the resonance is forced by the loudspeaker. Figure 6.4 shows the centreline profile of the simulated acoustic mode shape and the acoustic particle velocity across the whole width of the duct.

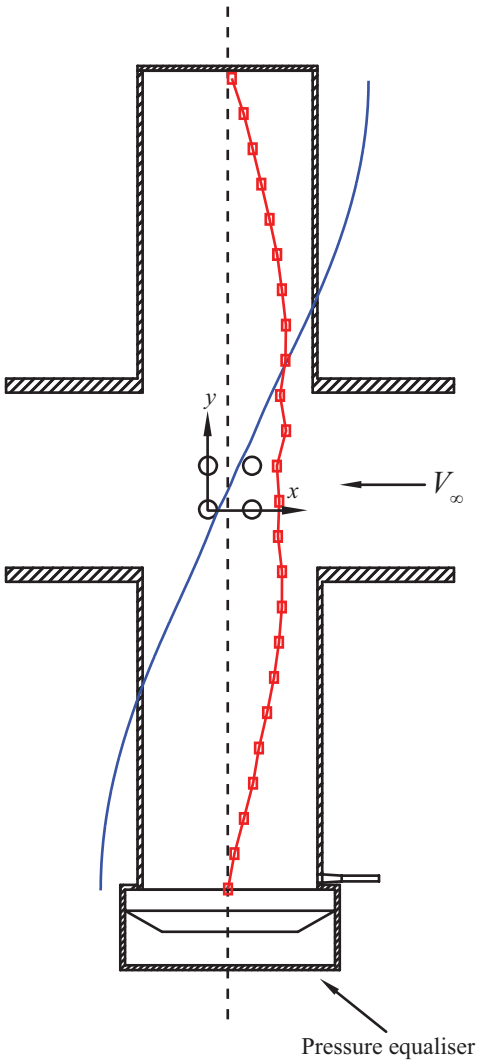

Figure 6.4: Profiles of the simulated resonant acoustic mode in the test section. — Acoustic pressure, □ Acoustic particle velocity.

6.2.3 PIV experimental issues

A typical example of a raw PIV image can be seen in Fig. 6.5. The flow is seeded homogeneously with good density and does not reveal the underlying flow structure. Also the particles are illuminated nearly everywhere in the flow, even in the shadow regions (the light sheet is entering the flow from the top of the image). Homogeneous seeding distribution and the proper illumination of the flow field are both issues that pose significant practical obstacles in completing meaningful PIV around multiple bluff body flows. Illumination was a particular problem as every time the laser sheet passed through a cylinder it lost some intensity. This is why fewer particles can be seen in the shadow of

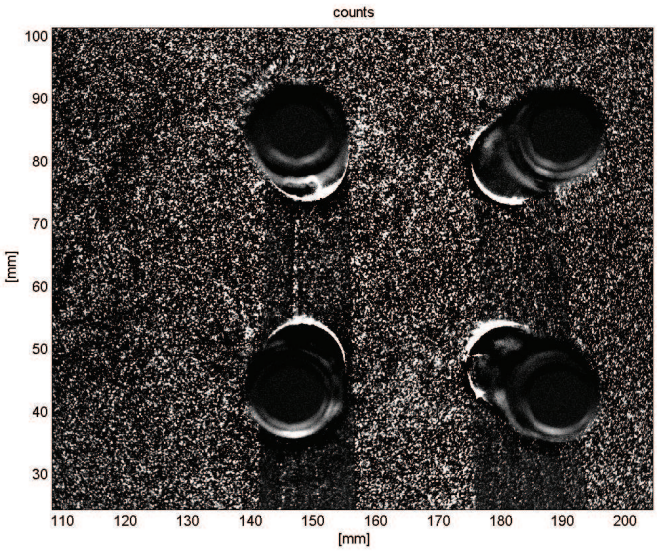

Figure 6.5: A typical raw PIV image around the four cylinders.

the shadows. The sum of correlation PIV algorithm is very robust with dealing with this type of loss in intensity.

A partial blocking of the flow field by out-of-focus parts of the cylinders occurs. This blocking is due to parallax and will prevent any velocity vectors (and hence acoustic sources) from being resolved in these regions. Parallax also significantly increases the reflections visible to the camera. As the cylinders were made from perspex, internal reflection caused the entire surface to light up when the laser sheet passed through. This issue is not problematic from a vector calculation point of view as these areas can be masked out. However, from a hardware point of view, these high intensity reflections can damage the CCD chip if it becomes over saturated. One solution is to paint the cylinders fluorescent orange and use a special bandpass filter on the camera lens as the paint changes the wavelength of the light. However, this solution is only useful up to a certain point as the whole cylinder cannot be painted (otherwise no light would get through at all). This is why high intensity halos of light are present in and just above the plane of the flow in Fig. 6.5. The only other solution is to reduce the laser power, which would have an adverse effect on the illumination of the particles. Unfortunately, this optical phenomenon is one of the compromises when completing full field PIV around the cylinders in the least amount of time and could not be avoided.

Case	V_∞ (m/s)	U_r	f_a/f_v	Speaker voltage (mV)	P_a (Pa)	$\widehat{U}_a/V_\infty$
Low velocity	20.76	4.85	1.15	212.5	700	0.078
	20.76	4.85	1.15	425	1044	0.117
High velocity	25.37	5.93	0.94	212.5	703	0.065
	25.37	5.93	0.94	425	1177	0.108

Table 6.1: Summary of the experimental parameters in the four cylinder square investigation, $f_a = 329$ Hz.

6.2.4 Resonant flow field

It is within the "lock-in" range that the energy transfer mechanism between the flow field and the sound field is of interest. Two different velocities labelled, "Low velocity" and "High velocity" in Fig. 6.1 were selected for the PIV study. The "Low velocity" case corresponded to a reduced velocity $U_r = 4.85$ and a frequency ratio of $f_a/f_v = 0.94$ whilst the "High velocity" case corresponded to $U_r = 5.93$ and a frequency ratio of $f_a/f_v = 0.94$. Table 6.1 summarises the experimental parameters.

Figure 6.6 shows the "locked-in" flow field during pre-coincidence ("Low velocity") for $\widehat{U}_a/V_\infty = 0.117$ whilst Fig. 6.7 shows the same during coincidence resonance ("High velocity") for $\widehat{U}_a/V_\infty = 0.108$. Figure 6.6(a) and Fig. 6.7(a) show the hydrodynamic velocity whilst Fig. 6.6(b) and Fig. 6.7(b) show the vorticity. Six different phases of the acoustic wave cycle are plotted in these figures including $\phi = 0°$, $67.5°$, $135°$, $202.5°$, $270°$ and $\phi = 337.5°$. The sum of correlation PIV algorithm was used with a multi-pass reducing interrogation window from 32 px $\times$ 32 px $\rightarrow$ 12 px $\times$ 12 px with 50% overlap between windows. A broad overview of the two figures shows that the general flow structures are the same which is interesting given that they are in different acoustic resonant regimes according to frequency ratio.

For both cases, if you consider the four cylinders to be equivalent to two pairs of tandem cylinders, inspection of the vorticity plots show that vortices are about to form from the bottom sides of both upstream cylinders at $\phi = 67.5°$. Between $\phi = 67.5°$ and $\phi = 135°$ the vortices roll up and continue to strengthen since they are still attached to the shear layers. By $\phi = 202.5°$ they are fully developed and about to impinge on the downstream cylinders. Even though they are about to impinge on the downstream

cylinders, they remain attached to the shear layers because configurations in the proximity interference region do not provide enough room for a vortex to fully separate. The fact that vortex shedding even occurs in the gap region is a feature of "locked-in" flow as shown previously in Ch. 5.

After the vortices impinge on the downstream cylinders, they trigger new vortices in the wake. These have opposite polarity from the vortices that triggered them and because there are no obstructions to block their formation, they eventually separate from the shear layers in the wake. This process will continue to occur alternatively between the top and bottom sides of the cylinders. As a result, two Von-Karman vortex streets form in the wake, one for each pair of tandem cylinders. Similarly to what was seen for the tandem cylinders at pre-coincidence, the flow structure between upstream and downstream cylinders is highly synchronised. Moreover, the flow structure between one pair of tandem cylinders and the other is also highly synchronised. The location and development of vortices shed from the same side of both upstream cylinders (or both downstream cylinders) match and are in-phase. This type of vortex shedding is considered anti-symmetric about the centreline of the four cylinders and is exactly that which occurs for intermediate and largely spaced inline tube arrays during acoustic resonance.

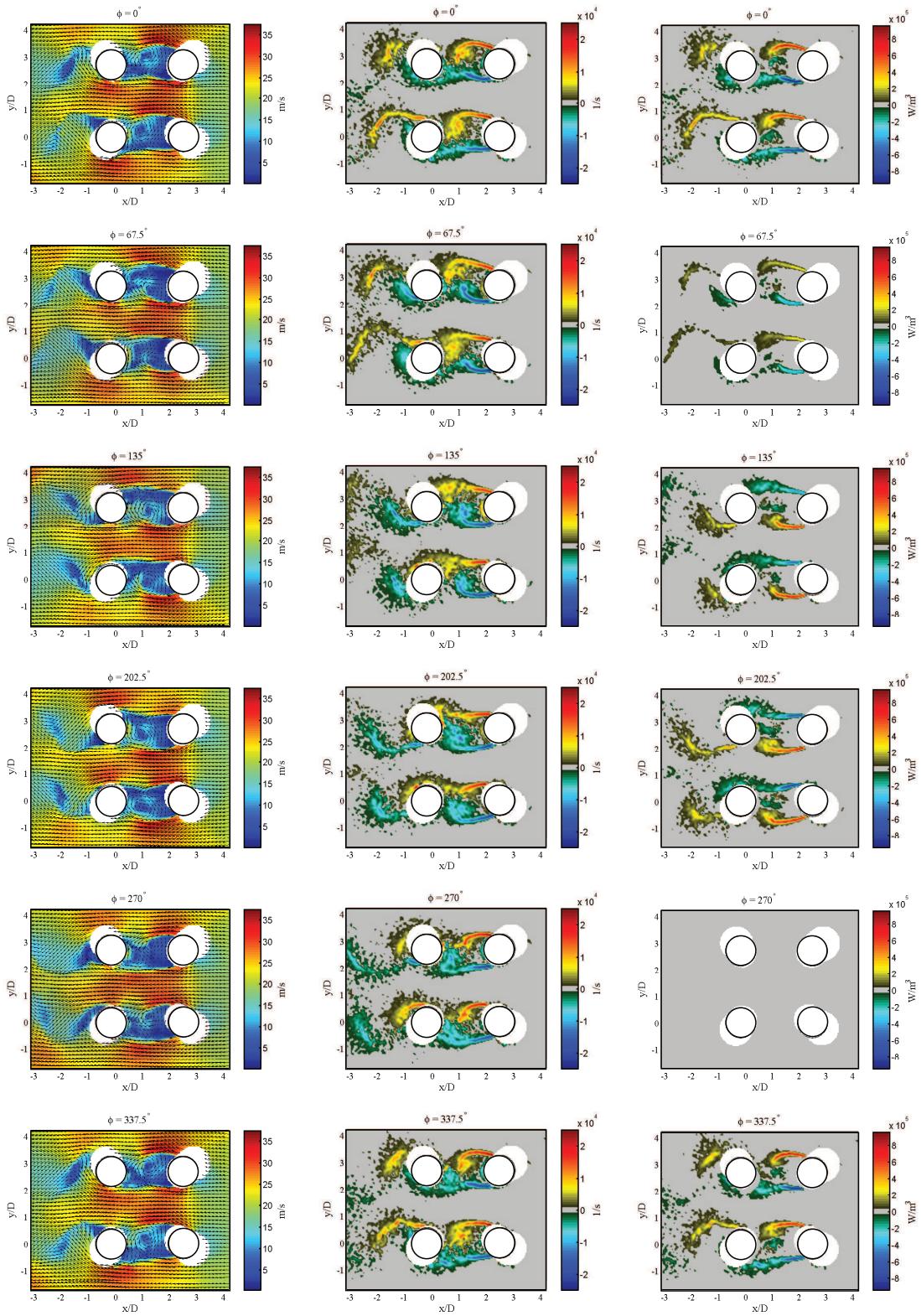

(a) Velocity (b) Vorticity (c) Acoustic power

Figure 6.6: Contours of the velocity, the vorticity and the acoustic power at various phases in the acoustic wave cycle during pre-coincidence resonance, $U_r = 4.85$ $f_a/f_v = 1.15$, $\widehat{U}_a/V_\infty = 0.117$.

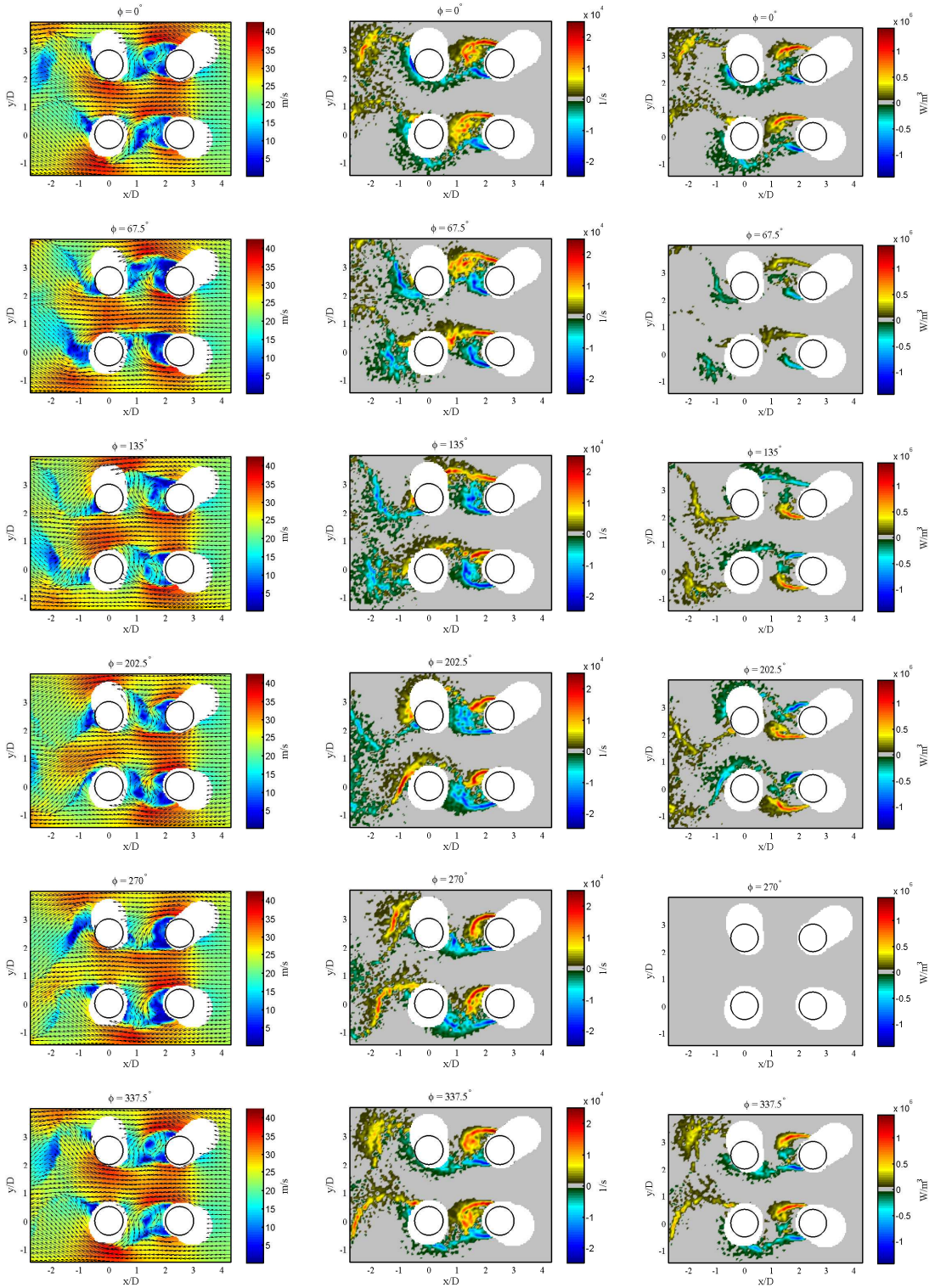

(a) Velocity (b) Vorticity (c) Acoustic power

Figure 6.7: Contours of the velocity, the vorticity and the acoustic power at various phases in the acoustic wave cycle during coincidence resonance, $U_r = 5.93$, $f_a/f_v = 0.94$, $\widehat{U}_a/V_\infty = 0.108$.

6.2.5 Flow/sound interaction

6.2.5.1 Phase averaged acoustic power

Contours of the phase averaged acoustic power generated by the flow-sound interaction for pre-coincidence and coincidence resonance can be seen in Fig. 6.6(c) and Fig. 6.7(c) respectively. Since the synchronised flow structure between the four cylinders causes anti-symmetric vortex shedding, the generation/absorption of acoustic power is also anti-symmetric. Figure 6.8(a) plots the total acoustic power generated per phase from the four cylinders during pre-coincidence resonance. At $\phi = 0°$ there is net contribution to the generation of acoustic resonance as the total power at this phase is $\Pi = 46.6$ W/m. This is reasonable as the acoustic particle velocity has a maximum magnitude at this phase. According to Fig. 6.6(c), the sources in the flow field at this stage are associated with the vortices shed from the top sides of the cylinders. Figure 6.6(b) indicates that the structures in the gap region are about to impinge on the downstream cylinders whilst the vortices in the wake are about to fully develop. At $\phi = 62.5°$ the system is still generating acoustic power but the energy transfer between the flow field and the sound field is much weaker. At this phase, the structures shed from the top sides of the cylinders are still acting as sources whilst those shed from the bottom are still acting as sinks. The reason for the net energy transfer being much lower at this phase in comparison to $\phi = 0°$ is because the acoustic particle velocity is much lower at $\phi = 67.5°$ than at $\phi = 0°$. Also, as the vortices shed from the bottom side of the cylinders (sinks) are just starting to strengthen and grow (whilst the vortices shed from the top sides of the cylinders (sources) are starting to weaken and dissipate), their contribution will be stronger and hence more power is absorbed. The fact that the vortices shed from the top sides of the upstream cylinders are now smeared across the surface of the downstream cylinders means they cannot increase in strength and so their contribution is diminished.

Moving forward to $\phi = 202.5°$, Fig. 6.8(a) indicates that the maximum amount of acoustic power is generated at this phase. Here, the vortices shed from the bottom sides of the upstream cylinders are about to impinge on the downstream cylinders. Since the timing of this event is close to the phase at which the acoustic particle velocity has maximum amplitude, a strong amount of acoustic power is generated. The reason why

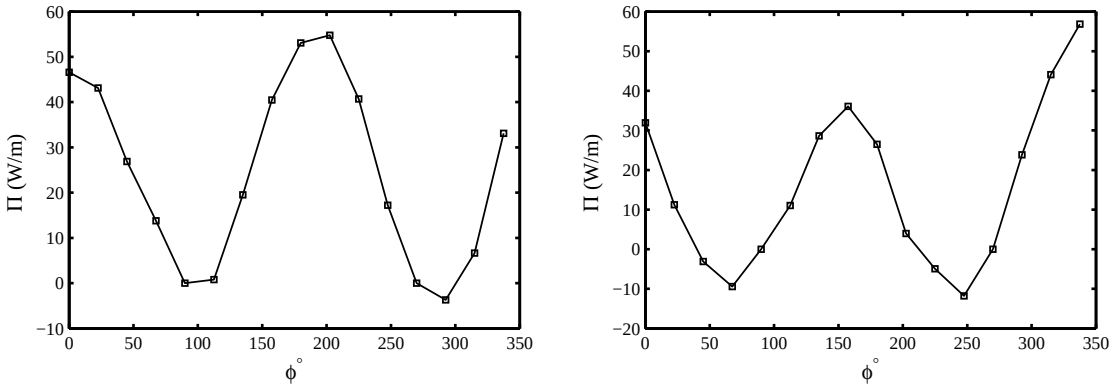

(a) Pre-coincidence resonance (b) Coincidence resonance

Figure 6.8: The total acoustic power generated by four cylinders at a given phase. (a) $f_a/f_v = 1.15$, $\widehat{U}_a/V_\infty = 0.117$; (b) $f_a/f_v = 0.94$, $\widehat{U}_a/V_\infty = 0.108$.

the structures shed from the bottom side of the cylinder (which were previously absorbing acoustic power) are now generating acoustic power is due to the fact that the acoustic particle velocity is travelling in a different direction from that at $\phi = 0°$. At $\phi = 270°$ the acoustic particle velocity is equal to zero and so no acoustic power is either generated or absorbed. The only phase which has a negative net contribution during pre-coincidence resonance occurs at $\phi = 292.5°$ and although not shown in Fig. 6.6, the sources at this phase are associated with vortices shed from the top sides of the cylinders whilst the sinks are associated with the bottom sides. It is corollary to the absorption of acoustic power from the tandem cylinder configuration described in Ch. 5, i.e., the sinks are smeared across the face of the cylinders yet still attached the shear layer from which they were formed. As a result, they are spread out over a larger area than the newly formed compact vortices generating power from the other side of the cylinders.

Inspection of the acoustic power plots in Fig. 6.7 (as well as those not shown) revealed that the mechanisms generating and absorbing acoustic power around the four cylinders during coincidence resonance are similar to those at pre-coincidence resonance in that the generation of acoustic power seems related to the development of vortices in the gap region and in the wake of the cylinders. Moreover, the maximum positive contribution to acoustic power at coincidence resonance occurs just as the vortices in the gap region are about to impinge on the downstream cylinders. Figure 6.8(b) plots the total acoustic power generated per phase from the four cylinders during coincidence resonance. The

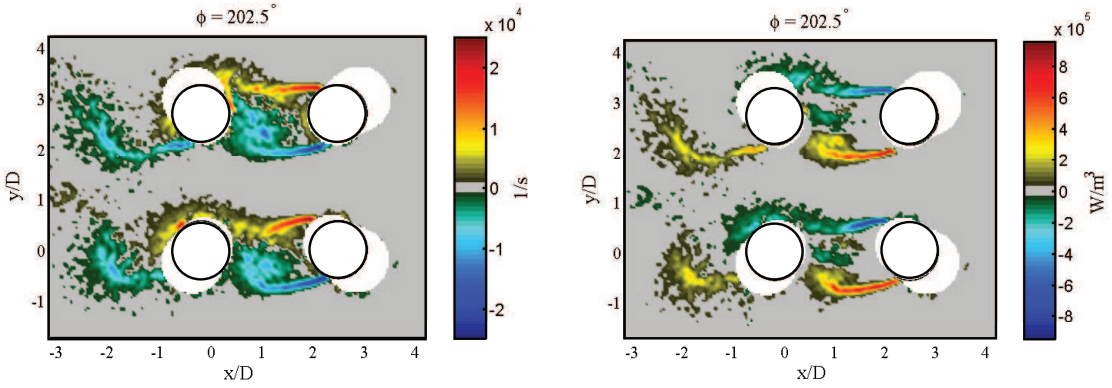

Vorticity Acoustic power

(a) Pre-coincidence acoustic resonance

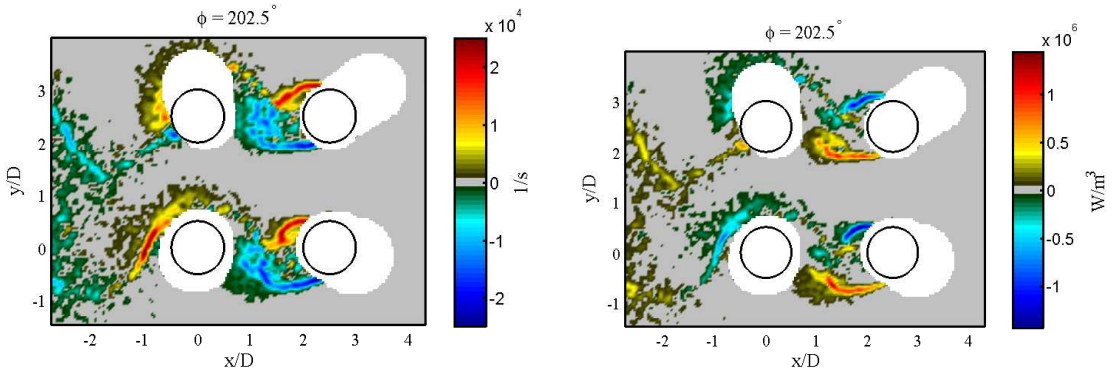

Vorticity Acoustic power

(b) Coincidence acoustic resonance

Figure 6.9: Comparison of the vorticity and acoustic power generated by the four cylinders at $\phi = 202.5°$ for pre-coincidence and coincidence acoustic resonance.

maximum acoustic power in this case is generated at $\phi = 157.5°$ which is 45° degrees early in the acoustic wave cycle compared to the pre-coincidence resonance. This phase shift is likely due to the higher convection velocity of the vortices in the wake of the cylinders during coincidence resonance.

Figure 6.9 compares the vorticity and acoustic power generated by the four cylinders at $\phi = 202.5°$ for both pre-coincidence and coincidence resonance. For pre-coincidence, four distinct sources form in the flow, two from the vortices in the gap region and two from the vortices in the wake at $x/D \approx -2$. For coincidence resonance, four sources are generated as well. Here however, the sources in the wake form at $x/D \approx -3$ and are therefore further downstream compared to the pre-coincidence case. Since they are further downstream, they dissipate more vorticity and thus have a weaker contribution.

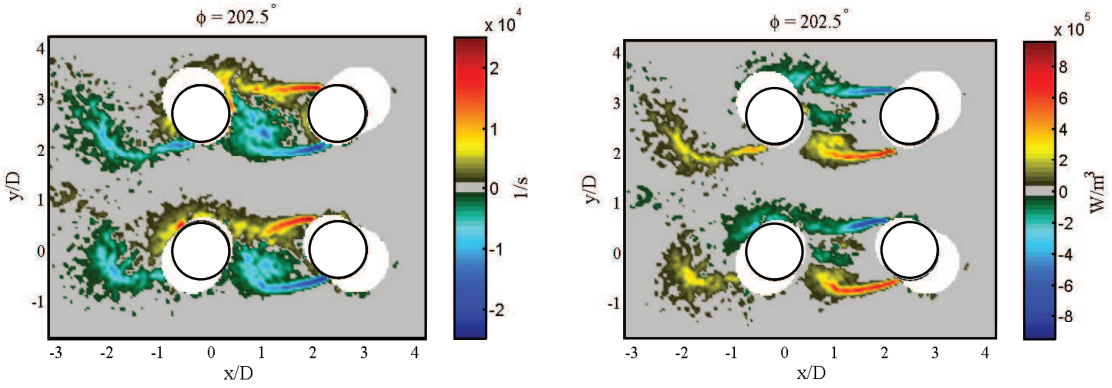

Vorticity Acoustic power

(a) Pre-coincidence acoustic resonance

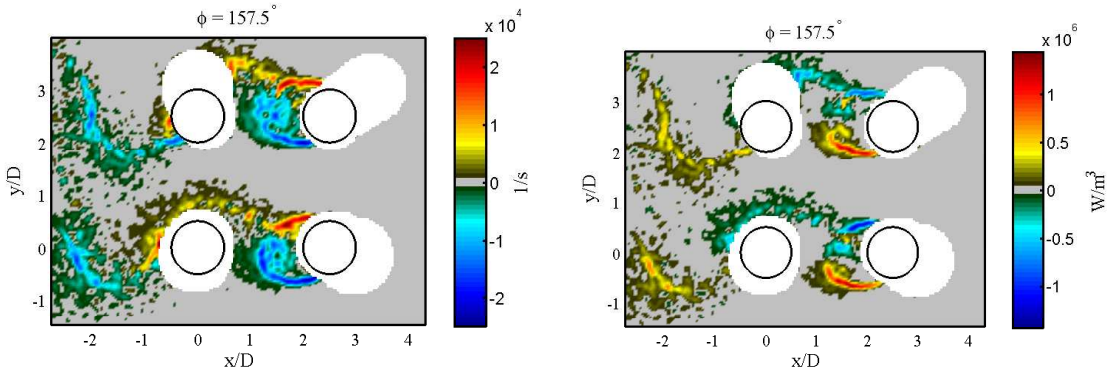

Vorticity Acoustic power

(b) Coincidence acoustic resonance

Figure 6.10: Comparison of the vorticity and acoustic power generated by the four cylinders at $\phi = 202.5°$ for pre-coincidence resonance and at $\phi = 157.5°$ for coincidence resonance. Both of these phases correspond to the maximum generated acoustic power from the cylinders.

Figure 6.10 compares the vorticity and acoustic power generated by the four cylinders at $\phi = 202.5°$ for pre-coincidence resonance and at $\phi = 157.5°$ for coincidence, which is the phase of maximum acoustic power generation for this regime. As can be seen, the location of the sources in the wake of the cylinders are much more aligned which supports that proposition that this phase shift is due to a higher convection velocity in the wake of the cylinders rather than a fundamental change in the mechanism itself. It should be noted that this analysis is slightly restricted by the fact that the PIV field is concentrated around the cylinders. However, as previously shown in Ch. 5, the contribution made by the vortices in the wake of the cylinders beyond the side-branches is continually diminished as they propagate.

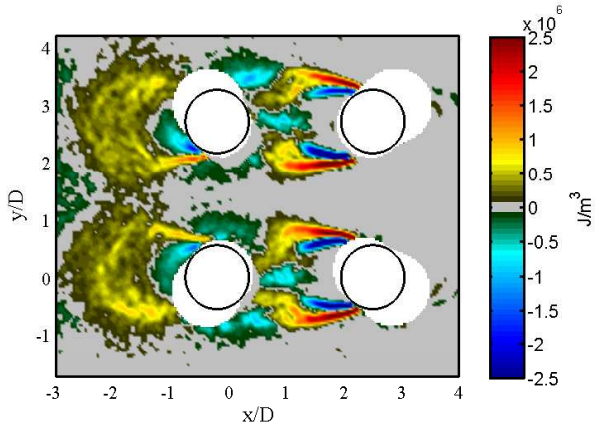

(a) Net acoustic energy per cycle

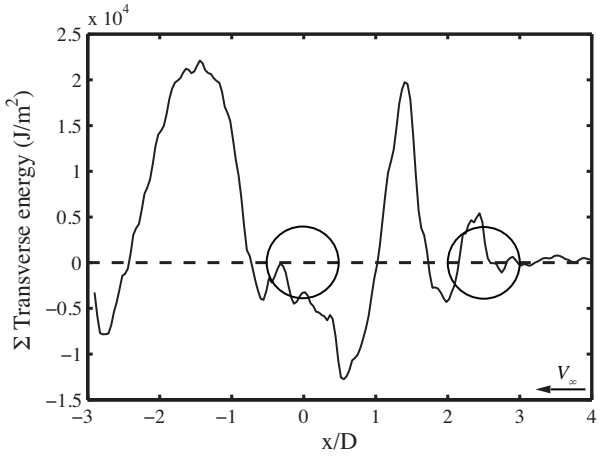

(b) Net acoustic energy transfer per streamwise location per cycle

Figure 6.11: The net acoustic energy distribution per cycle and the net acoustic energy transfer per streamwise location per cycle generated by the four cylinders during pre-coincidence resonance, $f_a/f_v = 1.15$, $\widehat{U}_a/V_\infty = 0.117$.

6.2.5.2 Net acoustic energy

Figure 6.11 shows the spatial distribution of the net acoustic energy and the net energy transfer per streamwise location per cycle during pre-coincidence resonance for the $\widehat{U}_a/V_\infty = 0.117$ case. If the four cylinders are considered to be two pairs of tandem cylinders, the distributions of sources/sinks between them are almost indiscernible. The sources and sinks are symmetric about the centreline of each tandem pair which as before is obviously due to the periodicity of the flow structure. The plot of the net energy transfer indicates that positive acoustic energy is generated roughly at the midpoint between the cylinders and at $x/D \approx -1.75$ in the wake.

This means that pre-coincidence resonance is driven by instability in the shear layers

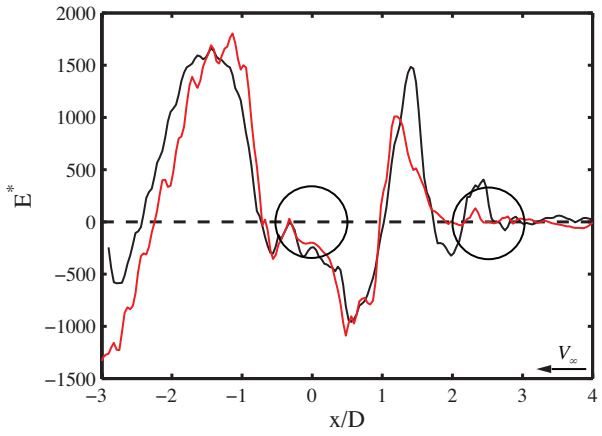

Figure 6.12: Comparison of the normalised net acoustic energy transfer per streamwise location per cycle for the two tested loudspeaker input voltages during pre-coincidence resonance. — $\widehat{U}_a/V_\infty = 0.117$; — $\widehat{U}_a/V_\infty = 0.078$.

and vortex shedding in the wake, which is similar to that observed for two tandem cylinders during pre-coincidence resonance. Figure 6.12 compares the normalised net acoustic energy transfer per streamwise location per cycle for the two loudspeaker voltages during pre-coincidence resonance. Varying the sound pressure level seems to have very little influence on the overall source/sink distribution apart from those in the gap region between the cylinders and in the wake of the wakes of the cylinders. However, given what was observed in the tandem cylinder study, whether or not this is an effect of the SPL or some inconsistency in the experiment is uncertain.

Figure 6.13 shows the spatial distribution of the net acoustic energy and the net energy transfer per stream wise location per cycle during coincidence resonance for the $\widehat{U}_a/V_\infty = 0.108$ case. In the gap region between the cylinders, intense acoustic sources lie in the outer shear layers, hugging two very intense sinks located in the inner shear layers. In the wake region, acoustic sinks surround the immediate vicinity of the downstream cylinders but are dominated by very large sources further downstream. The plot of the net energy transfer indicates that positive acoustic energy is generated just before the midpoint between the cylinders and at $x/D \approx -2$ in the wake. This means that coincidence resonance of the four cylinders is also driven by shear layer instability and vortex shedding in the wake of the cylinders. This is similar to that just described for the pre-coincidence case. Figure 6.14 compares the normalised net acoustic energy transfer per streamwise location per cycle

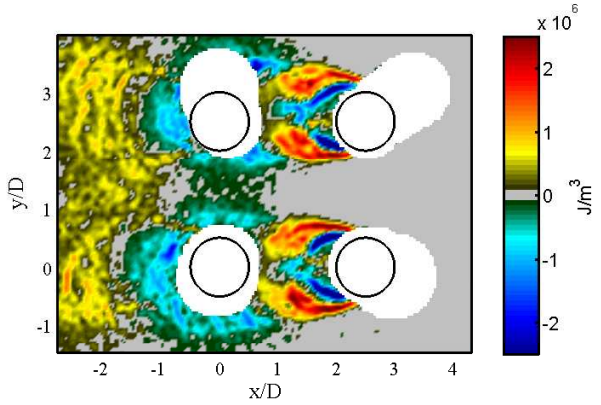

(a) Net acoustic energy per cycle

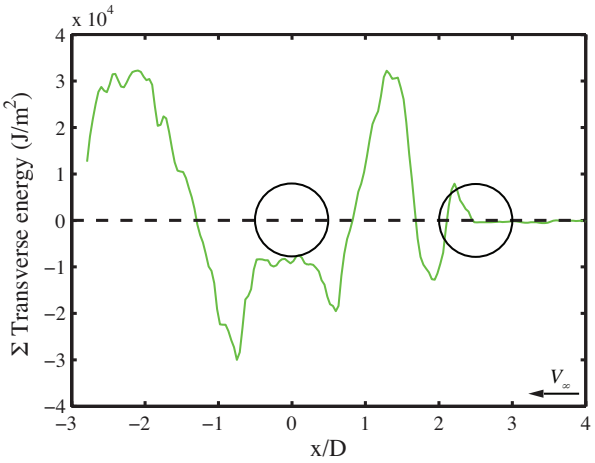

(b) Net acoustic energy transfer per streamwise location per cycle

Figure 6.13: The net acoustic energy distribution and the net acoustic energy transfer per streamwise location per cycle generated by the four cylinders during coincidence resonance, $f_a/f_v = 0.94$, $\widehat{U}_a/V_\infty = 0.108$.

for the two loudspeaker voltages. Varying the loudspeaker voltage has little influence on the acoustic source distribution which is why doubt was cast over the effect it showed at pre-coincidence resonance.

6.3 The effect of transverse spacing

The results presented above are for a four cylinder configuration orientated in a square where the streamwise and transverse spacing ratios are equal, i.e., $P/D = L/D$. There seems to be very little interaction between the vortices shed from one pair of tandem cylinders and those shed from the neighbouring pair. This is particularly evident in the vicinity of the cylinders and in the near wake. Thus, the four cylinders seem to be

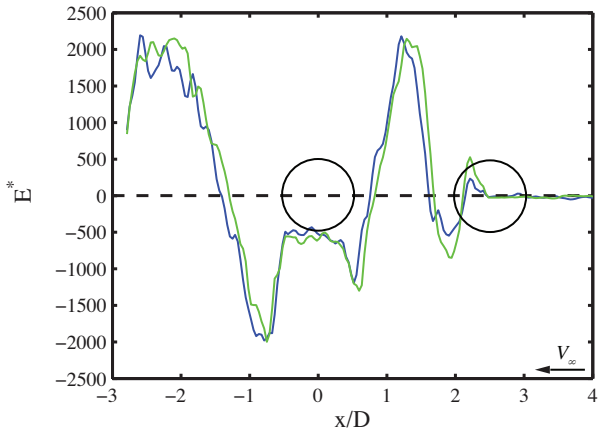

Figure 6.14: Comparison of the normalised net acoustic energy transfer per streamwise location for the two tested loudspeaker input voltages during coincidence resonance. — $\widehat{U}_a/V_\infty = 0.108$; — $\widehat{U}_a/V_\infty = 0.065$.

acting as two independent pairs of tandem cylinders. The fact that there was very little interaction between each pair is most likely due to their large transverse spacing ratio and the fact that the vortices become highly synchronised during resonance. The effect of the transverse spacing ratio (L/D) was investigated to see if it changed the nature of the energy transfer mechanism between the sound field and the flow field. For these tests, the streamwise pitch ratio was kept constant whilst the transverse spacing was varied in steps of 0.25 between $L/D = 1.5$ and $L/D = 2.75$. Tests similar to those described above and in Ch. 5 using microphone M1, hotwire HW2 and PIV were completed.

6.3.1 Microphone and hotwire analysis

Figure 6.15 plots the variation of the Strouhal number with the transverse pitch ratio measured by HW2 for various Reynolds numbers when there was no applied sound. The general trend of the graph is for the Strouhal number to increase as the spacing ratio decreases. Figure 6.6 and Fig. 6.7 showed that when the cylinders have a large spacing ratio, they tend to act as two independent pairs of tandem cylinders during "lock-in". This behaviour is reflected in Fig. 6.15 as the larger spacing ratios have Strouhal numbers comparable to the tandem cylinder configuration. As the spacing ratio gets smaller (and hence the bluffness increases) the four cylinders seem to behave more like a single bluff body. This is highlighted by the fact that the Strouhal number approaches 0.2 as the

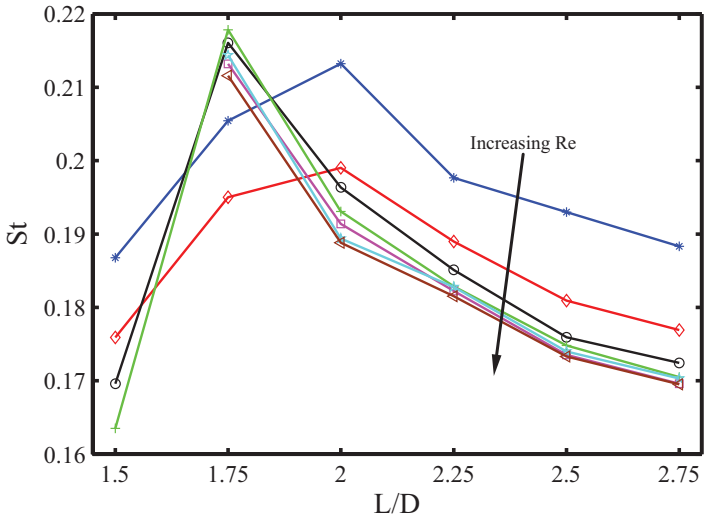

Figure 6.15: Variation of the Strouhal number with the transverse spacing ratio of the four cylinders measured by HW2, $P/D = 2.5$. $*$ $Re \approx 7100$; $\diamond$ $Re \approx 11000$; $\circ$ $Re \approx 15700$; $+$ $Re \approx 20500$; $\square$ $Re \approx 25300$; $\star$ $Re \approx 30000$; $\triangleleft$ $Re \approx 35000$.

pitch ratio decreases and is presumably due to increased interaction of the vortices in the wake of the cylinders. Interestingly, the Strouhal number drops abruptly to lower values (comparable with the larger spacing ratios) when $L/D = 1.5$. It is possible that as the transverse spacing gets very small, the four cylinders return to behaving like a pair of tandem cylinders. This is purely speculative and no other evidence can be provided as this effect was not studied in further detail. However, it would have been interesting to measure the Strouhal number behind the four cylinders as $L/D \rightarrow 1$ (i.e., when there is no transverse gap between the cylinders) as it might have resolved this issue. Another observation from Fig. 6.15 is that the variation of the Strouhal number for a given pitch ratio becomes less dependent on the Reynolds number as it increases. Mohany and Ziada [5] reported that the Strouhal number in the wake of two tandem cylinders becomes independent of Reynolds number for $Re > 5 \times 10^4$. The Reynolds numbers range tested here is well below 5×10^4 but the results seem to indicate that a similar phenomenon will occur here, particularly for the larger spacing ratios.

The mainstream flow velocity was measured for each configuration and no discernible differences were observed for a given fan input voltage. Hence, the variation in the Strouhal number with transverse pitch ratio is due to changes in the vortex shedding frequency. Exactly how this effected the "lock-in" range of the cylinders was investigated

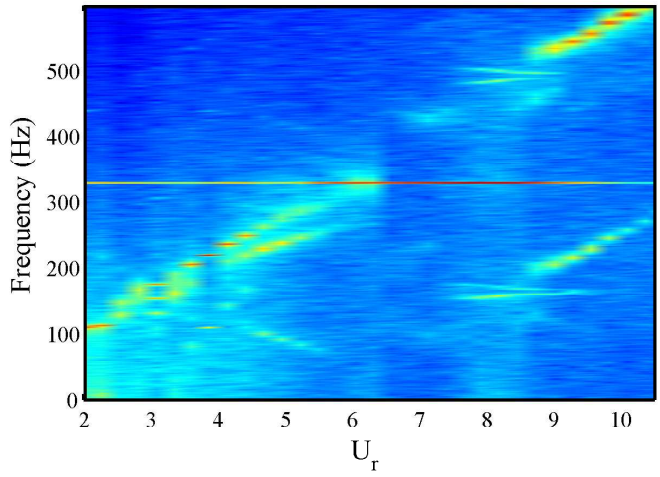

Figure 6.16: Waterfall plot of the vortex shedding frequency measured in the presence of applied sound for the $L/D = 2.25$ configuration, $P/D = 2.5$.

by applying a sound wave from the loudspeaker at a voltage of 425 mV and $f_a = 328$ Hz. Figure 6.16 shows a waterfall plot of the vortex shedding frequency measured by HW2 in the wake of the $L/D = 2.25$ configuration. Using the same criteria as the last section (and that in Ch. 5) indicates that the system remains "locked-in" until $U_r \approx 9$. This is equivalent to a frequency shift of 39%, i.e., $f_a/f_v = 0.61$. Mohany and Ziada [5] and Hall *et al.* [2] both reported large shifts in the vortex shedding frequency comparable to this for two tandem cylinders, see for example Fig. 2.21. However, based on the $P/D = L/D = 2.5$ results, a frequency shift this large for a four cylinder configuration seems unlikely. Similar behaviour was also observed for the smaller pitch ratios. Examining the spectra, what seems to be happening is that the sound wave completely drowns out the vortex shedding process, making it very difficult to determine the "lock-in" based on frequency. Thus, the pressure measured by the microphone was used instead.

Figure 6.17 plots the pressure measured by M1 at $f_a = 328$ Hz versus the reduced velocity for the $L/D = 2$, 2.25, 2.5 and 2.75 configurations. A rise in the acoustic pressure occurs at $U_r \approx 4.43$ whilst a distinct drop in the acoustic pressure occurs $U_r \approx 6.58$. This rise and fall in pressure is assumed to represent the reduced velocities at which "lock-on" and "lock-off" of the four cylinders occurs since they are in good agreement with the "lock-on" and "lock-off" reduced velocities of the $P/D = L/D = 2.5$ configuration. Using the assumption that the four cylinders "lock-on" and lock-off" at these reduced

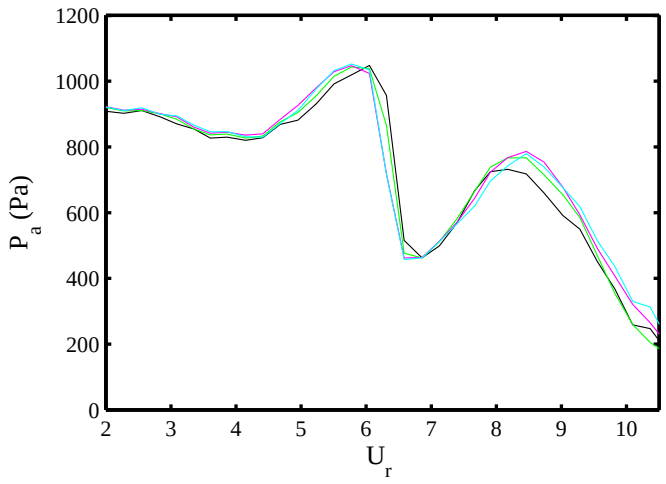

Figure 6.17: The acoustic pressure measured by M1 at the applied loudspeaker frequency, $f_a = 328$ Hz for a range of transverse spacing ratios, $P/D = 2.5$. — $L/D = 2$; — $L/D = 2.25$; — $L/D = 2.5$; — $L/D = 2.75$.

velocities when sound is applied from the loudspeaker, measuring the vortex shedding frequency when there is no applied sound will give an indication of the effect that varying the transverse spacing ratio has on the frequency at which acoustic resonance initiates and subsides.

Figure 6.18 plots the vortex shedding frequency measured by HW2 in the absence of applied sound at $U_r = 4.43$ and $U_r = 6.58$ for the $L/D = 2, 2.25, 2.5$ and 2.75 configurations. Reducing the transverse pitch ratio causes the frequency at which "lock-in" initiates to shift towards higher frequencies, i.e. closer to the natural acoustic frequency. As inferred in Fig. 6.15, the four cylinders behave more like a single bluff body as the pitch ratio decreases. This is evident in Fig. 6.18 as "lock-on" initiates closer to acoustic-Strouhal coincidence as the spacing ratio decreases. Thus the effect of reducing the spacing ratio is to suppress pre-coincidence acoustic resonance and promote coincidence acoustic resonance. Table 6.2 summarises the data plotted in Fig. 6.18. The overall width of the "lock-in" range increases by approximately 10% between $L/D = 2.75$ and $L/D = 2$. However, from Fig. 6.18 the more significant effect of varying the transverse spacing ratio seems to be its influence on the frequency at which "lock-in" initiates and hence the width of the pre-coincidence and coincidence resonance regimes.

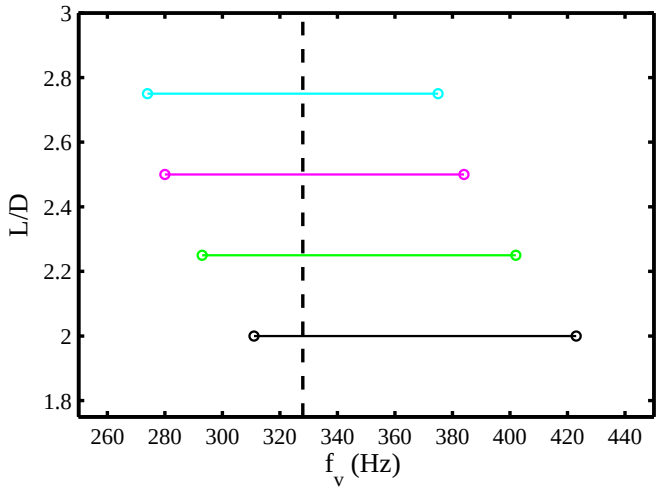

Figure 6.18: The frequency of vortex shedding from the four cylinders at $U_r = 4.43$ and $U_r = 6.58$ in the absence of applied sound, highlighting the effect that the transverse spacing ratio has on the frequency at which acoustic resonance initiates, $P/D = 2.5$. — $L/D = 2$; — $L/D = 2.25$; — $L/D = 2.5$; — $L/D = 2.75$.

Configuration	"Lock-on" Frequency (Hz)	"Lock-off" Frequency (Hz)	Resonance Frequency (Hz)
$P/D = 2.5$, $L/D = 2$	311	423	112
$P/D = 2.5$, $L/D = 2.25$	293	402	109
$P/D = 2.5$, $L/D = 2.5$	280	384	104
$P/D = 2.5$, $L/D = 2.75$	274	375	101

Table 6.2: The frequency of vortex shedding at $U_r = 4.43$ and $U_r = 6.58$ in the absence of applied sound, $P/D = 2.5$.

Configuration	Fan Voltage (V)	V_∞ (m/s)	f_v (Hz)	f_a (Hz)	f_a/f_v
$P/D = 2.5$, $L/D = 2$	5.4	24.4	367	322	0.877
$P/D = 2.5$, $L/D = 2.25$	5.4	24.2	338	322	0.953

Table 6.3: Experimental parameters used to compare the effect of the transverse spacing ratio on the flow-acoustic coupling of four cylinders.

6.3.2 Flow structure/flow-acoustic coupling

The $L/D = 2$ and $L/D = 2.25$ configurations were selected for further testing. For convenience, the same fan input voltage of 5.4 V was used for each test. This corresponded to flow velocities of $V_\infty = 24.4$ m/s and $V_\infty = 24.2$ m/s for the $L/D = 2$ and $L/D = 2.25$ configurations respectively. Table 6.3 lists the experimental parameters for the two configurations. As can be seen, both of the configurations were in coincidence acoustic resonance similar to the $L/D = 2.5$ configuration discussed above. Figure 6.19 compares the flow structure around the four cylinders at $\phi = 0°$ and $\phi = 180°$. The $L/D = 2.5$ configuration is also shown for comparison. Reducing the transverse spacing seems to have an insignificant effect on the distribution of vortices generated by the cylinders at any given phase. As can be seen, there is still very little interaction between the vortices shed by either tandem cylinder pair. The synchronous nature of the vortex shedding is preventing any interaction of neighbouring structures in both the regions around the cylinders and in the wakes. Moreover, moving the cylinders closer together does not seem to encourage interaction between a vortex (shed from one pair of cylinders) and the other pair of cylinders themselves. Figure 6.20 compares the net acoustic energy generated by the $L/D = 2$ and $L/D = 2.25$ configurations. Again, the $L/D = 2.5$ configuration is shown for comparison.

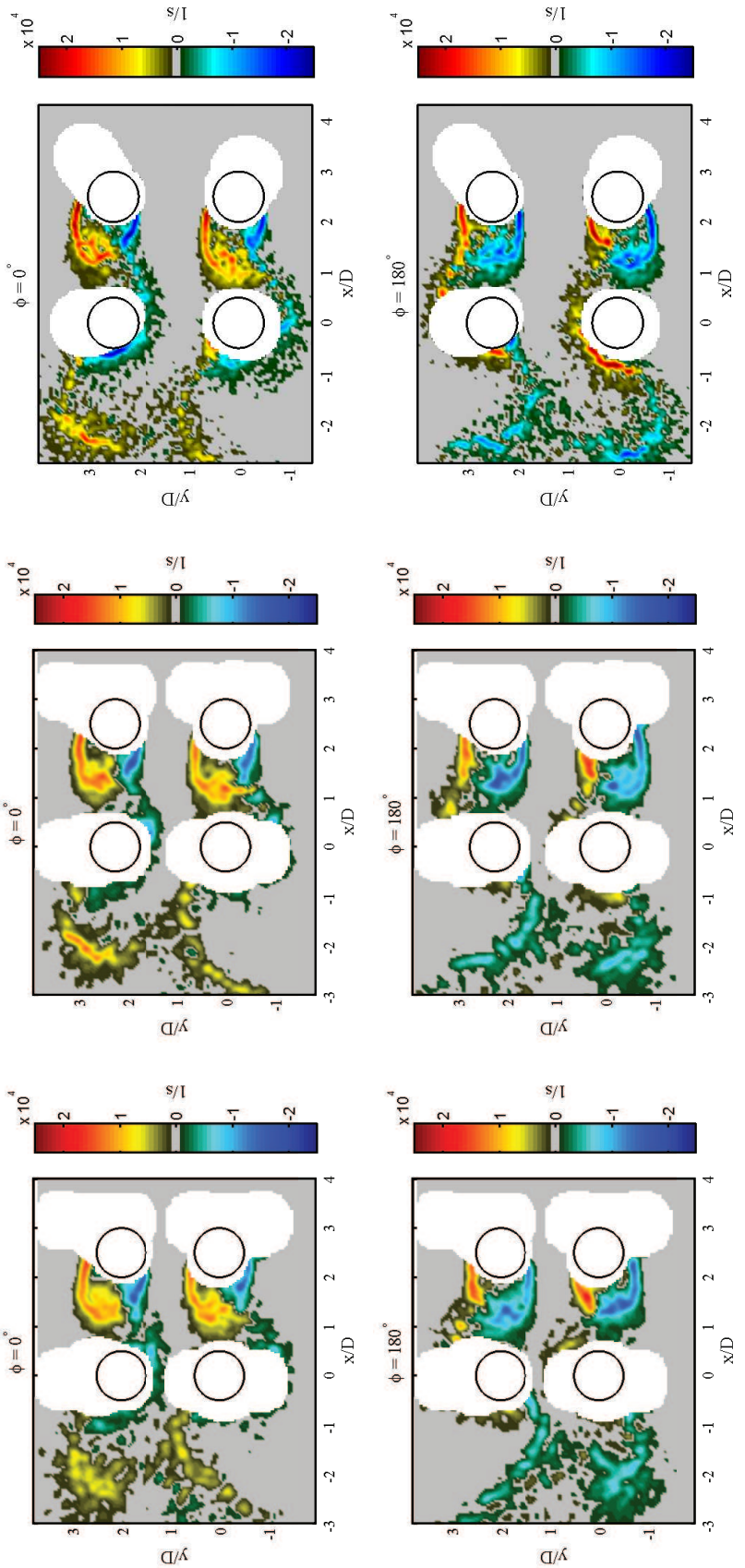

(a) $L/D = 2$ (b) $L/D = 2.25$ (c) $L/D = 2.5$

Figure 6.19: Comparison of the flow structure around the four cylinders at $\phi = 0°$ and $\phi = 180°$ for the three tested transverse spacing ratios, $P/D = 2.5$.

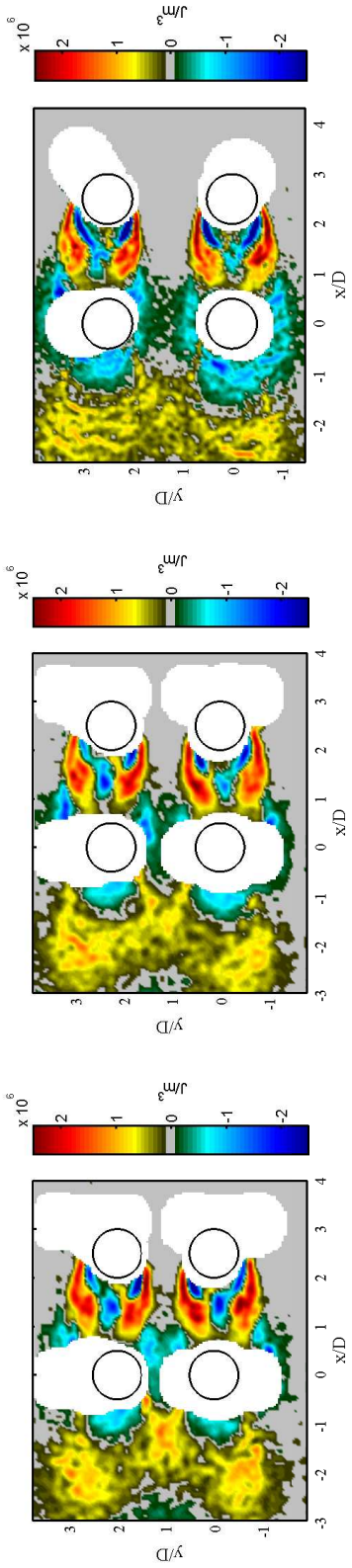

(a) $L/D = 2$ (b) $L/D = 2.25$ (c) $L/D = 2.5$

Figure 6.20: Comparison of the net acoustic energy per cycle generated by the four cylinders for the three tested transverse spacing ratios, $P/D = 2.5$.

6.4 The effect of streamwise spacing

The results presented thus far have only concentrated on a single streamwise spacing ratio, $P/D = 2.5$. It was discussed in Ch. 2 that the streamwise pitch ratio of a tandem cylinder configuration (as well as an inline array) has a substantial influence on the flow structure. Therefore, it should also have a substantial effect on the energy transfer mechanism between the flow field and the sound field. Thus, an investigation of the streamwise pitch ratio was completed. A configuration with $P/D = 3$ was selected. The tests were similar to those just described as the effect of the transverse spacing ratio between $L/D = 1.5$ and $L/D = 2.75$ was investigated as well.

6.4.1 Microphone and hotwire analysis

Figure 6.21 plots the variation of the Strouhal number with the transverse spacing ratio measured by HW2 for various Reynolds numbers when there was no sound applied by the loudspeaker. The general trend shown in this graph is similar to that of Fig. 6.15 in that the Strouhal number for a given Reynolds number increases as the transverse pitch ratio decreases. Therefore the observation made in the previous section about how reducing the transverse pitch ratio of the cylinders encourages the system to behave more like a single bluff body seems to be valid. Interestingly, the abrupt drop in the Strouhal number to lower values when the transverse spacing ratio is reduced to $L/D = 1.5$ (which was observed for the $P/D = 2.5$ configurations) does not occur. Also, the Strouhal number does not decrease with Reynolds number. In general, it increases.

The mainstream flow velocity was measured for each configuration and no discernible differences were observed for a given fan input voltage. This means that the variation in the Strouhal number with transverse pitch ratio noticed in Fig. 6.21 is due to changes in the vortex shedding frequency. Exactly how this effected the "lock-in" range of the cylinders was investigated by applying a sound wave from the loudspeaker at a voltage of 425 mV and a frequency $f_a = 328$ Hz. As before, determination of the "lock-in" range was not based on frequency but rather on pressure. Figure 6.22 plots the acoustic pressure measured by M1 at $f_a = 328$ Hz for the $L/D = 2, 2.25, 2.5$ and 2.75 configurations. A rise in the acoustic pressure occurs at $U_r = 4.91$ whilst a distinct drop in the acoustic pressure

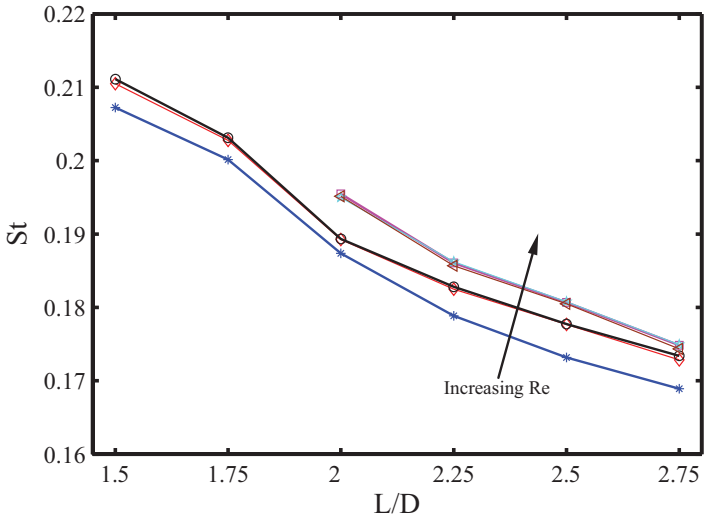

Figure 6.21: Variation of the Strouhal number with the transverse spacing ratio of the four cylinders measured by HW2, $P/D = 3$. $*$ $Re \approx 7800$; $\diamond$ $Re \approx 11400$; $\circ$ $Re \approx 15200$; $\square$ $Re \approx 24600$; $\star$ $Re \approx 30200$; $\triangleleft$ $Re \approx 34000$.

occurs $U_r = 6.77$. Both values show good agreement with the "lock-on" and "lock-off" reduced velocities of the $P/D = 2.5$ configurations and it is concluded that they represent the reduced velocities at which acoustic resonance initiates and subsides.

Figure 6.23 plots the vortex shedding frequency measured by HW2 in the absence of applied sound at $U_r = 4.91$ and $U_r = 6.77$ for the $L/D = 2, 2.25, 2.5$ and 2.75 configurations. Reducing the transverse pitch ratio increases frequency at which "lock-on" initiates. This is similar to what was observed in Fig. 6.18. In fact, for the $L/D = 2$ configuration, resonance initiates at acoustic-Strouhal coincidence. Table 6.4 summarises the data plotted in Fig. 6.23. Any change in the overall width of the "lock-in" range caused by varying the transverse spacing ratio is less significant compared to its influence on the frequency at which resonance initially occurs and hence its effect on the width of the pre-coincidence and coincidence resonance regimes.

6.4.2 Flow structure/flow-acoustic coupling

The $L/D = 2$ and $L/D = 2.25$ configurations were selected for further testing. For convenience, it was decided to select the same fan input voltage of 5.4 V for each test. This corresponded to flow velocities of $V_\infty \approx 23$ m/s for both configurations. Table 6.5 lists the experimental parameters for the two configurations.

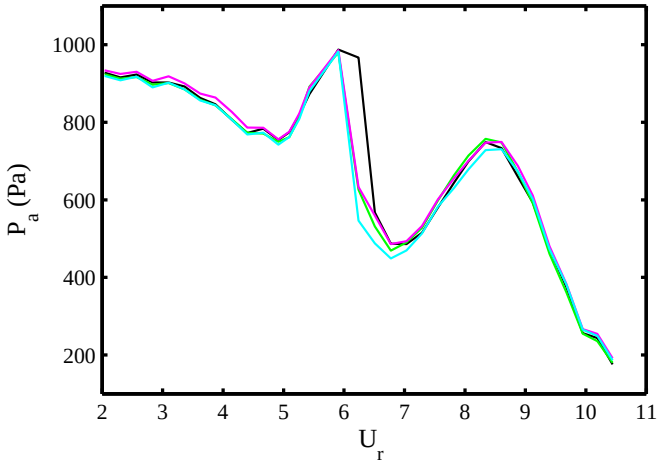

Figure 6.22: The acoustic pressure measured by M1 at the applied loudspeaker frequency, $f_a = 328$ Hz for a range of transverse spacing ratios, $P/D = 3$. — $L/D = 2$; — $L/D = 2.25$; — $L/D = 2.5$; — $L/D = 2.75$.

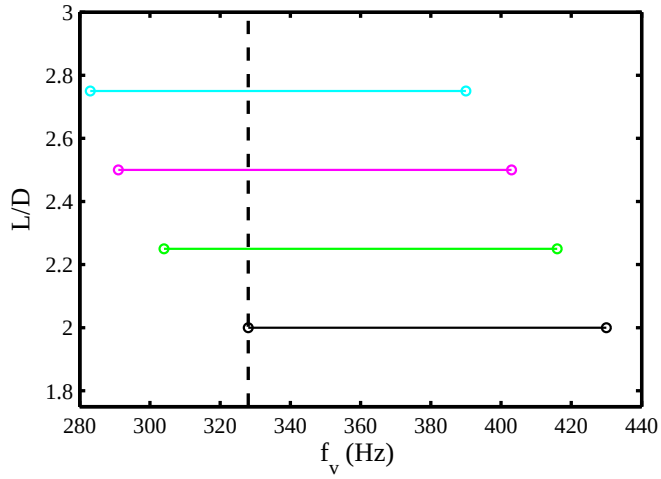

Figure 6.23: The frequency of vortex shedding from the four cylinders at $U_r = 4.91$ and $U_r = 6.77$ in the absence of applied sound, highlighting the effect that the transverse spacing ratio has on the resonant frequency range, $P/D = 3$. — $L/D = 2$; — $L/D = 2.25$; — $L/D = 2.5$; — $L/D = 2.75$.

Configuration	"Lock-on" Frequency (Hz)	"Lock-off" Frequency (Hz)	Resonance Frequency (Hz)
$P/D = 3$, $L/D = 2$	328	430	102
$P/D = 3$, $L/D = 2.25$	304	416	112
$P/D = 3$, $L/D = 2.5$	291	403	112
$P/D = 3$, $L/D = 2.75$	283	390	107

Table 6.4: The frequency of vortex shedding at $U_r = 4.91$ and $U_r = 6.77$ in the absence of applied sound, $P/D = 3$.

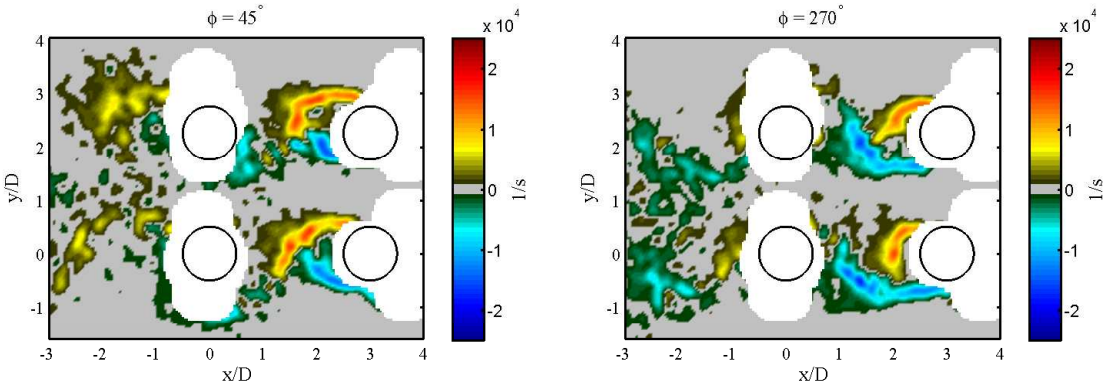

(a) $P/D = 3$

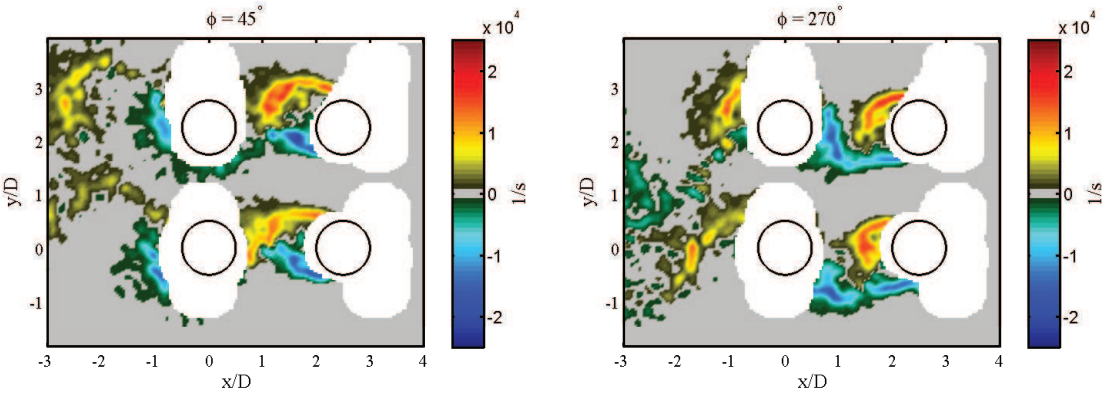

(b) $P/D = 2.5$

Figure 6.24: Comparison of the flow structure around the $P/D = 3$, $L/D = 2.25$ configuration with the $P/D = 2.5$, $L/D = 2.25$ configuration at $\phi = 45°$ and $\phi = 270°$.

Configuration	Fan Voltage (V)	V_∞ (m/s)	f_v (Hz)	f_a (Hz)	f_a/f_v
$P/D = 3$, $L/D = 2$	5.4	23.21	339	322	0.94
$P/D = 3$, $L/D = 2.25$	5.4	23.21	330	322	0.97

Table 6.5: Experimental parameters used to compare the effect of the streamwise spacing ratio on the flow-acoustic coupling of four cylinders.

As can be seen, both of the configurations were in coincidence acoustic resonance as $f_a/f_v < 1$. Figure 6.24 compares the flow structure around the $P/D = 3$ configuration with the $P/D = 2.5$ configuration at $\phi = 45°$ and $\phi = 270°$. The transverse spacing ratio in both Fig. 6.24(a) and Fig. 6.24(b) is $L/D = 2.25$. At $\phi = 45°$ the flow structure between the two configurations is similar in that the dominant vortices propagating in the gap regions are formed from the top sides of the cylinders. Moreover, at this phase, the vortices in both cases have travelled approximately 1.3 diameters from upstream cylinders which means they are developing at roughly the same rate. The difference between the two cases is that the vortices in the $P/D = 2.5$ configuration are just about to impinge on the downstream cylinders whilst the vortices in the $P/D = 3$ configuration are only about to reach the mid-point. A similar situation can be seen at $\phi = 270°$ where the dominant vortices in the gaps are shed from the bottom sides of the cylinders. The same observations were made for the $L/D = 2$ configuration.

The extra space, affords the vortices in the gap regions more time to develop which means they will be stronger by the time they impinge on the downstream cylinders and hence will have a stronger contribution the energy transfer mechanism. The acoustic power generated by the $P/D = 3$, $L/D = 2.25$ configuration at $\phi = 22.5°$, $\phi = 112.5°$, $\phi = 202.5°$ and $\phi = 292.5°$ can be seen in Fig. 6.25(a). Figure 6.25(b) shows the acoustic power generated by the $P/D = 2.5$, $L/D = 2.25$ configuration for comparison. The distributions of the acoustic power for a given phase are fairly similar between the two configurations. The main difference is that for the $P/D = 3$ configuration, acoustic sinks form in front of the downstream cylinders whereas in the $P/D = 2.5$ configuration, they form at the cylinder surface. This can be attributed to the fact that the downstream cylinders in the $P/D = 3$ configuration are an extra half diameter downstream from the upstream cylinders compared to the $P/D = 2.5$ configuration. These sinks will have a net negative contribution to the acoustic resonance.

Figure 6.26 compares the net acoustic energy generated by the $P/D = 3$ configurations with the $P/D = 2.5$ configurations. The overall source/sink distributions are fairly similar. The main difference is that the sinks which surround the downstream cylinders in the $P/D = 2.5$ configurations are located in the gap region for the $P/D = 3$ configurations.

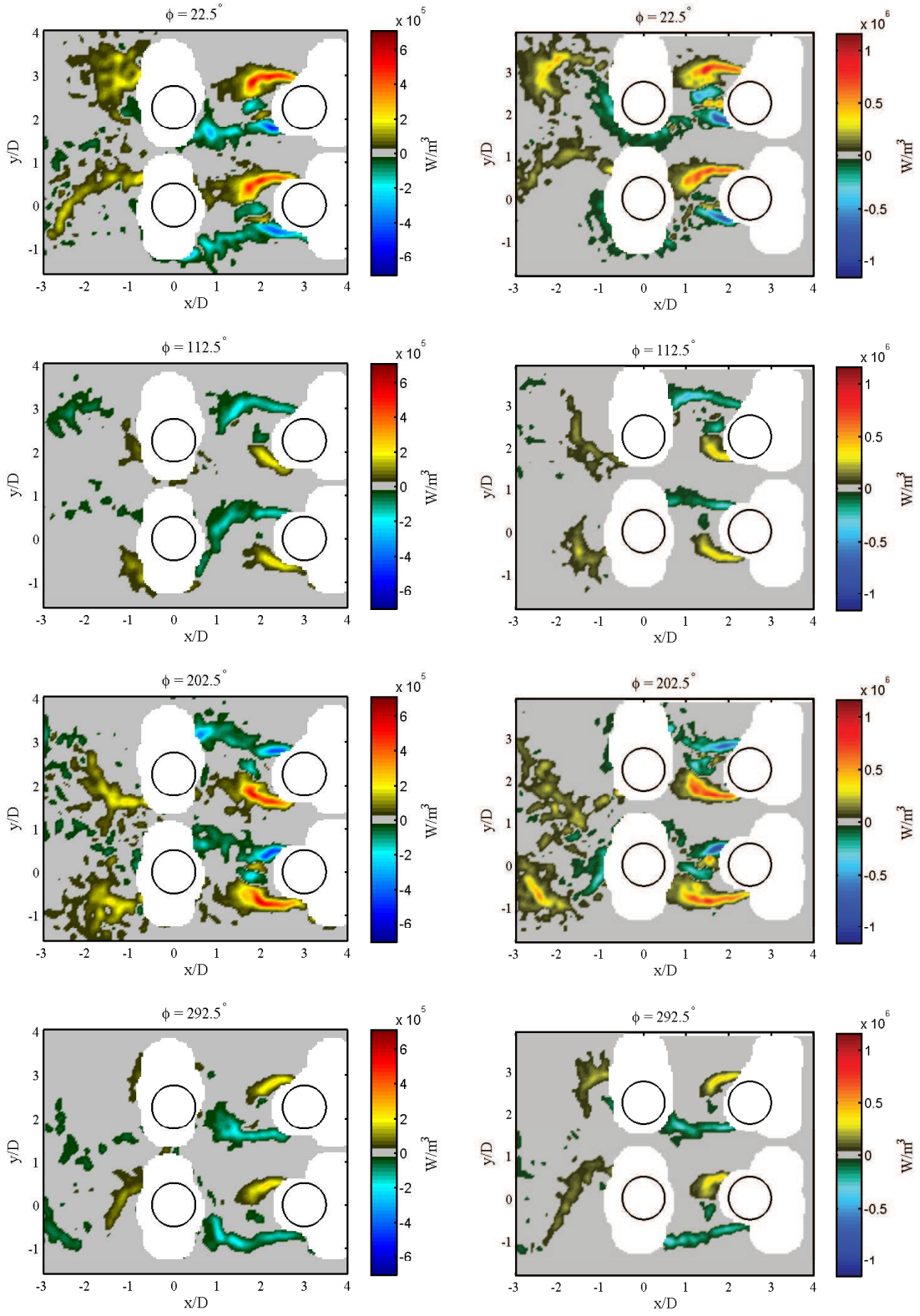

(a) $P/D = 3$ (b) $P/D = 2.5$

Figure 6.25: Comparison of the acoustic power generated by the $P/D = 3$, $L/D = 2.25$ configuration with the $P/D = 2.5$, $L/D = 2.25$ configuration at $\phi = 22.5°$, $\phi = 112.5°$, $\phi = 202.5°$ and $\phi = 292.5°$.

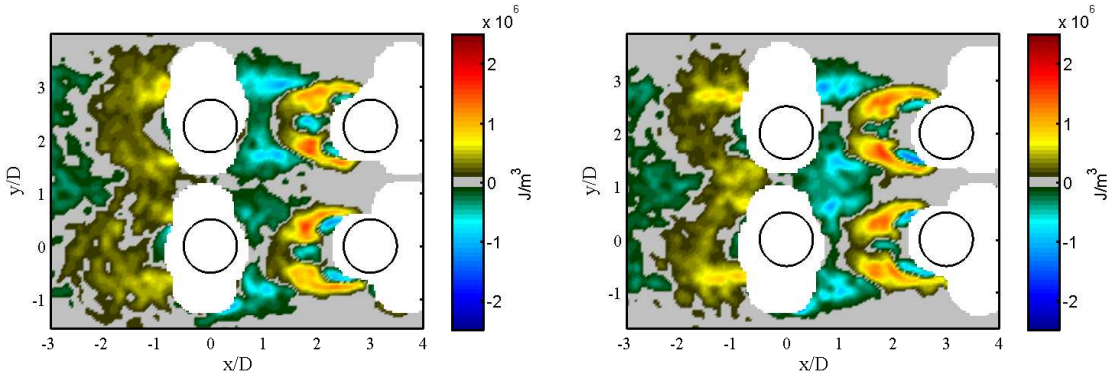

$L/D = 2.25$ $L/D = 2$

(a) $P/D = 3$

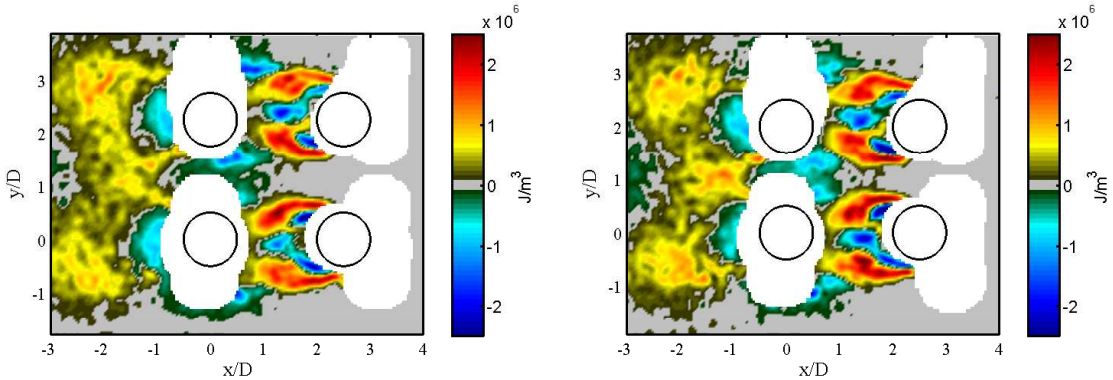

$L/D = 2.25$ $L/D = 2$

(b) $P/D = 2.5$

Figure 6.26: Comparison of the net acoustic energy per cycle generated by the $P/D = 3$ configurations with the $P/D = 2.5$ configurations.

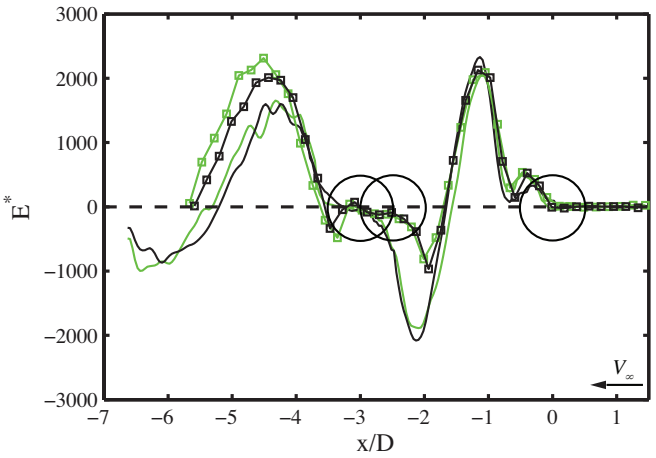

Figure 6.27: Comparison of E^* as a function of distance from the upstream cylinder generated by the $P/D = 3$ (solid lines) and $P/D = 2.5$ (square data tips) configurations. — $L/D = 2$; — $L/D = 2.25$.

L/D / P/D	1.5	1.75	2	2.25	2.5	2.75	U_r
2.5	981	1046	1048	1038	1023	1052	5.9
3	888	861	865	888	895	910	5.86

Table 6.6: Pressure (Pa) measured by M1 for the same loudspeaker voltage, 425 mV.

The normalised net acoustic energy transfer per streamwise location per cycle as a function of distance from the upstream cylinders can be seen Fig. 6.27 for the $P/D = 3$ configurations. The $P/D = 2.5$ configurations are overlaid for comparison and are represented by the square data tips. The locations of the peak sources/sinks are nearly identical for all cases. This means that varying the streamwise pitch ratio only alters the contribution that each source or sink has on the generation of acoustic resonance rather than altering the actual generation mechanism itself. The $P/D = 3$ configurations show significantly stronger sinks in the gap region and weaker sources in the wake compared to the $P/D = 2.5$ configurations. Therefore, the effect of increasing the transverse pitch ratio from $P/D = 2.5$ to $P/D = 3$ is to reduce the strength of the acoustic resonance. This is also evident in Tab. 6.6 which compares the acoustic pressure measured by M1 for the different configurations at similar reduced velocities. As can be seen, the pressure recorded for the $P/D = 3$ configurations is clearly much lower than that of the $P/D = 2.5$ configurations.

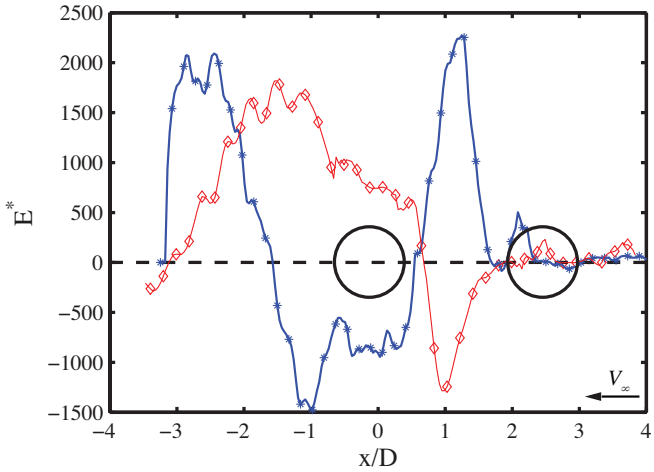

	Configuration	Resonance case	f_a/f_v	U_r
*	4 cylinders	Coincidence	0.94	5.93
◇	2 cylinders	Coincidence	0.86	7.7

Figure 6.28: Comparison of the normalised net acoustic energy transfer per streamwise location per cycle between the four cylinders orientated in a square and two tandem cylinders during coincidence resonance.

6.5 Comparison with two tandem cylinders

From the microphone and hotwire analysis, it seems as if the four cylinders are behaving like two pairs of two tandem cylinders in that they exhibit pre-coincidence acoustic resonance and coincidence acoustic resonance. The PIV analysis revealed that both pre-coincidence and coincidence acoustic resonance is generated by vortex shedding in gap region between the four cylinders and in their near wake. For pre-coincidence resonance, this is consistent with the observations made for two tandem cylinders. However, for coincidence resonance, this is not consistent with the observations made for two tandem cylinders. Figure 6.28 compares the normalised net acoustic energy transfer per streamwise location per cycle for the $P/D = L/D = 2.5$ four cylinder configuration with the $P/D = 2.5$ tandem cylinder configuration during coincidence resonance. The accompanying table describes the experimental parameters. Based on frequency ratio, both cases are clearly in coincidence acoustic resonance. However, they show completely different profiles and are not consistent because the source distribution generated by the four cylinders more closely resembles pre-coincidence of two tandem cylinders rather than coincidence resonance of two tandem cylinders.

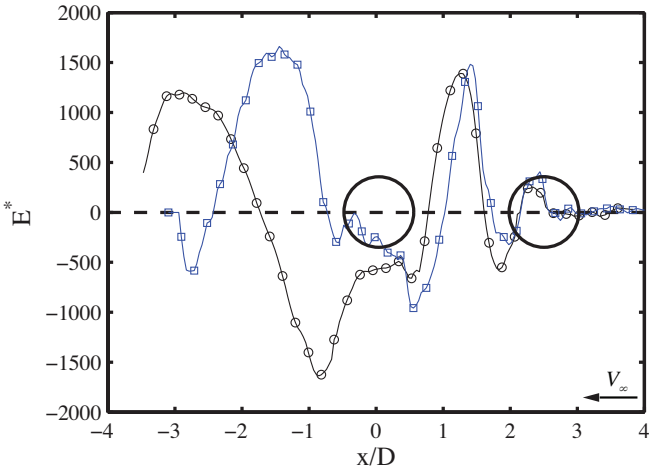

	Configuration	Resonance case	f_a/f_v	U_r
□	4 cylinders	Pre-coincidence	1.15	4.85
○	2 cylinders	Pre-coincidence	1.12	5.9

Figure 6.29: Comparison of the normalised net acoustic energy transfer per streamwise location per cycle between the four cylinders orientated in a square and two tandem cylinders.

Figure 6.29 compares the normalised net acoustic energy transfer per streamwise location per cycle for the $P/D = L/D = 2.5$ four cylinder configuration with the $P/D = 2.5$ tandem cylinder configuration during pre-coincidence resonance. Based on frequency ratio, the accompanying table suggests the acoustic resonance regimes are nearly the same. Moreover, the profiles show good consistency as net acoustic energy is generated in the gap region between the cylinders and in the wake of the cylinders for both configurations. However, there is one significant difference. The peak sources in the wake of the tandem cylinders form further downstream compared to the four cylinder configuration. As already shown in Fig. 6.10, a higher convection velocity in the wake of the cylinders causes the peak sources to form further downstream. The accompanying table in Fig. 6.29 clearly shows that the reduced velocity of the tandem cylinder configuration is higher than the four cylinder configuration and hence explains why the sources form further downstream.

A comparison of the velocities at which "lock-in" occurs for the two configurations can be seen in Fig. 6.30. It shows the vortex shedding frequency versus reduced velocity measured by microphone M1 for the four cylinders and the two tandem cylinders. As can be seen, they follow separate Strouhal dependencies and the resonances initiate and

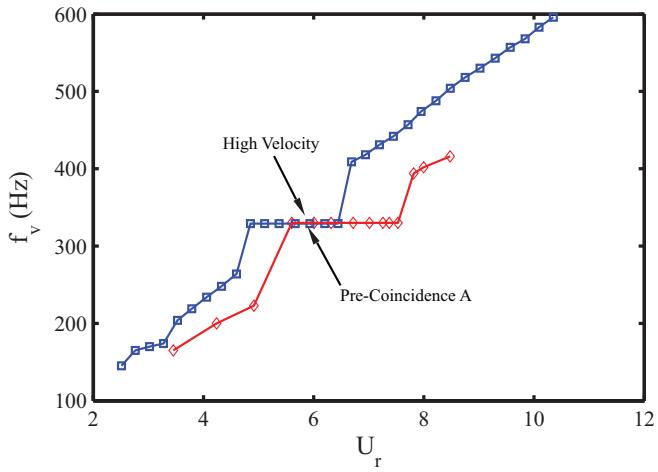

Figure 6.30: Comparison vortex shedding frequency versus reduced velocity measured by M1 for different cylinder configurations. □ Four cylinders $P/D = L/D = 2.5$; ◇ Two tandem cylinders $P/D = 2.5$.

subside at very different reduced velocities. However, an overlap between the velocities at which pre-coincidence resonance of the two tandem cylinders and coincidence resonance of the four cylinders happens to occur and since the geometries of the two configurations are similar, it is not unreasonable to assume that underlying flow structure will also be similar. If the underlying flow structures are similar, the generation of acoustic sources and sinks must also be similar. Figure 6.31 confirms this suggestion. It reproduces the data of Fig. 6.28 and also plots the normalised net energy transfer per streamwise location per cycle generated by the two tandem cylinders during pre-coincidence for comparison. Apart from relative magnitudes, the distributions between the four cylinders during coincidence resonance and the two tandem cylinders during pre-coincidence show remarkable similarity. The frequency ratios in the accompanying table suggest that they are in very different resonance regimes. However, the profiles and the reduced velocities suggests otherwise.

Since the spacing ratio between the four cylinders was quite large, it was initially assumed that the mechanisms generating pre-coincidence resonance and coincidence resonance would be similar, regardless of geometric configuration. This assumption was based solely on the frequency ratio. However, as the results show this is clearly not the case and the four cylinders cannot be considered to be two pairs of tandem cylinders. It seems that frequency ratio alone is a poor way of differentiating between pre-coincidence and

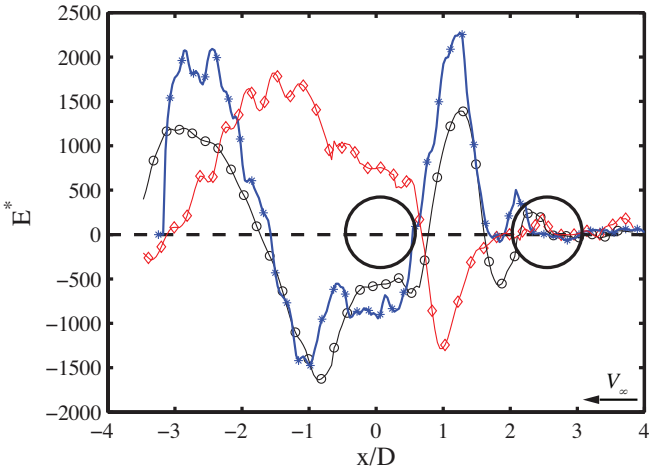

	Configuration	Resonance case	f_a/f_v	U_r
*	4 cylinders	Coincidence	0.94	5.93
○	2 cylinders	Pre-coincidence	1.12	5.9
◇	2 cylinders	Coincidence	0.86	7.7

Figure 6.31: Comparison of the normalised net acoustic energy transfer per streamwise location per cycle between four cylinders orientated in a square and two tandem cylinders.

coincidence resonance flow regimes, particularly when comparing bluff bodies with different geometries. Extra classification is needed. Exactly what extra information would be helpful is not clear in general. Based on Fig. 6.28, Fig. 6.29, Fig. 6.30 and Fig. 6.31 the convection velocity of the vortices in the wake of the cylinders seems to be a good candidate.

6.6 Summary

In this chapter, a study of the flow-acoustic coupling around a group of four cylinders subject to ducted flow has been presented. The four cylinders posed a significant increase in the geometrical complexity compared to that of the two tandem cylinders and served as an important link in moving towards an inline tube bundle. To allow for the larger field of view that needed to be illuminated, a hard wall blank was installed at the end of one of the side-branches and acoustic resonance was forced via one loudspeaker only. Various experimental parameters such as the effect of sound pressure level and spacing were studied. The main conclusions to be drawn from this chapter are:

- The acoustic response of four cylinders orientated in a square is similar to that of two tandem cylinders in that an applied acoustic excitation can induce "lock-in" before and after acoustic-Strouhal coincidence.

- Pre-coincidence resonance is driven by vortex shedding in the gap region between the cylinders and by vortex shedding in the wake of the cylinders which is similar to that observed for two tandem cylinders. The vortices shed from an upstream/downstream cylinder pair are synchronised and in-phase with each other. Moreover, the vortices shed from any given upstream/downstream pair are synchronised with those shed from the other upstream/downstream pair.

- Coincidence resonance is also driven by vortex shedding in the gap region between the cylinders and in the wake of the cylinders. As with pre-coincidence, the flow field is highly synchronous. This is different from that observed for two tandem cylinders. This difference is due to the fact that the mainstream flow velocity at which coincidence resonance of the four cylinders occurs is significantly lower than that of the two tandem cylinders. In fact, the flow velocities at which tandem cylinder pre-coincidence resonance occur, overlap with that of four cylinder coincidence resonance.

- Pre-coincidence and coincidence acoustic resonance of four cylinders are generated by similar mechanisms. However, the dominant sources in the wakes of the cylinders form further downstream in the coincidence case. This implies that the convection velocity of the vortices in the wake of the cylinders is an important parameter in deciphering between pre-coincidence and coincidence acoustic resonance. It should be used in conjunction with the frequency ratio.

- The main effect of reducing the transverse spacing ratio is to shift the "lock-in" range to higher frequencies. Configurations with smaller spacing ratios seem to behave like a single bluff body in that resonance is induced closer to acoustic-Strouhal coincidence thereby suppressing the pre-coincidence resonance regime.

- The main effect of varying the streamwise spacing ratio is to alter the relative contribution that the sources/sinks have in the generation of acoustic resonance rather

than altering the physical mechanisms themselves. A larger spacing ratio affords the vortices in the gap region more time to develop which means their contribution to the energy transfer mechanism will be more significant. For the configurations tested here, increasing the streamwise spacing ratio weakened the acoustic resonance.

- When the system is "locked-in", the amplitude of the acoustic particle velocity has a negligible effect on the distribution of the acoustic sources/sinks. It simply acts as a linear scaling factor of their magnitudes.

Chapter 7

Case 3 : Inline Tube Bundles

7.1 Introduction

In Ch. 5 and Ch. 6 , the energy transfer mechanism between the flow field and the sound field was presented for two tandem cylinders and a group of four cylinders. This chapter describes the final case that was studied: the inline tube bundle. The existence of acoustic resonance for a given inline tube array is dependent on many factors, a significant one being the geometric spacing of the cylinders. Table 2.1 summarised whether a particular inline tube bundle resonated as found experimentally by Blevins and Bressler [28] and also compared if the damping criteria proposed by various authors predicted resonance. This table was used as a reference when selecting which spacing to investigate. Table 7.1 outlines the three inline tube bundles that were studied in this work. Blevins and Bressler [28] observed resonance of the both the $P/D = 3$, $L/D = 3$ and $P/D = 3$, $L/D = 1.5$ configurations in their experiments. Moreover, all of the damping models listed in Tab. 2.1 also predicted acoustic resonance. The $P/D = 2.5$ and $L/D = 2.5$ was not studied by Blevins and Bressler [28] but was chosen as an extension of the two tandem and four cylinder studies. Figure 7.1 shows a schematic of the adopted layout and coordinate reference system. It should be noted that no half tubes were used.

Configuration	P (mm)	L (mm)	D (mm)	No. Tubes	No. Rows	No. Columns
$P/D = 2.5$, $L/D = 2.5$	32.5	32.5	13	16	4	4
$P/D = 3$, $L/D = 1.5$	39	19.5	13	24	4	6
$P/D = 3$,$L/D = 3$	39	39	13	12	4	3

Table 7.1: Geometric definition of the tested inline tube arrays.

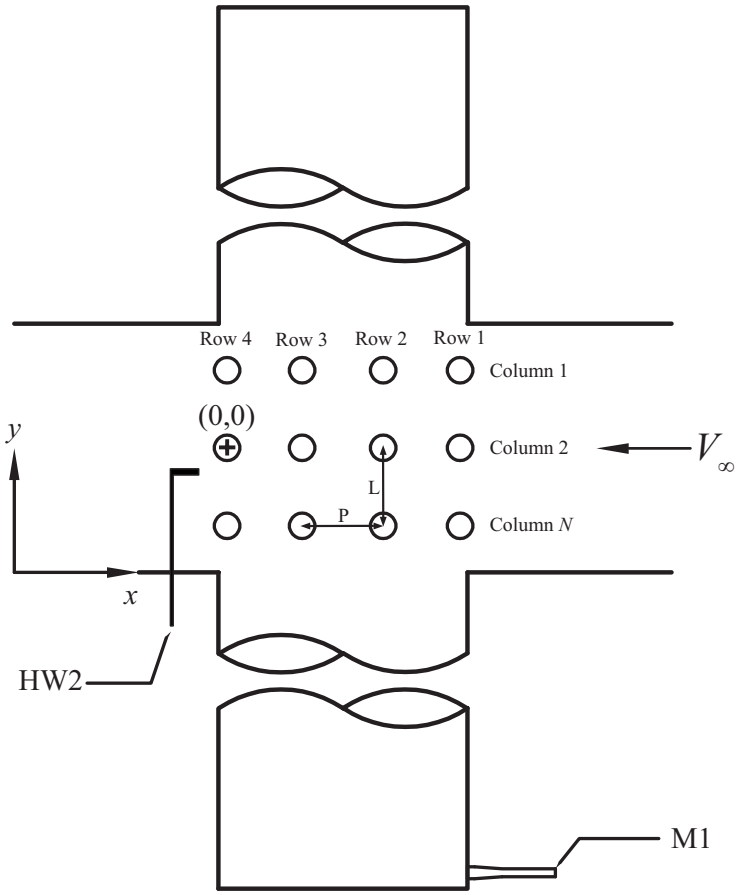

Figure 7.1: Schematic definition of the inline tube bundle geometric parameters.

7.2 Aeroacoustic response

7.2.1 Microphone and hotwire analysis

Many texts have reported that the noise emitted from a tube bundle can exceed deafening levels when resonating. Since Tab. 2.1 indicates that at least two of the selected configurations should resonate, it was decided to remove the loudspeakers from the side-branches and investigate their natural response. As in Ch. 5 and Ch. 6, the mainstream velocity for a given fan voltage when the cylinders are installed is lower than that observed for a clean duct. Furthermore, the mainstream velocity for a given fan voltage will be lower when the tube bundle is installed compared to the other configurations. This is due to the significantly increased blockage the upstream flow encounters. Figure 7.2 shows the upstream velocities recorded with the pitot tube for a given fan voltage. It is clear that as the transverse pitch ratio between neighbouring cylinders gets smaller, so too does

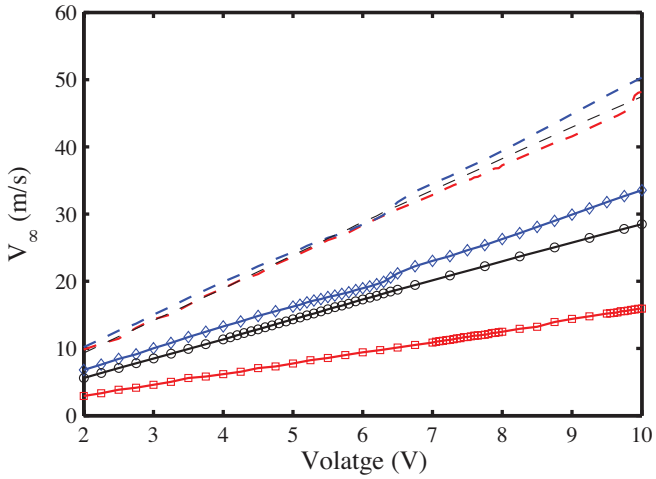

Figure 7.2: The relationship between the fan input voltage and the mainstream velocity measured upstream of the tube bundles. Dashed lines represent gap velocity V_g. □ $P/D = 3$, $L/D = 1.5$; ○ $P/D = 2.5$, $L/D = 2.5$; ◇ $P/D = 3$, $L/D = 3$.

the upstream velocity measured by the pitot tube for a given voltage. These velocities were measured by the pitot tube when the applied voltage to the fan was randomised to eliminate hysteresis.

The pitot tube was removed and tests were completed. Figure 7.3 shows the aeroacoustic response of the $P/D = 2.5$, $L/D = 2.5$ configuration, which according to Oengören and Ziada [34] has an intermediate streamwise spacing ratio. Figure 7.3(a) shows the acoustic pressure measured by M1. Figure 7.3(b) shows the frequency spectra measured by HW2. The hotwire was located behind the fourth row of cylinders in the wake of the array and had a transverse position nominally in the shear layer of the second column. The Strouhal peak increases with flow velocity until roughly $V_\infty = 14$ m/s after which a strong "lock-in" is initiated. The frequency of vortex shedding jumps up to a value of $f_v = 303$ Hz and is accompanied by a sudden increase in the acoustic pressure measured by M1. The system remains "locked-in" until roughly $V_\infty = 18$ m/s after which the acoustic pressure experiences a sudden drop and the vortex shedding frequency detected from the hotwire marches on with velocity. A line connecting the Strouhal dependencies before and after "lock-in" suggests that the resonance subsides near acoustic-Strouhal coincidence. In other words, the $P/D = 2.5$, $L/D = 2.5$ configuration experiences pre-coincidence resonance but not coincidence resonance.

Considering that this configuration is an intermediately spaced tube array, this finding

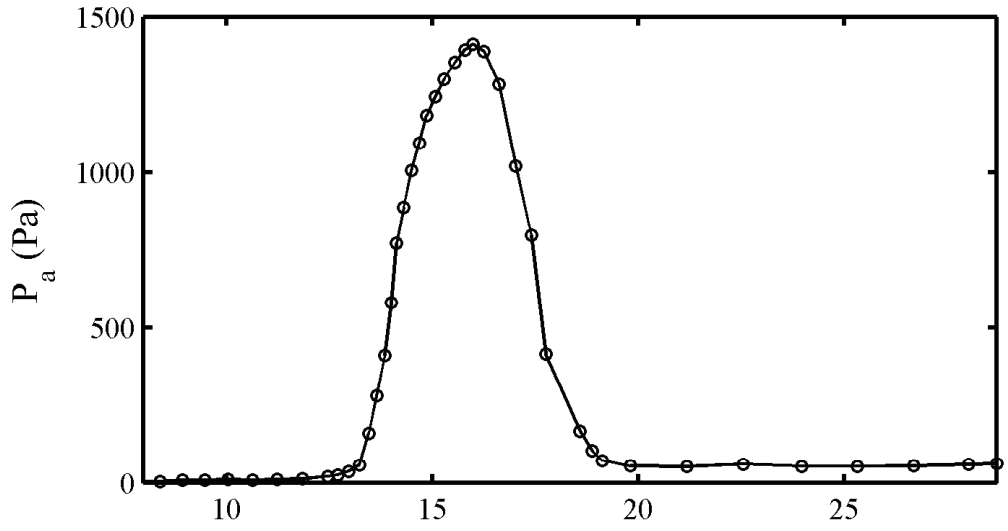

(a) Acoustic pressure

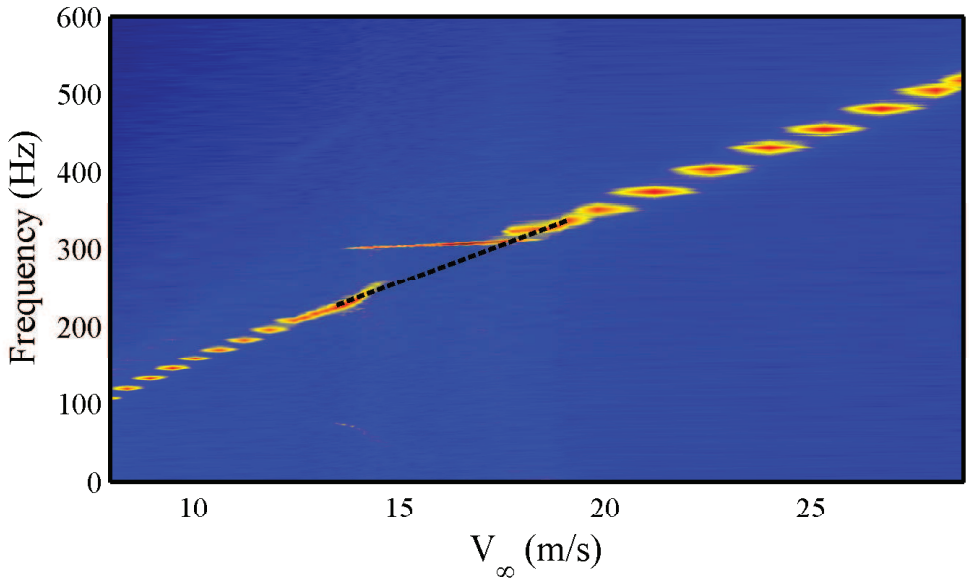

(b) Velocity spectra (Arbitrary Logarithmic Scale)

Figure 7.3: Aeroacoustic characteristics measured by M1 and HW2 for the $P/D = 2.5$, $L/D = 2.5$ inline tube bundle.

agrees well with those of Oengören and Ziada [34]. During the "lock-in" range, the acoustic pressure reaches a maximum value of $P_a = 1413$ Pa (157 dB) at $V_\infty = 16$ m/s, which is in the middle of the "lock-in" range. An interesting observation from the top plot in Fig. 7.3 is that after "lock-in" subsides, the acoustic pressure does not experience any significant increase with flow velocity. Recall that in the pressure plots of the two tandem and four cylinder configurations, the acoustic pressure would continue to increase after resonance subsided. This was attributed to the "lock-in" of the side-branches with the acoustic field of the duct. Since this behaviour is not observed here, it may suggest that the influence of the side-branches has been diminished or at least is not as prominent within this velocity range.

Figure 7.4 shows the aeroacoustic response of the $P/D = 3$, $L/D = 1.5$ configuration, which according to Oengören and Ziada [34] has a large streamwise spacing ratio. Both plots show the response of M1. Figure 7.4(a) shows the acoustic pressure whilst Fig. 7.4(b) shows a waterfall plot of the SPL and frequency components. From Fig. 7.4(b), it can be seen that the vortex shedding frequency increases with flow velocity. At the same time, the acoustic pressure gradually increases as well. As f_v approaches f_a, near $V_\infty = 10$ m/s, the increase in acoustic pressure begins to accelerate. No sudden jump in either the acoustic pressure or the vortex shedding frequency is observed at any time (which was the case for the $P/D = 2.5$, $L/D = 2.5$ configuration), but it is obvious that the vortex shedding frequency has become "locked-in" to the acoustic field. The resonance seems due to vortex shedding excitation and because "lock-in" initiates near acoustic-Strouhal coincidence, the system experiences coincidence acoustic resonance but not pre-coincidence acoustic resonance. As the transverse spacing of the cylinders (P) is considered large, this finding is consistent with Ziada and Oengören [23]. There is an abrupt drop in acoustic pressure at $V_\infty \approx 15$ m/s which signals the end of the "lock-in". Although much higher velocities were not measured for this test, it seems that the vortex shedding jumps up to a higher frequency near $f_v = 450$ Hz and continues to increase with velocity.

Figure 7.5 shows the aeroacoustic response of the $P/D = 3$, $L/D = 3$ configuration, which as with the $P/D = 3$, $L/D = 1.5$ configuration has a large streamwise spacing ratio according to Oengören and Ziada [34]. Figure 7.5(a) shows the acoustic pressure measured with M1 whilst Fig. 7.5(b) shows a waterfall plot of the turbulence spectra measured by

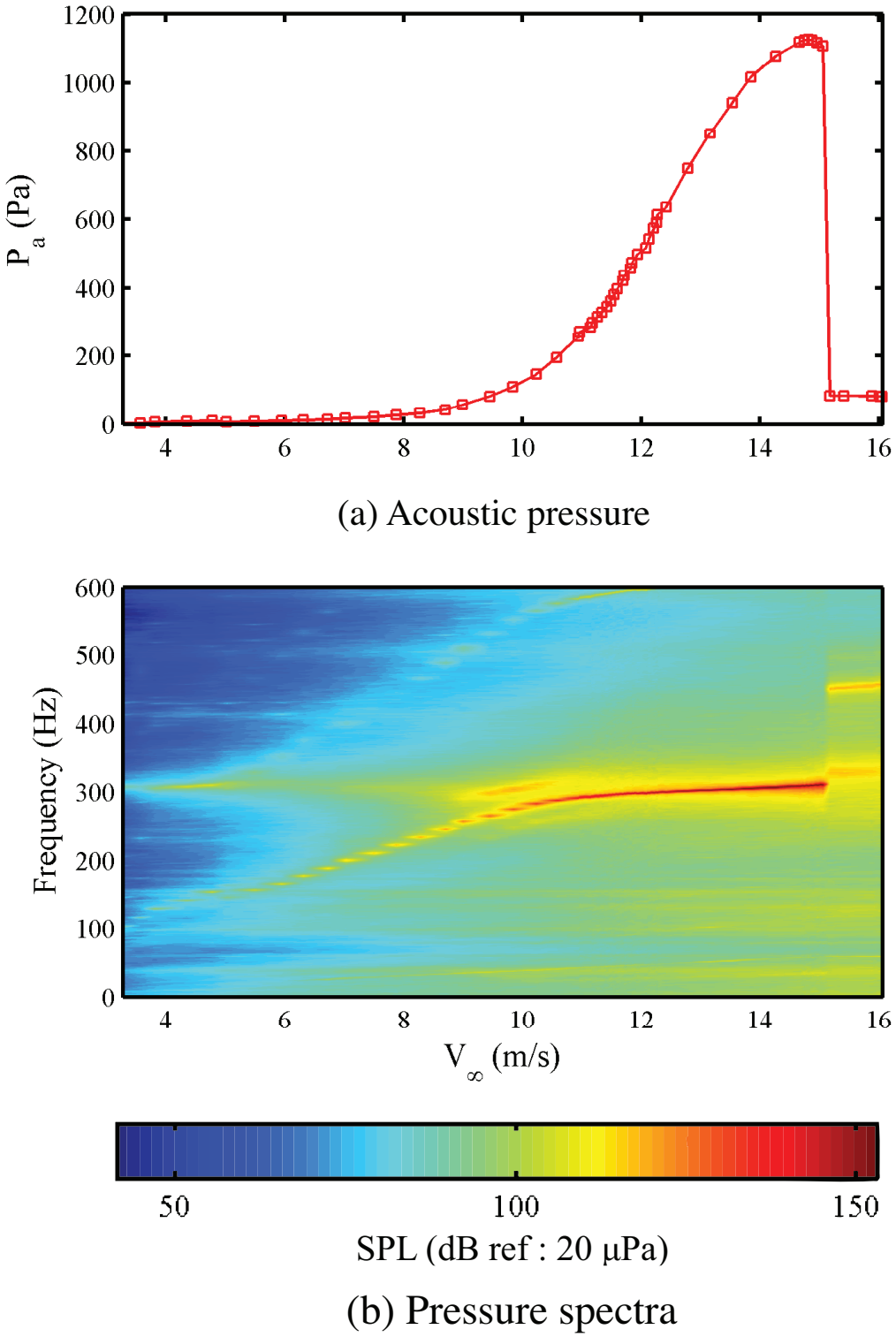

Figure 7.4: Aeroacoustic characteristics measured by M1 for the $P/D = 3$, $L/D = 1.5$ inline tube bundle.

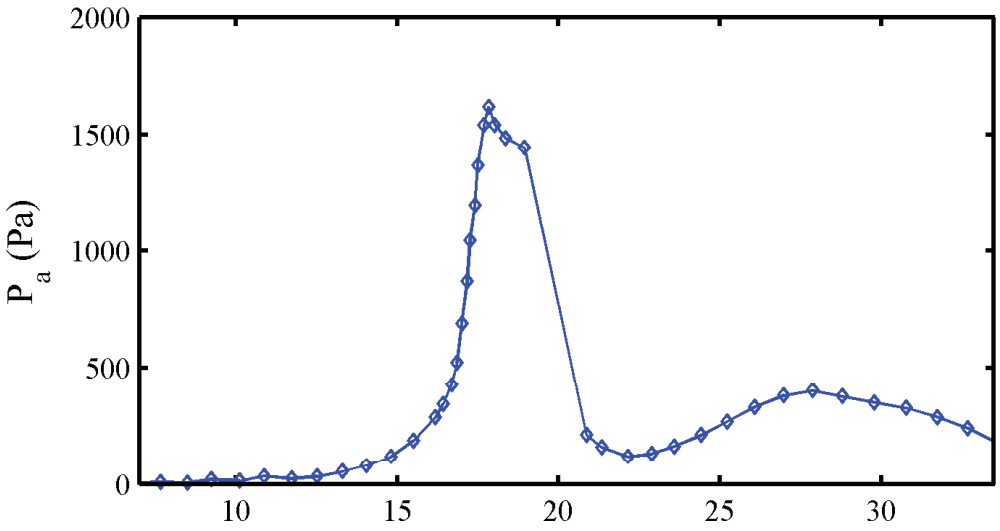

(a) Acoustic pressure

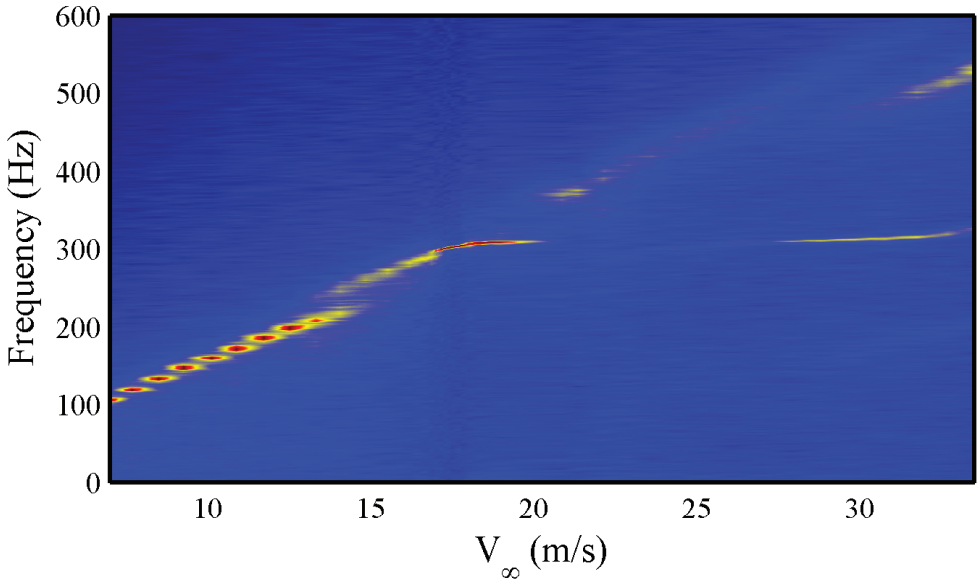

(b) Velocity spectra (Arbitrary Logarithmic Scale)

Figure 7.5: Aeroacoustic characteristics measured by M1 and HW2 for the $P/D = 3$, $L/D = 3$ inline tube bundle.

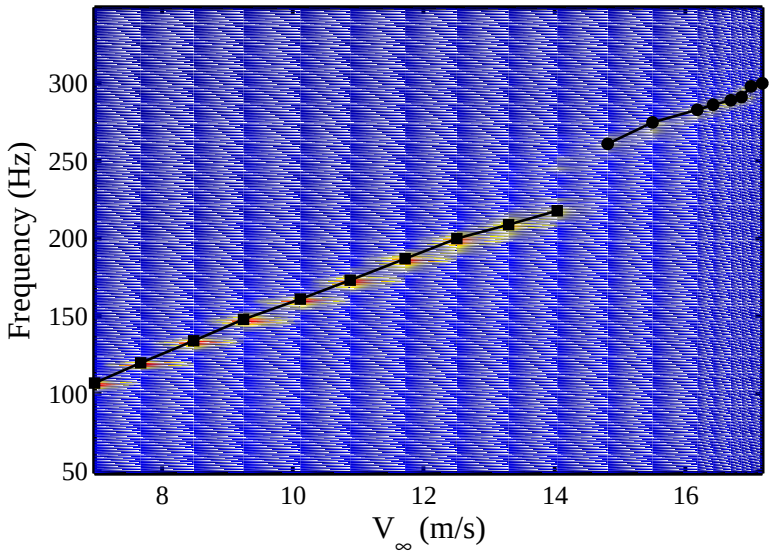

Figure 7.6: A close up of the waterfall spectra in Fig. 7.5 showing the jump from one Strouhal dependency to another at $V_\infty = 14$ m/s (Arbitrary Logarithmic Scale).

the hotwire. A similar excitation response to the $P/D = 3$, $L/D = 1.5$ configuration is observed as the acoustic pressure excitation is triggered by vortex shedding at acoustic-Strouhal coincidence. As with the $P/D = 3$, $L/D = 1.5$ configuration, the increase in acoustic pressure is gradual as f_v approaches f_a but accelerates at acoustic-Strouhal coincidence. Hence the $P/D = 3$, $L/D = 3$ configuration experiences coincidence resonance. The system remains "locked-in" for roughly 4 m/s. When "lock-in" is broken, f_v jumps up to a higher frequency and increases with flow velocity. However, at these higher velocities, the vortex shedding gradually diminishes into broadband turbulent structures. This is apparent in Fig. 7.5(b) as the strength of the Strouhal dependency after "lock-in" is much lower compared to the dependency before "lock-in".

Closer inspection of Fig. 7.5(b) reveals that the f_v suddenly jumps to a higher frequency at $V_\infty = 14$ m/s and follows a slightly different Strouhal dependency before "lock-in" occurs. Figure 7.6 shows a close up of the hotwire response around the velocity range where the jump occurs. Overlaid on the plot are the peak frequencies recorded by the hotwire. The jump is clear to see. This may correspond to the switch between global jet instability excitation and local wake instability excitation discussed by Ziada and Oengören [23]. The frequencies before the jump follow a Strouhal number based on

gap velocity of $St_g = 0.14$ whilst the frequencies after the jump follow a Strouhal number of $St_g = 0.15$. Ziada and Oengören [23] reported Strouhal numbers of 0.14 and 0.16 respectively in their water tunnel tests. In their air tests, the lower Strouhal dependency was not detected and they reported a value of $St_g = 0.17$. Their array had $P/D = 3.25$ and $L/D = 3.75$ (compared to $P/D = 3$, $L/D = 3$ in the present tests). Nonetheless, the Strouhal numbers show good agreement considering they are highly dependent on the transverse spacing ratio (see Ch. 6).

Figure 7.7 compares the resonant response of the three tested arrays. The acoustic pressure measured by M1 versus the reduced gap velocity, U_{rg} is shown in Fig. 7.7(a). The response of the $P/D = 3$, $L/D = 3$ and $P/D = 2.5$, $L/D = 2.5$ configurations are similar in that they have a comparable "lock-in" range. However, comparing the $P/D = 3$, $L/D = 3$ configuration and the $P/D = 3$, $L/D = 1.5$ it is clear to see that the responses are quite different. Reducing the transverse spacing ratio between the cylinders has caused the resonance to shift towards higher reduced gap velocities. This is the first effect that reducing the transverse spacing has. The second effect can be seen in Fig. 7.7(b) which plots the normalised acoustic pressure based on gap velocity (P_g^*) versus reduced gap velocity (U_{rg}). The normalised acoustic pressure takes the same form as Eqn. 2.6 except here, V_g has been substituted in for V_∞ and $Ma_g = V_g/c$ instead of $Ma = V_\infty/c$. Reducing the transverse spacing ratio from $L/D = 3$ to $L/D = 1.5$ has clearly reduced the strength of the resonance generated from the cylinders. In fact, it has nearly reduced it by a factor of five, which is interesting given that the $P/D = 3$, $L/D = 1.5$ configuration only has twice as many tubes. This is assumed to be caused by an increased dynamic head in the duct when the blockage ratio is smaller i.e., when the $P/D = 3$, $L/D = 3$ configuration is installed. The mainstream velocity measured by the pitot tube at the maximum acoustic pressure for the $P/D = 3$, $L/D = 1.5$ configuration was 14.9 m/s. The mainstream velocity measured by the pitot tube at the maximum acoustic pressure for the $P/D = 3$, $L/D = 3$ configuration was 17.8 m/s. The $P/D = 2.5$, $L/D = 2.5$ configuration also induces appreciably stronger resonance than the $P/D = 3$, $L/D = 1.5$ (based on the gap velocity). If the dynamic head in the duct is not the reason why the inline square arrays induce stronger resonances than the inline rectangular array, then maybe it is a question of "squareness". Perhaps a square array is more efficient at generating acoustic resonance

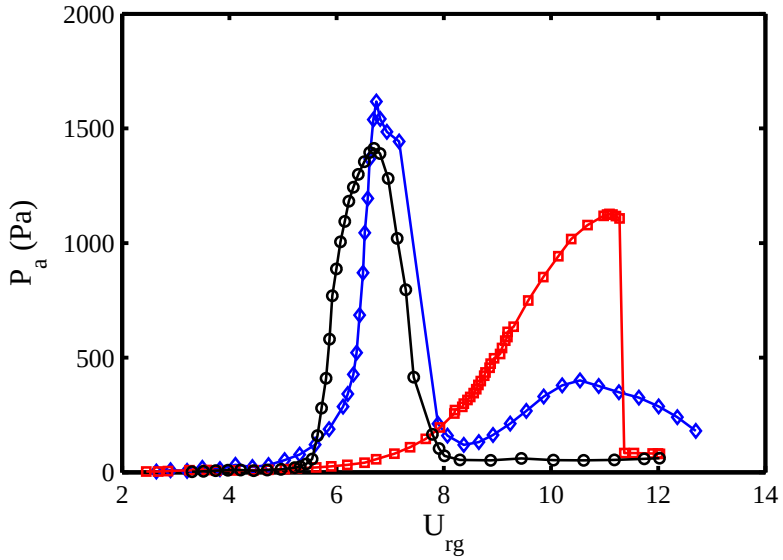

(a) Acoustic pressure versus reduced gap velocity

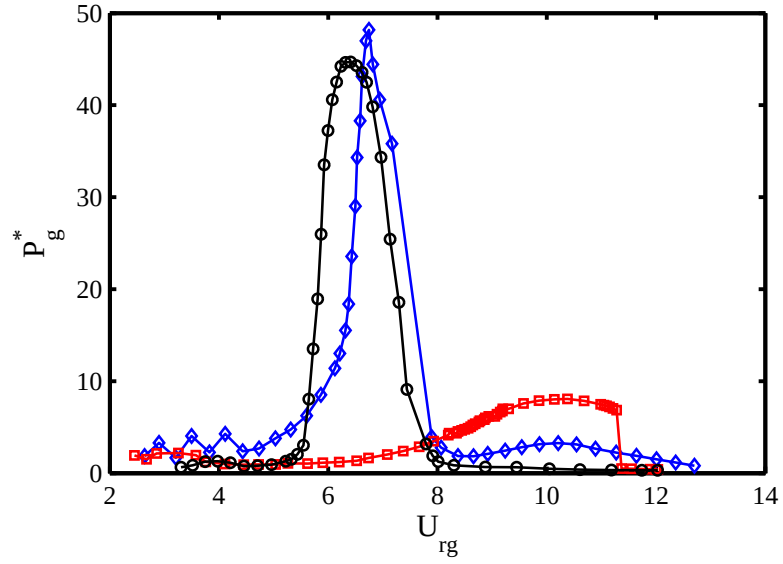

(b) Normalised acoustic pressure versus reduced gap velocity

Figure 7.7: Comparison of the acoustic response measured by M1 for the three tested inline tube bundle configurations. ◇ $P/D = 2.5$, $L/D = 2.5$; □ $P/D = 3$, $L/D = 1.5$; ○ $P/D = 3$, $L/D = 3$.

than a rectangular array? This is purely speculative based on some of the observations made when analysing the four cylinder data in Ch. 6 and needs to be studied further.

7.2.2 Resonant acoustic field

The resonant sound field was calculated using the same procedure as the two tandem and four cylinder cases. An example of the acoustic particle velocity at $\phi = 0°$ determined from the FEA model of the $P/D = 3$, $L/D = 3$ configuration can be seen in Fig. 7.8. The frequency of the first acoustic mode was determined to be $f_a = 294$ Hz. The resonant frequency determined from the naturally excited tests above was $f_a = 306$ Hz. This gives a 4% discrepancy between experiments and the model which is much better than previously reported. The contours show the magnitude of U_a normalised by the mainstream velocity at which tests were taken. In this case, $V_\infty = 18.2$ m/s. The distribution of the acoustic particle velocity is largely similar to what was observed for the other cases. High values of acoustic particle velocity develop at the edges of the cylinders where the acoustic wave has to squeeze through the gap. Moreover, the effect of the side-branches on the cylinders in the corners of the array (near the edges of the mouths) are evident as the acoustic particle velocity field in these locations is inclined relative to that around the central cylinders. This is better highlighted in Fig 7.9 which shows a close up comparing the acoustic particle velocity distribution around the cylinder in row 4, column 3 with the cylinder in row 2, column 2.

7.3 Flow structure

7.3.0.1 Completing PIV in a tube bundle

The microphone measurements have shown that each configuration can naturally induce a strong resonance over a range of flow velocities. The $P/D = 2.5$, $L/D = 2.5$ configuration resonates in a different fashion to the $P/D = 3$, $L/D = 1.5$ and $P/D = 3$, $L/D = 3$ configurations. As a reminder, the intermediately spaced array only experiences pre-coincidence resonance whilst the largely spaced arrays only experience coincidence resonance. The $P/D = 3$, $L/D = 3$ configuration was selected for further study. This configuration was chosen simply because it provided the easiest PIV conditions of the

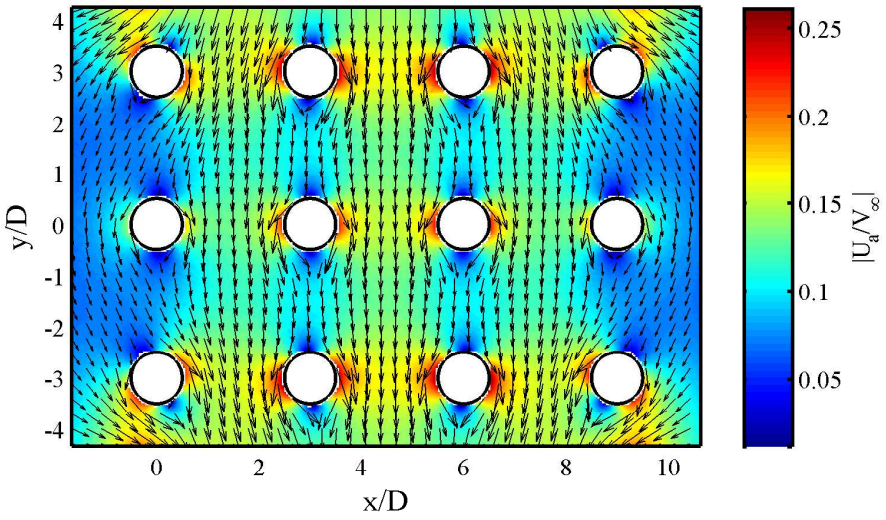

Figure 7.8: The acoustic particle velocity through the $P/D = 3$, $L/D = 3$ inline configuration at acoustic-Strouhal coincidence, $\phi = 0°$ and $V_\infty = 18.2$ m/s.

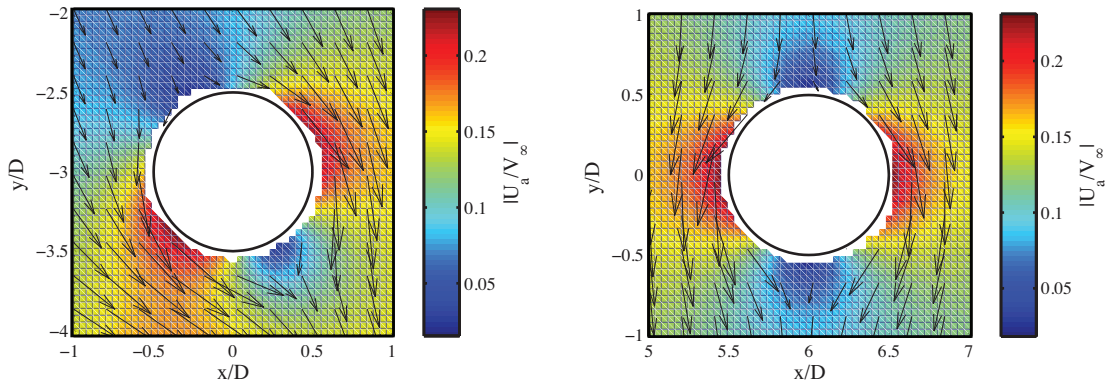

(a) Row 4 - Column 3 (b) Row 2 - Column 2

Figure 7.9: The acoustic particle velocity at two different cylinders in the bundle, highlighting the effect that the side-branches have on U_a for any cylinder in close proximity.

three. The spacing between the cylinders was large enough for a hand to reach in and clean the cylinders and the walls between tests. The other configurations did not facilitate this without having to remove many of the cylinders. If the perspex was not regularly cleaned, a build up of seeding would form and become too foggy to capture meaningful images.

A plan view schematic of the PIV setup can be seen in Fig. 7.10. One of the side-branches had a hard wall blank whilst the other had a loudspeaker installed. The hard wall blank allowed the flow field to be nearly fully illuminated with as little interference as possible whilst the loudspeaker provided the trigger signal. Figure 7.11 shows the acoustic pressure measured by M1 when only one loudspeaker was installed in the test section. The natural frequency of the tube bundle measured using white noise was $f_a = 311$ Hz. As can be seen, the response remains broadly the same with respect to the naturally induced case as the acoustic pressure experiences a sudden increase when the flow field becomes "locked-in". Also, as seen for the two tandem and four cylinder cases, increasing the SPL in the duct increases the range of flow velocities at which "lock-in" can occur. Installing the loudspeaker caused a slight shift in the resonance range towards a higher velocity. However, this is not an actual change in the physics of the system but is rather an effect of the different boundary conditions. It is interesting to see that when the speaker is installed but no sound is applied, the system still experiences resonance. It is very slight though as the acoustic pressure in the duct is four times less than that of the case with two hard wall blanks. Although a perforated disk made from hard plastic was installed between the loudspeaker cone and the side-branch (to simulate a hard wall), the existence of the speaker seems to strongly dampen the resonance.

It was necessary to split the tube bundle into zones for the PIV acquisition. The reason for this was that the area of the tube bundle was too large to be captured in a single image whilst still retaining the necessary condition that particles acquired by the CCD camera be $\sim$3 px in diameter. As discussed in Ch. 5, particles smaller than 3 px facilitate "peak-locking". It was decided to only include two cylinders in each PIV zone. That way, each zone effectively acted as an individual tandem cylinder test. The zones were overlapped in such a way that each one contained regions of a neighbouring zone. This ensured that areas of the flow field corresponding to adjacent zones could be identified

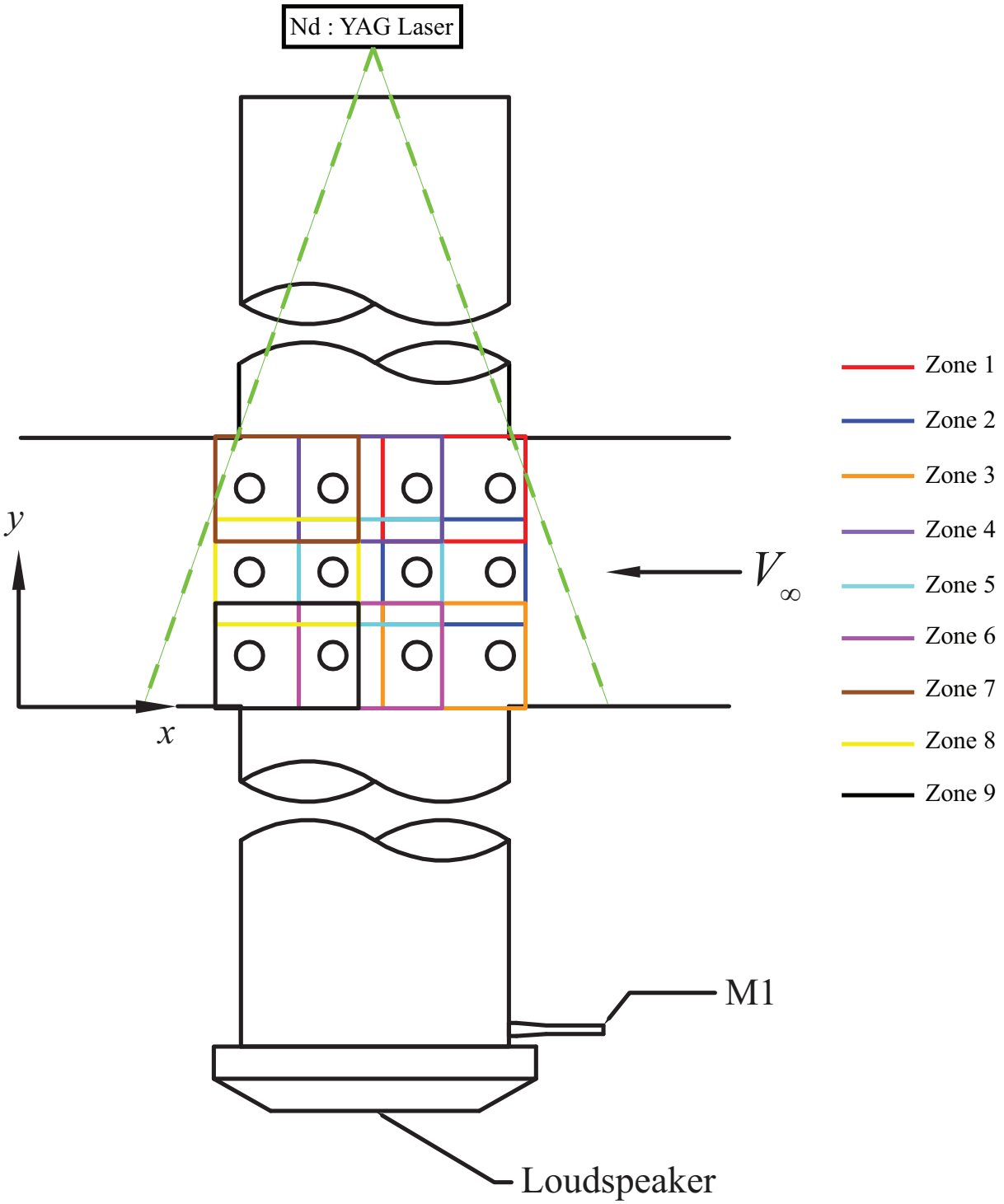

Figure 7.10: Schematic of the zones used to patch together full field PIV calculations of the $P/D = 3$, $L/D = 3$ inline tube bundle.

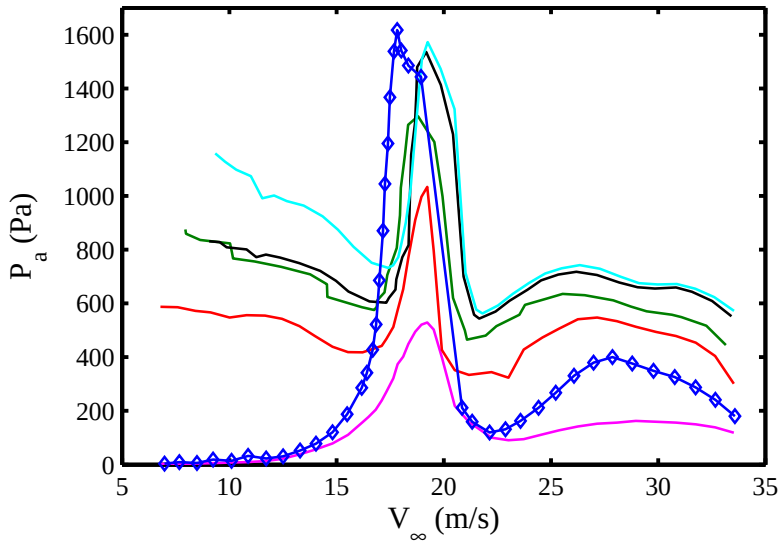

Figure 7.11: The acoustic pressure response of the $P/D = 3$, $L/D = 3$ inline tube bundle configuration measured by M1 when one hard wall is replaced by a loudspeaker operating a various input voltages, $f_a = 311$ Hz. – No applied sound; – 300 mV; – 525 mV; – 650 mV; – 750 mV; ◇ No applied sound with 2 hard walls.

and averaged. A large overlap was selected to achieve the smoothest transition between zones. Figure 7.10 sketches how the zones were divided and overlapped. Images in a particular zone were acquired by moving the camera, which for these tests was mounted on a traverse system that moved in both x and y directions. When positioning the camera to take images in a particular zone, cross-hairs were overlaid onto the image taken by the camera. These cross-hairs were at a fixed pixel location in the camera and were lined up with reference lines on a positional calibration plate in the plane of the light sheet. Figure 7.12 shows how the cross-hairs were used to match the position of the camera with the appropriate zone. The cross-hairs (the blue lines) were lined up with reference lines on the calibration plate in both the x and y direction to ensure the image was square. The cross-hairs and the reference lines were matched up by eye. The thickness of the reference lines drawn on the calibration plate were roughly 8 px. Since the resolution of the images were 14 px/mm, the positional accuracy of the measurements is estimated to be 0.55 mm. This only applies to the actual position of the camera and will not affect the velocity vector calculations as this is determined by the camera CCD calibration.

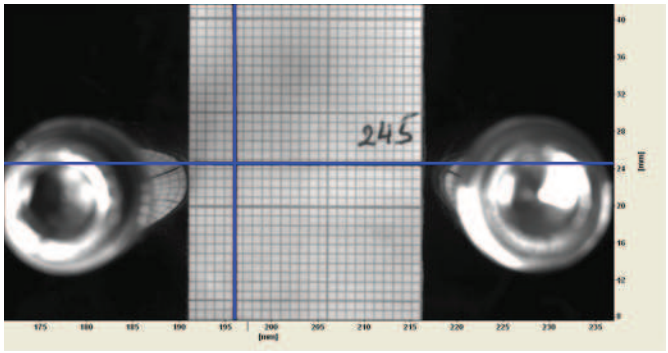

Figure 7.12: The positional calibration plate used to orientate the PIV camera.

7.3.0.2 PIV results

Figure 7.13 shows typical raw PIV images in zones 4, 5 and 6. In all three zones there is good seeding density and a homogeneous distribution as the underlying flow structure is not visible. The illumination in the cylinder lanes is also very good. In the shadows of the cylinders there is a clear drop in intensity that increases from zone 4 to zone 6. However, particles are still visible in the shadows of the third column of cylinders in zone 6. It is important to note that the intensity of these images has been scaled so that they can be plotted. The positional accuracy of the three zones is also evident in Fig. 7.13. This can be realised by following the path of the shadow from picture to picture and remembering that parallax is showing the same region of flow but from different angles. For example, compare the position of the shadow of row 2 column 1 in zone 4 with that of row 2 column 1 in zone 5.

The PIV images in Fig. 7.13 were recorded when a sound wave was applied at the natural frequency measured on the day of testing, $f_a = 311$ Hz. It was decided to use 650 mV as the speaker input voltage. The effect of flow velocity on the energy transfer mechanism was not studied for this tube bundle purely due to the number of tests that would have to be completed. Instead, only the velocity corresponding to acoustic-Strouhal coincidence was investigated. For the $P/D = 3$, $L/D = 3$ configuration with the loudspeaker installed and operating, this point occurred at $V_\infty = 18.2$ m/s or $V_g = 27.3$ m/s. The corresponding Reynolds numbers based on cylinder diameter were $Re_{V_\infty} = 1.44 \times 10^4$ and $Re_{V_g} = 2.15 \times 10^4$. The pressure measured by microphone M1 at acoustic-Strouhal coincidence was $P_a = 1376$ Pa (156.75 dB) which meant that the dimensionless

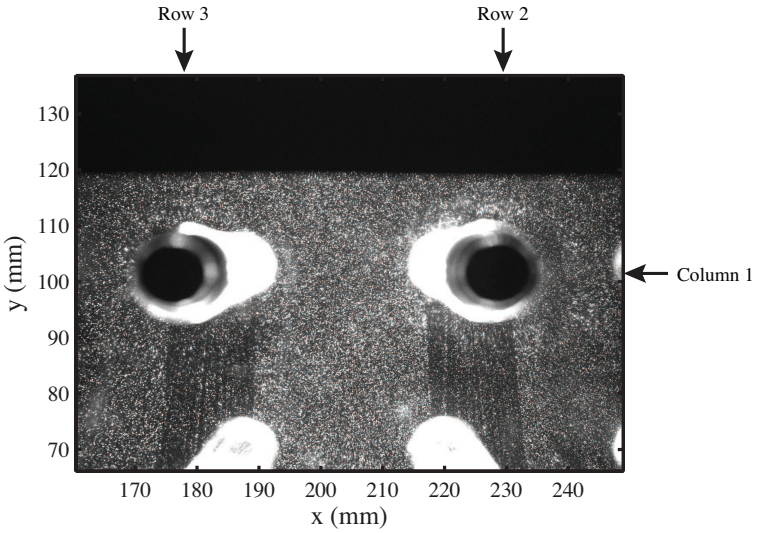

(a) Zone 4

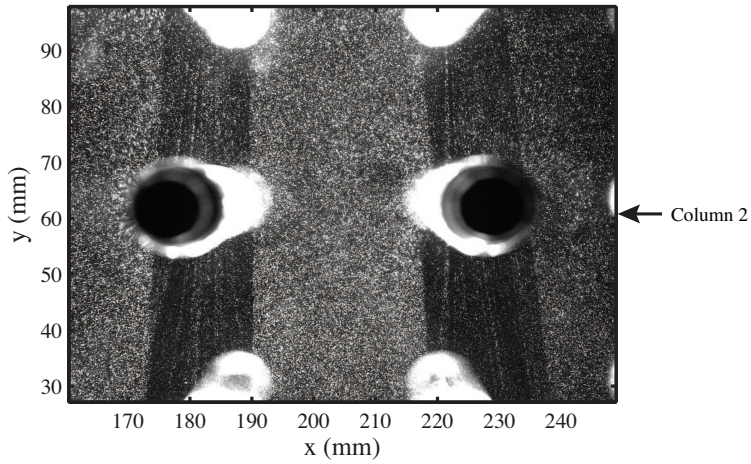

(b) Zone 5

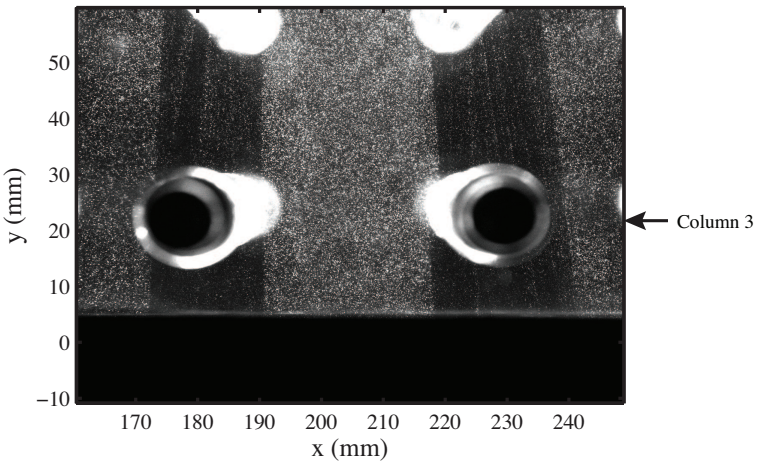

(c) Zone 6

Figure 7.13: Images of the seeding distribution in zones 4, 5 and 6 of the $P/D = 3$, $L/D = 3$ inline tube bundle configuration, $V_g = 27.3$ m/s.

acoustic particle velocity was $\widehat{U}_a/V_\infty = 0.18$ or $\widehat{U}_a/V_g = 0.12$.

Figure 7.14 shows the full field velocity and vorticity in the tube bundle at $\phi = 45°$, $\phi = 135°$, $\phi = 225°$ and $\phi = 315°$. Inspection of the velocity plots show that fast moving flow passes through the tube lanes whilst slow moving flow forms in the tube wakes. Inspection of the vorticity plots show that well defined vortices form from the first row of cylinders, propagate in the wake and impinge onto the second row. The vortices formed from one shear layer are out-of-phase with the vortices formed in the adjacent shear layer of the neighbouring column. As the vortex impinges, it induces a second, weaker vortex to form from the second row. This vortex forms on the other side of the cylinder from which the impinging vortex was shed and so has opposite polarity. The shedding of this second vortex is timed with the shedding of a strong vortex of similar sense from the first row. That is to say, the structures are highly synchronised across the bundle. The vortices formed in the second row are spread out over a larger area than the vortices shed from the first but have a smaller magnitude. Moreover, they also seem to be less coherent. When the vortices formed from the second row impinged on the third, even less coherent vortices were formed. At this stage, the flow has become mostly turbulent which is apparent from the noisy vorticity contours. Even though the structures in the deeper rows are less defined and much more turbulent compared to upstream rows, they continue to form alternatively in the wakes of the cylinders and synchronisation of the flow seems to remain between both the rows and the columns. The structure of the phased averaged flow field agree well with the findings of Ziada and Oengören [23].

Figure 7.15 shows the mean (time averaged) velocity and vorticity contours. Inspecting the vorticity plot first, it can be seen that the structures shed from each row in column 2 simply reattach onto the cylinders in the second row and that their overall structure seems unaffected by the presence of the side-branches. Additionally, the wake seems to widen slightly between rows 2 and 3. The same cannot be said for columns 1 and 3. These columns are in close proximity to the side-branches and seem to be strongly affected by their presence. The vortices shed from the first row are angled towards the side-branch mouths but still reattach to the downstream cylinder. Behind the second row, the path of vortex is clearly deflected away from the array towards the side-branch. This obviously causes the wake to widen drastically and is presumably due to a large scale

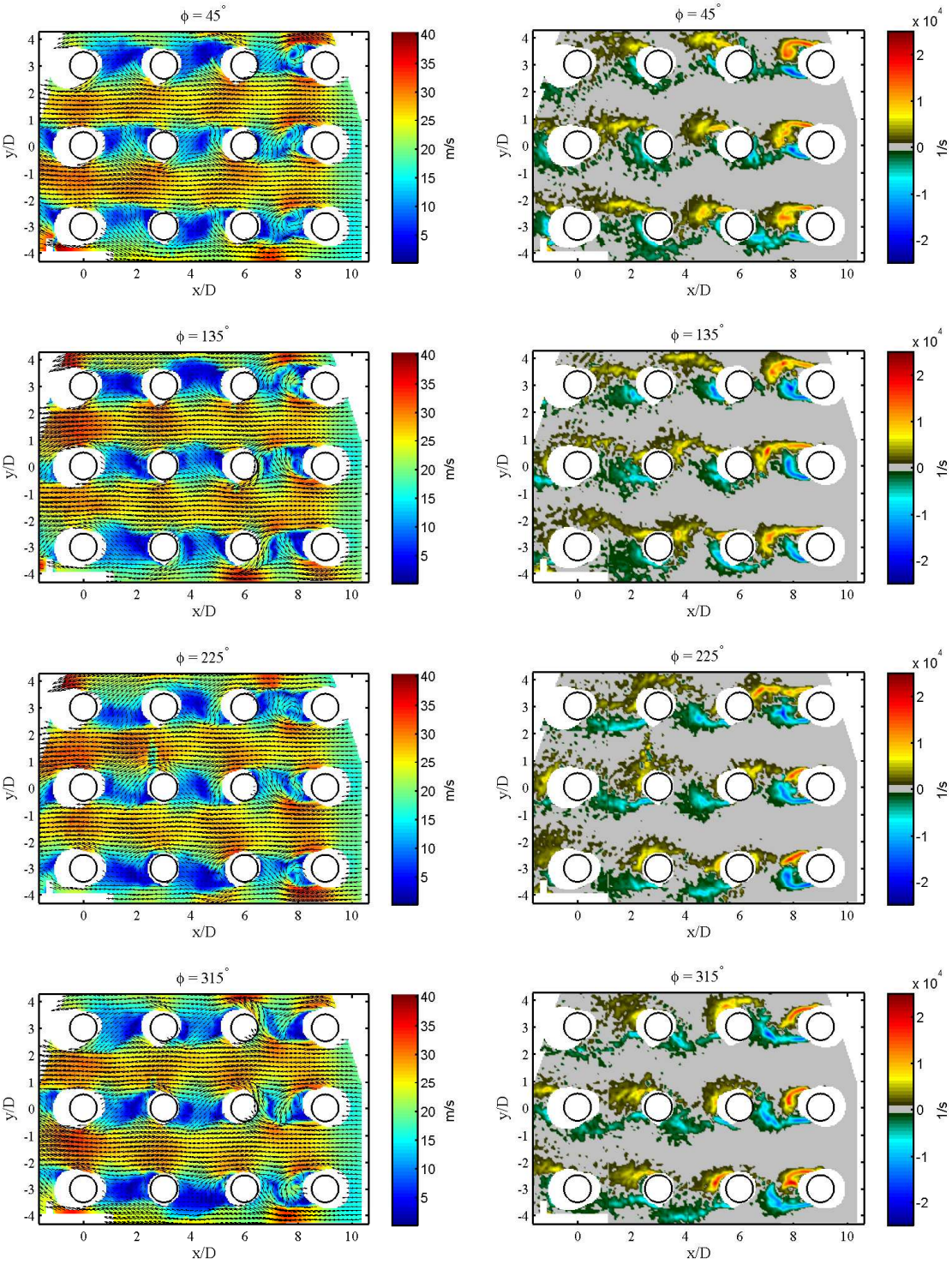

(a) Velocity (b) Vorticity

Figure 7.14: Hydrodynamic velocity and vorticity in the $P/D = 3$, $L/D = 3$ inline tube bundle at different phases in the acoustic wave cycle, $f_a = 311$ Hz, $\widehat{U}_a/V_\infty = 0.18$.

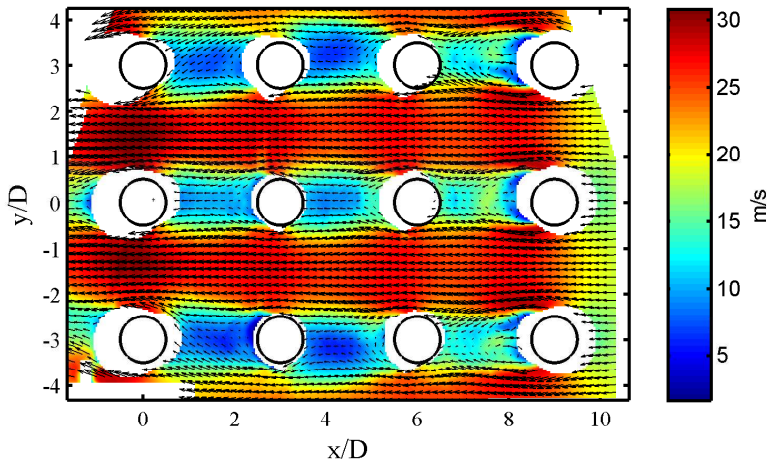

(a) Velocity

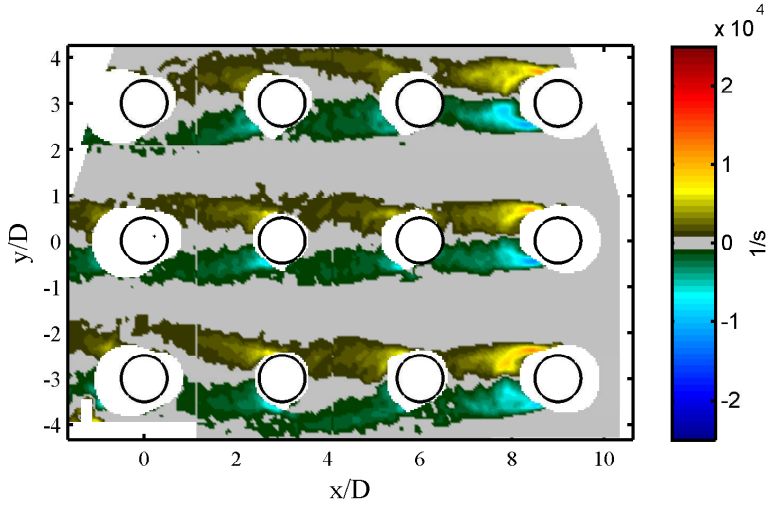

(b) Vorticity

Figure 7.15: Mean hydrodynamic velocity and vorticity in the $P/D = 3$, $L/D = 3$ inline tube bundle at acoustic-Strouhal coincidence, $f_a = 311$ Hz, $\widehat{U}_a/V_\infty = 0.18$.

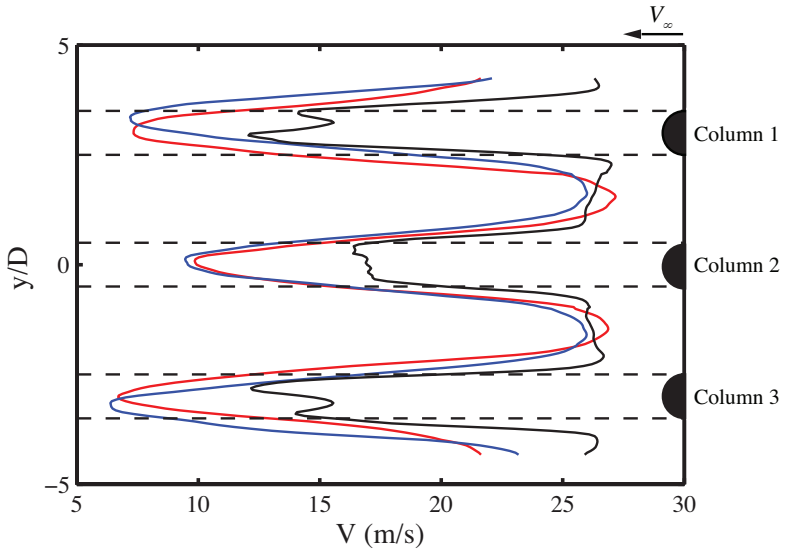

Figure 7.16: Mean velocity profiles across the width of the $P/D = 3$, $L/D = 3$ inline tube bundle at various streamwise positions. – $X/D = 7.5$ (Rows 1-2); – $X/D = 4.5$ (Rows 2-3); – $X/D = 1.5$ (Rows 3-4).

vortex propagating across the mouth of the side-branch being more developed and stronger than the vortex shed from the cylinder. The structures shed from the third row see the opposite effect as their path is deflected towards the interior of the tube bundle. This is presumably due to the impingement of the same vortex in the side-branches causing flow to spill out into the main duct. Dequand *et al.* [49] and Ziada [66] have both extensively investigated the path a vortex shed from side-branches follows.

Figure 7.16 shows the mean velocity profile across the width of the bundle at the midspan between each row. The black line is the profile between rows 1 and 2, the blue line is the profile between rows 2 and 3 and the red line is the profile between rows 3 and 4. The mean flow structure is highly symmetric about the centreline of the bundle (column 2) and some of the effects seen in the vorticity plots are evident here. The streamwise development of the velocity in the flow lanes between columns 1 and 2 and between columns 2 and 3 is shown in Fig. 7.17. The velocity in each lane increases rapidly as it enters the tube bundle. The general trend of the velocity profile as it proceeds downstream is to increase but at a much slower rate. The mean velocity across the minimum gap between the columns at row one, i.e., the gap flow velocity, was calculated from the PIV images to be 25.11 m/s. This gives a discrepancy of 7.9% from the value quoted previously, which was of $V_g = 27.28$ m/s. This discrepancy is not thought to

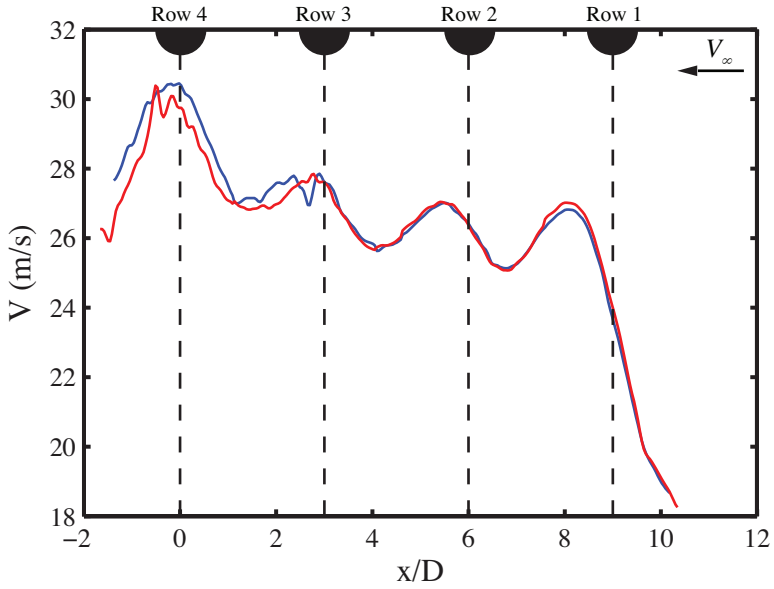

Figure 7.17: Mean streamwise velocity profiles along the centreline of the flow lanes though the $P/D = 3$, $L/D = 3$ inline tube bundle. – $Y/D = 1.5$ (Columns 1-2); – $Y/D = -1.5$ (Columns 2-3).

be due to error in the PIV measurements because none of the images showed "peak-locking" and inspection of the particle displacements revealed that none of the accepted vectors violated the "one-quarter rule". Moreover, the velocities upstream of the array (in Fig. 7.15(a)) show a mean error of 1.5% with the value measured from the pitot tube. Instead, this discrepancy between the gap velocities is probably a physical phenomenon. The gap velocity equation ($V_g = V_\infty(P/(P-D))$ assumes that the gaps across the whole bundle are equal. However, in this case, the gaps between columns 1 and 2 and columns 2 and 3 were 26 mm whilst the gaps between columns 1 and 3 and the walls were 17 mm.

7.4 Flow/Sound interaction

7.4.1 Phase averaged acoustic power

Figure 7.18 plots contours of the vorticity and the corresponding acoustic power calculated using Eqn. 3.12 at $\phi = 22.5°$, $\phi = 112.5°$, $\phi = 202.5°$, $\phi = 292.5°$. Much stronger sources and sinks are generated at $\phi = 22.5°$ and $\phi = 202.5°$ compared to $\phi = 112.5°$ and $\phi = 292.5°$ because the magnitudes of the acoustic particle velocities are much greater at $\phi = 22.5°$ and $\phi = 202.5°$ than at $\phi = 112.5°$ and $\phi = 292.5°$ (see Fig. 3.5).

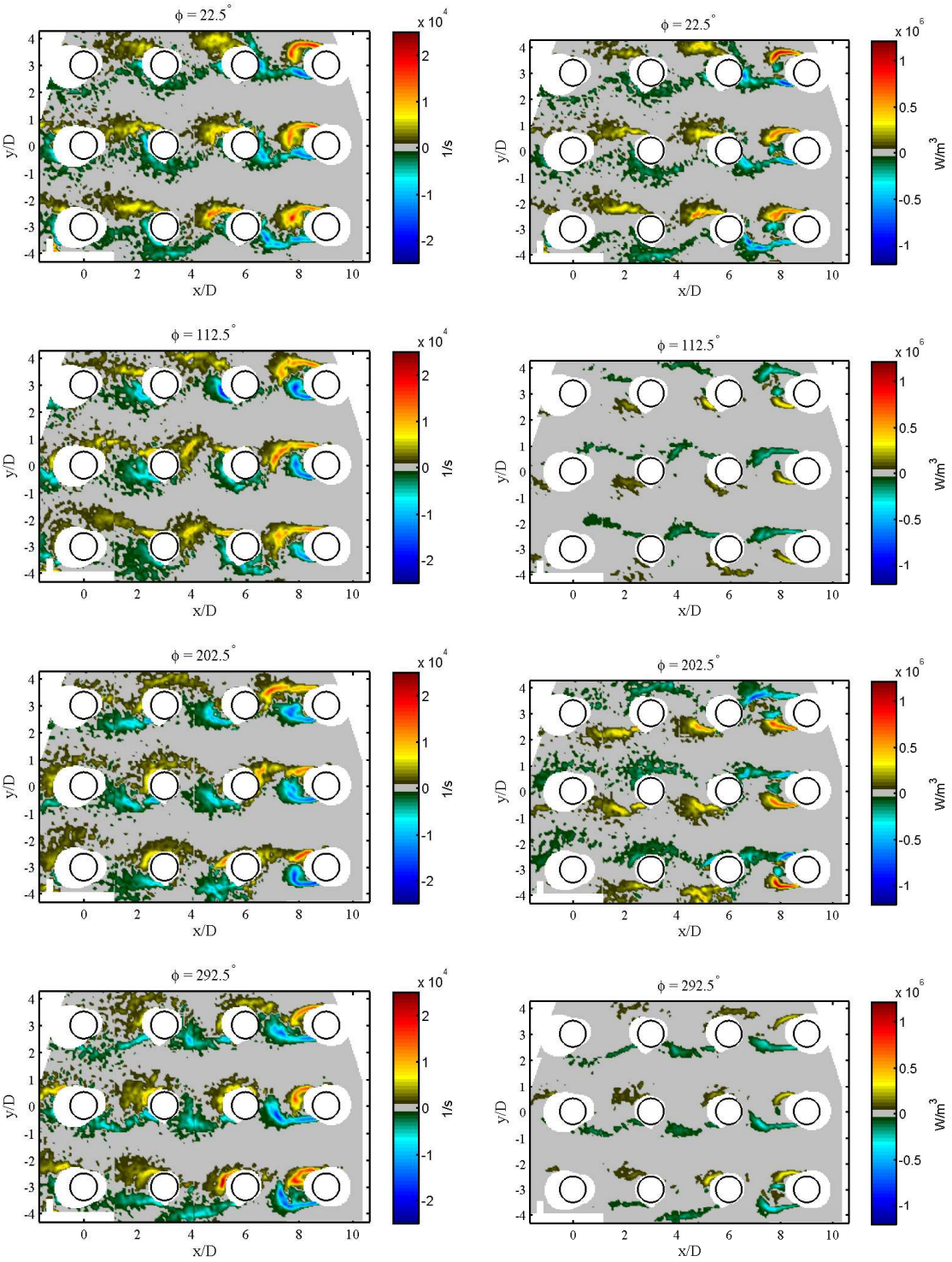

(a) Vorticity (b) Acoustic power

Figure 7.18: Hydrodynamic vorticity and acoustic power in the $P/D = 3$, $L/D = 3$ inline tube bundle at different phases in the acoustic wave cycle, $f_a = 311$ Hz, $\widehat{U}_a/V_\infty = 0.18$.

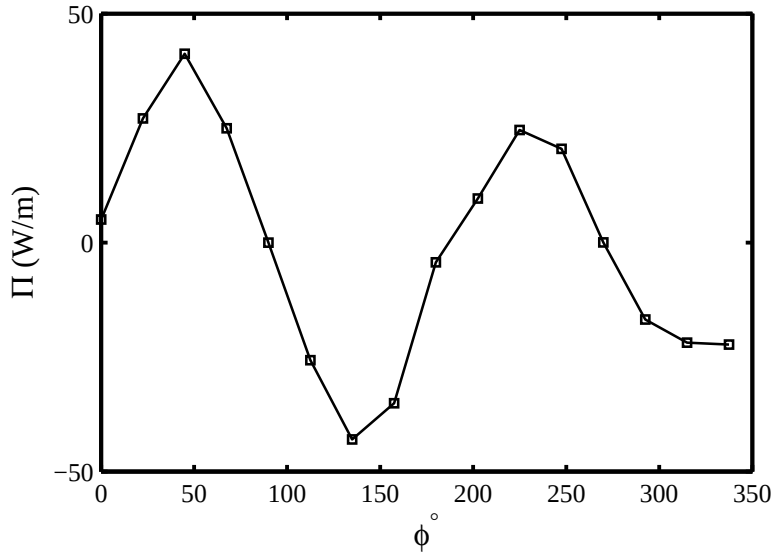

Figure 7.19: Total acoustic power generated per phase in the tube bundle.

Figure 7.19 plots the total acoustic power generated by the tube bundle per phase. According to the graph, acoustic power is generated at $\phi = 22.5°$ and $\phi = 202.5°$, which makes sense given the large acoustic particle velocity, whilst at $\phi = 112.5°$ and $\phi = 292.5°$ acoustic power is absorbed.

Concentrating on the phases that generate acoustic power first, inspection of Fig. 7.18 reveals that the sources generated at $\phi = 22.5°$ correspond to structures shed from the top sides of the cylinders whilst sources generated at $\phi = 202.5°$ correspond to structures shed from the bottom sides of the cylinders. At both of these phases, the vortices are still developing behind rows 1 and 2 and have not quite fully formed. They have a significant contribution to Eqn. 3.12 because they possess a high level of vorticity due to their attachment to the shear layer.

Concentrating on the phases that absorb acoustic power, inspection of Fig. 7.18 reveals that the sinks generated at $\phi = 112.5°$ correspond to structures shed from the top sides of the cylinders whilst sinks generated at $\phi = 292.5°$ correspond to structures shed from the bottom sides of the cylinders. At both of these phases, the vortices (which were previously still forming) are now fully developed and just about to impinge on a cylinder. Even though the acoustic particle velocity at these phases has a reduced influence on Eqn. 3.12, the fact that the vortices are fully developed and cover a large area means their contribution is still significant and hence absorption occurs.

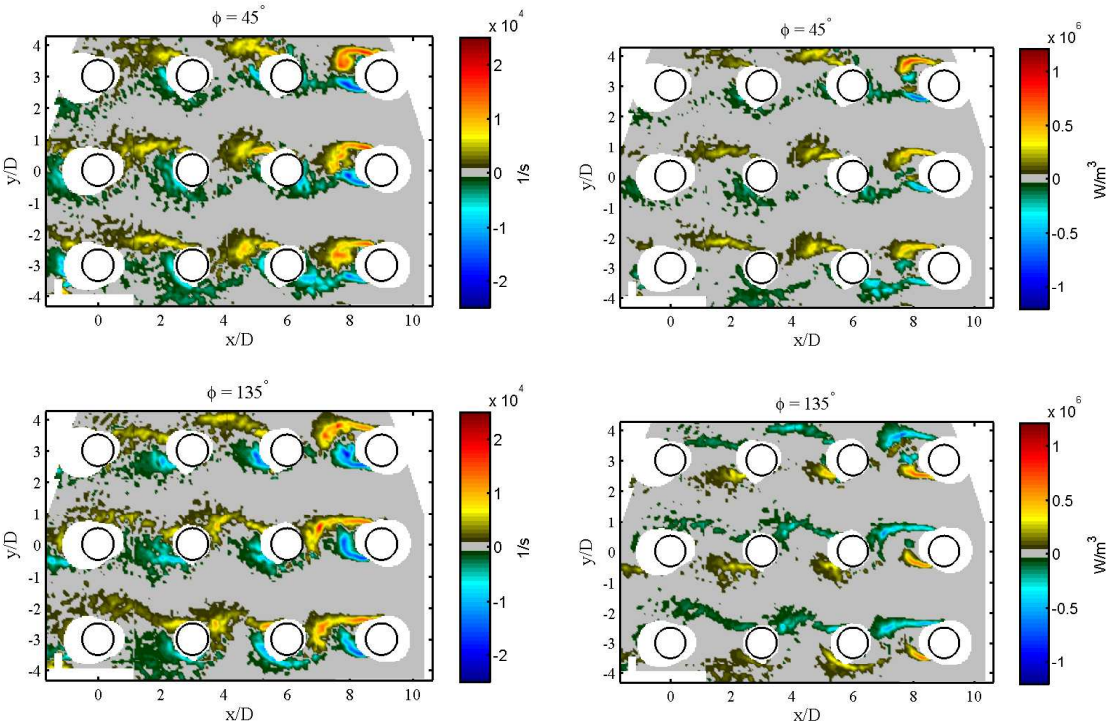

(a) Vorticity (b) Acoustic power

Figure 7.20: Vorticity and acoustic power corresponding to the maximum acoustic power generation at $\phi = 45°$ and the maximum acoustic power absorption at $\phi = 135°$.

It seems that the generation of acoustic power in this inline array is due to the generation and formation of new structures from the cylinders in the initial rows. Furthermore, the absorption of acoustic power seems to be due to the vortices interaction with a cylinder. Figure 7.20 shows the vorticity and acoustic power at $\phi = 45°$ and $\phi = 135°$. These phases correspond to the maximum generated acoustic power and the maximum absorbed acoustic power respectively. The maximum generation of acoustic power occurs just as the vortices reach the mid-span between the cylinders whilst the maximum absorption occurs just as the vortices impinge on the downstream cylinders.

7.4.2 Net acoustic energy

The spatial distribution of the net acoustic energy per cycle generated by the tube bundle is apparent in Fig. 7.21. The generation/absorption of acoustic energy occurs in a periodic fashion from the first row of the array to the last. Moreover, the distributions of the sources and sinks around each column are almost identical, at least for the first three rows. As discussed in the previous section, the generation of acoustic energy seems to be due to the

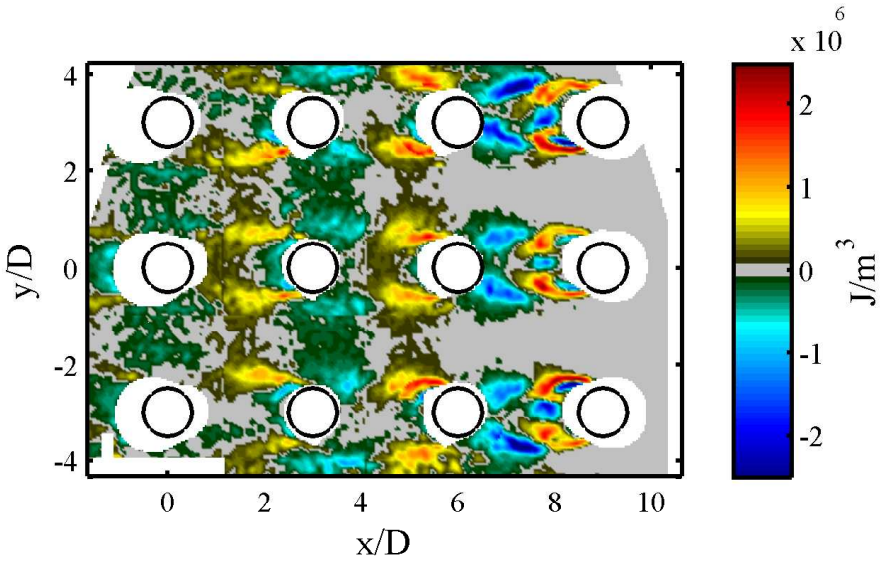

Figure 7.21: Net acoustic energy per cycle generated by the $P/D = 3$, $L/D = 3$ inline tube bundle at acoustic-Strouhal coincidence, $f_a = 311$ Hz, $\widehat{U}_a/V_\infty = 0.18$

formation of vortices behind the first and second rows, whilst the absorption of energy seems to be due to the vortices impinging on the cylinders.

Figure 7.22 shows the net acoustic energy transfer per streamwise location per cycle. From this, and from Fig. 7.21 one can see that the first two rows are the most important. The region near the second row seems to be particularly important as there are very large sinks situated just before it and very strong sources situated just after it. The sinks just in front of the second row cylinders have the strongest magnitudes of all the structures. The first and second rows have the strongest sources and sinks because they shed the most coherent structures. However, the less defined turbulent structures behind the third row are significant in the generation of acoustic power as well. A general observation is that the strength of the sources/sinks decreases from row to row. This is not thought to be due to the drop off in the acoustic particle velocity but rather to the breakdown in coherent vortex structures as the flow travels deeper into the array.

Figure 7.23 compares E^* as a function of the distance from the upstream cylinder generated by column 2 of the array with that generated by the two tandem cylinders during pre-coincidence resonance case A. The distributions of the sources and sinks between the two cases are remarkably similar which means the mechanisms generating acoustic power

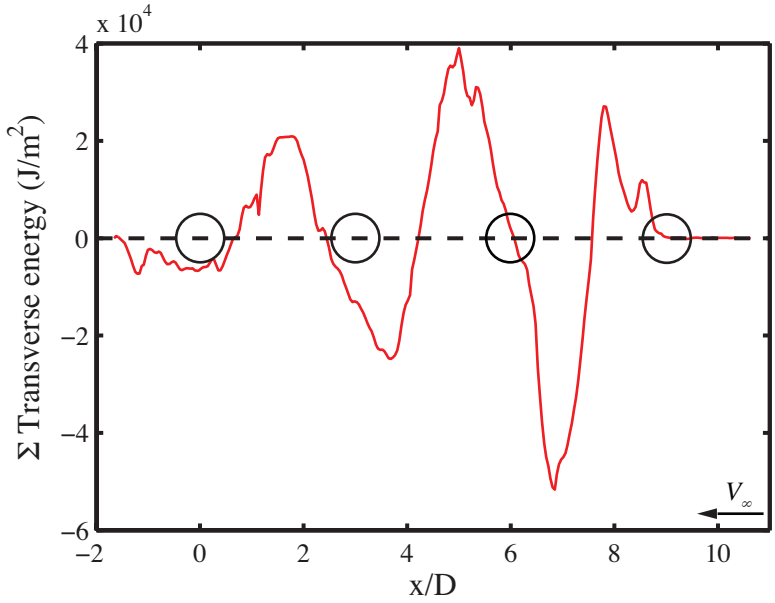

Figure 7.22: Net acoustic energy transfer per streamwise location per cycle generated by the $P/D = 3$, $L/D = 3$ inline tube bundle, $f_a = 311$ Hz, $\widehat{U}_a/V_\infty = 0.18$

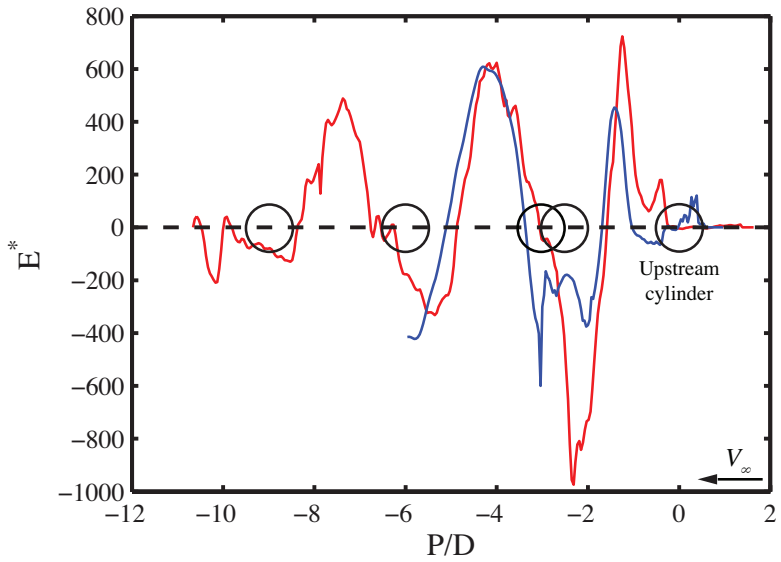

Figure 7.23: Comparison of E^* as a function distance from the furthest upstream cylinder between column 2 of the inline tube bundle and a pair of two tandem cylinders during pre-coincidence resonance. - Inline tube bundle ($P/D = 3$, $L/D = 3$); - Tandem cylinders $P/D = 2.5$).

and absorbing acoustic power are probably the same. This makes sense given that the flow conditions (based on gap velocity) and the streamwise spacing of the cylinders are comparable. The strongest sinks form at $x/D = -2.5$ for the tandem cylinder case and at $x/D = -2.2$ for the tube bundle. The biggest difference between the two plots is the relative magnitudes of the sources and sinks in the wake of the first row. This is thought to be due to the extra streamwise spacing between the cylinders for the inline tube bundle. For the tandem cylinder configuration, the downstream cylinder is located at $x/D = -2.5$ and the vortices in this region actually smear across the surface of the cylinder. Hence, they are not developing or strengthening. For column 2 of the inline array, the cylinder in the second row is at $x/D = -3$ which means the vortices can still grow and strengthen. The added space has afforded the vortex more time to develop which is why it has a stronger contribution. For the two tandem cylinder case, it was found that pre-coincidence acoustic resonance is generated by the formation of vortices in the gap between the two cylinders and that absorption of acoustic power is related to the impingement and smearing of the vortices across the face of the downstream cylinder. This is largely the case here. However, it is interesting how changing the spacing of the gap between two cylinders by only a small amount can drastically change the relative contribution of the sources and sinks.

Fitzpatrick and Donaldson [71] concluded that vortex shedding from the first few rows of a shallow inline tube bundle (no. rows < 5) is the primary source of acoustic resonance. The results presented here seem to agree. However, in saying this, the total acoustic power per cycle calculated from tube bundle was $\Pi = -10.51$ W/m which would suggest the bundle is absorbing energy and should not be resonating. This is a most peculiar result given that the SPL in the duct measured by M1 was $P_a = 1376$ Pa, or 156.75 dB. Further investigation showed that column 2 had a positive net contribution of $\Pi_2 = 46.81$ W/m whilst columns 1 and 3 had a negative contribution of $\Pi_1 = -25.69$ W/m and $\Pi_3 = -31.63$ W/m respectively. Without doubt, the negative contributions are due to extremely strong acoustic sinks generated in the gap between the first and second rows at $X/D = 6.8$. Figure 7.21 shows that these particular sinks in columns 1 and 3 are stronger on the sides of the cylinders closest to the side-branches. Whether or not this is an artefact of the setup is uncertain. However, one should assume it not to be as the

structures are in the free flow.

One possible explanation could be vortex damping. This occurs when the amplitude of the forced acoustic wave overwhelms the shear layers shed from the cylinders. When the vortices become overwhelmed they actually start to absorb energy rather than generate it. However this seems unlikely given the previous discussion about how the energy transfer mechanisms are very similar to those observed for tandem cylinders. Another explanation for the total negative acoustic energy may be the experiment itself. There was a strong parallax effect when recording the images which meant that some regions of the flow generating acoustic power could have been neglected. The way the zones were set up helped reduce the parallax in the second and third rows when the images were combined, but as can be seen, the setup was not perfect. Parallax in all images meant that portions of the cylinder surfaces above and below the PIV plane were visible which explains the non-circular shaped cylinders in rows 2 and 3. A better setup would have had only one cylinder in each zone thereby removing the parallax. However, as it stood, having two cylinders in each zone (forming nine different zones) meant that 144 separate tests were made. This roughly took four hours (not including computational time) to complete. Based on these numbers, having only one cylinder in each zone (forming twelve different zones) would have taken roughly five and a half hours (not including computational time) to complete. Given that 100 image pairs were recorded per test, a total of 14400 PIV image acquisitions were made and needed a significant amount of computer space to store and about two days worth of computational time. Increasing the number of zones to twelve would have nearly surpassed the limitations of the computer. Neither of these possible explanations were investigated further. This was purely due to the laborious nature of the actual experiment.

7.5 Summary

In this chapter, the flow-acoustic coupling of inline tube bundles has been presented. This array pattern was selected over other standard configurations because it has the least geometric complexity. Three different arrays were studied. Two were inline square configurations whilst the other was inline rectangular. The first inline square array had

$P/D = 2.5$, which is considered to be intermediately spaced in the streamwise direction whilst the second had $P/D = 3$, which is considered to be largely spaced in the streamwise direction. The third configuration studied also had $P/D = 3$ but was rectangular inline as its transverse spacing ratio was $L/D = 1/5$. Each configuration exhibited natural acoustic resonance similar to that previously reported in literature. Moreover, when a single loudspeaker was installed at the end of a side-branch, the acoustic response did not change appreciably. The $P/D = 3$ inline square configuration was selected for the PIV tests purely for practical reasons as the other configurations could not be easily cleaned between tests. Experiments to investigate the energy transfer mechanism between the flow field and the sound field in the array were completed at acoustic-Strouhal coincidence. The main conclusions to be drawn from this chapter are:

- Both inline square arrays exhibit significantly stronger acoustic resonance than the rectangular inline array.
- The flow structure between the first three rows of the array during "lock-in" is highly synchronous despite its geometric complexity.
- The mechanisms of acoustic resonance for the tested array are similar to those observed in the tandem cylinder and four cylinder configurations.
- Vortex shedding in the wake of the first and second rows provides the dominant sources in the flow field. The strength of the sources diminish with each row as the vortex structures become less and less coherent. However, the turbulent structures are significant. This is consistent with previous observations in literature for a shallow tube bank.
- The suppression of acoustic resonance in this particular array is associated with the vortices shed from the first row of cylinders impinging on the second row. In a similar manner to that seen for the four cylinder configuration with $P/D = 3$, the large streamwise spacing allows more time for the vortices to develop which means their contribution will be more significant.

Chapter 8

Conclusions and Future Work

8.1 Conclusions

An investigation into the flow-acoustic coupling of multiple bluff bodies subject to ducted flow has been described. The main objective of the study was to explore the mechanisms generating acoustic resonance in a tube bundle akin to what might be found in an industrial heat exchanger. A particular point of interest was the location of the dominant acoustic sources in the flow field.

To study this, Howe's integral was used to determine the energy transfer mechanisms between the flow field and the sound field when the system was "locked-in" and resonating under forced acoustic excitation. This study differs from similar investigations previously undertaken as mainly experimental techniques were employed. The non-intrusive flow measurement technique, PIV was used to resolve the hydrodynamic vorticity and velocity around the cylinders whilst a finite element analysis of the lossless wave equation combined with microphone measurements in the duct determined the acoustic particle velocity.

The conceptual approach was applied to two tandem cylinders, four cylinders in a group and inline tube bundles. Each configuration acted as a valuable stepping stone towards studying the next configuration as the complexity of the problem significantly increased with each one. Each tested configuration had a cylinder diameter of 13 mm and a streamwise spacing ratio within the proximity interference region [11].

The acoustic response of the tandem cylinder configuration is in good agreement with that reported in literature. "Lock-in" occurs before and after acoustic-Strouhal coincidence. For pre-coincidence resonance, vortex shedding in the gap region between the

cylinders and in the near wake provides the dominant sources. For coincidence resonance, the dominant sources form in the wake of the cylinders. In the gap region, the shear layers reattach to the downstream cylinder and acoustic energy is generated. However, much stronger sinks are formed here as well and net acoustic energy is actually absorbed from the system. This means that the mechanism of coincidence resonance of two tandem cylinders is vortex shedding from the downstream cylinder.

When orientated in a square, the acoustic response of the four cylinders is similar to that of two tandem cylinders as it exhibits pre-coincidence and coincidence acoustic resonance. However, the reduced velocities at which "lock-in" occurs are significantly lower than that of the tandem cylinder configuration. The experiments revealed that the dominant sources for both pre-coincidence and coincidence acoustic resonance, are associated with vortices shed in the gap region between the cylinders and in the wake of the cylinders. These vortices are highly synchronised. This deviation from what was observed at coincidence resonance compared to the two tandem cylinder configuration is directly attributed to the difference in reduced velocities at which "lock-in" occurs. It seems as if the convection velocity of the vortices in the wake of the cylinders should be used in conjunction with the frequency ratio to better describe the acoustic resonance response of a system. This is particularly prudent when comparing one configuration with another. Interestingly, the reduced velocity seems to have a negligible influence on the location of sources/sinks in the gap region across all configurations. The main effect of varying the transverse spacing ratio is to shift the frequency at which resonance initiates. For smaller spacing ratios, this occurs closer to acoustic-Strouhal coincidence. The main effect of varying the streamwise spacing ratio is to alter the contribution that each source or sink in the gap region has on the generation of acoustic resonance rather than altering the generation mechanism itself.

The inline tube bundles resonated naturally in a manner similar to that reported in literature. Moreover, the response did not change appreciably when forced by a loudspeaker. The experiments revealed that resonance of the $P/D = 3$, $L/D = 3$ configuration is generated predominantly by vortex shedding from the first and second row of cylinders. Conversely, the strongest suppression of acoustic resonance occurs in the gap region between the first two rows. Since the large streamwise spacing affords the vortices more

time to develop, they will have a stronger contribution to the energy transfer mechanism which is similar to that observed when the streamwise pitch ratio of the four cylinders was increased.

The effect of altering the sound pressure level across the cylinders is to increase the "lock-in" range. That is, higher frequency shifts away from natural frequency of vortex shedding can be achieved by the acoustics at higher sound pressure levels. However, because of hysteresis, larger shifts during coincidence resonance are more readily attainable. When "locked-in", varying the sound pressure level was found to have no significant effect on the distribution of the vortices shed from the cylinders. In fact, varying the sound pressure level simply acted as a linear scaling factor for the magnitudes of the acoustic sources as shown by the normalised net acoustic energy transfer per streamwise location.

8.2 Future work

This study has provided a new understanding of how various bluff body systems resonate. The resonance was forced by loudspeakers, which meant that all efforts were concentrated solely on the energy transfer mechanism between the flow field and the sound field during "lock-in". As such, the mechanism which initiates acoustic resonance was not investigated. From the work presented here and from that of others, it is possibly easier to understand why coincidence resonance is initiated. However, uncertainty remains about pre-coincidence resonance and it should be investigated. Personally, it is thought that a hysteresis effect caused by the impingement of the vortices on the downstream cylinders at off-resonant conditions builds the pressure perturbations at the surface of the cylinders. However, the triggering system used for the PIV would have to be improved before this can be investigated experimentally.

The PIV experiments were completed for an inline array with large spacing. It is not recommended to further pursue PIV in an inline tube array (at least with smaller spacing) simply due to the difficult nature of the experiment. However, it is strongly recommended to further pursue PIV of the tandem cylinder and four cylinder configurations. If the PIV system can be improved to remove the effect of parallax, all contributions from the flow could be resolved. The resulting acoustic power maps could then be used to validate

CFD simulations. In turn, these validated codes could be used to investigate compact inline tube arrays and even other array patterns typically found in a heat exchanger. Furthermore, if stereoscopic PIV (or maybe even tomographic PIV) could be completed around the less complex configurations, three dimensional CFD simulations could be properly validated.

Some of the other issues addressed in this study could be further developed as well. For example, the effect of the sound pressure level was found to be negligible on the vortex formation process in the gap region and the wake of the cylinders. However, Ziada [66] reported a significant change in the vortex formation from the mouths of side-branches. The sound pressures applied by the loudspeakers induced acoustic particle velocities in the order of 15% of the mainstream flow which is smaller compared to those of Ziada [66]. Thus, it is recommended that higher sound pressures be investigated. Also, the importance of the convection velocity in the wake of the cylinders should be further investigated.

Bibliography

[1] M. S. Howe. The dissipation of sound at an edge. *Journal of Sound and Vibration*, 70(3):407–411, 1980.

[2] J. W. Hall, S. Ziada, and D. S. Weaver. Vortex-shedding from single and tandem cylinders in the presence of applied sound. *Journal of Fluids and Structures*, 18(6):741–758, 2003.

[3] F. L. Eisinger and R. E. Sullivan. Acoustic resonance in a package boiler and its solution - a case study. *Journal of Pressure Vessel Technology*, 129:759–762, 2007.

[4] A. Mohany. *Flow-Sound Interaction Mechanisms of a Single and Two Tandem Cylinders in Cross-Flow*. PhD thesis, McMaster University, 2006.

[5] A. Mohany and S. Ziada. Flow-excited acoustic resonance of two tandem cylinders in cross-flow. *Journal of Fluids and Structures*, 21(1):103–119, 2005.

[6] B. Massey. *Fluid Mechanics*. Taylor and Francis, London, 8th edition, 2006.

[7] J. H. Gerrard. The mechanics of the formation region of vortices behind bluff bodies. *Journal of Fluid Mechanics*, 25:401–413, 1966.

[8] M. M. Zdravkovich. *Flow Around Circular Cylinders : Fundamentals*, volume 1. Oxford University press, New York, 1997.

[9] J.H Lienhard. Synopsis of lift, drag, and vortex frequency data for rigid circular cylinders. Technical report, Washington State University, College of Engineering , Research Division, 1966.

[10] M. M. Zdravkovich. Flow induced oscillations of two interfering circular cylinders. *Journal of Sound and Vibration*, 101(4):511–521, 1985.

[11] M. M. Zdravkovich. *Flow Around Circular Cylinders : Applications*, volume 2. Oxford University press, New York, 2003.

[12] L. Ljungkrona, Ch. Norberg, and B. Sundén. Free-stream turbulence and tube spacing effects on surface pressure fluctuations for two tubes in an in-line arrangement. *Journal of Fluids and Structures*, 5(6):701–727, 1991.

[13] D. Sumner, S. J. Price, and M. P. Paidoussis. Flow-pattern identification for two staggered circular cylinders in cross-flow. *Journal of Fluid Mechanics*, 411:263–303, 2000.

[14] G. Xu and Y. Zhou. Strouhal numbers in the wake of two inline cylinders. *Experiments in Fluids*, 37(2):248–256, 2004.

[15] T. Igarashi. Characteristics of the flow around two circular cylinders arranged in tandem. *Japan Society of Mechanical Engineers*, 24(188):323–331, 1981.

[16] K. Lam, W. Q. Gong, and R. M. C. So. Numerical simulation of cross-flow around four cylinders in an in-line square configuration. *Journal of Fluids and Structures*, 24(1):34–57, 2008.

[17] T. Farrant, M. Tan, and W. G. Price. A cell boundary element method applied to laminar vortex-shedding from arrays of cylinders in various arrangements. *Journal of Fluids and Structures*, 14(3):375–402, 2000.

[18] K. Lam and S. C. Lo. A visualization study of cross-flow around four cylinders in a square configuration. *Journal of Fluids and Structures*, 6(1):109–131, 1992.

[19] K. Lam and X. Fang. The effect of interference of four equispaced cylinders in cross flow on pressure and force coefficients. *Journal of Fluids and Structures*, 9(2):195–214, 1995.

[20] D. S. Weaver and J. A. Fitzpatrick. A review of cross-flow induced vibrations in heat exchanger tube arrays. *Journal of Fluids and Structures*, 2(1):73–93, 1988.

[21] S. Ziada and A. Oengören. Vorticity shedding and acoustic resonance in an in-line tube bundle part I : Vorticity shedding. *Journal of Fluids and Structures*, 6(3):271–288, 1992.

[22] S. Ziada, A. Oengoren, and E. T. Bühlmann. On acoustical resonance in tube arrays part I : Experiments. *Journal of Fluids and Structures*, 3(3):293–314, 1989.

[23] S. Ziada and A. Oengören. Vortex shedding in an in-line tube bundle with large tube spacings. *Journal of Fluids and Structures*, 7(6):661–687, 1993.

[24] S. Ziada. Vorticity shedding and acoustic resonance in tube bundles. *Journal of the Brazilian Society of Mechanical Sciences and Engineering*, 28:186–189, 2006.

[25] J. A. Fitzpatrick, I. S. Donaldson, and W. McKnight. Strouhal numbers for flows in deep tube array models. *Journal of Fluids and Structures*, 2(2):145–160, 1988.

[26] D. S. Weaver, J. A. Fitzpatrick, and M. ElKashlan. Strouhal numbers for heat exchanger tube arrays in cross flow. *Journal of Pressure Vessel Technology*, 109(2):219–223, 1987.

[27] N. Curle. The influence of solid boundaries upon aerodynamic sound. *Proceedings of the Royal Society of London. Series A, Mathematical and Physical Sciences*, 231(1187):505–514, 1955.

[28] R. D. Blevins and M. M. Bressler. Experiments on acoustic resonance in heat exchanger tube bundles. *Journal of Sound and Vibration*, 164(3):503–533, 1993.

[29] R. D. Blevins. The effect of sound on vortex shedding from cylinders. *Journal of Fluid Mechanics*, 161:217–237, 1985.

[30] S. C. Kacker and R. S. Hill. Flow over a circular cylinder in the presence of standing sound waves. Address to power plant division, clarke chapman ltd., University of Newcastle Upon Tyne, 1974.

[31] A. Mohany and S. Ziada. A parametric study of the resonance mechanisms of two tandem cylinders in cross-flow. *Journal of Pressure Vessel Technology*, 131(2), 2009.

[32] J. A. Fitzpatrick. Flow/acoustic interactions of two cylinders in cross-flow. *Journal of Fluids and Structures*, 17(1):97–113, 2003.

[33] D. Rockwell and E. Naudascher. Review - self-sustaining oscillations of flow past cavities. *Journal of Fluids Engineering-Transactions of the ASME*, 100(2):152–165, 1978.

[34] A. Oengören and S. Ziada. Vorticity shedding and acoustic resonance in an in-line tube bundle part II : Acoustic resonance. *Journal of Fluids and Structures*, 6(3):293–302, 1992.

[35] B. J. Grotz and F. R. Arnold. Flow-induced vibrations in heat exchangers. Technical report, Stanford University.

[36] Y. N. Chen and W. C. Young. The orbital movement and the damping of the fluidelastic vibration of tube banks due to vortex formation: Part 3 - damping capability of the tube bank against vortex-excited sonic vibration in the fluid column. *Journal of Engineering for Industry*, 96(3):1072–1075, 1974.

[37] J. A. Fitzpatrick and I. S. Donaldson. Effects of scale on parameters associated with flow induced noise in tube arrays. pages 243–250, New Orleans, LA, USA, 1984. ASME.

[38] S. Ziada, A. Oengören, and E. T. Bühlmann. On acoustical resonance in tube arrays part II : Damping criteria. *Journal of Fluids and Structures*, 3(3):315–324, 1989.

[39] M. J. Lighthill. On sound generated aerodynamically. i. general theory. *Proceedings of the Royal Society of London. Series A, Mathematical and Physical Sciences*, 211(1107):564–587, 1952.

[40] E Goldstein, M. *Aeroacoustics*. McGraw-Hill, New York, 1976.

[41] M. J. Lighthill. The bakerian lecture, 1961. sound generated aerodynamically. *Proceedings of the Royal Society of London. Series A, Mathematical and Physical Sciences*, 267(1329):147–182, 1962.

[42] S. W. Rienstra and A. Hirschberg. An introduction to acoustics. Technical Report IWDE 92-06, Eindhoven University of Technology, 2002.

[43] M. S. Howe. Sound generated by fluid-structure interactions. *Computers & Structures*, 65(3):433–446, 1997.

[44] O. M. Phillips. The intensity of aeolian tones. *Journal of Fluid Mechanics*, 1(6):607–624, 1956.

[45] A. Powell. Theory of vortex sound. *Journal of the Acoustical Society of America*, 36(1):177–195, 1964.

[46] M. S. Howe. Contributions to theory of aerodynamic sound, with application to excess jet noise and theory of flute. *Journal of Fluid Mechanics*, 71(4):625–673, 1975.

[47] M. P. Norton and D. G. Karczub. *Fundamentals of noise and vibration analysis for engineers*. Cambridge University Press, 2003.

[48] M. S. Howe. *Theory of vortex sound*. Cambridge University Press, 2003.

[49] S. Dequand, S. J. Hulshoff, and A. Hirschberg. Self-sustained oscillations in a closed side branch system. *Journal of Sound and Vibration*, 265(2):359–386, 2003.

[50] M. S. Howe. *Acoustics of fluid-structure interactions*. Cambridge University Press, 1998.

[51] B. T. Tan, M. C. Thompson, and K. Hourigan. Sources of acoustic resonance generated by flow around a long rectangular plate in a duct. *Journal of Fluids and Structures*, 18(6):729–740, 2003.

[52] M. C. Welsh, A. N. Stokes, and R. Parker. Flow-resonant sound interaction in a duct containing a plate, part I : Semi-circular leading edge. *Journal of Sound and Vibration*, 95(3):305–323, 1984.

[53] S. A. T. Stoneman, K. Hourigan, A. N. Stokes, and M. C. Welsh. Resonant sound caused by flow past 2 plates in tandem in a duct. *Journal of Fluid Mechanics*, 192:455–484, 1988.

[54] K. Hourigan, M. C. Welsh, M. C. Thompson, and A. N. Stokes. Aerodynamic sources of acoustic resonance in a duct with baffles. *Journal of Fluids and Structures*, 4(4):345–370, 1990.

[55] P. Oshkai and T. Yan. Experimental investigation of coaxial side branch resonators. *Journal of Fluids and Structures*, 24(4):589–603, 2008. Oshkai, P. Yan, T.

[56] A. Mohany and S. Ziada. Numerical simulation of the flow-sound interaction mechanisms of a single and two-tandem cylinders in cross-flow. *Journal of Pressure Vessel Technology*, 131(3), 2009.

[57] E. Reyes, S. L. Finnegan, and C. Meskell. Simulation of flow-induced acoustic resonance of bluff bodies in duct flow. In *ASME 2010 3rd Joint US-European Fluids Engineering Summer Meeting and 8th International Conference on Nanochannels, Microchannels, and Minichannels*, Montreal, Canada, 2010.

[58] Inc. ANSYS. *Acoustic Fluid Fundamentals, Release 11.0 Documentation for ANSYS*. SAS IP, Inc., 2007.

[59] R. Parker. Resonance effects in wake shedding from parallel plates: Calculation of resonant frequencies. *Journal of Sound and Vibration*, 5(2):330–343, 1967.

[60] M. Raffel, C. Willert, S. Wereley, and J. Kompenhans. *Particle Image Velocimetry: A Practical Guide*. Heidelberg, 2 edition, 2007.

[61] C. D. Meinhart, S. T. Wereley, and J. G. Santiago. A piv algorithm for estimating time-averaged velocity fields. *Journal of Fluids Engineering-Transactions of the ASME*, 122(2):285–289, 2000.

[62] M. Stanislas, K. Okamoto, C. Kähler, and J. Westerweel. Main results of the second international piv challenge. *Experiments in Fluids*, 39:170–191, 2005.

[63] J. Westerweel. *Digital particle image velocimetry - theory and application*. PhD thesis, Technical University of Delft, 1993.

[64] S. Ziada and E. T. Bühlmann. Self-excited resonances of two side-branches in close proximity. *Journal of Fluids and Structures*, 6(5):583–601, 1992.

[65] S. Ziada and S. Shine. Strouhal numbers of flow-excited acoustic resonance of closed side branches. *Journal of Fluids and Structures*, 13(1):127–142, 1999.

[66] S. Ziada. A flow visualization study of flow- acoustic coupling at the mouth of a resonant side-branch. *Journal of Fluids and Structures*, 8(4):391–416, 1994.

[67] S. Hein and W. Koch. Acoustic resonances and trapped modes in pipes and tunnels. *Journal of Fluid Mechanics*, 605:401–428, 2008.

[68] G.J. Bennett. *Noise source identification for ducted fans*. PhD thesis, University of Dublin, 2006.

[69] C. Tropea, A. L. Yarin, and J. F. Foss, editors. *Springer Handbook of Experimental Fluid Mechanics*. Heidelberg : Springer, 2007.

[70] N. Mahir and D. Rockwell. Vortex formation from a forced system of two cylinders. part I : Tandem arrangement. *Journal of Fluids and Structures*, 10(5):473–489, 1996.

[71] J. A. Fitzpatrick and I. S. Donaldson. Row depth effects on turbulence spectra and acoustic vibrations in tube banks. *Journal of Sound and Vibration*, 73(2):225–237, 1980.

[72] Y. A. Çengel, J. M. Cimbala, and M. Kanoglu. *Fluid mechanics: Fundamentals and applications*. McGraw-Hill Higher Education, 2006.

[73] S. Ziada, H. Ng, and C. E. Blake. Flow excited resonance of a confined shallow cavity in low mach number flow and its control. *Journal of Fluids and Structures*, 18(1):79–92, 2003.

[74] S. Ziada. Flow-excited acoustic resonance in industry. *Journal of Pressure Vessel Technology*, 132(1):015001, 2010.

[75] W. M. Jungowski, K. K. Botros, and W. Studzinski. Cylindrical side-branch as tone generator. *Journal of Sound and Vibration*, 131(2):265–285, 1989.

[76] P. C. Kriesels, M. C. A. M. Peters, A. Hirschberg, A. P. J. Wijnands, A. Iafrati, G. Riccardi, R. Piva, and J. C. Bruggeman. High amplitude vortex-induced pulsations in a gas transport system. *Journal of Sound and Vibration*, 184(2):343–368, 1995.

[77] D. A. Russell, J. P. Titlow, and Y. J. Bemmen. Acoustic monopoles, dipoles, and quadrupoles: An experiment revisited. *American Journal of Physics*, 67(8):660–664, 1999.

[78] A. Powell. Some aspects of aeroacoustics - from rayleigh until today. *Journal of Vibration and Acoustics-Transactions of the ASME*, 112(2):145–159, 1990.

Appendix A

Derivation of E^*

Buckingham-Pi analysis was used to non-dimensionalise the net acoustic energy transfer per streamwise location (E) in order to evaluate the effect that the SPL had on the distribution and strength of the sources. Figure A.1 shows a schematic of the variables in the system. From this, it can be seen that

$$E = f(P_a, D, V_\infty, P, \rho, \mu, c).$$

Table A.1 lists the dependent variable (E) and the independent variables in terms of their dimensions and primary dimensions. Mass (M), length (L) and time (t) have been chosen as the primary dimensions. There will be five separate dimensional groups. The acoustic pressure (P_a), the cylinder diameter (D) and the mainstream velocity (V_∞) have been selected as the repeating variables. The non-dimensional groups can be defined as

$$\Psi_1 = (P_a^{a1})(D^{b1})(V_\infty^{c1})(E) = (\mathrm{ML^{-1}t^{-2}})^{a1}(\mathrm{L})^{b1}(\mathrm{Lt^{-1}})^{c1}(\mathrm{Mt^{-2}})$$
$$\Psi_2 = (P_a^{a2})(D^{b2})(V_\infty^{c2})(P) = (\mathrm{ML^{-1}t^{-2}})^{a2}(\mathrm{L})^{b2}(\mathrm{Lt^{-1}})^{c2}(L)$$
$$\Psi_3 = (P_a^{a3})(D^{b3})(V_\infty^{c3})(\rho) = (\mathrm{ML^{-1}t^{-2}})^{a3}(\mathrm{L})^{b3}(\mathrm{Lt^{-1}})^{c3}(\mathrm{ML^{-3}})$$
$$\Psi_4 = (P_a^{a4})(D^{b4})(V_\infty^{c4})(\mu) = (\mathrm{ML^{-1}t^{-2}})^{a4}(\mathrm{L})^{b4}(\mathrm{Lt^{-1}})^{c4}(\mathrm{ML^{-1}t^{-1}})$$
$$\Psi_5 = (P_a^{a5})(D^{b5})(V_\infty^{c5})(c) = (\mathrm{ML^{-1}t^{-2}})^{a5}(\mathrm{L})^{b5}(\mathrm{Lt^{-1}})^{c5}(\mathrm{Lt^{-1}}).$$

E	P_a	D	V_∞	P	ρ	μ	c
$\mathrm{J/m^2}$	$\mathrm{kg/ms^2}$	m	m/s	m	$\mathrm{kg/m^3}$	$\mathrm{Ns/m^2}$	m/s
$\mathrm{Mt^{-2}}$	$\mathrm{ML^{-1}t^{-2}}$	L	$\mathrm{Lt^{-1}}$	L	$\mathrm{ML^{-3}}$	$\mathrm{ML^{-1}t^{-1}}$	$\mathrm{Lt^{-1}}$

Table A.1: Dependent and independent variables used for non-dimensional analysis.

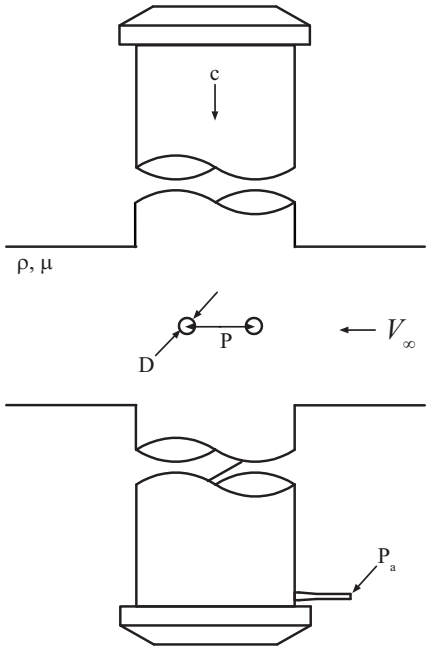

Figure A.1: Parameters of the system used for non-dimensional analysis.

As these groups are non-dimensional, each Ψ term can be related to the primary dimensions using $M^0L^0t^0$. It follows that

$$\Psi_1 = \frac{E}{P_a D}$$
$$\Psi_2 = \frac{P}{D}$$
$$\Psi_3 = \frac{\rho V_\infty^2}{P_a}$$
$$\Psi_4 = \frac{\mu V_\infty}{P_a D}$$
$$\Psi_5 = \frac{c}{V_\infty}$$

Ψ_3, Ψ_4 and Ψ_5 can be modified into the same form as other established dimensionless numbers. Using the guidelines set out by Çengel and Cimbala [72] it follows that

$$\Psi_3 \Rightarrow 2(\Psi_3)^{-1}\Psi_5 = \frac{2P_a}{\rho V_\infty^2 Ma} = P^*$$
$$\Psi_4 \Rightarrow (\frac{\Psi_4}{\Psi_5})^{-1} = \frac{\rho V_\infty D}{\mu} = Re$$
$$\Psi_5 \Rightarrow (\Psi_5)^{-1} = Ma$$

Thus the non-dimensional acoustic energy transfer per stream wise location can be described by

$$E^* = \frac{E}{P_a D} = f(P/D, P^*, Re, Ma).$$

Appendix B

Sum of Correlation PIV Versus Standard PIV

The ensemble correlation or sum of correlation PIV algorithm was used for each cylinder configuration. The reason for this is because the ensemble correlation algorithm provides a better signal to noise ratio when there are fluctuations in the seeding density or illumination. Using four cylinders, tests were completed at a mainstream velocity of $V_\infty = 24.2$ m/s. The loudspeaker frequency was set to $f_a = 329$ Hz and the input voltage was 424 mV. Contours of the net acoustic energy calculated using the ensemble correlation PIV algorithm can be seen in Fig. B.1(a). Contours of the net acoustic energy calculated using the standard PIV algorithm can be seen in Fig. B.1(b). It should be noted that the algorithms were applied to the same data set and that the same calculation parameters were used for each algorithm. The overall distributions of the sources are qualitatively very similar. However, the standard PIV algorithm seems to smooth out the sources/sinks compared to the ensemble correlation PIV algorithm.

Figure B.2 plots E^* for each algorithm. The maximum difference between the two algorithms is roughly 25% and this occurs in the wake of the cylinders. However, for the most part, the profiles show decent correlation which means that despite the discrepancy in the local acoustic energy in the wake of the cylinders, the average amount of acoustic energy is actually quite similar. The difference in the scales of Fig. B.1 simply means that the sum of correlation PIV algorithm resolves more intense acoustic energy locally whilst the conventional PIV algorithm smoothes the intensity over a larger area. Figure B.3 shows typical correlation maps for the same interrogation window calculated by the two

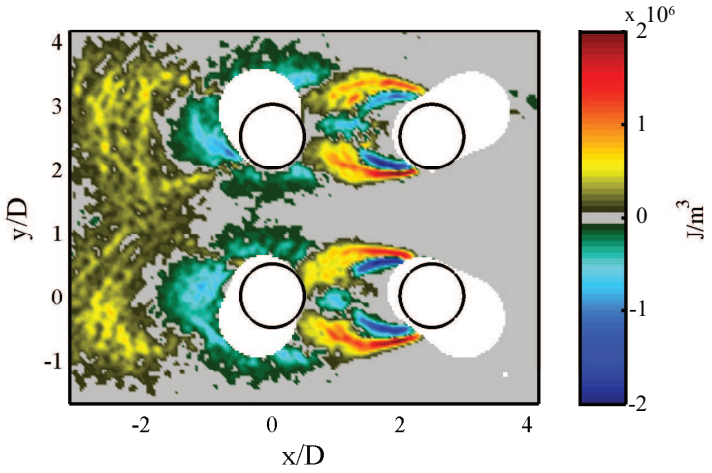

(a) Ensemble correlation PIV

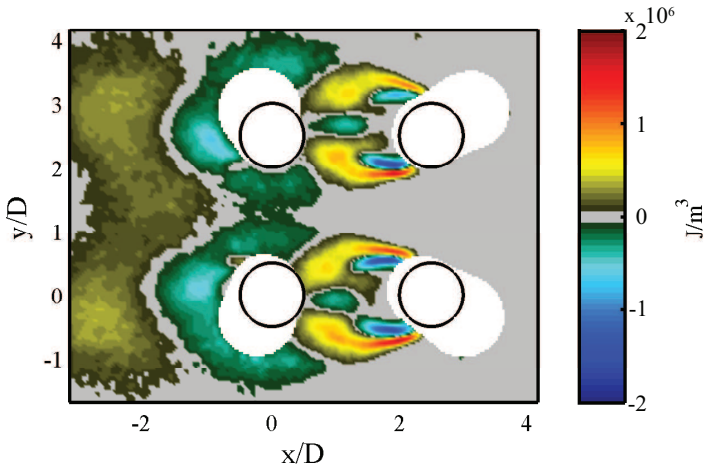

(b) Standard PIV

Figure B.1: Comparison of the net acoustic energy per cycle calculated using two different PIV algorithms.

techniques. Figure B.3(a) is the correlation map generated from the ensemble PIV technique with 100 image pairs whilst Fig. B.3(b) shows the correlation map generated by a single image pair. The signal to noise ratio of the ensemble correlation method is much stronger than that of the single image pair which means that it is more likely to produce a correct vector in challenging PIV conditions. Hence, it should be more forgiving in a geometrically complex setup which is why it was chosen for use over the standard PIV algorithm.

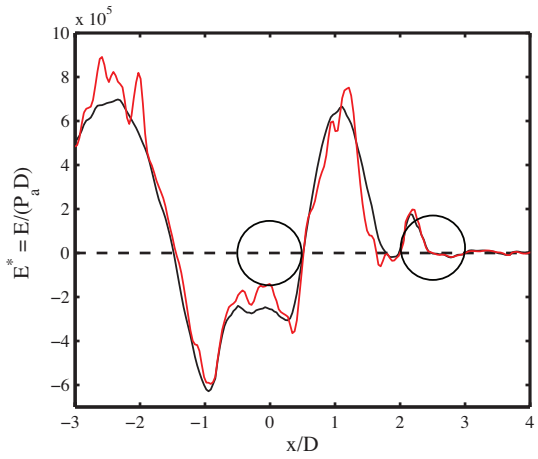

Figure B.2: Comparison of E^* calculated using two different PIV algorithms. — Ensemble correlation PIV; — Standard PIV.

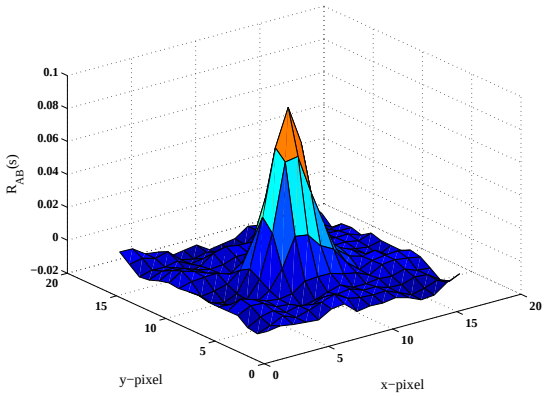

(a) Ensemble correlation PIV - 100 image pairs

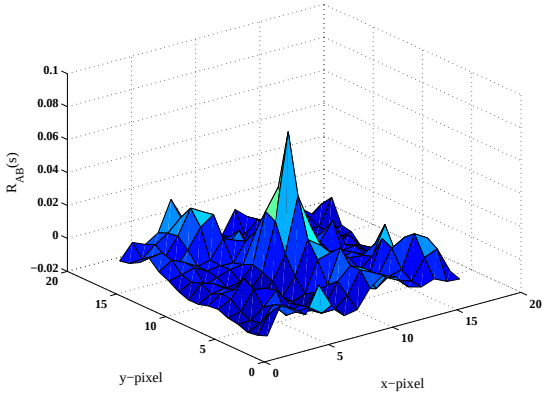

(b) Conventional PIV - 1 image pair

Figure B.3: Correlation maps of an interrogation window using two different PIV algorithms.

Appendix C

Cavities

C.1 Fluid mechanics

Piping systems found in gas power plants often involve interactions between the main duct and a side-branch or cavity. A series of classifications have been made to describe cavities based on the characteristics of the flow over and within them. The flow over the cavity strongly depends on its geometry, which as shown in Fig. C.1 has two limiting dimensions. These are the cavity length L_c and the cavity depth D_c. Defining the cavity length to depth ratio, L_c/D_c gives two broad classifications of cavity: shallow cavities and deep cavities. Shallow cavities have $L_c/D_c \geq 1$ whilst deep cavities have $L_c/D_c < 1$. Shallow cavities can be further sub-classified into open and closed cavities. Open shallow cavities occur when the flow from the upstream corner impinges on the downstream corner. Closed shallow cavities occur when the flow from the upstream corner attaches onto the base of the cavity before impinging on the downstream corner [73].

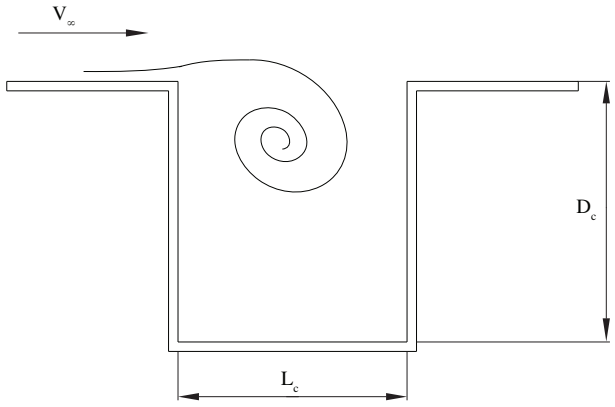

Figure C.1: The geometric parameters of a side-branch cavity.

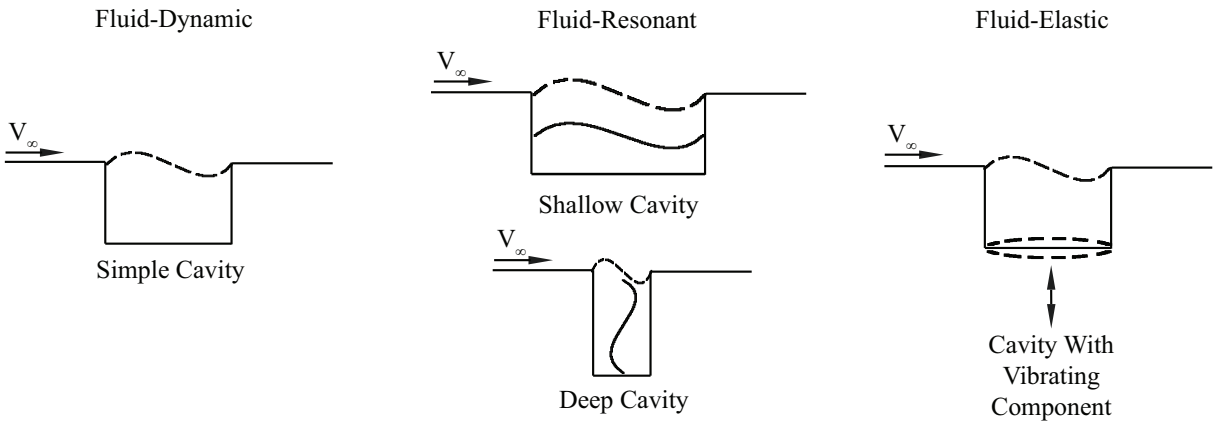

Figure C.2: Cavity classifications, redrawn from Rockwell and Naudascher [33].

An in depth review of the unstable pressure an oscillation over the mouth of a cavity was completed by Rockwell and Naudascher [33]. They classified the oscillating flow in three ways: fluid-dynamic, fluid-resonant and fluid-elastic. Fluid-dynamic oscillations occur when L_c is much smaller than the acoustic wavelength of the noise generated in the cavity [33]. Oscillations occur due to amplification of the unstable disturbances in the cavity shear layer and their magnitude depends heavily on the presence of the downstream edge [33]. Interaction with the downstream edge induces up a feedback loop with the upstream edge. Perturbations caused by the downstream impingement produce vorticity fluctuations near the shear layer origin. This in turn feeds back into the shear layer and hence amplifies the disturbances even more [33]. This feedback loop is necessary in order to produce coherent oscillating flow in the cavity [33].

Fluid-resonant oscillations are strongly coupled to the resonant acoustic wave within the cavity. Here, the oscillation frequencies are high enough that the acoustic wave length is of the same magnitude as a characteristic dimension of the cavity [33]. For a fluid-resonant cavity flow, the feedback loop which sustains the oscillations is due solely to the resonant sound field [74]. For shallow cavities the associated wave form is longitudinal whilst for deep cavities the acoustic wave form is transverse, as can be seen in Fig. C.2.

The final classification is fluid-elastic oscillation and this refers to applications where at least one of the walls in the cavity is free to move, as long as the displacement is large enough to exert a feedback control on the shear layer perturbations [33]. An example of a fluid-elastic application might be a loud speaker mounted at one end of the cavity which

is allowed to vibrate freely. The oscillations of the flow obviously depend on the elastic, inertial and damping properties of the system, thus this type of fluid-elastic flow can be quite limited in its applications.

C.2 Resonant acoustic behaviour

Acoustic resonance in cavity piping systems has been studied in some depth by various authors including Ziada and Shine [65], Ziada and Bülhmann [64], Jungowski *et al.* [75], Ziada *et al.* [73], Dequand *et al.* [49], Kriesels *et al.* [76], Oshkai and Yan [55]. It has been agreed that flows in the main duct can generate self sustaining oscillations at resonant conditions within the side-branches. These oscillations can exceed the dynamic head in the main pipe by several multiples. This obviously poses concerns over the vibratory stability of these systems. Typical side branch geometries included single t-junctions, tandem t-junctions and coaxial side-branch junctions. Figure C.3 shows the aeroacoustic response for a coaxial side-branch measured by Kriesels *et al.* [76] but adapted from Dequand *et al.* [49]. The resonant behaviour of the system is similar to that of bluff bodies in that "lock-in" can occur when the hydrodynamic modes across the mouths of the branches are near to the acoustic modes of the duct. As before, when "locked-in", the flow field becomes entrained to the sound field and there is a sudden increase in the acoustic pressure. The first mode shape for the three junctions mentioned above is shown in Fig. C.4. For the first mode, each individual branch consists of an odd multiple of quarter wavelengths [65].

Acoustic resonance in cavities depends on various factors. Some of these factors include the number of branches, the diameter ratio L_c/H (where H is the width/diameter of the main channel), the Strouhal number with respect to the cavity diameter St_{L_c} and the dimensionless acoustic velocity ratio in the duct. The resonance of multiple branch systems is much stronger than that of a single branch system. This is because acoustic coupling between the branches greatly reduces acoustic radiation into the main pipe. For single branches, radiation losses increase with diameter ratio [75]. However the converse is true for multiple branches, particularly coaxial systems with large diameter ratios. They dissipate the least amount of energy into the main duct. This makes them very susceptible

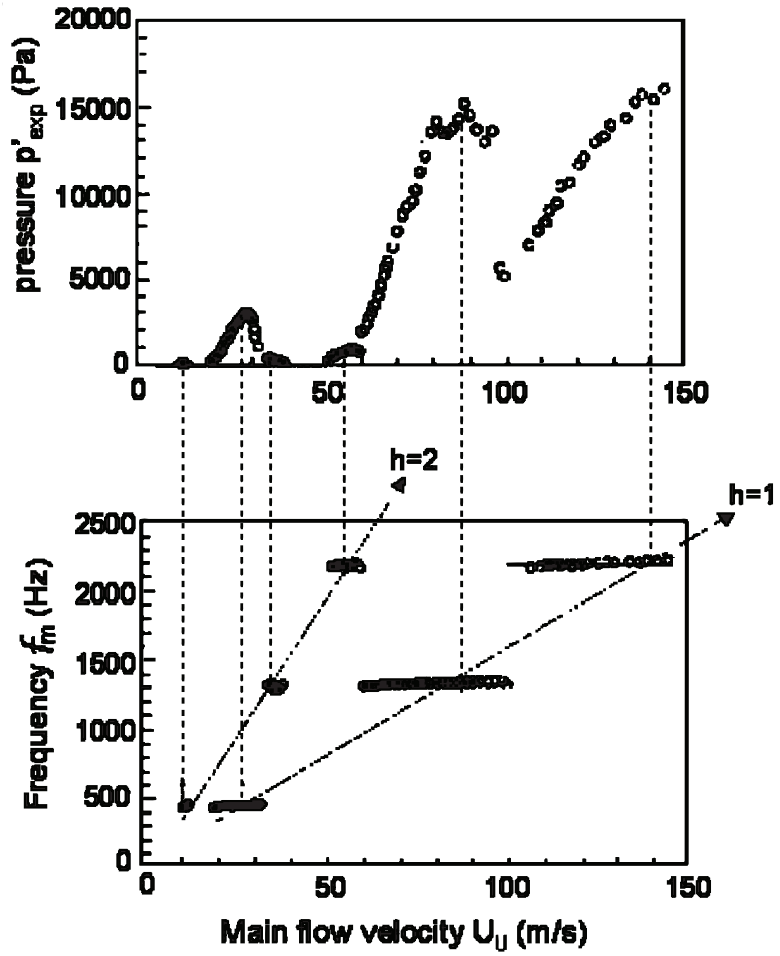

Figure C.3: The aeroacoustic response of a coaxial side-branch resonator measured by Kriesels *et al.* [76]. It shows that hydrodynamic flow across the mouths of the branches can "lock-in" to different acoustic modes of the duct in a similar fashion to that of bluff bodies, adapted from Dequand *et al.* [49].

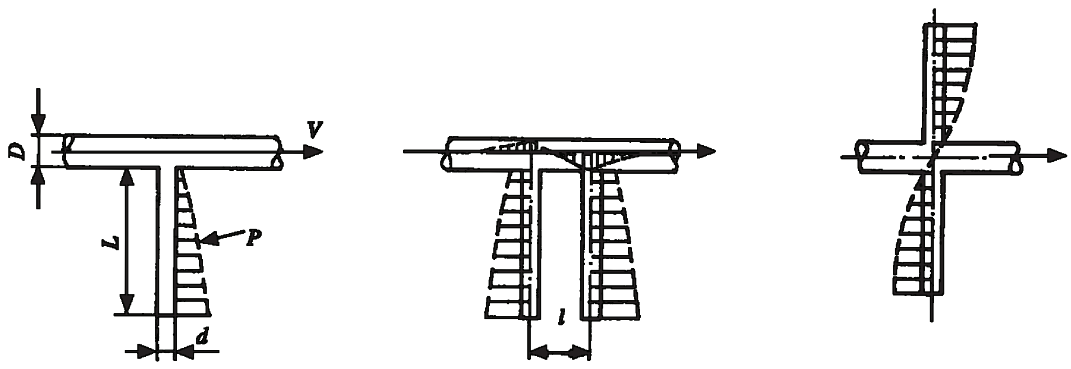

Figure C.4: Acoustic mode shapes in different piping systems, Ziada and Shine [65].

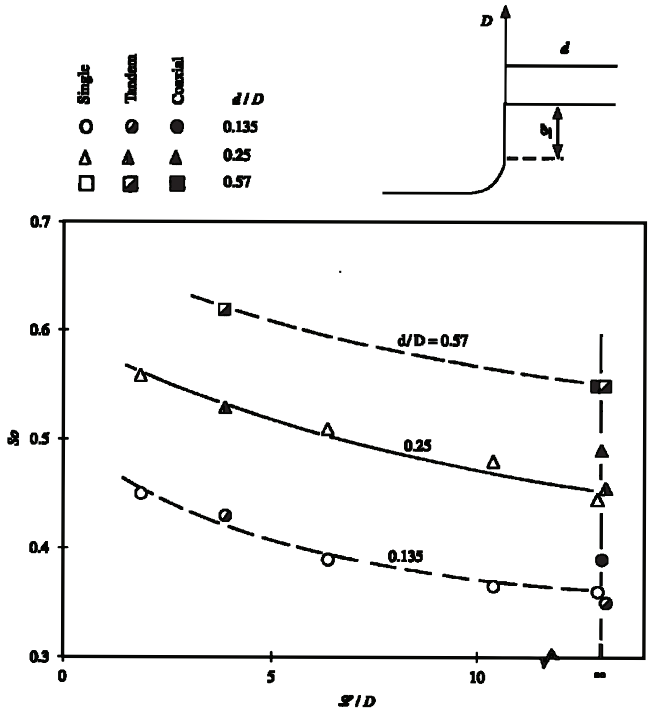

Figure C.5: Design chart of critical Strouhal numbers at the onset of resonance in a side-branch cavity, Ziada and Shine [65].

to acoustic resonance [65, 64]. For self-excited co-axial systems, acoustic resonance occurs over for Strouhal numbers in the range $St_{L_c} = 0.27 - 0.55$. However, the actual onset of resonance greatly depends on the diameter ratio [64]. Ziada and Shine [65] found that as the diameter ratio of the system decreases, so too does the Strouhal number at the onset of resonance. This means that acoustic resonance occurs at higher flow velocities as L_c/H gets smaller. This behaviour was attributed to changes in the convection speed of the vortices across the mouths of the branches. According to Ziada and Shine [65], stronger vortices formed from large side-branch mouths have more favourable phasing between the convection speed of the vortex and the fluctuating acoustic particle velocity through the branch. Interestingly, Ziada and Shine [65] also found that visco-thermal and radiation losses had no effect on Strouhal number at the onset of resonance. The design chart developed by Ziada and Shine [65] to predict the onset of resonance is shown in Fig. C.5.

To study the effect of the acoustic particle velocity on the onset of acoustic resonance, Ziada [66] completed an in depth study and flow visualisation of a co-axial side branch system. He investigated the vortex shedding patterns and acoustic responses of the sys-

tem to a loudspeaker, which controlled the excitation level in the branches. The study highlighted that the mechanisms causing impingement in the shear layers are considerably different between resonant and off-resonant conditions. It was found that the instantaneous position and phase speed of the vortices in the shear layer depend on St_{L_c} and the amplitude of U_a.

Large values of the velocity ratio ($U_a/V_\infty > 0.05$) tend to force the formation of the vortex to occur near the upstream edge whilst simultaneously pushing it into the freestream as it propagates downstream. Increasing the amplitude of the acoustic oscillation preserves the vorticity of the shear layer and increases its ability to generate acoustic power. However, there is a limit to how large an oscillation amplitude can be applied to a system and still be able to generate acoustic power. Beyond this limit, increasing U_a/V actually tends to saturate the vortex and sound starts to be absorbed by the system rather than generated. This is referred to as "vortex-damping". The value of U_a/V_∞ at which the vortices form near the upstream edge depends on St_{L_c}. As a result, the limiting amplitude for the onset of vortex-damping is found to be higher for lower Strouhal numbers than for higher Strouhal numbers.

The study by Ziada [66] published extensive flow visualisation images but could only provide a qualitative impression of the vortex shedding process throughout a whole acoustic wave cycle. Furthermore he could only qualitatively describe how the system generated or absorbed acoustic power. Oshkai and Yan [55] completed a similar study of a coaxial side-branch resonator using PIV rather than flow-visualisation. In doing so, they gathered quantitative and qualitative information on the flow structure, which agreed well with the flow visualisation of Ziada [66]. Moreover, they used this flow field information along with Howe's theory of aerodynamic sound, see Ch. 3.2, to calculate the net acoustic sources and sinks across the mouths of the branches. For a wide duct where the opposite shear layers cannot interact, Oshkai and Yan [55] found the dominant acoustic source generated power in the region just in front of the downstream edge. This highlighted the importance of vortex impingement on the downstream edge for the generation of acoustic energy. However, as the duct width got narrower, they found the interaction between the opposite shear layers caused the dominant source to move upstream towards the leading edge.

Appendix D

Acoustic Sources

Classical acoustics deals with the sound generated by the vibration of solid bodies while aeroacoustics deals with the sound generated by airflow. Lighthill [39] described three ways in which kinetic energy in airflow can be converted into acoustic energy:

1. By forcing the mass in a fixed region of space to fluctuate
2. By forcing momentum in a fixed region of space to fluctuate or alternatively by forcing the rates of mass flux across a fixed surface to vary
3. By forcing the rates of momentum flux across a fixed surface to vary

The first case describes the most basic acoustic mechanism, the source, or acoustic monopole. Here it is changes in the mass outflow from the monopole that generates sound [41]. The strength of a monopole is equal to the rate of variation of matter out of the source, $\dot{q}(t)$. As the pressure away from a monopole drops off with the first inverse power of distance [39, 41], its pressure fluctuations takes the form:

$$p - p_0 = \frac{\dot{q}(t - r/c)}{4\pi r} \tag{D.1}$$

where $t - r/c$ is the retarded time i.e., the time which a wave travelling at the speed of sound c had to leave the source in order to arrive at the receiver at time t. It should be noted that the above equation only describes the pressure fluctuations for concentrated matter into a point. However, a distribution of sources can be used to describe the sound generated into an extended region [41]. In this case, the pressure fluctuations need to be described by a volume integral and take the form:

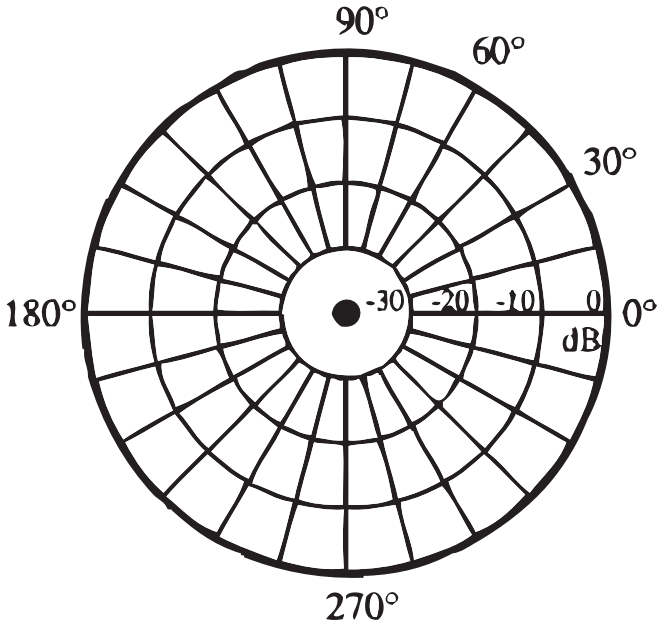

Figure D.1: Far field directivity of a compact acoustic monopole, Russell *et al.* [77].

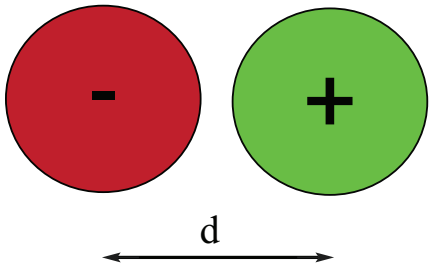

Figure D.2: Representation of an acoustic dipole using two acoustic sources.

$$p - p_0 = \frac{1}{4\pi} \int \frac{\partial}{\partial t} Q \left(\mathbf{y}, t - \frac{|\mathbf{x} - \mathbf{y}|}{c} \right) \frac{\mathrm{d}\mathbf{y}}{|\mathbf{x} - \mathbf{y}|} \tag{D.2}$$

where $\partial d / \partial t$ is the source strength per unit volume [39]. The directivity of a simple monopole is shown in Fig. D.1. As can be seen, sound radiates omni-directionally forming concentric circles making it a very efficient mechanism in the far field. An example of a monopole sound field is one where new matter is introduced into the medium, such as that generated by a siren.

The second case described above is that of a dipole which may also be thought of as two monopoles of equal strength but opposite phase separated from each other by some small distance d. A conceptual schematic of a dipole can be seen in Fig. D.2. A dipole generates sound by injecting momentum rather than mass into the sound field and so is

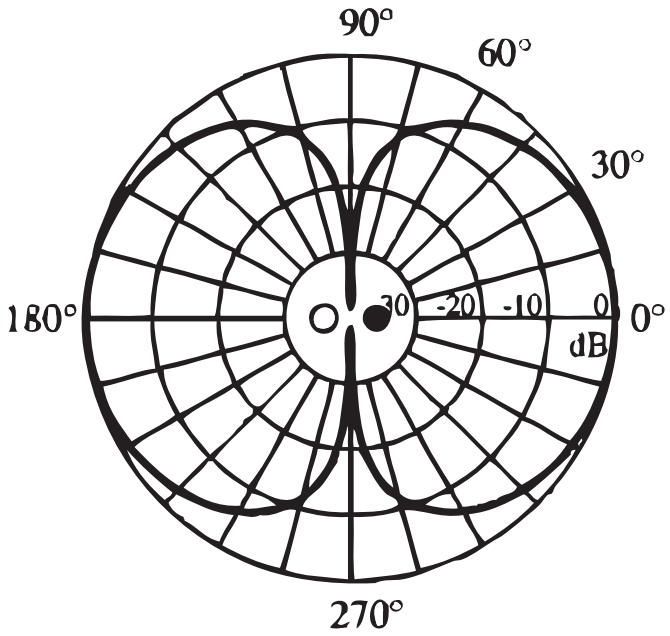

Figure D.3: Far field directivity of a compact acoustic dipole, Russell *et al.* [77].

equivalent to a force concentrated at a point. The magnitude and direction of a dipole can vary [41], which means a dipole is a vector quantity. The strength of the dipole is equal to the force exerted onto the field whilst its magnitude is equal to its strength multiplied by the separation between the two monopoles, d. The fluctuating pressure field of a dipole takes the form:

$$p - p_0 = -\frac{\partial}{\partial x_i}\left(\frac{f_i(t - r/c)}{4\pi r}\right) \tag{D.3}$$

where the subscript i represents the spatial dimensions of the receiver and f_i is the force [39]. In similar fashion to the monopole, a distribution of dipoles can be used to describe the sound generated in an extended region. In this case the fluctuating pressure takes the form:

$$p - p_0 = -\frac{1}{4\pi}\frac{\partial}{\partial x_i}\int F_i\left(\mathbf{y}, t - \frac{|\mathbf{x} - \mathbf{y}|}{c}\right)\frac{\mathrm{d}\mathbf{y}}{|\mathbf{x} - \mathbf{y}|} \tag{D.4}$$

where F_i is the strength of the dipole per unit volume and is equal to the applied force [41]. The directivity pattern of a dipole is shown in Fig. D.3. As can be seen, most of the flow oscillates on lobbed paths in opposite directions away from the two sources. According to Powell [78], this pattern is comparable to that of a vortex ring. As the fluid near the two

sources has a greater degree of freedom than a monopole, it is less effective in pushing fluid outwards to drive radiation into the far field. This makes the acoustic dipole an inefficient acoustic mechanism compared to the monopole [39]. An example of a dipole sound field is one generated by a force exerted on the medium, such as vortex shedding from a cylinder.

The third case described above refers to a quadrupole. Here the rate of momentum flux, or the rate of transfer of momentum across a unit area is forced to vary. Quadrupoles are constructed by pairing two dipoles (or four monopoles) of equal strength but opposite phase at a small distance, D apart from each other. Figure D.4 shows a conceptual schematic of an acoustic quadrupole. The relative orientation of the two dipoles determines whether the quadrupoles is a lateral quadrupole or a longitudinal quadrupole. Lateral quadrupoles occur when the axes of the two dipoles are perpendicular to each other whilst longitudinal quadrupoles occur when the axes of the dipoles coincide. The directivity patterns of a longitudinal and lateral quadrupole are sketched in Fig. D.5. The lateral quadrupole consists of four lobes of equal strength but opposite sign whilst the longitudinal quadrupole consists of only two lobes. In the same manner as before, the fluid near the quadrupole has more degrees of freedom than a dipole so is even less effective in driving the far field and hence is less efficient than both the monopole and the dipole. Each dipole exerts equal but opposite forces on the fluid element and the resulting stress field is a measure of its strength. The distribution of quadrupoles to describe the sound generated in an extended region takes the form:

$$p - p_0 = \frac{1}{4\pi} \frac{\partial^2}{\partial x_i \partial x_j} \int T_{ij} \left(\mathbf{y}, t - \frac{|\mathbf{x} - \mathbf{y}|}{c} \right) \frac{\mathrm{d}\mathbf{y}}{|\mathbf{x} - \mathbf{y}|} \tag{D.5}$$

where T_{ij} is the strength per unit volume, $T_{i,j}$ of the quadrupole. T_{ij} is also called the Lighthill Stress tensor and will be discussed more in the next section. An example of a quadrupole sound field is one induced by stress on the medium, such as aerodynamic sound generated by a jet.

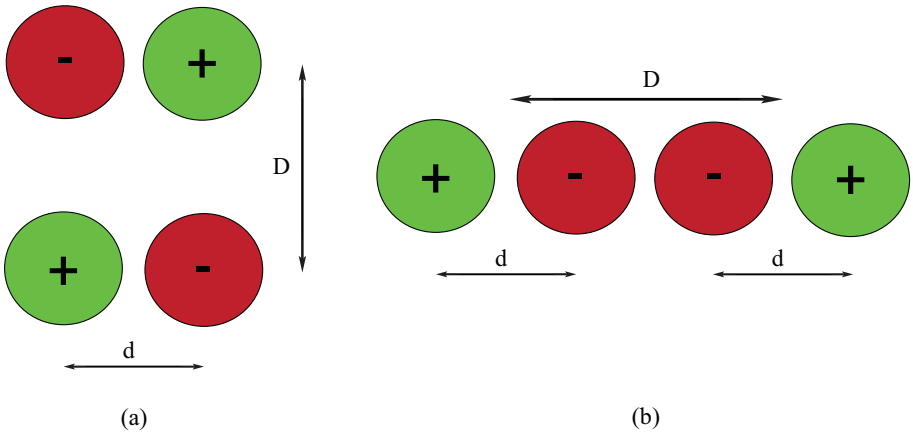

Figure D.4: Representation of an acoustic quadrupole using four acoustic sources or two acoustic dipoles. (a) Lateral quadrupole; (b) Longitudinal quadrupole.

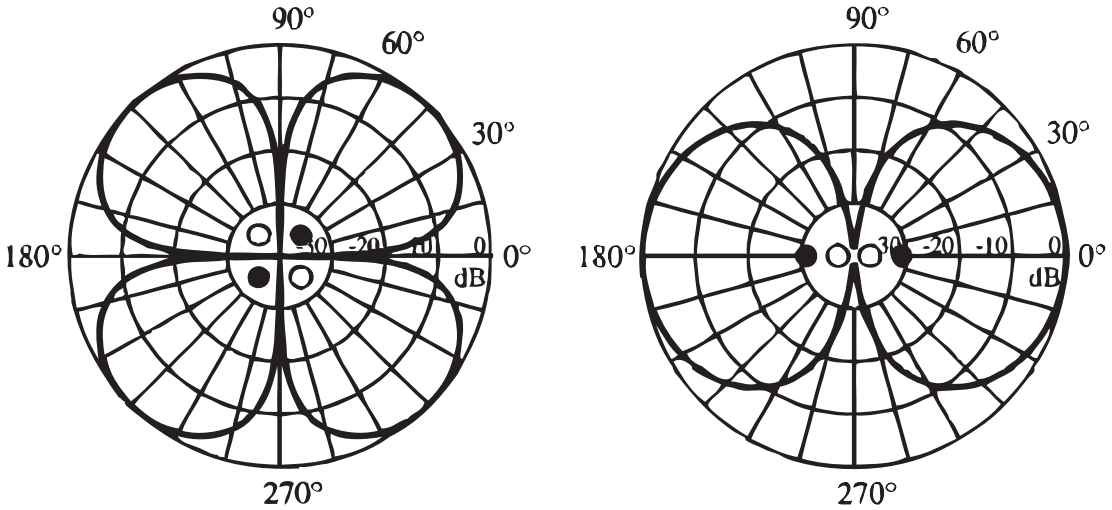

(a) Lateral quadrupole (b) Longitudinal quadrupole

Figure D.5: Far field directivity of a compact acoustic quadrupole, Russell *et al.* [77].